

ASN 6897

SPECTROSCOPIC CHARACTERIZATION OF NOVEL CLUSTER IONS

By

DANIEL E. LESSEN

A DISSERTATION PRESENTED TO THE GRADUATE SCHOOL
OF THE UNIVERSITY OF FLORIDA IN PARTIAL FULFILLMENT
OF THE REQUIREMENTS FOR THE DEGREE OF
DOCTOR OF PHILOSOPHY

UNIVERSITY OF FLORIDA

1992

ACKNOWLEDGEMENTS

The completion of this work would not have been possible without the help of the other members of the research group: Dr. Philip Brucat, my principal advisor, and fellow graduate student Robert Asher. Dr. Brucat, served as scientific mentor, motivator and friend. His enthusiasm in the quest for scientific knowledge was infectious. In the beginning years of my graduate career, it was Phil who taught me the art of many different occupations besides chemist: namely, electrician, machinist, plumber, and computer programmer.

I would like to thank Robert Asher, not only for his friendship, but for sharing the physical and mental burden of operating the experimental apparatus. Much of the research presented in this Dissertation is a consequence of effective teamwork between Robert and myself.

Special thanks go to my wife, Christine, for her patience and support in all those trying moments.

I dedicate this Dissertation to my parents. Without their support throughout my educational career I would not have succeeded in this accomplishment.

TABLE OF CONTENTS

ACKNOWLEDGEMENTS	ii
LIST OF TABLES	v
LIST OF FIGURES	vii
ABSTRACT	x
INTRODUCTION	1
EXPERIMENT	7
Overview	7
Beam Generation	10
Mass Selection	19
Optical Spectroscopy	27
Computer Control	36
INDUCTIVELY BOUND DIATOMICS	42
Threshold to Photodissociation	42
Resonant Photodissociation of VAr^+ and VKr^+	54
Photodissociation of $CoAr^+$ and $CoKr^+$	74
Resonant Photodissociation of $ZrAr^+$	91
Photodissociation of $CaKr^+$	105
Discussion	108
DIATOMIC POTENTIAL ENERGY SURFACES	116
Analytic Potentials	116
Vibrational Eigenvalues from the WKB Approximation	119
METAL RARE-GAS CLUSTERS	133
METAL CATIONS WITH PHYSISORBED POLYATOMICS	143
Predissociation of $V(OCO)^+$	143
Vibration Structure of Electrostatically Bound $V^+-(H_2O)$	154
Resonant Photodissociation of $V(NH_3)^+$	162
Resonant Photodissociation of $Cr(N_2)^+$	165
Resonant Photodissociation of $Ca(N_2)^+$	167

METAL-METAL SYSTEMS	171
Threshold Photodissociation of Cr_2^+	186
Photodissociation of Ca_2^+	194
CONCLUSIONS	199
APPENDIX A ELECTRICAL CIRCUITS	203
APPENDIX B COMPUTER CODE	205
WKB Grid Program	205
CAMAC Low Level Routines	213
CAMAC Header File	220
Control Program	220
Supporting Assembly Language Routines	258
APPENDIX C ANALYTIC PAIR POTENTIALS	284
Lennard-Jones Potentials	284
Born-Meyer Potential	291
APPENDIX D UNASSIGNED PHOTODISSOCIATION SPECTRA	295
REFERENCES	303
BIOGRAPHICAL SKETCH	310

LIST OF TABLES

Table 1. Optogalvanic Positions for Neon.	31
Table 2. Ground State Spectroscopic Parameters for NiAr ⁺ and CrAr ⁺	52
Table 3. Line positions for ⁵¹ V ⁴⁰ Ar ⁺ and ⁵¹ V ⁸⁴ Kr ⁺ in wavenumbers.	58
Table 4. Spectroscopic Parameter for VAr ⁺ and VKr ⁺ . .	71
Table 5. Line positions of assigned ⁵⁹ Co ⁴⁰ Ar ⁺ transitions in wavenumbers.	80
Table 6. Line positions of assigned ⁵⁹ Co ⁴⁰ Kr ⁺ vibronic transitions in wavenumbers.	81
Table 7. Experimental Molecular Constants for ⁵⁹ Co ⁴⁰ Ar ⁺ and ⁵⁹ Co ⁸⁴ Kr ⁺ in cm ⁻¹	88
Table 8. Line Positions for assigned vibronic transitions of ⁹⁰ Zr ⁴⁰ Ar ⁺ in wavenumbers.	94
Table 9. Unassigned line positions (cm ⁻¹) for ⁹⁰ Zr ⁴⁰ Ar ⁺ grouped by progression.	94
Table 10. Spectroscopic Parameters of Excited State in ZrAr ⁺	98
Table 11. Dissociation Energy for ZrAr ⁺ Excited States.	101
Table 12. Ground State Adiabatic Bond Strength. . . .	109
Table 13. Spectroscopic Parameters for Excited States.	109
Table 14. WKB Parameterization of Born-Meyer Potential with Experimental Eigenvalues.	125
Table 15. Line Positions for R2PD of Ni ₂ ⁺ (cm ⁻¹). . . .	181

Table 16.	Excited State Parameters for Metal-Ligands.	200
Table 17.	Ground State Adiabatic Bond Strength. . . .	201
Table 18.	Lennard-Jones [8,4] Relations.	288
Table 20.	Lennard-Jones [6,4] Relations.	289
Table 22.	Lennard-Jones [12,4] Relations.	290

LIST OF FIGURES

Figure 1. Experimental Apparatus.	9
Figure 2. Cross Section of Source Block.	12
Figure 3. Mass Spectrum of Cobalt Helide Cations. . .	22
Figure 4. Mass Spectrum of Aluminum Anions.	24
Figure 5. Photofragmentation of Co_8^+	26
Figure 6. Laser Dye Curve for Rhodamine R6G.	28
Figure 7. Optogalvanic Transitions for Neon.	30
Figure 8. Error in Quantel Dye Laser.	33
Figure 9. Doppler Shift for Coaxial versus Cross beam Photoexcitation of V(OCO)^+	35
Figure 10. Sweet Spot of Solenoid Pulse Valve.	41
Figure 11. Photodissociation Threshold for NiAr^+ . . .	44
Figure 12. Laser Fluence Dependence for Photodissociation of NiAr^+	46
Figure 13. Isotopic Shift for Photodissociation of NiAr^+	48
Figure 14. Photodissociation Threshold for CrAr^+	51
Figure 15. Resonant Photodissociation of VAr^+	55
Figure 16. Vibrational Fit for VAr^+ and VKr^+	61
Figure 17. Residuals to the Vibrational Fit of VAr^+ . .	63
Figure 18. LeRoy-Bernstein Fit for VAr^+ and VKr^+ . . .	69
Figure 19. Vibrational Binding Energy for VAr^+ and VKr^+	73

Figure 20. Resonant Photodissociation of CoAr^+	76
Figure 21. Photodissociation Spectrum of CoKr^+ Isotopes.	78
Figure 22. Vibration Fit to Band Origins for CoKr^+ States	83
Figure 23. Dissociation Limits of CoAr^+	87
Figure 24. Vibrational Binding Energy for CoAr^+ and CoKr^+ States.	90
Figure 25. Resonant Photodissociation of ZrAr^+	92
Figure 26. Isotopic Shifts for ZrAr^+	97
Figure 27. Vibrational Fit of ZrAr^+	99
Figure 28. ZrAr^+ C State Dissociation Limit.	103
Figure 29. Photodissociation of CaKr^+	107
Figure 30. RMS Contour Plot of CoKr^+ C state.	123
Figure 31. Potential Energy Curves of CoKr^+ Excited States.	127
Figure 32. WKB Error for Morse Potential.	129
Figure 33. Residuals to WKB.	131
Figure 34. Potential Energy Surfaces for VKr^+	132
Figure 35. Mass Spectra for the Uniquely Stable CoAr_6^+	135
Figure 36. Relative Abundance of VAr_n^+ and CoAr_n^+ . . .	138
Figure 37. Collision Induced Dissociation of CoAr_{11}^+ . .	140
Figure 38. Stick Plot of V(OCO)^+ Photodissociation. .	145
Figure 39. Photoexcitation Spectrum of V(OCO)^+	148
Figure 40. $[\text{VO}^+]/[\text{V}^+]$ Branching Ratio.	150
Figure 41. Energetics for Photodissociation of VCO_2^+ . .	153
Figure 42. Resonant Photofragmentation Spectrum of $\text{V(H}_2\text{O)}^+$	156

Figure 43. Isotope Shifts of $V^+(^{18}OH_2)$ minus $V^+(^{16}OH_2)$. . .	159
Figure 44. Photodissociation Spectra of Deuterated Isotopes of $V(\text{Water})^+$	161
Figure 45. Resonant Photodissociation of $V(NH_3)^+$. . .	163
Figure 46. Photodissociation Threshold for $Cr(N_2)^+ \rightarrow$ $Cr^+ + N_2$	166
Figure 47. Vibrationally Excited Photofragments of $Ca(N_2)^+$	168
Figure 48. Mass Spectrum of Argon Seeded Nickel Beam.	173
Figure 49. Photofragmentation of Ni_2Ar^+	177
Figure 50. Resonant Two-Photon Dissociation of Ni_2^+ . .	180
Figure 51. Photodissociation Threshold of $Cr_2^+ \rightarrow Cr^+ + Cr$	187
Figure 52. Cr_2^+ Photodissociation Mechanisms.	189
Figure 53. R2PD of Cr_2^+	191
Figure 54. Resonant Photodissociation of Ca_2^+	195
Figure 55. Valve Driver Circuit.	203
Figure 56. Bias Conditions for Microchannel Plate Detector.	204
Figure 57. Photodissociation Spectrum of Fe_2^+	296
Figure 58. Photodissociation of $NiO^+ \rightarrow Ni^+ + O$	297
Figure 59. Photodissociation Spectrum of $ZrOAr^+ \rightarrow ZrO^+$ $+ Ar$	298
Figure 60. Photodissociation Spectrum for $Zr(OCO)^+ \rightarrow$ $Zr^+ + OCO$	299
Figure 61. Photodissociation of $Co(HOH)^+ \rightarrow Co^+ + H_2O$.	300
Figure 62. Photodissociation of $Co(OCO)^+ \rightarrow Co^+ + CO_2$.	301
Figure 63. Photodissociation of $Co(NN)^+ \rightarrow Co^+ + N_2$. .	302

Abstract of Dissertation Presented to the Graduate
School of the University of Florida in Partial Fulfillment
of the Requirements for the Degree of Doctor of Philosophy

SPECTROSCOPIC CHARACTERIZATION OF NOVEL CLUSTER IONS

By

Daniel E. Lessen

December 1992

Chairman: Philip J. Brucat
Major Department: Chemistry

A variety of molecular ions, many without conventional covalent bonds, have been generated by adiabatic supersonic expansion of a laser driven plasma and spectroscopically probed in the visible region. Photofragmentation of these mass selected ions with a tunable visible laser reveals spectroscopic parameters of both excited and ground states. Specifically, the spectra of the systems of $\text{Cr}(\text{N}_2)^+$, CrAr^+ , and NiAr^+ , exhibit a sharp change in photodissociation cross section corresponding to a diabatic threshold from which the ground state binding energy is determined. Resonant photodissociation spectra display sharp vibronic features of bound quasi-bound transitions corresponding to excited state vibrational progressions for the inductively bound diatomic systems of VAr^+ , VKr^+ , CoAr^+ , CoKr^+ , CaKr^+ , and ZrAr^+ . Often, analysis of the vibronic transitions for a given system

will accurately determine the excited state vibrational frequency, anharmonicities, and electronic origin besides the ground and excited state binding energy. Additionally, vibrational structure for many of these diatomic systems is used to parameterize a variety of analytic potentials that incorporate a charge-induced dipole attractive term via the semiclassical Wentzel-Kramers-Brillouin method.

Transition metal cations with physisorbed polyatomic adducts are spectroscopically probed in the visible region. Resonant photodissociation spectra of $V(H_2O)^+$, $V(CO_2)^+$, and $V(NH_3)^+$ are discussed. The photodissociation spectrum of $V(H_2O)^+$ reveals an electrostatically bound system. The resonant photodissociation of the system $V(CO_2)^+$ displays two distinct dissociation pathways that arise from the same photoexcited state: $V(OCO)^+ \rightarrow V^+ + CO_2$ and $V(OCO)^+ \rightarrow VO^+ + CO$.

A cursory treatment of diatomic metal-metal cation behavior is discussed from the one-photon dissociation spectrum of Ca_2^+ , the resonant 2-photon dissociation spectrum of Ni_2^+ , and the threshold photodissociation spectrum of Cr_2^+ .

INTRODUCTION

The description of chemical phenomena at a molecular level is the ultimate goal of any chemist. Unfortunately such a goal would require a detailed knowledge of the forces between all the present atoms, a formidable task for any sizable system. One may, however, dissect a large system or chemical reaction into smaller model systems consisting of a few isolated atoms. A small, experimentally tractable system may then be chosen to model a chemically interesting part of the extended system; for instance, a solvated ion with its nearest neighbors or the active atoms in the discrete step of a reaction mechanism may be modeled. In this way, a complicated system may be understood by the behavior of its integral subunits.

Under this philosophy, both experimentalist and theorist have labored to understand the quantal details of interatomic interactions in the smallest of such model systems, the diatomic. Due, in part, to their ease of production and good stability, many main-group diatomic systems have been successfully described through the synergistic effort of experiment and theory.¹ The forces found in main-group diatomic molecules, for example H_2 , N_2 , and CO , are

quintessential examples of covalent interactions. The understanding of the nature of covalent bonding is currently being extended to include the effects of d orbitals by the study of diatomics from the transition-metal series.²

Part of this dissertation will discuss the behavior of three transition metal diatomic systems specifically, Ni_2^+ , Cr_2^+ , and Ca_2^+ , via spectroscopic information. Although calcium is not considered a transition-metal, many of its excited states will involve 3d orbitals. The interatomic forces in these systems are expected to display some covalent character, but also, inductive and electrostatic forces will be present since the diatomic systems are charged. Interestingly, a molecular orbital picture for the neutral analogues, Cr_2 and Ca_2 , suggests an adiabatic bond order of six and zero, respectively. Experimentally, the chromium neutral dimer has been found to have a surprisingly small bond strength. While the calcium dimer is found to be bound via van der Waals forces in difference to the zero bond order prediction of molecular orbital theory.

The importance of d orbitals in chemical interactions extends beyond their role in metal-metal bonding to their ability to lower the activation barrier for many reactions. Transition metal containing molecules and surfaces are important in the catalysis of many chemical reactions both at interfaces³ and in solution.⁴ The effectiveness of such catalysts is derived, in part, from partially-filled d

orbitals that provide low-energy, short-term electron sites along the reaction coordinate. Much insight will be gained by an accurate description of the pair potential between a transition metal and a reactant. Within this dissertation we will present the results from the spectroscopically probed system of $V(OCO)^+$. Photodissociation spectra of this system reveal an energy barrier of 1.6 eV to cleave a carbon-oxygen bond to form VO^+ and CO. The bond energy of the carbon-oxygen bond is ca. 5.43 eV in the gas phase molecule.⁵

As previously mentioned, the cations of homonuclear diatomic molecules will exhibit non-covalent interactions as well as covalent interactions. Empirically, an interaction may be described as consisting of some percentage of the following types of force: covalent, electrostatic, inductive, and dispersive. Although covalent interactions are important, they cannot account for the behavior of solute-solvent chemistry, or surface adsorption, for example. Solute-solvent behavior, especially ion-solvent systems, will be dominated by electrostatic and inductive forces.

Small gas-phase isolated systems, consisting of an ion solvated with a number of water or ammonia molecules, have been used as models of solute-solvent behavior before.^{6,7,8,9,10} These high-pressure mass spectrometric studies are able to quantify the thermodynamics of solvent-ion binding as a function of the number of solvent molecules. However, due to their size, the solvated ions have not been spectroscopically

probed, and therefore little is known about the configuration or potential energy surface of these systems.

To simplify the study of electrostatic and inductive forces, one may isolate a specific pair (an ion with an atom or molecule) that contains virtually no covalent forces. Through the formalism of classical electrostatics, the interactions between ions, dipoles and other multipoles may be expressed as the sum of separate contributions. The attractive part of an electrostatic potential for a metal ion and a water molecule would consist of a charge-dipole term, a charge induced-dipole term, and a charge-quadrupole term.

As an initial step in understanding the chemical behavior of a solvated metal ion, one may begin with the study of the most chemically simple solvent imaginable, a rare gas. A rare-gas atom possesses no permanent dipole, and it is virtually inert. The metal ion to which this polarizable partner is bound will have a considerably lower ionization potential: therefore, charge transfer is minimal. A single cation with a rare-gas adduct will display binding interactions that are dominated by inductive forces, and provide an ideal system to begin the understanding of physical forces found in solution chemistry. All solvents, monatomic or polyatomic, will have an inductive contribution to the total solvation energy.

A rare-gas solvent is not novel. Liquid krypton and liquid argon have been used to slow the kinetics of metastable

transition-metal carbonyl reactions.^{11,12} Significant effort has also been given to the isolation of charged species in rare-gas matrices.^{13,14,15} But how isolated are these ions? As will be shown, the interaction of a transition-metal cation is significant, ca. 0.5 eV. Thus, for optical studies of ions in a matrix, large spectral shifts may be expected. It is reasonable that the behavior of cation rare-gas systems be described in order to understand the role of the matrix environment with an ionic species.

Within this dissertation, spectroscopically acquired data will be presented on several small cluster ions, specifically, the number of atoms in the systems = 2 → 10, that exhibit binding dominated by electrostatic or inductive forces. Major emphasis is placed on the characterization of several transition-metal cations with rare-gas adducts. The understanding of the nature of inductive forces from these systems will then lend support to the analysis of metal cations with physisorbed or electrostatically bound polyatomic molecules such as N₂, CO₂, or H₂O. Direct comparison between the systems of VRg⁺ (Rg = Ar, Kr) and V-H₂O⁺ suggests that inductive forces will contribute significantly to the aqueous solvation energy of a monovalent cation.

In some cases, the vibrational information for metal-cation rare-gas diatomic systems is so extensive that over 80% of the total bound levels, which cover ca. 99% of the potential energy surface, are experimentally observed. This

provides a unique opportunity to accurately determine both the vibrational frequency, and dissociation energy. In addition, the extensive vibronic data may be used to parameterize some simple analytic potential functions over the full potential surface. An accurate knowledge of the pair potential will provide a powerful tool with which extended solutions may be modeled.

EXPERIMENT

Overview

The experimental apparatus was designed to generate and gas-phase isolate a variety of internally-cold cluster ions for photo-interrogation. Both types of systems presented in this dissertation, metal-metal and metal-ligand, require unique conditions for optimal production. Inductively bound species, by nature, such as transition-metal rare-gas diatomics are particularly troublesome to make routinely due to their weak binding interactions. Sufficient quantities of refractory material must be atomized, ionized, and then internally cooled before physisorption of rare-gas atoms to the ionic site is possible. Production of transition-metal rare-gas species, therefore, involves an extreme change in temperature, spanning vaporization to condensation. This seemingly improbable set of conditions is achieved by the combination of a laser driven plasma and supersonic expansion.

A laser driven plasma is seeded within an inert carrier gas, usually helium. Collisional cooling initializes cluster formation. Subsequent adiabatic expansion results in the generation of a variety of internally cool aggregates. Such

techniques have been successfully used to generate internally cool neutral clusters of refractory material previously.¹⁶ This technique has also been applied with success to the formation of both negative and positive metal cluster ions.¹⁷

Mass selection of the molecular ion beam provides a microscopic window into the success of the expansion technique for generating a given system. A variety of experimental conditions, such as the backing pressure and laser vaporization fluence, may be adjusted to maximize the production of a desired chemical system. The experiment will often generate a variety of cluster sizes. Effective mass selection and detection require a fundamental understanding, and intelligent incorporation, of various static and pulsed ion optics. Once the mass components of the molecular ion beam are established, photointerrogation may be performed with a confident knowledge of the species under study.

Due to the nature of the expansion and the pumping limitations of the apparatus, the experiment is pulsed at 9.1 Hz. Limiting the total throughput by lowering the duty cycle of the gas allows one to maintain a high jet density and not exceed the pumping capacity of the apparatus. However, the pulsed nature of the experiment demands real time computer control over the many events that occur in a cycle. A custom computer program controls the relative timing of the vaporization laser, the carrier gas pulse, the acceleration stack, and the dissociation laser.

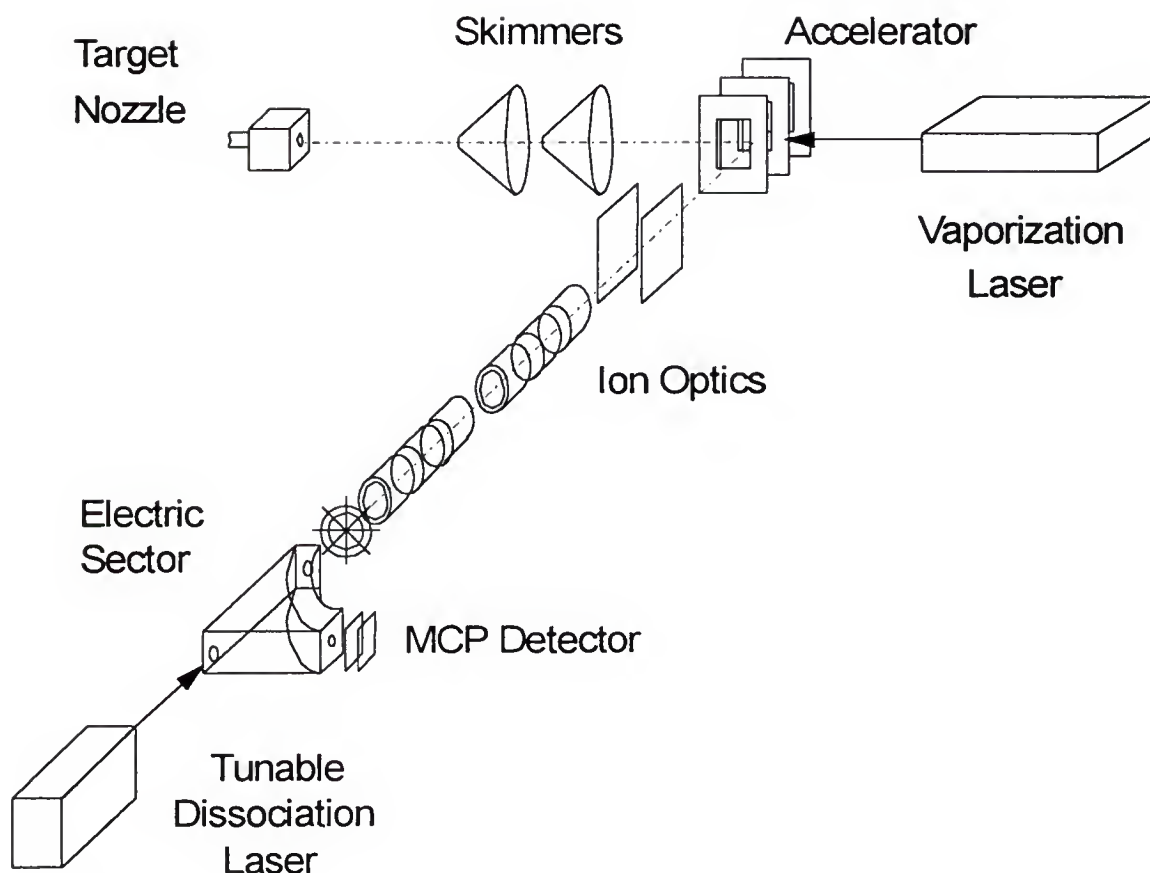


Figure 1. Experimental Apparatus.

The figure displays a sketch of the experimental apparatus. A plasma is generated at the upper left of the figure in the beam source at high pressure by the second harmonic of a $\text{Nd}^{3+}:\text{YAG}$ laser. Ions and neutrals then supersonically expand in an inert carrier (ca. 99 % He), cool, and then travel through differential pumping orifices (skimmers) and into the accelerator of a custom time-of-flight mass spectrometer. Here, positive or negative ions may be extracted at 90° to the supersonic beam axis with a kinetic energy of ca. 1.45 keV. Mass separation takes place as the ions pass through a 2.45 m flight tube containing focussing and deflection optics. Fragmentation of any ions is detected by laboratory kinetic energy analysis performed by a 127° electrostatic sector at the end of this flight tube. Laser photoexcitation may occur colinearly, as shown in the figure, or may intersect the beam at 90° prior to entrance of the electrostatic sector.

Figure 1 displays the salient features of the experimental apparatus that was used for this research. The experiment is detailed below by following the journey of a cluster ion from inception to mass selection to photodissociation.

Beam Generation

The start of an experimental cycle occurs in the beam source and is marked by the birth of a chemical system. Production of a desired system is achieved when the surface of a sample rod is laser vaporized within the high pressure pulse of a carrier gas. Focussed light of a Quantel Nd³⁺:YAG laser (model 580), via the second harmonic (532 nm), will generate a plasma. Laser light, 7 ns in duration, is typically chosen in the range of 15-40 mJ/pulse. The light is focussed to a point smaller than 1 mm in diameter. This corresponds to a photon fluence of ca. 10^8 W/cm² (lower limit) at the rod surface. The laser generated plasma is thermally quenched in the carrier gas through collisions. Carrier gas for the present research is either pure He, for metal-metal clustering, or a mixture that has a small percentage (ca. 1-2% mole fraction) of ligand (L) in helium. As will be shown, an assortment ML⁺ systems, where L = Ne, Ar, Kr, CO₂, or N₂, may

be generated from the appropriate gas mixture. Three-body collisions initialize clustering to form a variety of M_x or M_xL_y neutral and ionic clusters.

Figure 2 displays a cross section of the source assembly used to house the sample rod and provide a reaction zone where the nascent clusters may be formed. Optimizing the configuration of a nozzle source is rather enigmatic. Nucleation to molecular species is kinetically controlled and therefore critically dependant on the local pressure in the plasma generation zone. With low gas density, typically only a single adduct is observed to physisorb to a metal cation. The clustering efficiency improves with an increase in carrier gas density; a direct reflection of the fact that both three-body and two-body collisions will increase with pressure. However, too much gas pressure has been observed to quench the positive ion beam and is believed to be due to electron recombination with the positive ions.

Note, the onset of expansion is similar to quenching a reaction; the observance of ionic species is an attestment to the fact that the cluster ensemble is not at thermodynamic equilibrium. Even the vibrational and rotational temperatures for a given molecular species are known not to correspond to the same temperature after an expansion.¹⁸ Molecular vibrations equilibrate more slowly than rotational degrees of freedom and will therefore be at a higher temperature with respect to the translational temperature of the beam.

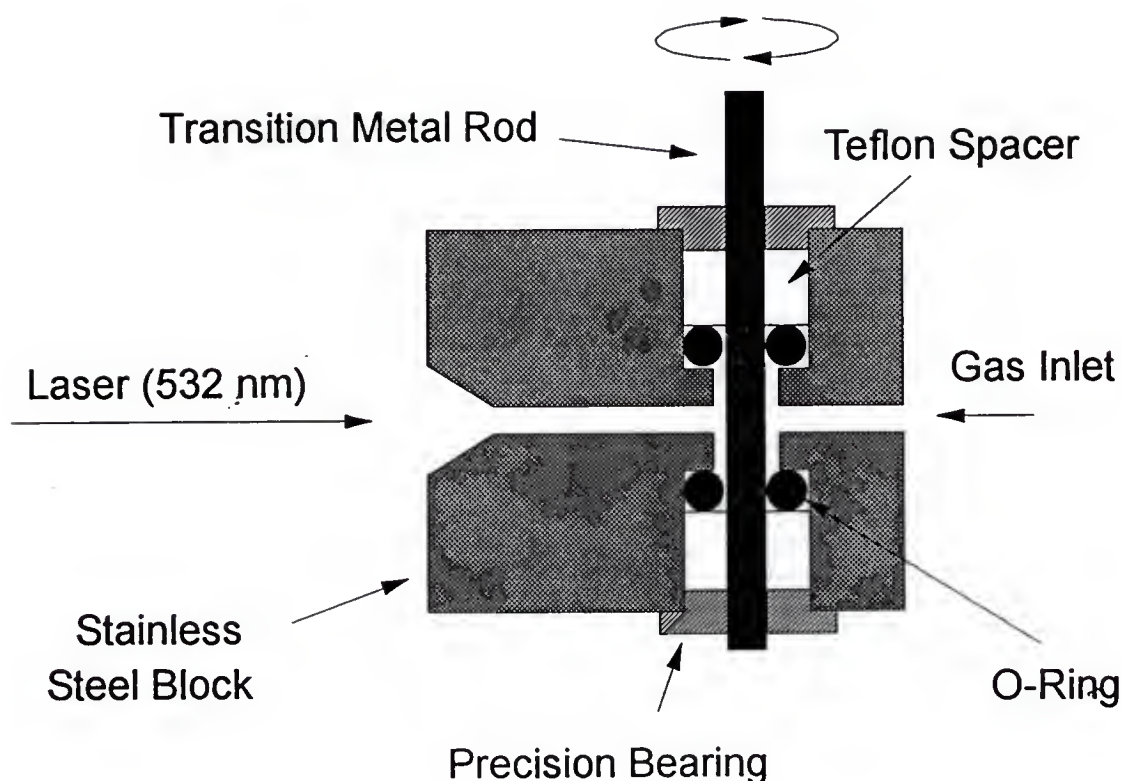


Figure 2. Cross Section of Source Block.

This figure displays a sketch of the source block used for generation of metal-cation rare-gas systems. The channel to the right of the sample rod allows laser access for plasma generation and exit orifice for expanding carrier gas. The plasma is collisionally thermalized in the carrier gas pulse within the channel prior to expansion. Three-body collisions initialize the aggregation of cluster systems. The rod is mounted in precision bearings to ensure a wobble-free rotation. O-rings seal off the volume near the sample plasma generation zone to maximize the carrier gas density thereby maximizing the cooling/clustering capability.

Nonetheless, an estimated 5,000 to 10,000 internally cool M_2^+ and/or ML^+ may be routinely generated 9.1 times a second.

A given vaporization laser pulse produces a finite number of neutral and ionic atoms. Yield for a desired species is then in competition with the production of other clusters for the available material. In attempts to produce rare-gas ligated metal cations, metal-metal clusters have been observed at the expense of metal-ligand systems for higher carrier gas pressures.¹⁹ The, presumably, more weakly bound metal-ligand systems would find the collisional frequency, and therefore the progression to equilibrium imposed by a high pressure regime deleterious while in competition with more strongly bound metal-metal systems. Unfortunately, one may not easily predict the exact source conditions necessary to generate a particular system.

Several theoretical and experimental studies have been done to characterize the cooling properties of supersonic expansions. For compressible, adiabatic, and isentropic flow, the following relations for temperature (T), pressure (P), and density (ρ) in terms of mach number (M) and heat capacity ratio (γ) have been derived:²⁰

$$\frac{T_2}{T_1} = \left(\frac{P_2}{P_1}\right)^{\frac{\gamma-1}{\gamma}} = \left(\frac{\rho_2}{\rho_1}\right)^{\gamma-1} = \frac{1 + \left(\frac{\gamma-1}{2}\right)M_1^2}{1 + \left(\frac{\gamma-1}{2}\right)M_2^2} . \quad (1)$$

These relations are valid for compressible flow of a gas that is confined in varying area channels. The first two equalities are the familiar adiabatic relations that may be found in any thermodynamic textbook.²¹ For an adiabatic expansion of an ideal gas, a drop in pressure will be accompanied by a reduction in temperature. The last term expresses the physical characteristics of a system to the mach number. From this term, one observes that an adiabatic expansion of a gas will results in an increase in the mach number.

The mach number is defined as v/a where v refers to the mass flow velocity and ' a ' is the local speed of sound. The speed of sound is a function of temperature given by $(\gamma RT/m)^{1/2}$. J. B. Anderson and J. B. Fenn²² have determined the limiting flow velocity as mach number approaches infinity as $(5/\gamma)^{1/2}a$. Initial source temperature will determine the speed-of-sound. Notice that a high mach number does not reflect a large mass velocity but rather a reduction of the local speed-of-sound as the gas expands from a high pressure region to a low pressure region. High mach numbers are therefore desirable because they correspond to a small translational velocity distribution and hence a cold beam.

Using the above pressure relationship, Eq. (1), it is possible to calculate the exit mach number of a nozzle with a known pressure ratio. The cross sectional area, A , of the

channel is related to the mach number and heat capacity ratio with the following equation:²⁰

$$\frac{A_2}{A_1} = \frac{M_1}{M_2} \left[\frac{1 + \left(\frac{\gamma - 1}{2} \right) M_2^2}{1 + \left(\frac{\gamma - 1}{2} \right) M_1^2} \right]^{\frac{\gamma+1}{2(\gamma-1)}}. \quad (2)$$

Immediately, one may determine the pressure conditions in which the nozzle is choked²³ (also referred to as an underexpanded condition); i.e., for what cross-sectional area in a diverging nozzle is $M = 1$. The ratio of background to reservoir pressure for a monatomic gas is 0.487. This ratio under typical experimental conditions of our apparatus is ca. 10^{-8} . The expansion for the apparatus is supersonic: it is so supersonic that the above equation results in an unrealistic nozzle exit-mach number of 80.

Obviously, as the molecular density drops from a decrease in pressure, a point is reached in which the molecules can no longer communicate. The beam becomes discontinuous and a terminal mach number is reached. J. P. Toennies and K. Winkelmann²⁴ have determined the terminal mach number as a function of downfield distance (x) normalized to the nozzle diameter (x/d) for various $p_0 d$. The variable p_0 is stagnation pressure and the quantity $p_0 d$ is proportional to the bimolecular collision frequency.

One may estimate the quantity of $p_0 d$ experimentally to determine the terminal mach number for a typical set of

conditions. For our apparatus, the stagnation pressure may be determined from a knowledge of the flow rate and the volume of a single gas pulse. Flow rate is easily measured and is ca. 100 SCCM (standard cubic centimeters per minute) with an applied cylinder pressure of ca. 70 psi. The temporal width of the gas pulse is determined by varying the plasma generation event within the gas pulse. Presence of seeded ions reveals a pulse width of ca. 1.0 msec. The volume of gas per pulse is found from the product of the nozzle cross section area, the pulse width, and the gas velocity as $3.8 \text{ cm}^3/\text{pulse}$, or, at the experimental cycle of 9.1 Hz, $35 \text{ cm}^3/\text{sec}$. The ratio of flow rates, before and after expansion, multiplied by the backing pressure will estimate the pressure in the nozzle channel as ca. 30.7 torr. The quantity $p_0 d$, with a nozzle diameter of ca. 2 mm, is ca. 6.0 torr-cm and corresponds to a terminal mach number of ca. 10. This is considered a low to moderate expansion for our apparatus. More extreme pressure drops are possible that would correspond to a terminal mach number of ca. 20.

Several versions of nozzle blocks, in which the channel and exit orifice configurations were varied, have been tried. The one described below is particularly suited to the generation of weakly bound M^+L species (refer to Figure 2). The source block is made of stainless steel with outer dimensions of 3.17 cm by 3.17 cm by 3.81 cm. A central gas channel of length 3.17 cm and diameter 2.2 mm perpendicularly

bisects the sample rod through-hole. At the exit end of the gas channel is a diverging 18° cone ca. 6.4 mm depth. O-rings capture the sample rod and make a hermetic seal on either side of the gas flow channel equidistant from the center at 1.7 mm. The rotating rod is supported by precision bearings. Teflon spacers provide further rod support and apply the necessary force to make the o-rings seal. The total volume, excluding the gas inlet and exit channel volume, around the rod is ca. 49 mm³, which is about 40% of the total possible gas volume in the block. A pulse of gas originates upstream, 6.3 mm from the rotating rod and subsequently flows around the circumference of the rod before exiting down a 1.9 cm long channel.

A commercial solenoid valve (General Valve series 9) controls the carrier gas pulse. An exit orifice of 0.76 mm diameter is plugged with a Kelef popet in the de-energized state. The valve is overdriven* with an electrical pulse of 150 V and ca. 150 μ sec in duration. This extreme pounding will shorten the lifetime of the Kelef popet and necessitate its replacement after several weeks of operation. Nevertheless, a gas pulse of ca. 1.0 ms, which corresponds to a flow rate of ca. 40-500 SCCM, will result at the experimental cycle of 9.1 Hz. The flow-rate is adjustable with backing pressure and limited by the diffusion pump

*Manufacturer's recommendation for continuous duty is 28 volts.

throughput. Interactive computer control allows the timing adjustment of the vaporization laser impingement on the rod surface to coincide within the gas pulse.

The resulting cluster neutral and ion ensemble expands from the high pressure region of the nozzle channel into a 500 L aluminum cylindrical chamber (inner diameter 114 cm and height 61 cm) evacuated by three diffusion pumps. Conversion of the random motion of the gas/cluster ensemble within the nozzle channel into directed flow upon adiabatic expansion results in a supersonic beam. A supersonic nozzle will therefore convert enthalpy into kinetic energy. The cooling properties of this technique have routinely generated diatomic species with vibrational temperatures of less than 60 K and rotational temperatures of 5 K.²⁵ From the observance of blackbody radiation, a temperature change of 7,000 K to a few Kelvin has occurred in a fraction of a second.

The neutral/ion cluster ensemble traverses two differential-pumping orifices. Passage through these regions is gained through two conical, 55°, electroformed skimmers that are positioned 12 cm and 60 cm downstream of the nozzle exit with apertures of 1.0 and 1.5 cm, respectively. The skimmers define regions of successively lower vacuum pressure and skim out a region within the mach bottle of the supersonic expansion.¹⁸ The main chamber, in which the molecular beam first expands, is pumped by two differential pumps, a 10"

(NRC) and a 6" (Varian model VHS-6) that provide an operating pressure of 10^{-5} torr via a total pumping speed of 9600 l/s.

The two skimmers mark the entrance and exit of a wedge shaped sector that is 15% of the total volume of the main expansion chamber. This region is pumped separately by a 6" diffusion pump with a water cooled baffle. Under operation the background pressure in this region is ca. 10^{-6} torr.

Mass Selection

The second downfield skimmer stands at the entrance of the acceleration stack of a time-of-flight mass spectrometer. After ca. 110 cm of travel and 620 μ sec, the cluster ensemble reaches the center of the stack. In this region, ions, either positive or negative, may be extracted at 90° to the molecular beam. A computer triggered acceleration pulse imports ca. 1.45 keV of kinetic energy to the cluster ions in a two-stage, Wiley-McLaren accelerator.²⁶ The first stage contains the weaker field, 35 V/cm, with the second stage being considerably larger at 1450 V/cm. This allows one to maximize temporal resolution of ions at the detector (2.45 m downfield) by correcting for space deviations at the accelerator. The space deviation is defined by the skimmers mentioned earlier. The electrical pulse is supplied by a Cober (model 605P) high

voltage pulse generator that is capable of delivering 1.5 keV pulse with ≤ 100 ns risetime.

The acceleration stack consists of seven, stainless steel parallel plates (dimension 15.24 by 15.24 cm by 1.6 mm thick) separated by 1.0 cm Teflon insulating spacers. Ions enter the low field region in the rear of the stack approximately between the second and third plates. All plates have centrally located slots of 2.54 cm by 7.62 cm to allow for unhindered ion passage. Two of the seven plates, which define the high field region, are grided with 90% open screen to keep the field region flat. The ratio of the high and low electric fields may be optimized with a simple voltage divider by maximizing the mass resolution at the detector. Discrete components are used to minimize capacitance thus keeping the acceleration pulse sharp. The voltage divider consists of a network of resistors and a high voltage switch. Five internal, i.e., within the vacuum hardware, 1.0 k Ω , $\pm 1\%$ -tolerance glass resistors determine the low field strength. The last plate is grounded so that the ions are in a field-free region upon departure from the acceleration stack.

The acceleration stack marks the beginning of a time-of-flight mass spectrometer (TOFMS). Ions are subjected to a variety of deflecting and focusing optics before detection by dual microchannel plates. Horizontal deflectors correct for the forward momentum of the expanded molecular beam. Two electrostatic einzel lenses make a parallel to point focusing

device for the ions. Each einzel assembly consists of three cylindrical aluminum tubes of length 7.62 cm and inner diameter of 6.99 cm. The three concentric elements are spaced 6.35 mm apart. An applied potential of 450 V (positive potential for cations) on the central einzel element provides an ion focal length of ca. 85 cm for 1450 keV ions.

After 2.45 m of travel, the ions are detected by a dual microchannel plate detector. Ideally the acceleration stack imparts equal kinetic energy to all species; thus, arrival time is proportional to the square of the mass-to-charge ratio. Figure 3 displays the parent mass distribution for cobalt cation with physisorbed helium atoms. The ability to physisorb multiple helium atoms to a cation nucleation site attests to the extreme cooling capabilities of the apparatus. Also, notice that mass peaks are well separated with the four amu spacing among CoHe_n^+ peaks being well resolved. Unit mass resolution is possible with the primary mass resolving power of ca. 300 at 100 amu.

The ion detector consists of two Galileo microchannel plates²⁷ (MCP) captured in a custom assemblage. The two plates are separated by a 0.127 nm nickel-lifesaver shim that electrically contacts the outer perimeter while leaving the detection area open. Metal shim provides an electrical connection for a resistive voltage divider. An individual microchannel plate in this configuration has been biased with up to 900 V without a breakdown. Incoming ions generate

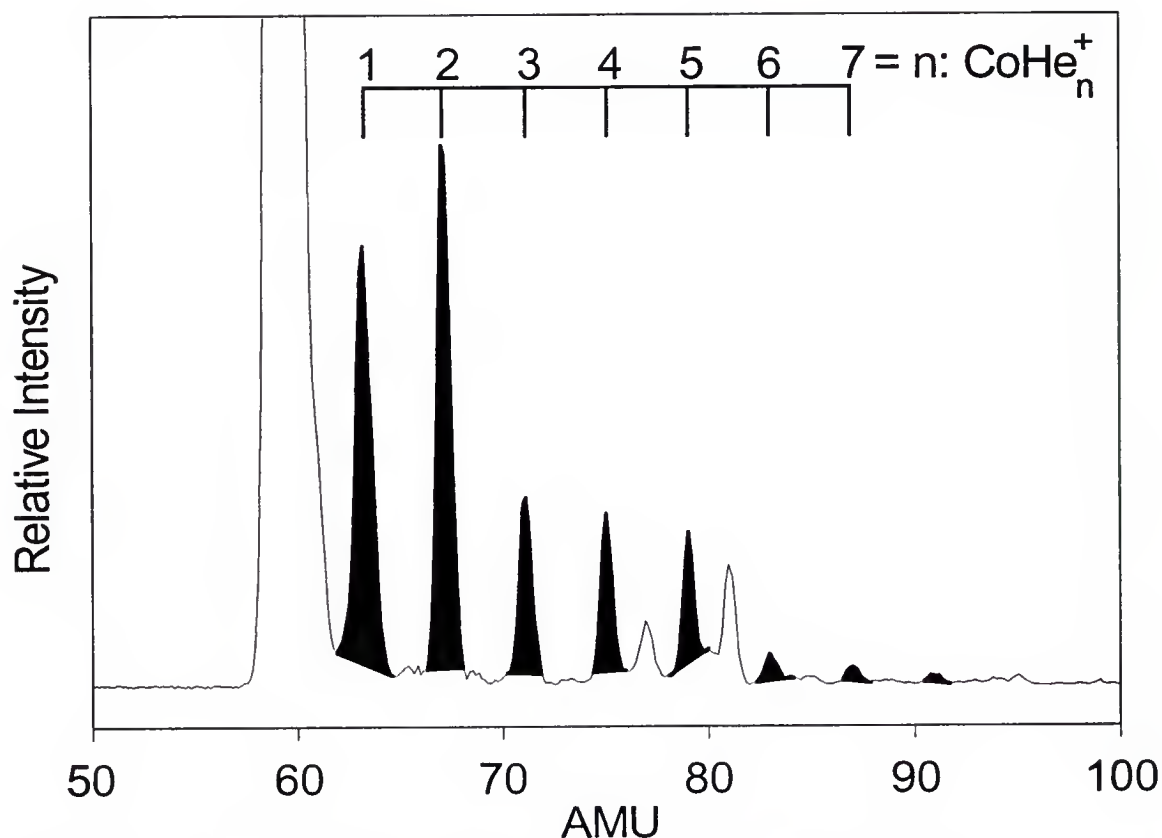


Figure 3. Mass Spectrum of Cobalt Helide Cations.

The figure displays a portion of the parent mass spectrum, relative abundance versus amu, for a single cobalt cation with several physisorbed helium atoms. The naked cobalt cation at 58 amu is shown off scale to reveal the helium substituents; it is approximately a factor of eight larger than CoHe_2^+ . The ability to physisorb several helium atoms, upwards of seven (shaded in black for emphasis), is an attestation to the cooling and clustering property of the supersonic expansion.

secondary electrons in the dual detector. These ions are detected at a stainless steel electrode ca. 2.8 mm behind the exit surface of the second microchannel plate. The gain of an MCP is ca. 10^7 . Detection efficiency is exponential as a function of gain voltage with roughly a factor of five increase in signal level per one-hundred volts of bias. Single ion detection is possible although not preferred for optical studies.

Slight electrical modification is required to mass select negative species. All potentials of electrostatic ion optics and the acceleration stack are merely reversed in polarity. Only the detector assembly requires special handling. Regardless of the polarity of the ions, secondary electrons must still be generated and detected. For detection of cations, a negative potential is applied to the entrance MCP. Conversely, for detecting anions a positive potential must be applied to the entrance MCP but the electrical bias must ensure that secondary electrons are accelerated through the second MCP. This problem may be overcome by floating the entire assembly with respect to ground. Proper electrical connections are discussed in Appendix A. Figure 4 displays a parent mass spectrum for anions of aluminum. Mass resolution is similar to that of a cation mass spectrum.

Before detection, a 127° electrostatic sector turns the ions off the flight tube axis.^{28,29} The electrostatic sector is a kinetic energy analyzer. A field strength of 600 V/cm

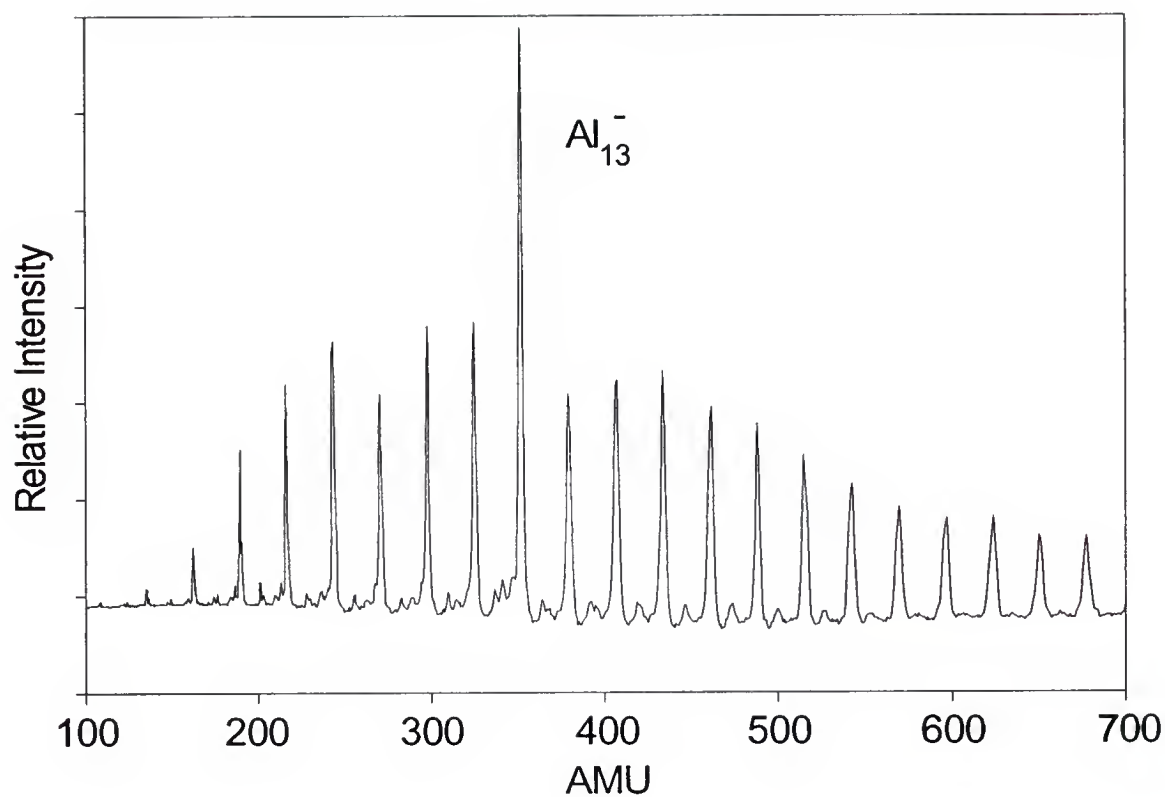


Figure 4. Mass Spectrum of Aluminum Anions.

The figure displays the cluster anions of aluminum over a mass region of 100 to 700 amu. This region of the mass distribution encompasses cluster anions of 5 to 25 aluminum atoms. Notice the anion Al_{13}^- is relatively larger than any other anion in the beam and represents a 'magic number'.

for this optic is necessary to turn parent ions of 1.45 keV kinetic energy. The aluminum sector provides an ion path on an 8.9 cm radius with a channel width of 2 cm. The sector electrodes are 7 cm wide. Resolution is proportional to the radius and is a function of the initial velocity spread of the ions. The magic $127^{\circ} 17'$ angle between entrance and exit apertures has been found to optimize the refocusing and resolving properties of an electrostatic sector.

Collision induced dissociation (CID), metastable decay, and photoinduced dissociation of a parent molecule may be observed by tuning the sector field to transmit fragment ions of lower kinetic energy. The daughter ions will arrive at the same time of the parent ions but at a proportionately smaller kinetic energy. The first generation of this sector had a 1.27 cm entrance and exit aperture and gave a kinetic energy resolving power of ca. 10. In a later version of the sector, the apertures were narrowed to 4.7 mm, thereby limiting the off-axis velocity spread at the entrance without significant parent throughput loss. This configuration increased the resolving power to 15. Figure 5 displays a sector scan of Co_8^+ photodissociated with a fixed laser frequency of $28\,169\text{ cm}^{-1}$ and power of 35 mJ/pulse.

An electrostatic sector in tandem with a TOF is a powerful combination. This combination allows one to mass select a given parent ion, perform some experiment on that parent, then mass select the fragments.

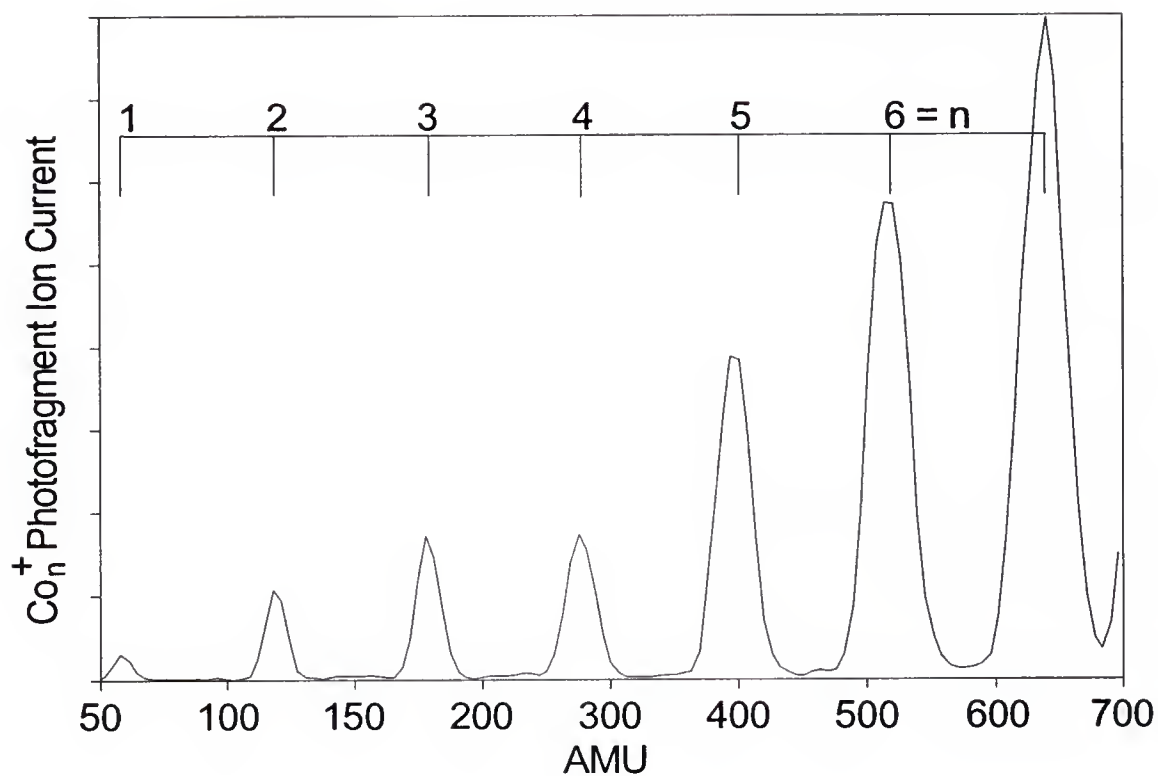


Figure 5. Photofragmentation of Co_8^+ .

This figure displays the photofragments of Co_8^+ with 355 nm light. The field strength of the 127° electrostatic sector is scanned to transmit fragment ions from a given parent system. The parent mass of 472 amu is not displayed under the gain conditions of the detector. Secondary mass resolving power is about 15.

Optical Spectroscopy

The ability to mass select provides only moderate insight into the chemical behavior of molecular systems. For this experiment it is considered a prerequisite for optical interrogation. Optical analysis will directly access the quantal details of a system. Such information is invaluable for describing the interatomic forces among the bound atoms.

The tunable light source for this experiment is a Quantel (model 581) Nd^{+3} :YAG pumped dye laser that provides both fixed and tunable light. The laser is timed to photo-intersect the ion packet prior to entrance of the 127°. The sector may then be scanned to observe the photo-induced fragments at a fixed frequency, as discussed in the preceding section, or, a particular fragment may be monitored as a function of wavelength.

The visible region is accessed through a variety of organic dyes dissolved in methanol. A total range of 540 cm^{-1} to 780 cm^{-1} may be easily reached with approximately seven different dyes. The dye laser tunes over the fluorescence region of each dye. Figure 6 displays the laser intensity as a function of wavelength for 532 nm pumped rhodamine R6G ($\text{C}_{28}\text{H}_{31}\text{N}_2\text{O}_3\text{Cl}$).³⁰ This particular dye will allow access to a ca. 25 nm (700 cm^{-1}) wavelength region centered at 590 nm. The picture symbolizes the 'tuning curve' for the dye. The R6G dye has a conversion efficiency of ca. 20% with a 200 mJ/pulse

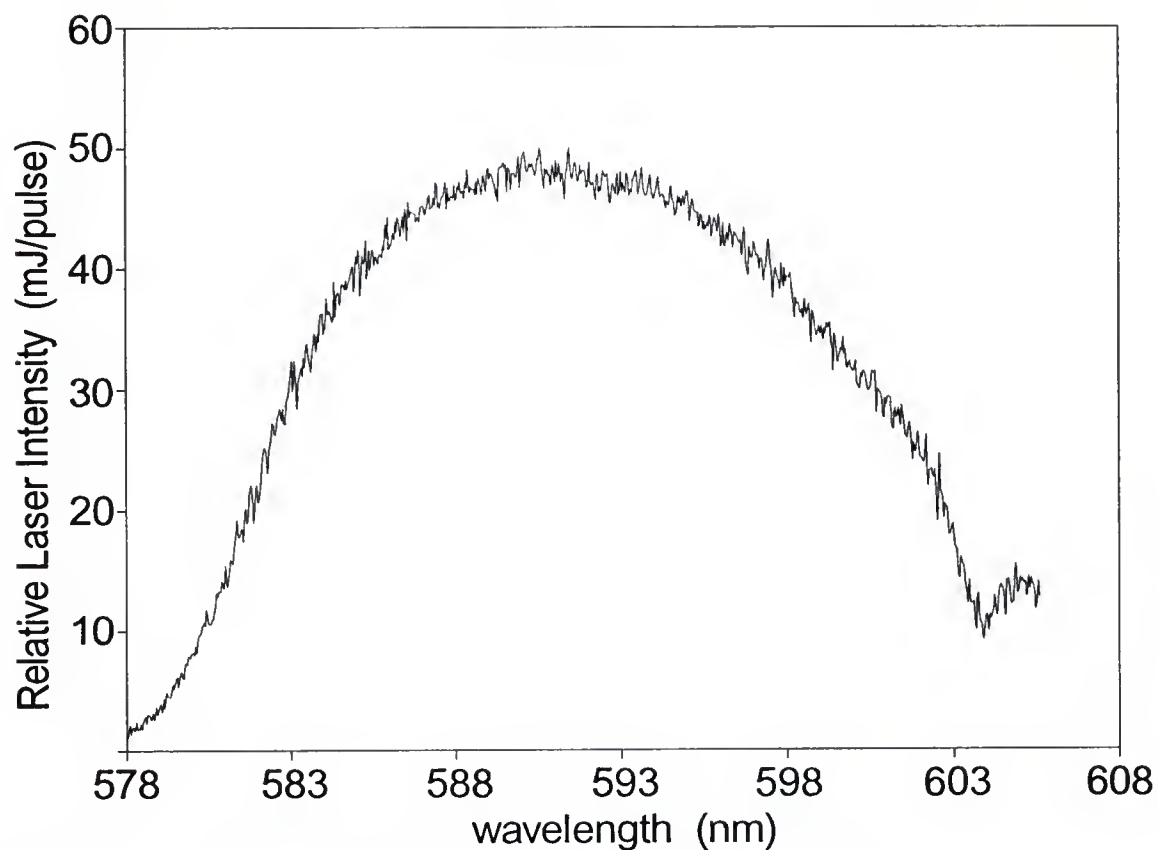


Figure 6. Laser Dye Curve for Rhodamine R6G.

The figure displays the dye laser intensity as a function of wavelength (tuning curve) for rhodamine R6G dye. This particular dye will access a wavelength region of ca. 25 nm (700 cm^{-1}).

pump beam. Many of the photodissociation spectra presented in this dissertation result from scanning in several different dye regions. These scans must be combined, with good overlap, to form a complete photodissociation picture.

The dissociation laser scans linearly in time with respect to wavelength. Several pairs of points taken manually relate the wavelength to a computer generated data index. The computer-collected photodissociated event is then correlated to a wavelength position. Unfortunately, normal optical optimization and play in the mechanical parts of the scanning mechanism may cause consecutive scans to be different by as much as 0.1 nm. This corresponds to an unacceptable 2.5 cm^{-1} error at 630 nm. For this reason, the spectra are calibrated to a primary standard.

Optical spectra may be calibrated with optogalvanic transitions found in a neon discharge. A conventional neon indicator lamp is powered by a current-limited power supply at ca. 100 V (DC) and 10.0 mA. A 4% reflection of the primary beam off a turning optic intersects the discharge region of the neon bulb. Simultaneous scanning of optogalvanic transitions with the photodissociation event provides an accurate method to determine the absolute wavelength position of the dye laser. These optogalvanic line positions are well known and may be used a primary standard.^{31,32}

Figure 7 displays an optogalvanic spectrum over the region 580 to 720 nm. Notice that optogalvanic transitions

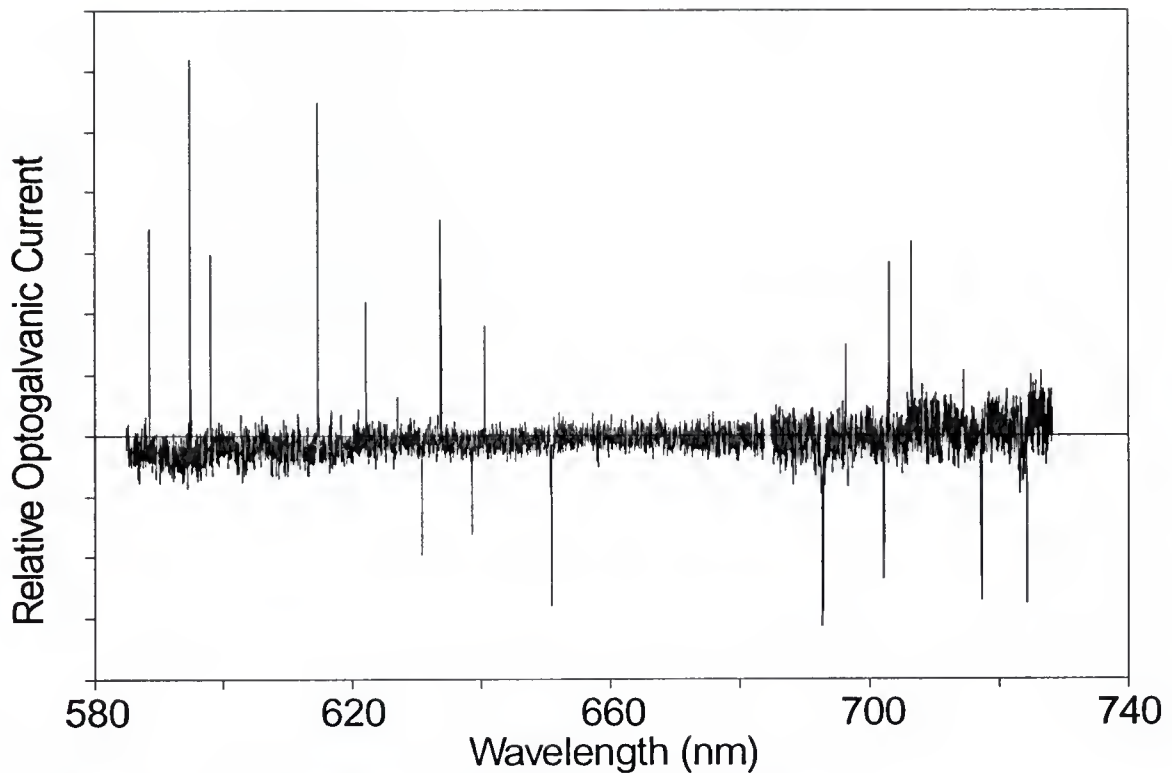


Figure 7. Optogalvanic Transitions for Neon.

This figure displays the optogalvanic transitions found in a neon discharge lamp over the wavelength region 580 to 720 nm. Incident laser light may enhance or deplete charge carriers in the discharge region, thus changing the resistance of the lamp and appearing as either a positive or negative going electrical signal across a capacitively coupled load. The line positions are well known and provide a primary standard for calibration of optical spectra taken with a pulsed laser in the visible region. The small gap in the spectrum near 684 nm is due to the poor overlap of two dye regions (see text for explanation).

Table 1. Optogalvanic Positions for Neon.

Laser Dye ^a	nm	cm ⁻¹	sign	Source
R610	585.250	17,086.72	-	b,c
	588.190	17,001.31	+	b,c
	594.483	16,821.34	+	b,c
	597.553	16,734.92	+	b,c
R640	603.000	16,583.75	-	b,c
	607.434	16,462.69	-	b,c
	609.616	16,403.77	-	b,c
	612.845	16,317.34	-	b,c
	614.306	16,278.53	+	b,c
	616.359	16,224.31	+	b,c
DCM	621.728	16,084.20	+	b,c
	626.650	15,957.87	+	b,c
	630.479	15,860.96	-	b,c
	633.443	15,786.74	+	b,c
	638.299	15,666.64	-	b,c
	640.225	15,619.51	+	b,c
	650.653	15,369.18	-	b,c
	653.288	15,307.18	+	b,c
DCM/LD	659.895	15,153.93	-	b
	667.828	14,973.92	-	b
	671.704	14,887.51	-	b
	692.947	14,431.12	-	b
	696.543	14,356.615	+	d
	702.405	14,236.801	+	d
LD-700	703.241	14,219.88	+	b
	717.394	13,939.34	-	b
	724.517	13,802.30	-	b
	743.890	13,442.85	-	b

^aCommon name. ^bRef.[31]. ^cRef.[32]. ^dRef. [33].

may occur in either the positive or negative direction corresponding to an increase or decrease in the charge carriers in the discharge region. Table 1 provides a list of optogalvanic transitions easily observed on the wavelength region of 585 to 740 nm. These transitions were taken in air and are grouped according to the dye region in which they are observed.

After the first attempt to calibrate the Quantel laser scan box to optogalvanic transitions, it was determined that the laser did not scan linearly in time but had a systematic and increasing deviation. Figure 8 shows the error of the Quantel dye laser readout as a function of wavelength. This annoying error is easily corrected by a least-linear-squares method relating the Quantel scan box to the optogalvanic transitions.

Once the scan data has been corrected to air wavelength it must then be corrected to vacuum. This is done by using the dry air refractive index of 1.0002926.⁽³³⁾ Simply multiply the optogalvanic corrected air wavelength by the refractive index to get the vacuum number. Conversion to wavenumbers is accomplished by taking the inverse of the wavelength and multiplying by the correct conversion factor of 10^7 nm/cm.

Finally, for those spectra that are taken along the ion flight tube axis one must correct the frequency for the Doppler shift. For absorption, the Doppler shift is determined by the following equation:³⁴

$$\nu_{corrected} = \frac{\nu_{observed}}{(1-v/c)} \quad (3)$$

where ν is frequency in wavenumbers, v is the ion velocity and c is the speed of light.

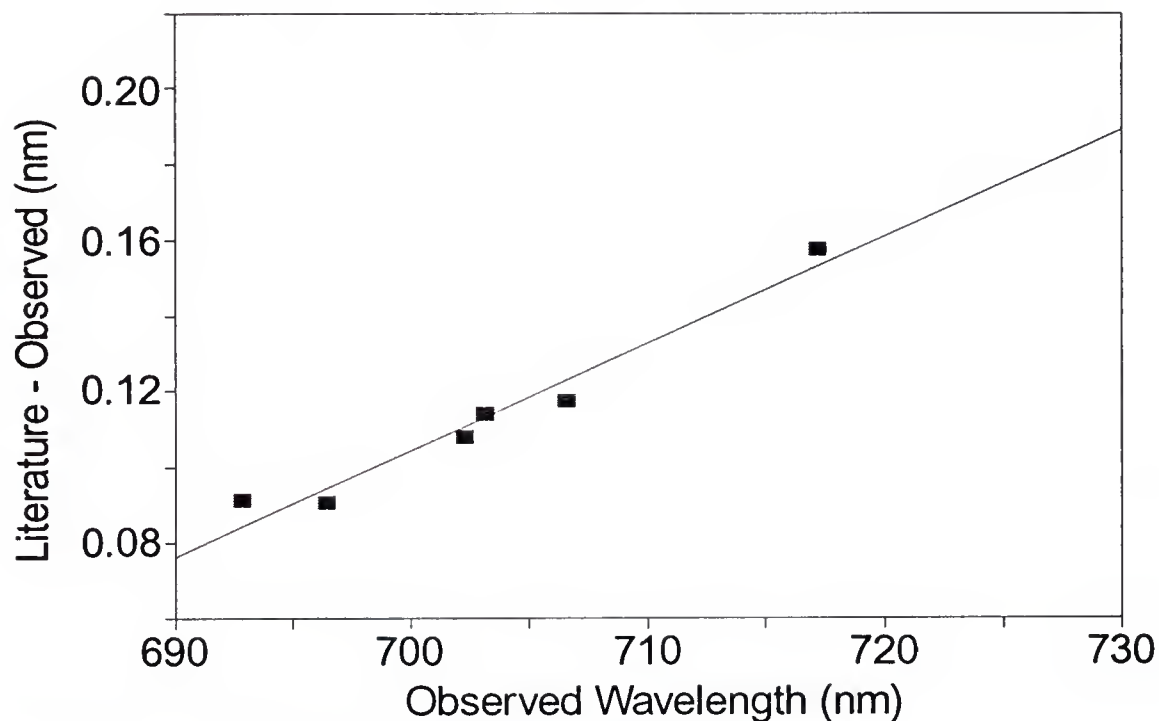


Figure 8. Error in Quantel Dye Laser.

The figure displays the error (the literature value for an optogalvanic transitions minus the quantel scanbox readout) of the Quantel dye laser as a function of wavelength. Optogalvanic transitions for neon are used as a primary standard and compared to the readout offered from the Quantel laser system. The dye laser has provisions to correct the wavelength for a constant value. However, as the plot confirms, the error (shown as solid squares) as a function of wavelength describes a line with slope as well as intercept. This plot was derived from a single uninterrupted scan.

The ion speed is calculated from the kinetic energy that the ion receives in the acceleration stack of the mass spectrometer. The ion speed may be calculated with the following equation (non-relativistic approximation):³⁵

$$v = 1.3891 \sqrt{\left(\frac{K}{m}\right)} \quad (4)$$

where K is the imparted kinetic energy in volts, m is the mass in amu. The velocity, v, will then be in cm/ μ sec.

Figure 9 displays the Doppler shift for a photodissociation band of $V(\text{OCO})^+ \rightarrow V^+ + \text{OCO}$. Comparing the photodissociation spectra of coaxial (top spectrum) and cross beam (bottom spectrum) laser excitation, one observes that the coaxial spectrum is red shifted by 2.93 cm^{-1} . This suggests the kinetic energy imparted to the ions in the acceleration stack of the time-of-flight is ca. 1.45 keV. Apparently the acceleration stack is quite efficient; recall that the applied voltage in the TOF acceleration stack is 1.5 keV.

The tunable laser system is capable of scanning at different rates. For preliminary scans, a faster scan rate (0.6 nm/min.) is used to economize the data acquisition time. Eventually some photodissociation spectra demand a closer look and therefore a slower scan rate (0.04 nm/min.) to utilize the narrow linewidth. The dye laser resolution is ca. 0.2 cm^{-1} at 16 000 cm^{-1} . In this event, several repeating but slow scans

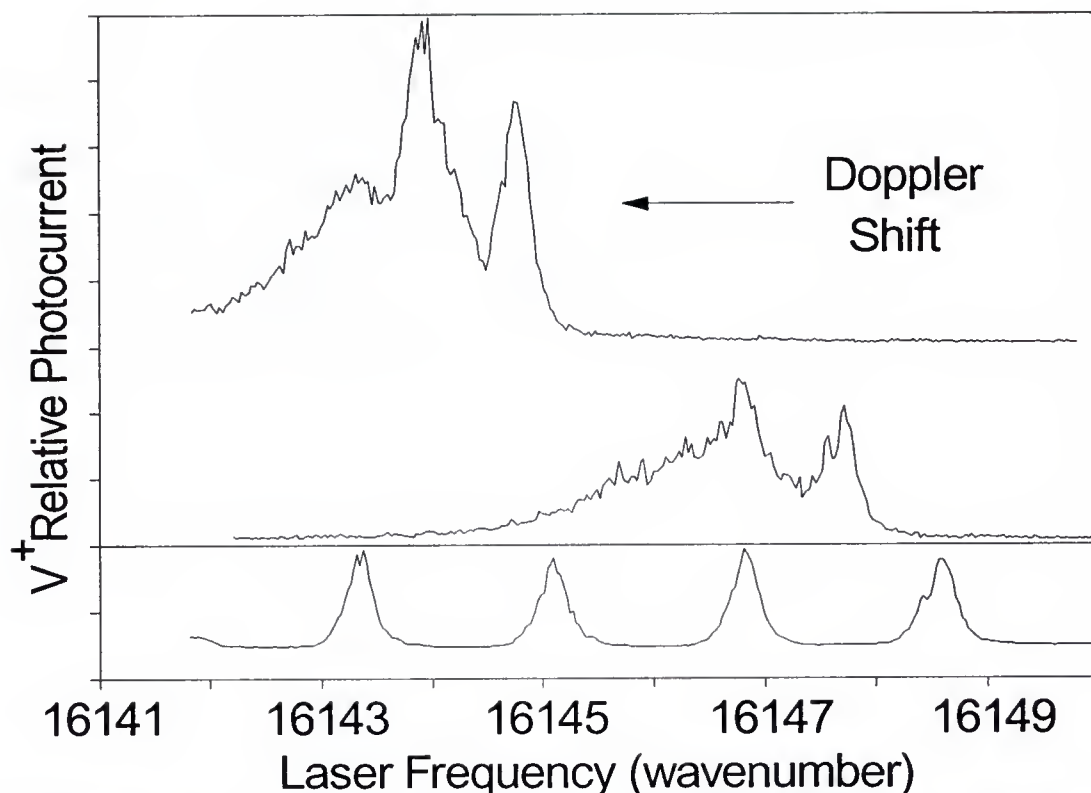


Figure 9. Doppler Shift for Coaxial versus Cross beam Photoexcitation of $V(OCO)^+$.

The figure displays the Doppler shift for coaxial excitation (upper scan) and cross beam excitation (middle curve) of a band in the photodissociation spectrum of $V(OCO)^+ \rightarrow V^+ + OCO$. The lower scan corresponds to a wavelength interference pattern of an etalon with free a spectral range of ca. 1.73 cm^{-1} . The Doppler shift of 2.93 cm^{-1} corresponds to a parent ion kinetic energy of 1.45 keV. This is consistent with the applied acceleration voltage of 1.5 keV.

may be done over an interesting region of the spectrum. These repeating scans may be averaged to increase the signal-to-noise ratio. Unfortunately, accurate overlay of multiple spectra is complicated by the poor re-setability of the mechanical grating drive. An optical device that has been found useful for aligning separate but repeating scans is an etalon. An etalon is an interferometer; constructive and destructive interference is a function of incident wavelength. This interference may be monitored simultaneously with the photodissociation event for a given scan. The peaks corresponding to constructive interference may be easily aligned between different scans. See the bottom trace of Figure 9 for an example of an etalon scan.

Computer Control

The experiment would be impossible to run without computer control. Within the experimental time period of approximately 100 msec, sample generation, mass selection, and optical interrogation all occur. Experimental success depends the proper timing of many events: in chronological order, the carrier gas pulse, the vaporization laser light, the acceleration stack pulse, and the dissociation laser light. To ensure success, data collection, relative timing of experimental events, and waveform digitization are all

controlled with a personal computer and a CAMAC (Computer AutoMated data Acquisition and Control)³⁶ crate.

Optical interrogation of the ion beam demands precise timing control. This is especially important for cross-beam optical interrogation because the spread in arrival time of a given ion size is roughly 100 nsec. Even fluctuations in the power line will affect the acceleration stack voltage, and are easily seen in the arrival time of the ion packet for photodissociation in a cross-beam configuration. Critical timing parameters are controlled by a LeCroy model 4222 programmable delay generator that has ± 200 psec accuracy.

Precise timing control demands that the computer operate in real-time. This is accomplished with a custom computer program that make use of the internal clock of a personal computer. All timing pulses are initiated at 9.1 Hz by an interrupt routine. Other computer tasks are suspended in the background until the experimental timing sequence is completed. The computer code (C language) for the real-time control and data acquisition of the experimental apparatus is included in Appendix B.

Electrical signals induced in the MCP detector by cluster ions are pre-amplified by a factor of 100 (Pacific video amplifier) before digitation by a 100MHz transient recorder (DSP model 2001S transient recorder). Time-of-flight mass spectra are recorded and averaged at the experimental rate of

9.1 Hz. Optical spectra are recorded in single sweep fashion. Low resolution optical scans require about one hour for 20 nm.

Signal Optimization

When making transition-metal rare-gas systems care must be taken before experimentation to minimize perennial oxide and water contaminants. These contaminants preferentially bind to the transition-metal cation and hence minimize the amount of desirable ML^+ product. Gas mixtures are prepared by a specially dedicated manifold system. Typically, a 50 L cylinder is pumped out thoroughly to remove any contaminants. When possible, gas is delivered in the appropriate amount from a new and fully pressurized cylinder. This insures that the partial pressure of volatile contaminants in the tank is at a minimum.

Stainless steel gas lines leading into the vacuum chamber are pumped for 8 hrs then purged with the appropriate gas/gas-mix just before an experimental run. Further precautions against water contamination warrants the use of a Molesieve trap in a liquid nitrogen bath. The Molesieve is housed in a copper coil. The copper coil represents the only non-stainless tubing in the gas inlet system. The gas line is set up so that the copper tubing may be optionally bypassed.

Sample rod and source block preparation also requires similar scrutiny. All transition metal rods are ca. 99% pure with the exception of the chromium rod. This rod was plated locally and no effort has been made to characterize its purity. The transition metal rod is lightly filed or sanded to remove surface contaminants and to crudely smooth the surface. The source-block channel is meticulously cleaned with Q-tips and methanol. The entire stainless steel block is then ultrasonicated in a soap solution for 5 min, another 5 min. in methanol, and then two successive 5 min. intervals in water. After this cleaning process the source block is heated to 200°C for ca. 10 min to remove water. Expediently, the sample rod is secured within the nozzle block, appropriate connections are made, and the assemblage is placed back in the vacuum chamber before it can cool.

For the production of $V(HOH)^+$, water is a desirable component of the carrier gas. To cluster water, a two-stage pressure system is incorporated. A pure tank of helium provides the backing pressure of 100 psi to a small ca. 200 cm³ cylinder. About 2 ml of water is placed in this cylinder. This corresponds to approximately 0.3% mole fraction of water in carrier gas. A second regulator controls the final gas-valve backing pressure.

In addition to worrying about contaminants one must also optimize the signal-to-noise (S/N). There are three major factors that influence the signal-to-noise ratio

significantly: the gas pulse, the rod surface, and the vaporization laser stability. Unfortunately, little can be done to improve shot-to-shot stability of the laser system. However, vibrations may be minimized with a solid table and sturdy optical mounts.

The valve is adjusted to produce a reasonable flow rate in the 'sweet spot'. Figure 10 displays a picture of the flow rate verse the applied electrical pulse duration. Notice that the flow rate has a local minimum near 158 μ sec corresponding to ca. 100 sccm. For best stability the electrical pulse is set to this minimum. Overall S/N critically depends on pressure fluctuation and therefore it is best to minimize flow rate fluctuation by minimizing the first derivative of this curve.

The rod is constantly turned at 1/3 RPM with a Hurst synchronous motor to prevent burning a hole in the surface and therefore to maintain long term signal-to-noise stability.

The journey of a cluster ion from inception to detection has been followed. The combination of a laser generated plasma with a supersonic expansion enables one to produce virtually any imaginable system. The use of two mass selection stages provides superb control over parent and daughter ions. This particular apparatus is quite facile at producing weakly bound ions for the purpose of optical probing.

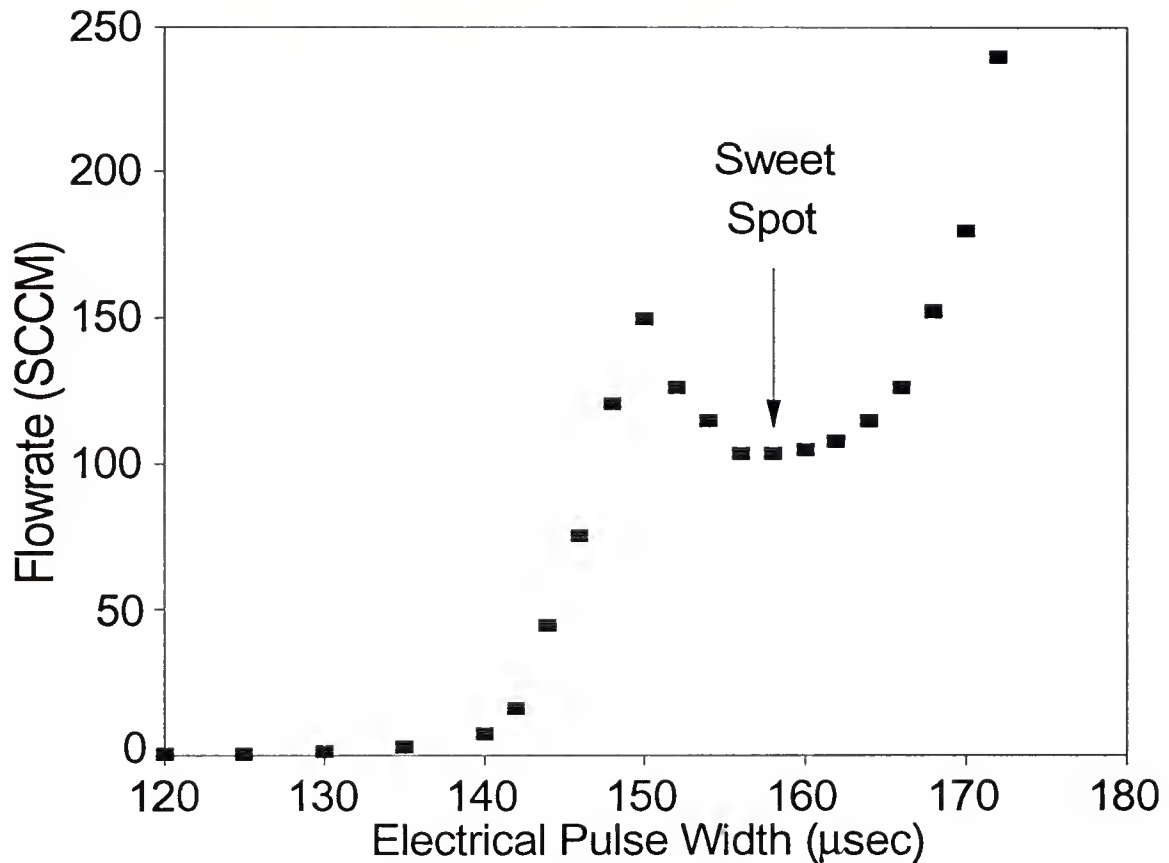


Figure 10. Sweet Spot of Solenoid Pulse Valve.

The figure displays flow characteristics of the solenoid valve as a function of applied electrical pulse width. Flow rate is measured in standard cubic centimeters per minute (SCCM). In the de-energized state the solenoid valve is closed with the aid of a stiff spring. The valve may be opened against the force of the spring with a 150 V electrical pulse. The figure displays a unique position, the 'sweet spot', which corresponds to a local minimum in flowrate. Mechanically, a dynamic equilibrium between the restoring force of the spring and the opening force of the electromagnet will result in the limitation of poppet bouncing. In addition, operating the valve at the sweet spot minimizes fluctuations in flowrate with any change in valve behavior, i.e. the first derivative of this curve is small in the vicinity of the minimum.

INDUCTIVELY BOUND DIATOMICS

Threshold to Photodissociation

This chapter is dedicated to the presentation and analysis of data obtained from the photodissociation of several cation, rare-gas containing, diatomic systems. The photophysics leading to dissociation may be divided loosely into two types depending on the lifetime of the dissociative event. If the lifetime is very short, as in direct dissociation, only a broad spectrum will be observed. This is the case for the photodissociation of NiAr^+ and CrAr^+ . In contrast to this behavior, the lifetime of the photoexcited state may be sufficiently short to be observed in photodissociation, but sufficiently long to reveal vibrational and rotational information. The systems, specifically VAr^+ , VKr^+ , CoAr^+ , CoKr^+ , ZrAr^+ , and CaKr^+ , all display resonant transitions, i.e., bound-bound vibronic transitions, followed by dissociation. Obviously, more information may be garnered from the systems that display vibrational transitions than from those that display only a featureless threshold. But also, the analysis of these systems is more demanding and will therefore be deferred to the next section. We will introduce

the analysis of metal rare-gas diatomics with the systems of NiAr^+ and CrAr^+ , which display only a featureless threshold. Nonetheless, a featureless threshold is quite informative.

Figure 11 displays the photofragmentation of $\text{NiAr}^+ \rightarrow \text{Ni}^+ + \text{Ar}$ as a function of dissociation laser frequency on the interval from 17 400 to 18 100 cm^{-1} . The production of Ar^+ is not observed as a photoproduct of NiAr^+ at these photon energies as expected from the large disparity in the ionization potential of the two atoms: $\text{IP}(\text{Ar}) = 15.755 \text{ eV}$ and $\text{IP}(\text{Ni}) = 7.633 \text{ eV}$.³⁷ Internal electronic excitation of the Ar atom is not energetically possible either; the first excited state is at 11.54 eV (93 143 cm^{-1}).³⁷ Excitation of argon would require the energy of five visible photons in this wavelength region, an unlikely event. Therefore, photofragmentation of NiAr^+ is monitored as the Ni^+ fragment ion current transmitted by the 127° electrostatic sector.

With the high intensity of laser light, a multi-photon event, i.e., the concerted absorption of two or more photons, is possible. The Quantel dye laser is capable of delivering a power fluence of 10^8 W/cm^2 to the ion packet. This corresponds to a photon fluence of ca. $10^{17} \text{ photons/cm}^2$ in the visible region which is more than sufficient for the process of multiphoton absorption.

Of course the probability for a multiphoton event will depend on exact nature of the transition involved. One-photon dissociation cross sections of resonant transitions have been

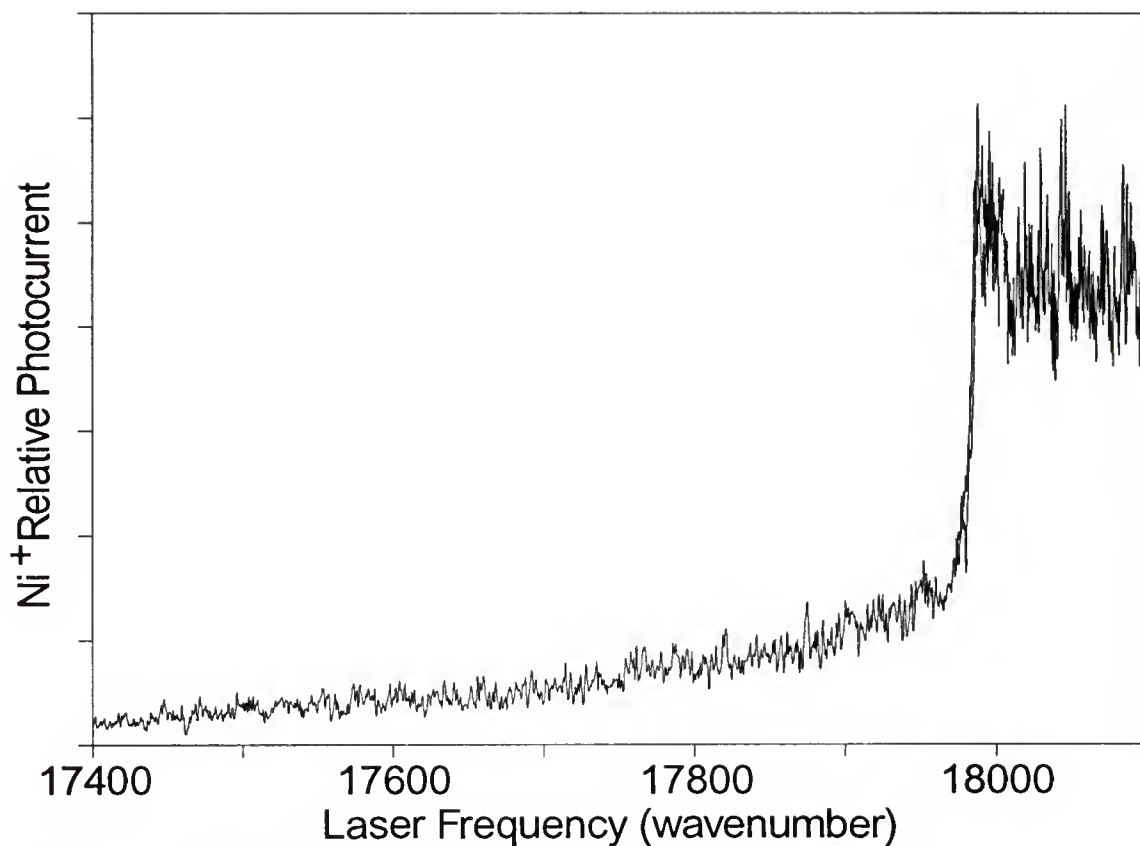


Figure 11. Photodissociation Threshold for NiAr^+ .

The figure displays the relative photofragmentation of $\text{NiAr}^+ \rightarrow \text{Ni}^+ + \text{Ar}$ as a function of laser frequency over the interval 17 400 to 18 100 cm^{-1} . A jump in the one photon photofragmentation is observed at 17 984 cm^{-1} indicating a threshold for producing excited $^2\text{F}_{7/2}$ Ni^+ ions. This establishes the binding energy of NiAr^+ as 0.55 eV.

estimated at the aforementioned power for MRg^+ systems as $5 \times 10^{-17} \text{ cm}^2$.⁽³⁸⁾ Thus, one in five photons that cross the interaction region defined by the cross section will result in dissociation. A two-photon cross section will be smaller. Nonetheless, two-photon processes have been observed under similar laser power in the photodissociation of Ni_2^+ .⁽³⁹⁾ In any case, correct analysis of an optical transition is necessary for accurate description of chemical behavior.

Figure 12 displays the relative Ni^+ photocurrent as a function of incident laser fluence. The laser fluence dependence of the dissociation yield at $18\,020 \text{ cm}^{-1}$ (ca. 40 cm^{-1} above the dissociation edge) shows a linear fragmentation response over a range of 0.5 to $8.0 \text{ mJ/pulse cm}^2$. Recall, in a weak field approximation the absorption intensity is proportional to the incident light intensity (Beer-Lambert Law).⁴⁰ Thus, a linear relation between fragmentation and laser fluence indicates that the photodissociation at this energy involves a simple one-photon absorption event. This leaves no ambiguity as to the value of the excitation energy imparted to the NiAr^+ by the laser.

Under the normal operating conditions of the mass spectrometer, a trace amount of Ni^+ from NiAr^+ is observed from collision-induced dissociative processes. The data presented here are in the form such that the small CID contribution to the dissociation has been nullified.

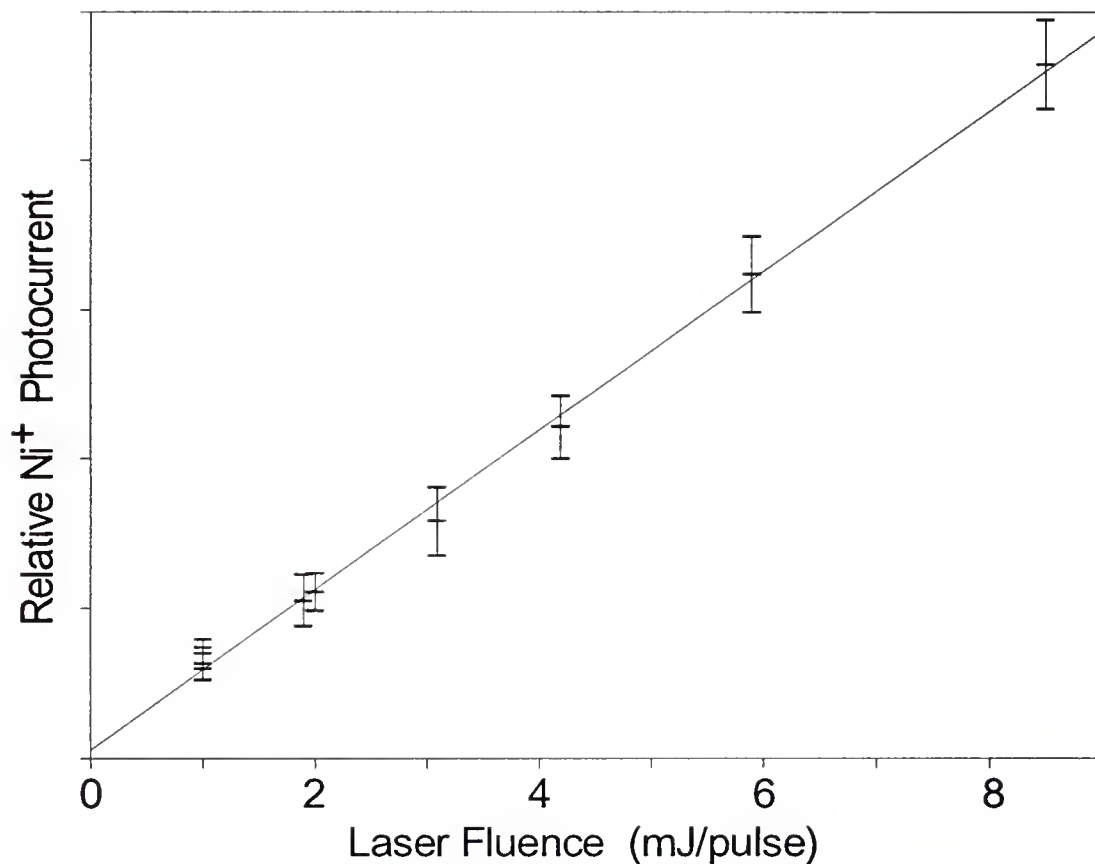


Figure 12. Laser Fluence Dependence for Photodissociation of NiAr⁺.

The figure displays the fluence dependence for the photodissociation of NiAr⁺ at the wavelength of ca. 554 nm. This wavelength position is to the blue of the photodissociation threshold of displayed in Figure 11. A linear curve for the fluence dependence determines that the threshold is one photon is nature.

To within the signal-to-noise of the present data, the photodissociation action spectrum of NiAr^+ in the region of $18\,000\text{ cm}^{-1}$ appears as a featureless edge. Presumably, this indicates the onset of a photodissociation threshold, i.e., the point at which the laser photon has just enough energy to produce (excited state) products with zero kinetic energy. Therefore, one may attribute the edge energy of 2.23 eV ($17\,984\text{ cm}^{-1}$) as the sum of the binding energy of NiAr^+ and some promotion energy in the isolated Ni^+ ion. The absence of any vibrational or electronic hot band features associated with the threshold at $17\,984\text{ cm}^{-1}$ implies extensive cooling of the NiAr^+ emanating from the supersonic-expansion ion source.

Since it is energetically impossible to excite the argon atom in the probed spectral region, the absorption spectrum of NiAr^+ must be similar to the absorption of the bare Ni^+ ion. Consultation of the energy levels of Ni^+ shows that electric dipole allowed transitions would not be expected within the manifold of states arising from the $3d^9$ configuration since all of these states have the same parity. The lowest, fully-allowed electronic state corresponding to $3d^84p$ configuration (and electric dipole connected to the ground state) is $6.39\text{ eV}^{(37)}$ above the $^2D_{5/2}$ ground state of Ni^+ . The photodissociation of NiAr^+ appears to occur through a weakly allowed one-photon transition at 2.3 eV where no isolated Ni^+ transitions are expected. However, the ground state system is

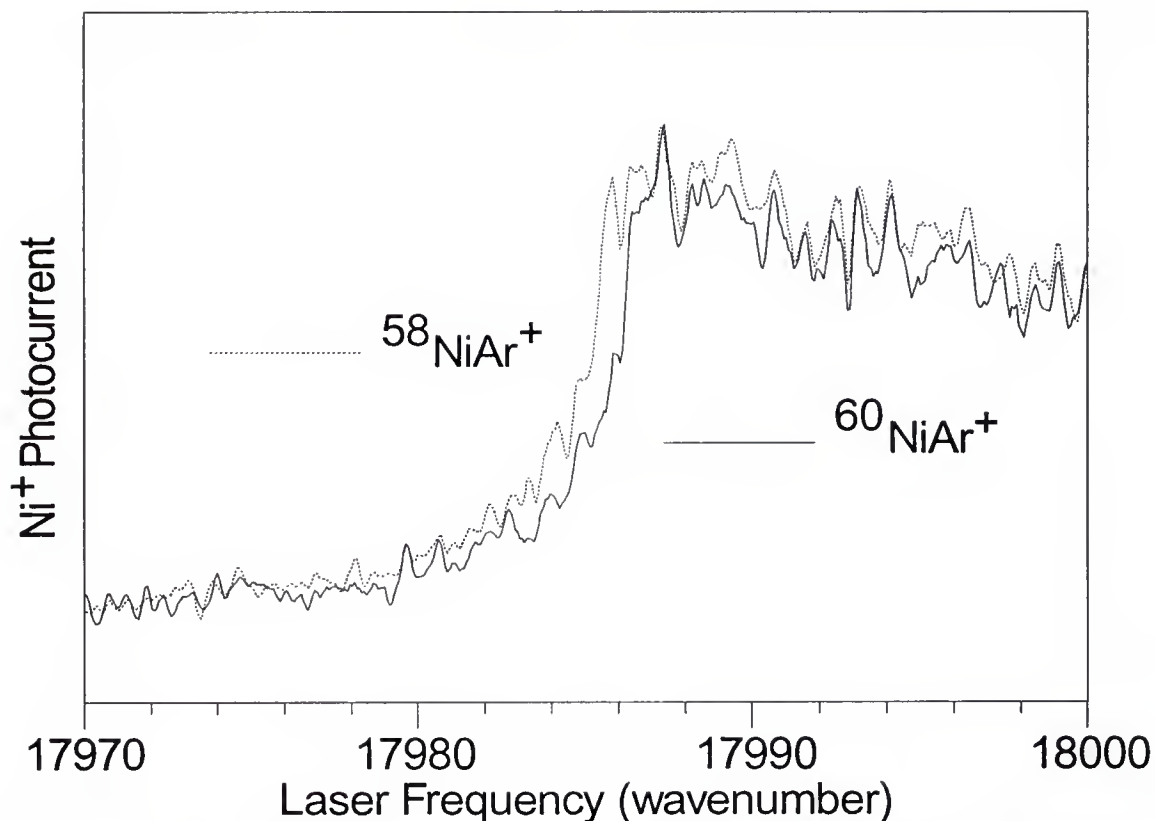


Figure 13. Isotopic Shift for Photodissociation of NiAr⁺. The figure displays a closeup of the region near the photodissociation threshold displays a spectroscopic shift for two isotopes of NiAr⁺. The lighter isotope, ⁵⁸Ni⁴⁰Ar⁺ (dotted line), is shifted $0.8 \pm 0.15 \text{ cm}^{-1}$ to the blue of the threshold for ⁶⁰Ni⁴⁰Ar⁺ (solid line). This shift corresponds to a ground state vibrational frequency of $235 \pm 50 \text{ cm}^{-1}$.

undoubtedly bound and, thus, the magnitude of the observed diabatic limit would be larger than any suspected separated atomic limit energy. One possible assignment of the photodissociation feature in Figure 11 is the threshold for production of ${}^2F_{7/2}$ Ni⁺ and 1S Ar. The transition derives its nature from the parity forbidden, but spin allowed $3d^84s$ (${}^2F_{7/2}$) \leftarrow $3d^9$ (${}^2D_{5/2}$) transition in isolated Ni⁺. If this is the case, the NiAr⁺ ground state binding energy (D_0) is the difference between the Ni⁺ ${}^2F_{7/2} \leftarrow {}^2D_{5/2}$ transition energy of 1.68 eV (13 550.3 cm⁻¹) and the observed threshold energy of 2.23 eV, or 0.55 eV.

Since nickel has several naturally occurring isotopes (${}^{58}\text{Ni}$, ${}^{60}\text{Ni}$ predominantly at 68.3% and 26% respectively)³³ it is possible to simultaneously measure the photodissociation spectrum of both isotopes. Figure 13 displays a closeup of the region near the diabatic threshold at 17 970 to 18 000 cm⁻¹. The isotope shift between the photodissociation features of ${}^{58}\text{Ni}^{40}\text{Ar}^+$ and ${}^{60}\text{Ni}^{40}\text{Ar}^+$ is 0.8 ± 0.15 cm⁻¹ with the heavier isotope being shifted to higher energy. This shift corresponds to the difference in the vibrational energy of the ground state of these two species. An equation relating the isotopic shift to the vibrational frequency and the reduced mass is easily derived from the definition of the force constant, $k = \mu(2\pi\omega_e)^2$.⁽⁴¹⁾ After some manipulation, the vibrational frequency may be expressed in terms of the isotope shift, $\Delta\nu$, as follows:

$$\omega_e = \frac{2\Delta v}{(1 - \rho)}.$$

The variable ρ is the square root of the ratio of reduced masses. Presumably, this vibrational energy is zero point and the ground state vibrational frequency of NiAr^+ may be determined as ca. $235 \pm 50 \text{ cm}^{-1}$.

Besides NiAr^+ , the photodissociation spectrum of CrAr^+ also displays a threshold in the visible region. Figure 14 displays the photodissociation spectrum for the process $\text{CrAr}^+ \rightarrow \text{Cr}^+ + \text{Ar}$ over the region of $14\,440$ to $14\,700 \text{ cm}^{-1}$. A significant increase in photodissociation intensity is seen to begin at $14\,500 \text{ cm}^{-1}$ which marks the onset to a diabatic dissociation into excited fragments. Perturbations due to background states irregularly modulate the photodissociation spectrum for photon energies above $14\,490 \text{ cm}^{-1}$.

The separated atomic configuration of the photofragments for the dissociation is $\text{Cr}^+(\text{}^6\text{D}) + \text{Ar}(\text{}^1\text{S})$. The excited atomic state electronic configuration of the transition metal cation is in accord with the only spin allowed transition³⁷ within ca. 6 eV of the ground state, $\text{Cr}^+(\text{}^6\text{S})$. The large disparity in ionization potentials ($\text{IP}(\text{Ar}) - \text{IP}(\text{Cr}) = 9.0 \text{ eV}$)³⁷ between Cr and Ar indicates that Cr^+ is the only possible charged photoproduct. Dissociation into excited state Ar atoms is also impossible, as previously discussed in NiAr^+ system, since the first excited state lies ca. 11.5 eV above the ground state. Due to the cooling the parent ions suffers in

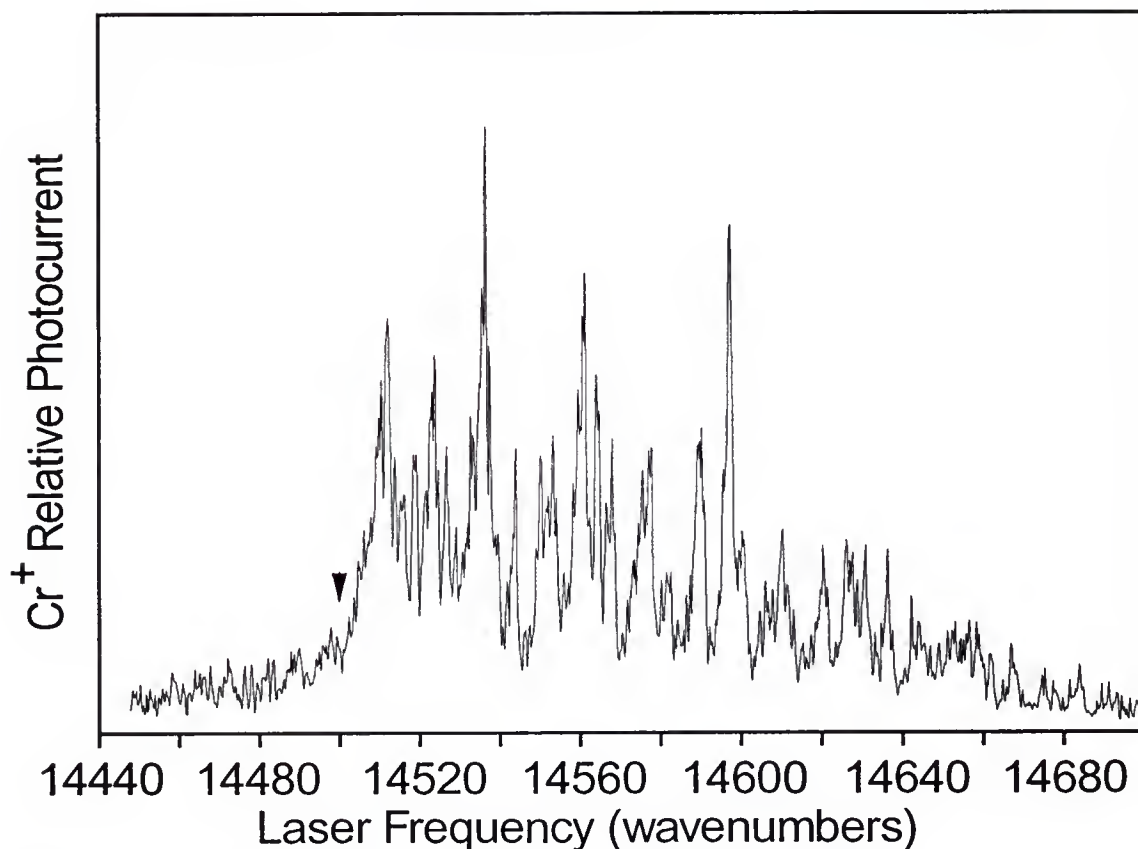


Figure 14. Photodissociation Threshold for CrAr^+ .

The figure displays the relative photofragmentation spectrum of $\text{CrAr}^+ \rightarrow \text{Cr}^+ + \text{Ar}$ as a function of laser frequency over the region of 14 440 to 14 700 cm^{-1} . The onset to a one-photon diabatic dissociation limit corresponding to the separated atomic levels of $\text{Cr}^+(\text{}^6\text{D})$ and $\text{Ar}(\text{}^1\text{S})$ is marked with an arrowhead. The ground state binding energy of this molecule is determined from this threshold and the Cr^+ promotion energy to be 0.29 ± 0.04 eV.

Table 2. Ground State Spectroscopic Parameters for NiAr⁺ and CrAr⁺.

System	Config. ^{a)}	D ₀ (eV)	ω_e (cm ⁻¹)	k _e (N/m)
NiAr ⁺	3d ⁹	0.55	235	77
CrAr ⁺	3d ⁵	0.29		

^{a)}Metal ion atomic configuration in separated atom limit.

the supersonic expansion, the origin of the optical feature is assumed to be the vibrationless level of the molecules. Similar fluence dependence measurements as performed in NiAr⁺ confirm that the diabatic threshold corresponds to a one-photon event. The adiabatic dissociation energy may then be determined by subtraction of the atomic promotion energy in Cr⁺ from the observed diabatic dissociation limit to yield $0.29 \pm .04$ eV for CrAr⁺. The uncertainty in the adiabatic dissociation limit arises from the uncertainty in the J state of the Cr⁺ ion upon dissociation.

Unfortunately, isotopic information is not reliable for CrAr⁺, unlike that of NiAr⁺. Attempts to determine the isotopic shift of ⁵²Cr⁴⁰Ar⁺ versus ⁵³Cr⁴⁰Ar⁺ (and/or ⁵⁴Cr⁴⁰Ar⁺), which occur naturally at 84%, 9.5% (2.4%)³³ respectively, are complicated by the rough nature of the photodissociation spectrum and the relatively low natural abundance of another isotopically substituted system.

Both systems discussed in this section, NiAr^+ and CrAr^+ , have similar properties. A singly-charged cation is physisorbed to a rare-gas atom. Spectroscopy performed in the visible region on these systems, results in a photodissociation feature that is derived from an excited state of the cation. Neither excitation nor charge transfer of the rare-gas atom is energetically impossible. In addition, all photodissociation events correspond to a one-photon excitation. The spectroscopically determined characteristics of NiAr^+ and CrAr^+ are listed in Table 2.

Since there is little likelihood of any formal charge residing on the Ar atom in either NiAr^+ or CrAr^+ , a good approximation of the nature of the binding in these molecules may be derived from a picture of an almost unperturbed transition-metal cation with a polarized Ar atom. The binding forces would be dominated by simple charge induced-dipole forces. If this is the case, the attractive part of a classical potential surface is proportional to $1/r^4$.⁽⁴²⁾ Thus, the binding energy for a given system is significantly dependent on the internuclear separation. This would explain the difference in adiabatic binding energy between NiAr^+ and CrAr^+ . The respective valence electronic configuration is $(3d^9)$ for Ni^+ and $(3d^5)$ for Cr^+ . Allowing for d orbital contraction across the transition-metal row, one would expect that the NiAr^+ system, having the smaller radius, would be bound by more than the CrAr^+ .

Resonant Photodissociation of VAr^+ and VKr^+

The diatomics VAr^+ and VKr^+ will be the first systems to be discussed that display resonant photodissociation of bound levels. The kind of data manipulation found in this section is representative of the remaining systems discussed in this chapter. For the sake of completeness, the results of the data analysis are included in each section. A detailed treatment of vibrational fitting and the application of the LeRoy-Bernstein procedure for determination of the dissociation limit is included in this section. The determination of vibrational numbering through isotopic analysis is postponed to the $ZrAr^+$ section.

One may notice that the line positions for the systems of VAr^+ , VKr^+ , $CoAr^+$, $CoKr^+$ presented in this Chapter have been revised from previously published data.^{43,38} This was before we were aware of the nonlinearity of the Quantel scan box (see experimental section). Correct wavelength positions will be published in a future paper that will include recently acquired results for the photodissociation spectra of VXe^+ and $CoXe^+$. All vibronic line positions listed in this Dissertation are accurate to ca. $\pm 1.5 \text{ cm}^{-1}$.

Figure 15 displays a portion of the one-photon resonant photodissociation spectrum for the process of $VAr^+ \rightarrow V^+ + Ar$ over the visible region of 16 150 to 16 650 cm^{-1} . A series of bound-bound vibronic transitions belonging to an excited state

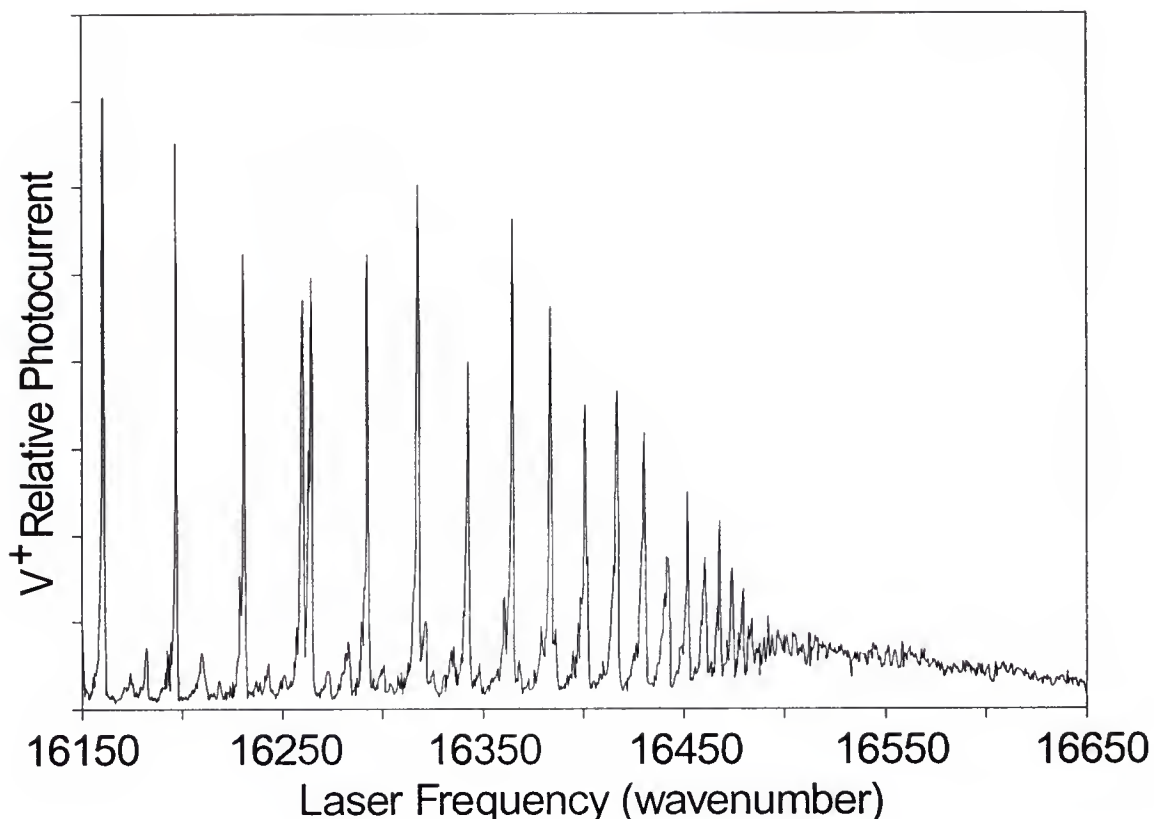


Figure 15. Resonant Photodissociation of VAr^+ .

This figure displays a portion of the one-photon resonant photodissociation spectrum of VAr^+ . Relative V^+ photocurrent (ordinate) is displayed as a function of laser frequency (abssisa). The horizontal axis indicates zero photodissociation. No Ar^+ photofragments are observed in this spectral region. Note the strong upper state vibronic progression converging to a diabatic dissociation limit at $16\,581\text{ cm}^{-1}$. Note also, the perturbation occurring near $16\,330\text{ cm}^{-1}$ and the weak bands belonging to different progressions evident in the red end of the figure. The spectrum above $16\,600\text{ cm}^{-1}$ is weak and apparently continuous indicating a direct bound-continuum photodissociation at these regions.

of VAr^+ is evident. At this excitation energy, photoproduction of Ar^+ (similarly, Kr^+ is not observed from VKr^+) is not possible due to the large disparity of ionization potential of the atoms. The ionization potentials³⁷ of Kr, Ar, and V are 13.996 eV, 15.755 eV, and 6.74 eV, respectively.

Under the normal operating conditions of the mass spectrometer, a trace amount of V^+ from VAr^+ is observed from collision-induced dissociation with the residual He gas (ca. 1×10^{-7} Torr) in the flight tube. For this system, collision-induced dissociation (CID) produces only a small, and relatively constant background to the photoproduction yield and may be nullified. The bottom of the horizontal axis of Figure 15 therefore corresponds to zero photo-production of V^+ .

The portion of the spectrum shown in Figure 15 is especially revealing. A progression of red-degraded vibronic bands converges to a diabatic dissociation limit of $16\,581\text{ cm}^{-1}$ at which point the spectrum becomes continuous. More than one upper state progression is evident (see particularly the red end of the spectrum) and numerous perturbations indicate that the upper state of these transitions interact, as shown by two closely spaced bands near $16\,330\text{ cm}^{-1}$. The upper state anharmonicity is also made apparent by the diminishing interval among transitions with increasing laser frequency.

The resonant photodissociation spectrum for VKr^+ is similar to that of VAr^+ . This spectrum also displays a

vibrational progression, but unlike the spectrum of VAr^+ it is not visibly perturbed by another state. The band shapes in both these spectra demonstrate partially resolved rotational structure indicative of a large increase in average internuclear distance upon photoexcitation and a cold (< 10 K) initial rotational distribution of the parent molecule. No electronic or vibrational hot bands have been assigned for either molecule. The partially resolved rotational structure of the vibronic transitions places a lower limit on the lifetime of the upper levels of the transition at 10 ps. The upper limit to the excited state lifetime is placed by the time between excitation and kinetic energy analysis, about $5 \mu s$ for travel time in the 127° electrostatic sector.

Dissociation laser fluence dependence, for both V^+ -(rare gas) systems, of the resonant photodissociation transitions indicates a one-photon absorption event is responsible for the photoproduction of V^+ . A more thorough description of using laser fluence dependence to determine the number of photons of a given photodissociation feature was given in the section of $NiAr^+$. Poor temporal/spatial quality of the excitation source unfortunately prevents accurate absolute cross-section measurements. However, the strongest photodissociation transitions have cross sections of ca. 10^{-17} cm^2 .

Table 3. Line positions for $^{51}\text{V}^{40}\text{Ar}^+$ and $^{51}\text{V}^{84}\text{Kr}^+$ in wavenumbers.

VAr^+			VKr^+		
v'	Observed	$o-c^a$	v'	Observed	$o-c^a$
1	15303.0	0.73	2	15548.0	0.82
2	15387.9	-0.83	3	15639.1	1.56
3	15470.7	-0.76	5	15807.7	-2.35
4	15550.4	-0.13	6	15891.1	-1.18
5	15625.9	-0.11	7	15971.4	-0.55
6	15698.4	0.43	8	16049.3	0.24
7	15766.9	0.52	9	16123.8	0.17
8	15832.2	0.70	10	16195.7	0.10
9	15893.9	0.69	11	16265.5	0.37
10	15952.1	0.44	12	16331.7	-0.49
11	16007.5	0.47	13	16397.0	0.23
12	16059.0	-0.19	14	16459.1	0.14
13	16108.0	-0.20	15	16519.3	0.51
14	16152.5	-1.83	16	16576.0	-0.20
15	16192.9	-4.66	17	16631.2	-0.13
*15	16199.3	1.76	18	16685.8	1.63
16	16239.0	1.09	19	16734.9	0.12
17	16276.1	0.69	20	16784.2	1.12
18	16310.3	0.11	21	16829.6	0.35
19	16339.9	-2.55	22	16872.2	-1.00
*19	16344.3	1.87	23	16915.8	0.82
20	16372.7	0.70	24	16954.0	-0.55
21	16398.3	-0.77	25	16991.0	-1.18
*21	16401.9	2.85	26	17026.5	-1.12
22	16423.9	0.22	27	17060.7	-0.41
23	16445.9	-0.03	28	17092.5	-0.11
24	16465.4	-0.47	29	17121.8	-0.29
25	16482.6	-0.88	30	17149.6	0.04
26	16498.9	-0.11	31	17176.5	1.34
27	16512.7	0.26	32	17199.4	0.46
28	16524.3	0.56	33	17222.3	1.50
29	16534.3	1.23	34	17243.1	2.35
30	16543.0	2.41	35	17262.5	3.49
31	16550.7	4.52	36	17279.2	3.83
32	16556.9	6.90	37	17296.5	6.47
33	16562.0	9.78	38	17311.3	8.24
34	16566.4	13.70	39	17323.4	9.08
35	16570.0	18.38	40	17337.1	13.19
36	16572.8	23.76	41	17348.2	16.31
37	16575.1	30.07	42	17358.2	19.93

(a) Observed minus calculated.

(*) Extra lines due to perturbation.

Table 3 lists the positions of the assigned VKr^+ and VAr^+ photodissociation excitation transitions in the interval from 15 000 to 18 000 cm^{-1} . The most intense point of the vibronic band (typical width 2-6 cm^{-1}) is taken to be the vibronic band origin in this analysis. Only the strongest and least perturbed progression in VAr^+ has been presented. Most of the transitions for the photoexcitation spectra of VAr^+ are attributed to excitation of three upper electronic states, all of which dissociate into $\text{V}^+(\text{}^5\text{P}_j) + \text{Ar}(\text{}^1\text{S})$. Although hampered by the perturbations and intensity anomalies in the weaker progressions, one may tentatively assign the dissociation limit corresponding to the strongest progression as $\text{V}^+(\text{}^5\text{P}_2) + \text{Ar}$ by correlation of the extrapolated molecular dissociation limits with the fine structure intervals in atomic V^+ . Only one progression is observed in the VKr^+ spectrum, presumably corresponding to the most intense transition in VAr^+ . In any case, the misassignment of the separated atomic limit could lead to maximum error of 147 cm^{-1} , which corresponds to the $\text{}^5\text{P}_3 - \text{}^5\text{P}_2$ fine structure interval.

Further evidence for the correct assignment of the separated atomic limit may be found in the spin-allowed selection rule for diatomic systems. The ground state atomic configuration for vanadium cation is $\text{}^5\text{D}$, which, upon combination with a $\text{}^1\text{S}$ Ar would produce a variety of quintet molecular terms. Similarly, the excited atomic state, $\text{}^5\text{P}$, for

V^+ would produce quintet molecular terms. The excited state, which lies ca. 1.68 eV above the ground state, is the only quintet occurring within 4 eV of the ground state.³⁷ This argument, of course, is dependent on the exact angular coupling cases of the two electronic states.

Vibrational Analysis

Vibrational transitions may be fit to third order in $(v' + 1/2)$ with the following well-known formula:⁴⁴

$$E(v) = T_{e0} + \omega'_e(v' + 1/2) - \omega_e x'_e(v' + 1/2)^2 + \omega_e y'_e(v' + 1/2)^3. \quad (6)$$

This allows one to determine the electronic term (T_{e0}), the equilibrium vibrational frequency (ω'_e), and the anharmonicity terms, $(\omega_e x'_e)$ and $(\omega_e y'_e)$ of the excited state. For the VAR^+ system, the exact vibrational numbering is not known and therefore represents an arbitrary numbering scheme. However, the numbering has been chosen to yield a reasonable vibrational frequency. Accuracy of this numbering scheme will be tested in the following chapter. The zero of energy for the vibrational fit and all subsequent manipulations is taken as the zero-point level of the ground electronic state. Electronic term T_{e0} is determined directly from a fit of the observed transitions Eq. (6) and is $1/2 \omega_e$ smaller than the electronic term commonly denoted⁴⁵ as T_e .

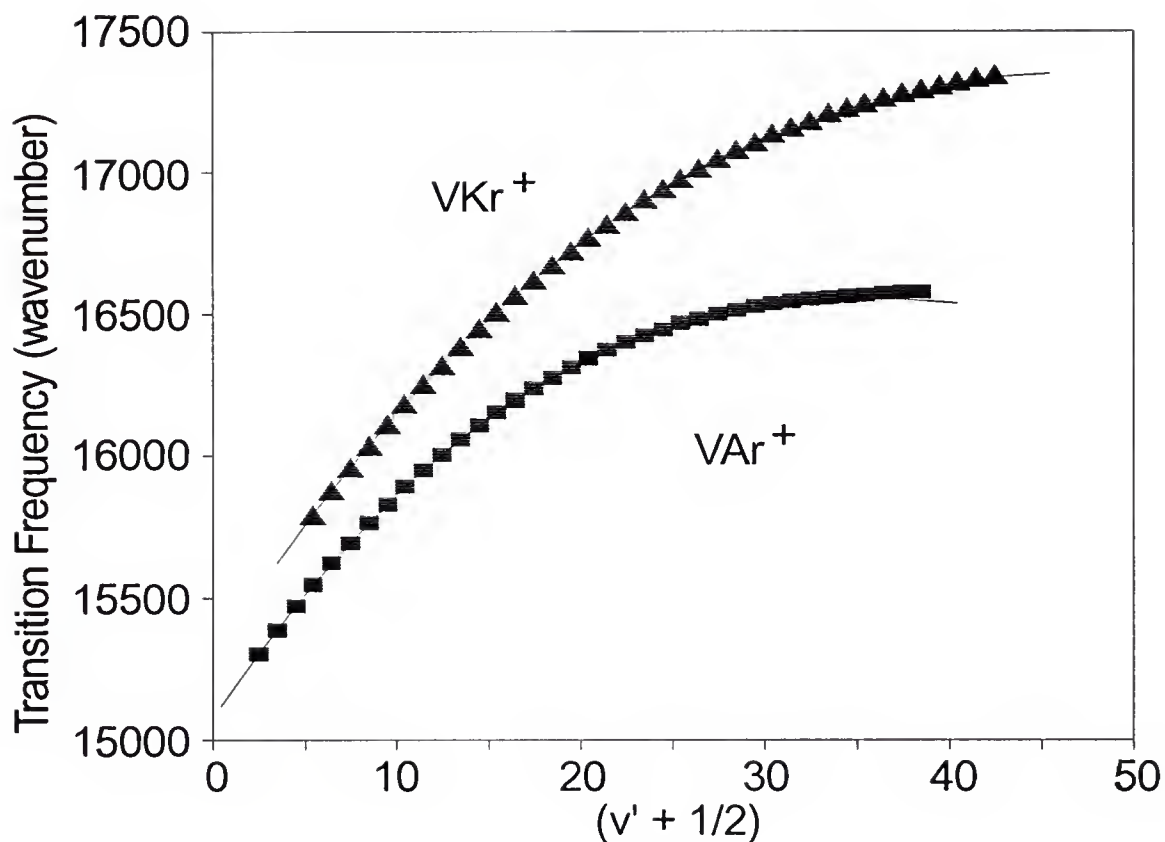


Figure 16. Vibrational Fit for VAr⁺ and VKr⁺.

The figure displays the vibrational fit of the observed vibronic transitions for VKr⁺ (triangles) and VAr⁺ (squares). The observed transition are least-squares fit to Eq. (6) to determine the vibrational frequency and anharmonicities of each system. The solid lines for each system represent the calculated levels from the least-squares fit.

Figure 16 displays the calculated and experimental points for the vibrational fit. The accuracy with which Eq. (6) describes the observed vibronic structure depends upon the degree of anharmonicity of the molecular forces and the existence of any local perturbations between the electronic states. The best fit is obtained for the lowest vibrational levels of each system. The residuals to the least squares fit are also included in Table 3 and, except for very large v' values, show no significant deviation.

In practice, the criterion for an acceptable vibrational fit depends upon the behavior of the residuals of the observed and calculated vibrational levels. If the vibrational information is sufficient, such as is found in VAr^+ in which 37 bands are observed, one may fit the levels to several anharmonic terms. Figure 17 displays the residuals to the vibrational fit of Eq. (6) to observed levels in VAr^+ . A vibrational fit, containing one anharmonic term, to the lowest 31 bands (squares) displays a systematic error in the residuals. This systematic error may be removed by the inclusion of a second anharmonic term (triangles). Of course one may continue to fit more vibrational levels with the addition of more anharmonic terms but this is unrevealing. In some cases attempts to fit the larger v' often increase the residual error of the lower states, thus the determination of ω_e will be poor. Accurate parameterization of larger v'

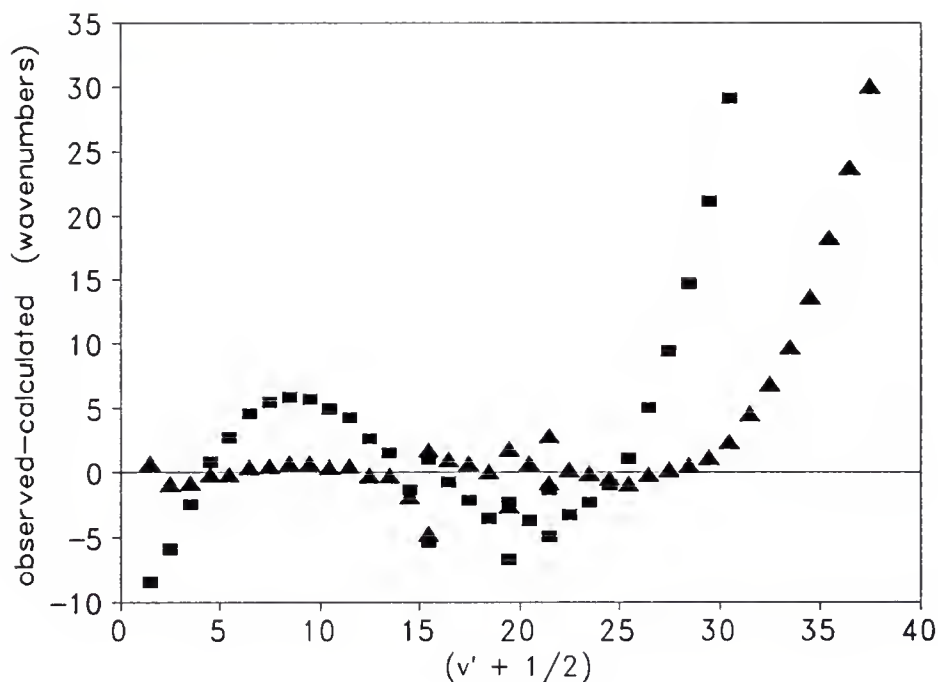


Figure 17. Residuals to the Vibrational Fit of VAr^+ . The figure displays the residuals (observed - calculated) for the vibrational fit of the observed bands of VAr^+ to Eq. (6). A least-squares fit to the equation containing one anharmonic term (squares) and a least-squares fit to the equation contain two anharmonic terms (triangles). Two entries occur at $v' = 15$, 19 and 21 corresponding to a splitting of the vibrational levels by a perturbation. The plot displays a pictorial representation of the effect of adding more terms the Taylor's series expansion of the vibrational equation to the residuals, specifically, the removal of a systematic error. Generally, if vibrational information is available two anharmonic terms are included in the fit of the bottom most vibrational levels. The number of vibrational levels is increased until the root-mean-square deviation of the residuals, in the absence of perturbed states, exceeds 1.5 cm^{-1} for those fitted levels.

vibrational levels with Eq. (6) is not of significant consequence as a modified analysis treating the vibrational levels closest to the dissociation limit will be presented below.

Absolute vibrational numbering of the transitions listed in Table 3 is made from the measurement of the spectral shift among the ^{86}Kr , ^{84}Kr , ^{83}Kr , and ^{82}Kr isotopomers of VKr^+ . This yields a unique absolute vibrational numbering for the upper level of the transition. A detailed description of the utilization of isotopes for the determination of vibrational numbering will be addressed in the ZrAr^+ section. At present, neither the spectrum of $^{59}\text{V}^{36}\text{Ar}^+$ nor $^{59}\text{V}^{38}\text{Ar}^+$ (0.34% and 0.07% natural abundance,³³ respectively) has been obtained. Without isotopic substitution, the firm assignment of absolute vibrational quantum numbers to the VAr^+ transitions listed in Table 3 is impossible. Thus, the upper state vibrational quantum number listed in Table 3 is merely an effective vibrational index, chosen to be close to the absolute value. The correct numbering is, of course, important for the vibrational fit and the subsequent determination of the vibrational frequency and the electronic term. Assignment of the reddest observed transition to the origin band lowers the vibrational frequency by ca. 5%.

All of the transitions observed in this study appear to originate from the ground electronic and vibrationless state of the molecule: i.e., no hot bands have been identified.

This is understandable due to the extensive cooling these ions suffer in the supersonic expansion. From a conservative estimate of the sensitivity of the experiment (1% of a strong transition) and a guess of the ground state vibrational frequency (200 cm^{-1} ; see discussion below), one may infer the vibrational temperature of these ions to be less than 65 K. The low internal temperature of the ions simplifies the spectrum greatly but prevents direct determination of the ground state vibrational frequency via photodissociation excitation spectroscopy.

Not all of the electronic states predicted from the accessible V^+ atomic ion states combined with a 1S rare-gas atom have been detected in this photodissociation study. Optical selection rules for absorption would limit the number of accessible transitions for excitation and not all the upper levels of those accessible transitions may efficiently dissociate. The fate of the excited states of these ions is determined by a competition among radiative stabilization (fluorescence to a bound level), radiative dissociation (fluorescence to a dissociative level), and non-radiative dissociation through direct coupling to a continuum level (predissociation). Since optical absorption is detected in this study through a vibrational predissociation of the upper state on an appropriate time-scale, many transitions in these molecules may go undetected.

LeRoy-Bernstein Derived Dissociation Limits

Vibrational levels near the dissociation limit are poorly parameterized by a series expansion about equilibrium in Eq. (6), but are better described by a functional form that considers the nature of the attractive forces at work at large internuclear separations. LeRoy and Bernstein^{46,47} have proposed a procedure for the determination of the dissociation energy from the observed vibrational levels. Their derivation begins with the semiclassical WKB** approximation:

$$(v + 1/2) = \frac{2}{h} (2\mu)^{1/2} \int_{R_1(v)}^{R_2(v)} [E(v) - U(R)]^{1/2} dR. \quad (8)$$

The variable μ is the reduced mass and $E(v)$ corresponds to the v^{th} vibrational energy level. The integral bounds are a function of the integrand where $E(v) = U(R_2) = U(R_1)$; the variables R_1 and R_2 refer to the internuclear distance on the repulsive and attractive potential surface, respectively. At large internuclear separation, the vibrational index v may be treated as a continuous variable. The derivative of the above equation with respect to v results in the following equation:

$$\frac{dv}{dE(v)} = \frac{2}{h} (2\mu)^{1/2} \int_{R_1(v)}^{R_2(v)} [E(v) - U(R)]^{-1/2} dR. \quad (9)$$

**WKB approximation will be discussed in the next Chapter.

For a diatomic molecule that dissociates according a $-C/R^n$ potential, one may approximate the interatomic potential in the limit of large R with the potential of the form

$$U(R) = D - \frac{C}{R^n}. \quad (10)$$

Dissociation energy is given by the variable D and R is the internuclear separation. The vibrational eigenvalues may then be expressed as a function of C and the outer turning point, R_2 , of the potential,

$$E(v) = D - \frac{C}{R_2^n}. \quad (11)$$

Substitution of $U(R)$ from Eq. (10) into Eq. (9) and then elimination of C with Eq. (11) from the integrand results in the following equation:

$$\frac{dv}{dE(v)} = \frac{2(2\mu)^{1/2}}{h[D - E(v)]^{1/2}} \int_{R_1(v)}^{R_2(v)} \left[\frac{R_2(v)^n}{R^n} - 1 \right] dR. \quad (12)$$

This integral may be put in a more convenient form by changing the variable of integration to $y = R_2(v)/R$. The following equation results:

$$\frac{dv}{dE(v)} = \frac{2(2\mu)^{1/2} C^{1/n}}{h[D - E(v)]^{(1/2+1/n)}} \int_1^{R_2/R_1} \frac{dy}{y^2(y-1)^{1/2}}. \quad (13)$$

In the limit of $R_2/R_1 \rightarrow \infty$ the integral is known³³ and results in an analytic expression involving the Γ function,⁴⁸

$$\frac{dE(v)}{dv} = \frac{hC^{-1/n}n\Gamma(1 + 1/n)}{(2\pi\mu)^{1/2}\Gamma(1/2 + 1/n)} [D - E(v)]^{(n+2)/2n}. \quad (14)$$

Several terms may be combined to form a constant, K;

$$K = \frac{hC^{-1/n}n\Gamma(1 + 1/n)}{(2\pi\mu)^{1/2}\Gamma(1/2 + 1/n)}. \quad (15)$$

For the molecules under study in this work, the long range attraction forces between the vanadium atomic ion and the rare-gas atom will be dominated by simple charge induced-dipole forces. Therefore C and n in Eq. (10) are fixed⁴⁹, respectively, as

$$C = \frac{q^2\alpha}{2}, \quad n = 4. \quad (16)$$

In this expression α is the polarizability of the rare-gas atom. Thus, the constant K is equal to 0.501 and 0.374 (cm⁻¹)^{1/4} for CoAr⁺ and CoKr⁺, respectively.

For sufficiently dense vibronic levels, the derivative of the eigenvalues may be approximated with the following equation:

$$\frac{dE(v)}{dv} \approx \Delta G(v) = \frac{[E(v+1) - E(v-1)]}{2}. \quad (17)$$

Thus, substitution of the above equation into Eq. (14) results in an expression that may be easily plotted:

$$(\Delta G)^{4/3} = [D - E(v)] K^{4/3}. \quad (18)$$

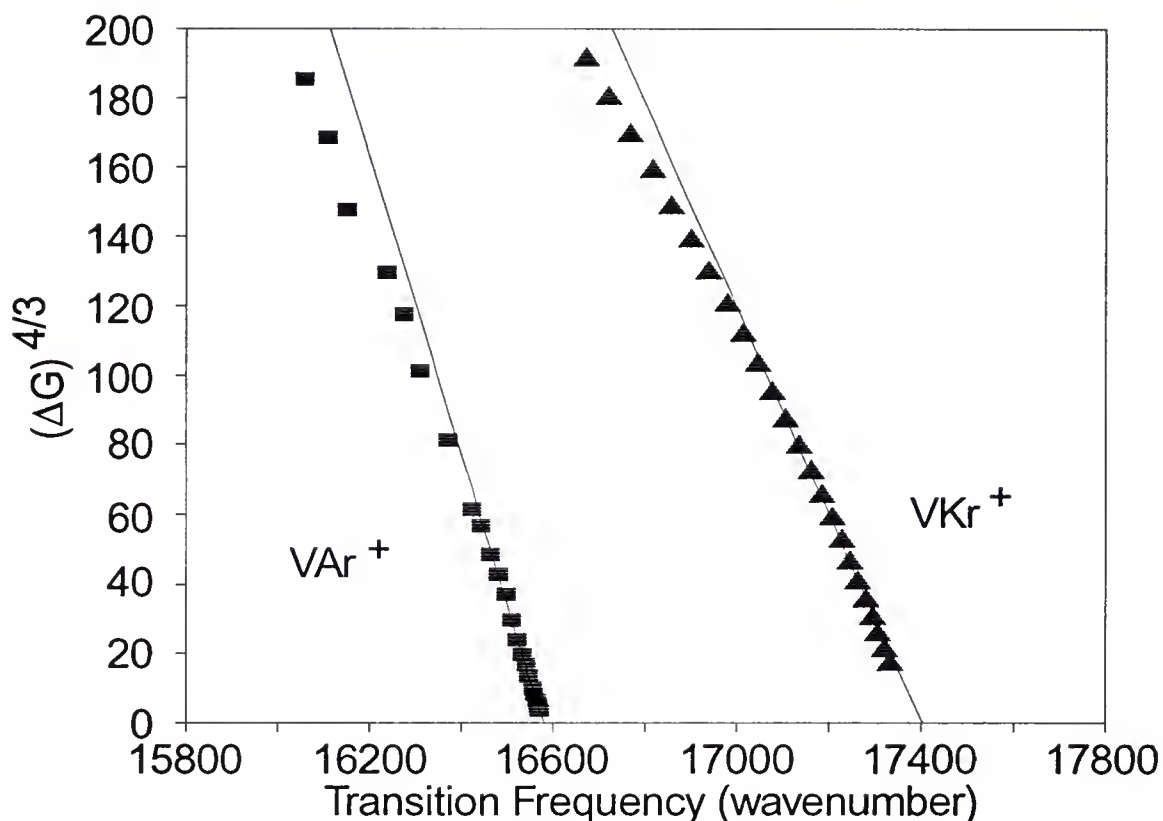


Figure 18. LeRoy-Bernstein Fit for VAr^+ and VKr^+ .

Dissociation limits of VAr^+ and VKr^+ from LeRoy-Bernstein fit. A plot of the derivative of the vibrational energy with respect to vibrational index to the $4/3$ power versus transition frequency (LeRoy-Bernstein plot) for the observed electronic transitions in VKr^+ (triangles) and VAr^+ (squares). For molecules which dissociate under the influence of a $-C/r^4$ attractive force (charge induced-dipole) these data may be linearly extrapolated (lines) to the abscissa to obtain the dissociation limit of the excited states of the respective molecules. The slopes of the extrapolated lines are different due to the difference in polarizability and reduced mass of the two molecules and are in accord with predicted values.

Figure 18 shows the dependence of the derivative of the vibrational energy with respect to the transition frequency for the band systems observed in VAr⁺ (squares) and VKr⁺ (triangles). The plot shows that $(\Delta G)^{4/3}$ is indeed linearly dependent on transition frequency near the dissociation and a linear least squares extrapolation may be used to estimate the dissociation limits, D. These extrapolated values are listed in Table 4. Note that the values of D are not dependent on the absolute vibrational numbering.

A useful expression may be obtained by the integration of Eq. (17). The vibrational energy levels near the dissociation limit will be of the form

$$[D - E(v)]^{(n-2)/n} = [(n-2)/2n] (v_D - v) K. \quad (19)$$

The parameter v_D , a constant of integration, is the fictitious vibrational quantum number of the dissociation limit itself, i.e. $E(v_D) = D$. Recall that for this discussion the zero-of-energy for both D and $E(v)$ is taken to be the zero-point level of the ground state of the molecule. Thus, a particular electronic state has the diabatic dissociation energies (in conventional nomenclature) of $D_0 = D - E(0)$ and $D_e = D - T_{\infty}$.

The dissociation energies listed in Table 4 correspond to the difference in energy between the zero point level of the molecule and a particular excited state of the $V^+ + \text{Ar(Kr)}$

Table 4. Spectroscopic Parameter for VAr⁺ and VKr⁺. All values are in (cm⁻¹) unless otherwise noted.

	VAr ⁺		VKr ⁺	
	Ground	Excited	Ground	Excited
T _{co}		15166		15310
ω _e		94.1		98.6
ω _e x _e		1.95		1.40
ω _e y _e		0.011		0.005
k _e (N/m)		11.7		18.2
ν _D		48.7		68.8
D ^a		16581		17406
D ₀	2986 ^b	1368 ^c	3811 ^b	2047 ^c
D _e ^c		1415 ^d		2096 ^d

^aDiabatic threshold

^bGround state binding energy determined by $D - \Delta E_{\text{atomic}}$.

^cExcited state binding energy; $D_0' = D_e' - 1/2\omega_e' + 1/4\omega_e x_e' - 1/8\omega_e y_e'$.

^dExcited state equilibrium dissociation energy; $D_e' = D - T_{\text{co}}$.

separated atoms. It is not possible for these dissociation limits to correspond to excited argon (krypton) atoms, as mentioned previously, due to the large, first excitation energy of the closed-shell rare-gas systems. Comparison of the observed D values in VAr⁺ and VKr⁺ with the V⁺ atomic energy levels³⁷ suggests the assignment of this dissociation limit as V⁺ (3d³4s ⁵P_J) + Ar/Kr (¹S). The identity of the fine structure level to which excited VAr⁺ dissociates has been made by the partial analysis of the weak progressions in the same spectral region as the transitions listed in Table 3.

The transitions presented in Table 3 appear to arise from an excited state dissociating into $V + {}^5P_2$. Only one progression is observed in the VKr^+ spectrum, presumably it corresponds to the most intense transition in VAr^+ , which is a level dissociating into $V + {}^5P_2$. This is the limit used in the analysis; misassignment of which could lead to a maximum error of 147 cm^{-1} , the 5P_3 - 5P_2 fine structure interval. The adiabatic dissociation energy of the ground state of VAr^+ or VKr^+ is simply the difference between any experimentally determined excited state dissociation limit, D , and the isolated V^+ promotion energy to the state corresponding to that limit. From Table 4 and the above assignment of the dissociation limits ($V + {}^5P_2 \leftarrow {}^5D_0 = 13594.7311$), the adiabatic dissociation energy for the ground state of VAr^+ and VKr^+ is found to be 2986 cm^{-1} and 3811 cm^{-1} , respectively.

After D has been determined for a particular excited electronic state, the vibrational binding energy, $(D - E(v))$, is used to derive the number of bound vibrational levels in the potential via the application of Eq. (19) to yield v_D . The number of bound levels in each potential surface is the largest integer less than v_D . These values, included in Table 3, are 48.7 and 68.8 for VAr^+ and VKr^+ respectively. According to this, one observes approximately 76% and 69% of the bound vibronic transitions in the potential surface for VAr^+ and VKr^+ , respectively.

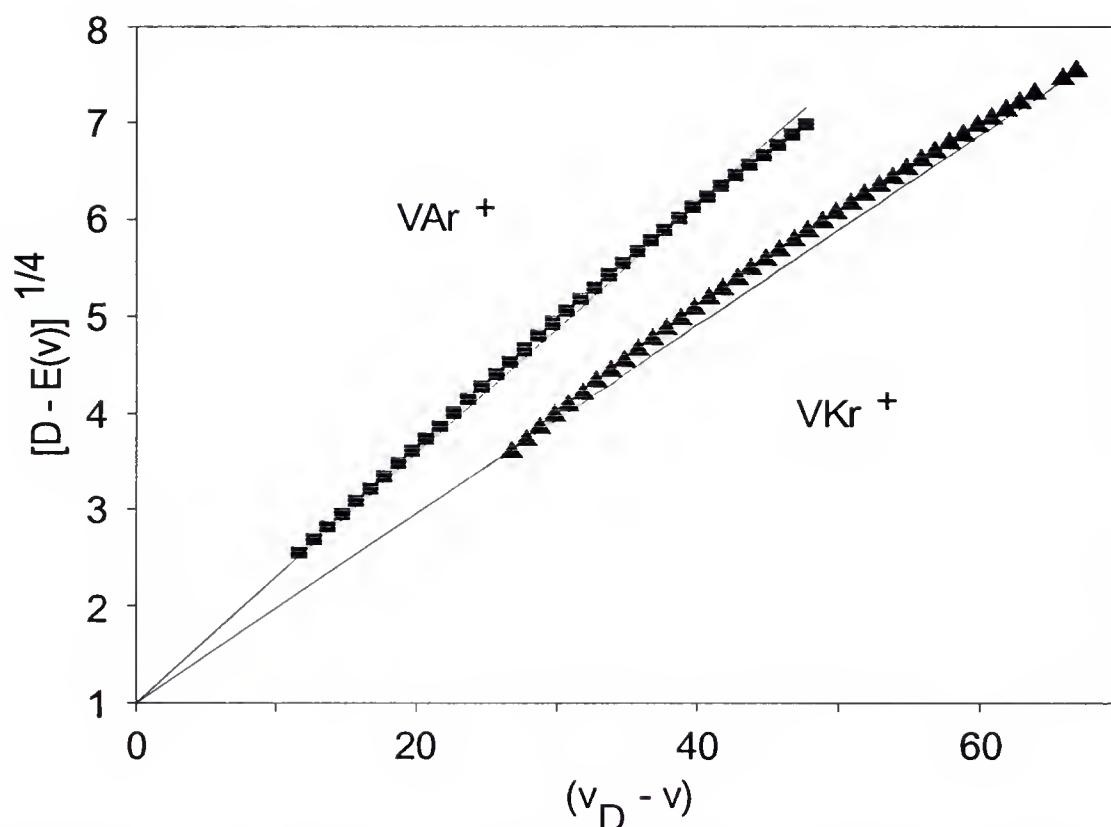


Figure 19. Vibrational Binding Energy for VAr^+ and VKr^+ . The Figure displays a plot of the vibrational binding energy to the $1/4$ power versus the vibrational index $(v_D - v)$ for the observed excited state of VKr^+ (triangles) and VAr^+ (circles). The quantity v_D is the hypothetical vibrational index of the dissociation limit of the potential, i.e., $E(v_D) = D$. The solid lines are the vibrational binding energies predicted for VAr^+ and VKr^+ from Eq. (19) and the literature values of the rare-gas polarizabilities.

Figure 19 shows a plot of the vibrational binding energies to the 1/4 power versus vibrational quantum number for the excited states of VKr^+ and VAr^+ . Also shown in the figure is the predicted dependence (lines) of vibrational binding energy for VAr^+ and VKr^+ using Eq. (15) and literature values⁵⁰ for the rare-gas polarizabilities ($1.66 \times 10^{-24} \text{ cm}^3$ for Ar and $2.52 \times 10^{-24} \text{ cm}^3$ for Kr). One can see that the theoretical values closely match the experimentally derived points. The predictive power of this simple model of vibrational structure implies that inductive forces dominate the binding in these systems. One may then postulate, that the attractive part of a potential surface, and for many Lennard-Jones analytic potentials, the dissociation energy (see Appendix C), is proportional to α/r^4 . An increase in binding energy between the systems VAr^+ and VKr^+ may therefore be attributed to the change in polarizability of the rare-gas partner.

Photodissociation of CoAr^+ and CoKr^+

The second group of metal-cation rare-gas systems to be presented in this Chapter, CoAr^+ and CoKr^+ , also displays resonant bound-bound transitions in the visible region. These systems, unlike $\text{VAr}^+(\text{Kr})$, each have three prominent vibrational progressions in their photoexcitation-dissociation

spectrum. The congestion perturbs the spectrum slightly but it is nevertheless experimentally tractable. Similar vibrational analysis found in the $\text{VAr}^+(\text{Kr})$ section is applied here as well.

Figure 20 displays a portion of the resonant photodissociation spectrum of $\text{CoAr}^+ \rightarrow \text{Co}^+ + \text{Ar}$ over the region of 14 800 to 16 300 cm^{-1} . Bound quasi-bound transitions for three progressions are easily observed in this region. Approximately eleven transitions of one progression, ca. 150 cm^{-1} in interval, account for the largest peaks in the figure. Several transitions belonging to another excited state, within the region 14 800 to 15 450 cm^{-1} , are seen to converge to a diabatic dissociation limit. This portion of the spectrum is similar in appearance the photodissociation spectrum of VAr^+ found the in previous section. Dwarfed remnants of a third progression may also be observed in the region of 15 460 to 15 710 cm^{-1} . The curved appearance of the peak intensities, i.e. a drop off in intensity near either end of this spectrum is a result of the laser dye emission spectrum (the dye tuning curve, see experimental Chapter) and does not represent a change in the dissociation cross-section.

The photofragmentation spectrum of CoKr^+ is similar to that of CoAr^+ . This system also displays three prominent vibronic progressions. Fortunately, isotopic variants of Kr are naturally occurring and may be used to help assign the vibrational spectra of these systems. Figure 21 shows the

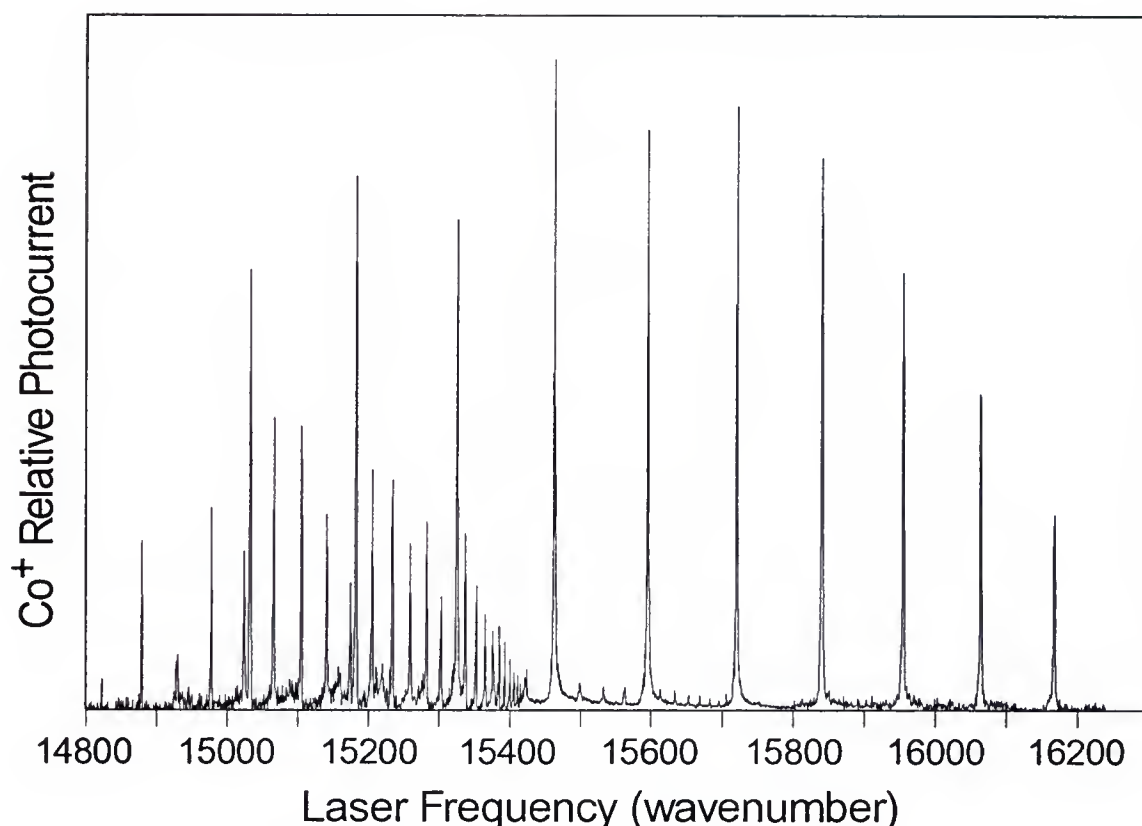


Figure 20. Resonant Photodissociation of CoAr^+ .

This figure displays a portion of the CoAr^+ resonant dissociation spectrum in the visible region. Plotted is the observed Co^+ fragment current arising from the one-photon dissociation of isolated CoAr^+ as a function of incident laser frequency. The relatively smaller dissociation at the low- and high-frequency sides of the plot represents a drop-off in the dissociation laser output intensity and not a systematic change in the peak dissociation cross-section. Each peak in the spectrum corresponds to an entire vibronic band, which, because of the 2 K rotational temperature of the ions has collapsed to less than 3 cm^{-1} FWHM (Full Width Half Maximum). Three upper-state vibrational progressions corresponding to three different electronic states are evident in the figure.

photofragmentation of $\text{CoKr}^+ \rightarrow \text{Co}^+ + \text{Kr}$ as a function of dissociation laser frequency in the interval from 15 420 to 15 620 cm^{-1} . The top trace shows the photofragmentation of all naturally occurring Kr isotopic variants of the CoKr^+ molecule and the bottom trace shows the photofragmentation of $^{59}\text{Co}^{86}\text{Kr}^+$ only (17.37% natural abundance¹²) on an increased vertical scale. The ability to acquire the signal of selected isotopic variants of a molecular ion considerably simplifies the spectrum (note the region near 15540 cm^{-1} in Figure 21) and facilitates vibrational assignment.

A similar set of experimental conditions applies to the spectra of $\text{CoAr}^+(\text{Kr})$ as discussed for the previous rare-gas containing diatomics. At these photon energies Kr^+ is not observed as a photoproduct of CoKr^+ (similarly Ar^+ is not observed from CoAr^+) as expected from the large disparity in the ionization potential of the atoms ($\text{IP}(\text{Kr}) = 13.996 \text{ eV}$; $\text{IP}(\text{Ar}) = 15.755 \text{ eV}$; $\text{IP}(\text{Co}) = 7.86 \text{ eV}$)¹³. Under the normal operating conditions of the mass spectrometer, a trace amount of Co^+ from CoKr^+ (CoAr^+) is observed from collision-induced dissociative processes with residual He gas in the flight tube of the TOFMS. In the present experiment, collision-induced dissociation produces a small background to our laser-induced dissociation yield that is constant and may be easily nullified. The bottom of the abscissa axis on the photodissociation spectra of CoAr^+ and CoKr^+ therefore represents zero photodissociation intensity.

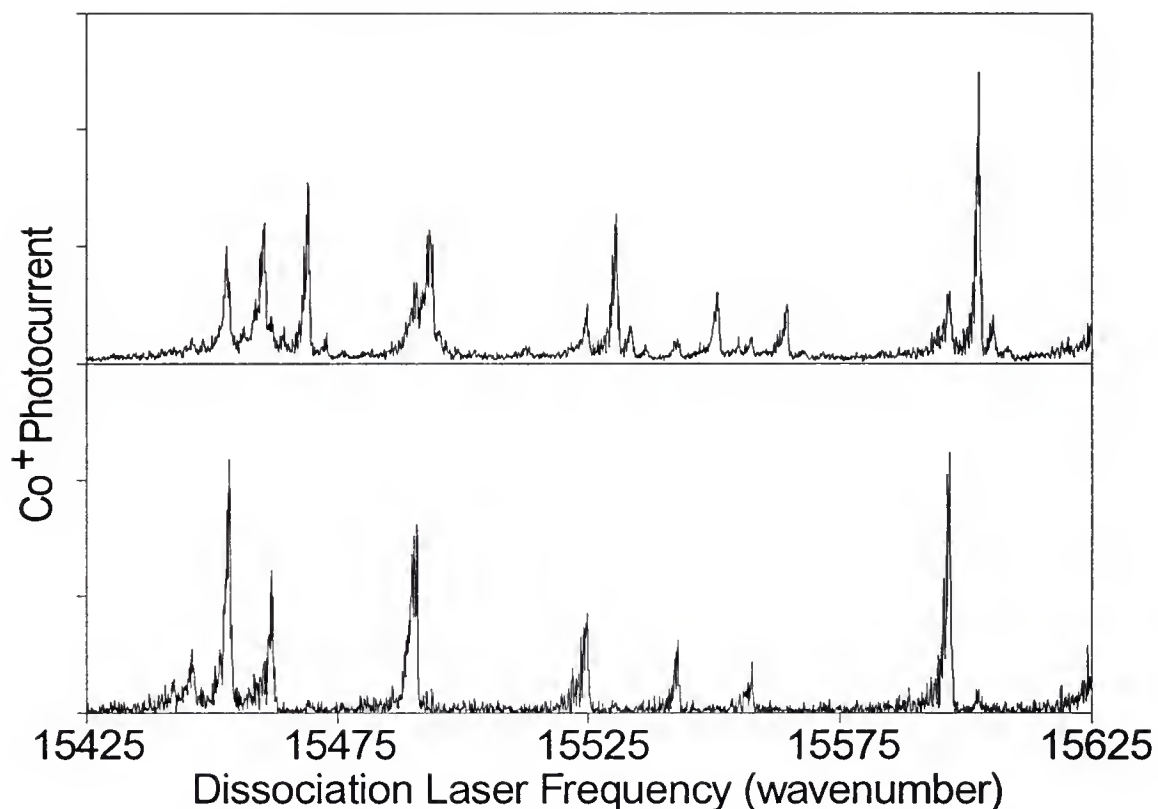


Figure 21. Photodissociation Spectrum of CoKr^+ Isotopes.

The figure displays a portion of the photoexcitation spectrum over the region of 15 420 to 15 620 cm^{-1} for CoKr^+ . The top half of the figure shows the photodissociation, Co^+ relative photocurrent as a function of laser frequency, of all naturally occurring isotopes of CoKr^+ . In the lower panel, only the photodissociation of $^{59}\text{Co}^{86}\text{Kr}^+$ is displayed. Isotopic shift information is necessary to assign the absolute vibrational numbering of the observed bands. This region of the spectrum displays peaks from three prominent progression that are listed in Table 6.

Dissociation laser fluence dependence of the resonant photodissociation indicates a one-photon absorption event. Poor temporal/spatial quality of the excitation source prevents accurate absolute cross section measurements, but the strongest photodissociation transitions have cross sections of ca. of 10^{-17} cm². Partially resolved rotational structure on the vibronic transitions place a lower limit on the lifetime of the upper levels of the transition at 10 ps. The upper limit to the excited state lifetime is placed by the time between excitation and kinetic energy analysis, about 5 μ sec. The features in Figure 21 are representative of the over 100 sharp vibronic bands found in the photodissociation spectrum of CoKr⁺ in the region of 18 000 cm⁻¹ to below 13 500 cm⁻¹. Most (>95%) of these vibronic transitions fall into three simple upper state progressions from, presumably, the same lower vibronic state. We identify these three progressions as distinct electronic band systems.

Vibrational Analysis

The assigned vibronic positions for the photodissociation excitation spectra, over the frequency interval of 13 500 to 18 000 cm⁻¹, of CoAr⁺ and CoKr⁺ are listed in Table 5 and Table 6, respectively. In each case the positions of the assigned transitions are grouped into three band systems

Table 5. Line positions of assigned $^{59}\text{Co}^{40}\text{Ar}^+$ transitions in wavenumbers.

A-X			B-X			C-X		
v'	observ.	o-c ^a	v'	observ.	o-c ^a	v'	observ.	o-c ^a
6	14026.3	0.87	6	14076.8	1.01	0	14544.7	-0.71
7	14149.0	0.37	7	14167.2	-0.09	1	14714.3	-0.36
8	14265.4	-0.71	8	14254.4	-0.56	2	14878.6	1.11
9	14375.7	-2.48	9	14338.0	-0.68	3	15034.7	0.69
10	14488.3	3.59	10	14418.7	-0.01	4	15184.7	0.40
11	14577.6	-8.39	11	14494.6	-0.32	5	15328.2	-0.26
*11	14589.7	3.75	12	14567.6	0.12	6	15466.1	-0.48
12	14677.0	-5.02	13	14636.6	0.04	7	15598.6	-0.16
*12	14688.0	6.02	14	14701.9	-0.12	8	15725.0	0.00
13	14767.1	-5.85	15	14763.8	-0.22	9	15845.1	-0.48
*13	14773.7	0.77	16	14822.5	-0.14	10	15960.1	-0.31
*13	14780.3	7.39	17	14877.7	-0.13	11	16069.5	-0.17
25	15502.2	-0.22	18	14930.1	0.23	12	16173.8	0.33
26	15536.3	0.01	19	14979.3	0.58	13	16272.0	0.11
27	15565.9	-0.50	20	15025.6	1.25	14	16364.9	-0.03
28	15592.6	-0.35	21	15067.6	0.57	15	16453.0	0.11
29	15616.7	0.76	22	15106.7	0.08	16	16535.4	-0.26
30	15637.5	1.83	23	15142.9	-0.38	17	16614.1	0.67
31	15656.7	4.55	24	15176.9	-0.19	18	16686.0	-0.30
32	15672.9	7.53	25	15207.7	-0.40	19	16754.9	0.54
33	15687.3	11.65	26	15236.1	-0.29	20	16817.8	0.19
34	15699.5	16.63	27	15261.3	-0.72	21	16875.9	-0.34
35	15710.7	23.35	28	15284.9	-0.16	22	16930.4	-0.04
			29	15305.3	-0.27	23	16979.8	-0.31
			30	15323.3	-0.22	24	17025.0	-0.44
			31	15340.2	1.02	25	17066.9	0.48
			32	15354.9	2.50	26	17104.4	1.04
			33	15368.2	4.74	27	17138.8	2.67
			34	15378.9	6.68	28	17169.4	4.36
			35	15388.3	9.45	29	17197.0	7.02
			36	15396.6	13.08	30	17221.8	10.66
			37	15403.6	17.52	31	17243.2	14.58
			38	15409.3	22.59	32	17262.5	20.00
			39	15414.3	28.83	33	17279.6	26.81
			40	15418.5	36.07	34	17294.6	34.84
			41	15421.8	44.05	35	17307.3	43.97
						36	17318.3	54.52
						37	17327.8	66.79
						38	17336.1	80.80
						39	17343.1	96.55
						40	17348.9	113.94
						41	17353.9	133.28
						42	17358.0	154.28
						43	17361.3	177.15
						44	17363.9	201.78
						45	17366.1	228.39
						46	17367.6	256.59

(a) Observed minus calculated

(*) Extra bands due to perturbation.

Table 6. Line positions of assigned $^{59}\text{Co}^{40}\text{Kr}^+$ vibronic transitions in wavenumbers.

A-X			B-X			C-X		
v'	observ.	o-c ^a	v'	observ.	o-c ^a	v'	observ.	o-c ^a
2	13696.5	0.14	2	14161.4	1.03	4	15354.4	0.35
3	13835.4	-0.12	3	14270.7	0.61	5	15495.9	0.21
4	13970.8	-0.91	4	14377.4	0.26	6	15633.5	-0.41
4	13981.0	9.32	5	14481.4	-0.26	7	15768.4	-0.21
5	14098.3	-6.53	6	14583.5	0.07	8	15899.8	-0.22
*5	14110.1	5.20	7	14679.6	-3.01	9	16027.4	-0.66
6	14219.7	-15.3	8	14779.6	0.44	10	16152.4	-0.23
*6	14233.8	-1.22	9	14873.2	0.05	11	16273.3	-0.67
7	14356.9	-5.34	10	14964.9	0.44	*11	16276.0	2.04
8	14489.0	2.59	11	15051.0	-2.33	12	16390.5	-1.38
9	14605.0	-2.50	12	15138.9	-0.75	*12	16393.3	1.43
*9	14625.2	17.67	13	15223.2	-0.25	13	16506.3	-0.18
10	14728.6	2.98	14	15305.2	0.45	14	16618.4	0.51
11	14840.1	-0.63	15	15384.7	1.25	15	16725.5	-0.44
13	15061.0	-0.67	16	15462.7	2.93	16	16830.4	-0.33
*13	15063.3	1.64	17	15532.5	-1.05	17	16932.3	0.02
14	15167.0	-0.49	18	15604.7	-0.28	18	17030.4	-0.21
15	15268.0	-2.23	19	15674.1	0.23	19	17126.1	0.36
16	15368.0	-1.99	20	15743.3	2.96	20	17218.2	0.52
17	15455.4	-11.1	21	15803.9	-0.63	21	17306.3	-0.07
*17	15471.5	4.98	22	15864.9	-1.33	22	17392.0	0.01
18	15553.0	-7.02	23	15925.5	-0.05	23	17474.1	-0.29
*18	15566.8	6.83	24	15984.9	2.38	24	17553.4	-0.37
19	15640.9	-9.46	25	16036.9	-0.26	25	17630.0	0.06
*19	15655.8	5.49	26	16088.3	-1.18	26	17702.9	-0.14
21	15818.2	-3.43	27	16139.3	-0.18	27	17773.2	0.12
*21	15837.7	16.04	28	16187.7	0.61	28	17840.1	0.04
24	16048.2	-6.67	29	16231.3	-1.24	29	17904.2	0.18
*24	16057.8	2.86	30	16273.3	-2.42	30	17964.8	-0.06
			*30	16276.0	0.29			
			31	16315.8	-0.74			
			32	16355.0	-0.23			
			33	16390.5	-1.12			
			*33	16393.3	1.69			
			34	16426.1	0.31			
			35	16459.2	1.32			

(a) Observed minus calculated

(*) Extra lines due to perturbation.

labeled C-X, B-X, and A-X. The current labeling is a matter of convenience; the ground and three observed excited states are labeled X, A, B, and C, in order of increasing electronic origin energy. This choice by no means indicates that the 'A' state observed in this study is the first excited state nor that no other electronic states lie between the A, B, and C states. However, the chosen nomenclature is such that the A (B,C) state of CoAr^+ and CoKr^+ correspond to the same Co^+ atomic ion state at the dissociation limit. The most intense point of the vibronic band (typical width 2-3 cm^{-1} ; see Figure 21) is taken to be the vibronic band origin for the present analysis. Table 5 and Table 6 also list the residuals to the least squares fit of the vibronic bands to the standard¹⁴ formula given previously in Eq. (6) from which the constants T_{co} , w_e , $w_e x_e$, $w_e y_e$ are derived. As in the analysis of VAr^+ and VKr^+ , the zero of energy for this fit and all the following discussion is taken as the zero-point level of the ground electronic state of the molecule. The accuracy with which Eq. (6) describes the observed vibronic structure depends on the degree of anharmonicity of the molecular forces and the existence of any local perturbations between the electronic states. The best fit in this study is obtained for the lowest vibrational levels ($v' = 0 \rightarrow 25$) of the C state of CoAr^+ which shows no apparent anomalous behavior. Even for this state, however, the transition frequencies involving the highest vibrational levels ($v' = 30 \rightarrow 46$) are severely

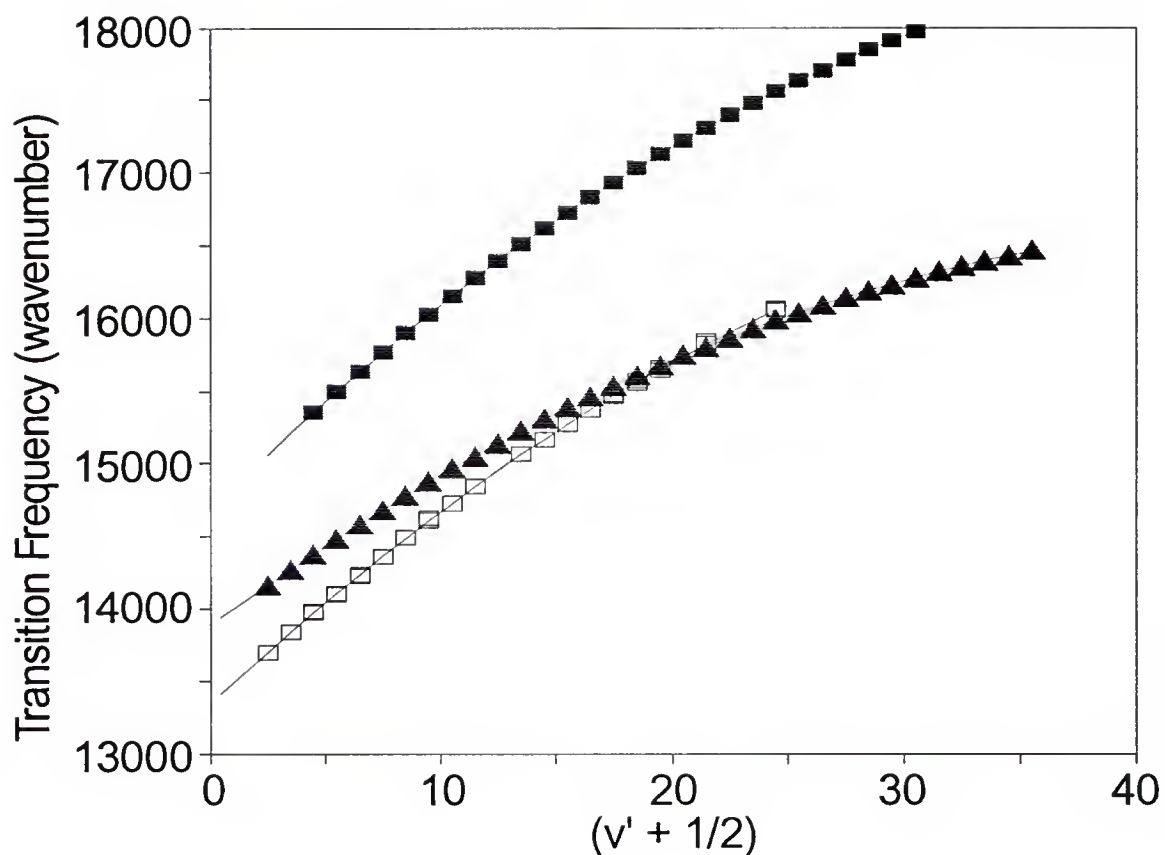


Figure 22. Vibration Fit to Band Origins for CoKr^+ States.

This figure displays a least-squares fit to Eq. (6) (solid curves) of the observed vibrational band origins of the C-X (solid squares), B-X (triangles) and A-X (open squares) systems of CoKr^+ . Absolute vibrational numbering is obtained from isotopic shift information. The molecular constants obtained from this fit are listed in Table 7.

underestimated by Eq (6). and so are not included in the fit. Complications arise, however, from the local perturbations that all band systems other than CoAr^+ C-X exhibit to some extent.

Figure 22 shows the vibrational structure of CoKr^+ in a plot of transition energy of the C-X, B-X, and A-X systems versus excited state quantum number, $(v'+1/2)$. The solid curves represent the fit to Eq. (6) and the symbols are the experimental band origins. Despite the evidence of perturbation from the missing and extra lines apparent in this plot the overall fit is quite good. Absolute vibrational numbering of the transitions shown in Figure 22 and listed in Table 6 are made from the measurement of the spectral shift among the ^{86}Kr , ^{84}Kr , ^{83}Kr , and ^{82}Kr isotopomers of CoKr^+ . This yields a unique absolute vibrational numbering for the C and B states but the extensive perturbations in the A state make its vibrational numbering uncertain by ± 1 quantum.

Figure 22 clearly shows that the three excited electronic states observed in photodissociation have similar but not identical vibrational structure. Also from Figure 22, it is evident that the electronic origin of the A state is lower than the B state, but the dissociation limit of the A state is higher than the B state which means that the A and B state potential curves cross.

The nature and extent of the perturbations present in this spectrum are varied. A perturbation between the C and B

states of CoKr^+ occurs at an accidental degeneracy between the $v' = 11$ of the C state and $v' = 30$ of the B state and again at $v' = 12$ and $v' = 33$ of those states. This perturbation appears to involve only these two electronic states with an estimated interaction matrix element of about 3 cm^{-1} . The A state of this molecule is more severely and ubiquitously perturbed than the B or C states as is evidenced by the diminished quality of the fit to Eq. (6) (see Table 6). Extra lines in this band system arise from perturbations with at least one otherwise undetected state. The perturbation shifts in the A-X system indicate a much stronger coupling between interacting electronic states than is seen in the C-B perturbation of the same molecule.

At present, neither the spectrum of $^{59}\text{Co}^{36}\text{Ar}^+$ nor $^{59}\text{Co}^{38}\text{Ar}^+$ (0.34% and 0.07% natural abundance¹², respectively) have been obtained. Without isotopic substitution, the firm assignment of absolute vibrational quantum numbers to the CoAr^+ transitions listed in Table 5 is impossible. Thus, the upper state vibrational quantum number listed in Table 5 is merely an effective vibrational index, chosen to be close to the absolute value.

All of the transitions observed in this study appear to originate from the ground electronic and vibrational state of the molecule, i.e. no hot bands have been identified. This is understandable due to the extensive cooling these ions suffer in the supersonic expansion. From a conservative estimate of

the sensitivity of the experiment (1% of a strong transition) and a guess of the ground state vibrational frequency (200 cm^{-1} ; see discussion below), we infer the vibrational temperature of these ions to be less than 65 K. This is significantly lower than the vibrational temperatures of transition metal dimer neutrals¹⁶ supersonically expanded under similar conditions. It is possible that ion-molecule vibrational relaxation collisions are longer ranged or more efficient than neutral-neutral V-T collisions, leading to a lower final vibrational temperature for ions relative to that of neutrals in the beam. Nonetheless, the low internal temperature of the ions simplifies the spectrum greatly but prevents direct determination of the ground state vibrational frequency by photodissociation excitation spectroscopy.

Determination of dissociation limits

Similar treatment of the vibrational levels near the dissociation limit is done here as in the treatment of vibrational levels for the systems of VAr^+ and VKr^+ . Figure 23 shows the dependence of the derivative of the vibrational energy with respect to the transition frequency for the C-X, B-X, and A-X band systems of CoAr^+ . The plot shows that $(\Delta G)^{4/3}$ is indeed linearly dependent on transition frequency near the dissociation and a linear least squares extrapolation may be used to estimate the dissociation limits,

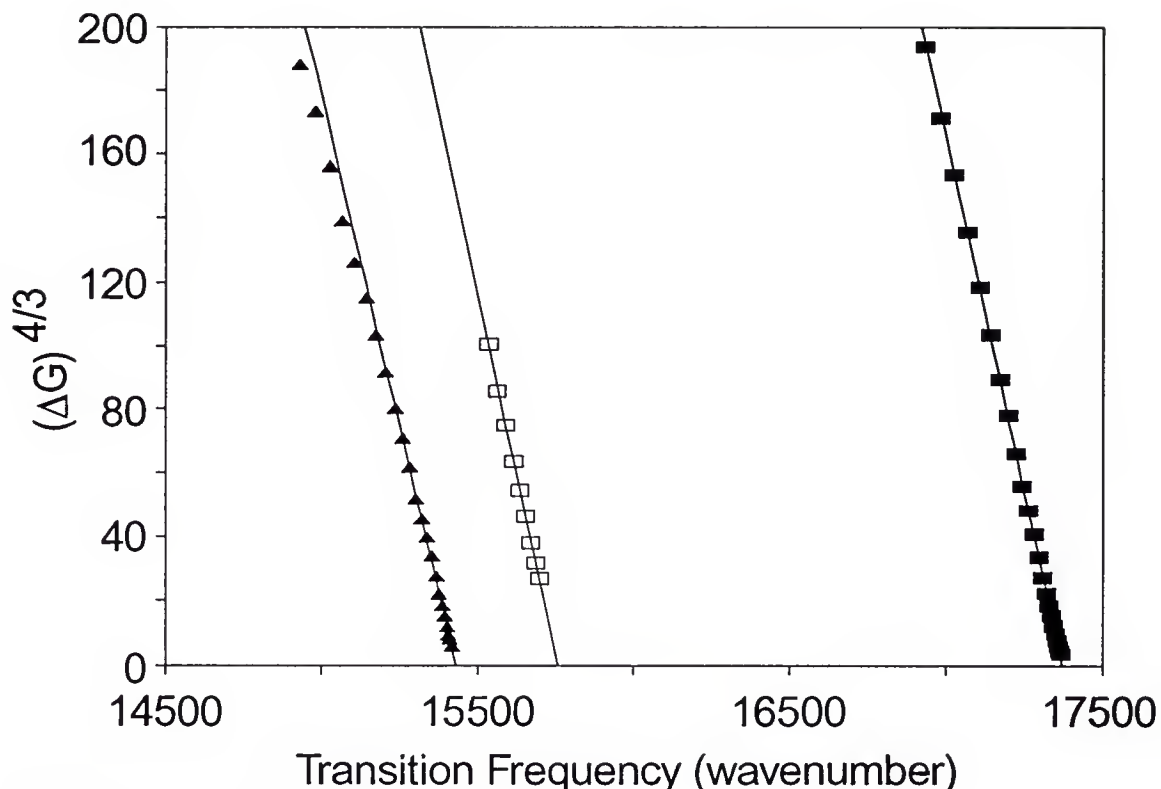


Figure 23. Dissociation Limits of CoAr^+ .

The Figure displays a plot of the derivative of the vibrational energy with respect to vibrational index to the $4/3$ power versus transition frequency (LeRoy-Bernstein plot) for the A (open squares), B (triangles), and C (solid squares) states of CoAr^+ . For molecules which dissociated under the influence of a $-C/r^4$ attractive force (charge-induced dipole) these data may be linearly extrapolated (lines) to the abscissa to obtain the dissociation limit of the respective excited states. These limits, D, are listed in Table 7 for both CoAr^+ and CoKr^+ .

D. These extrapolated values are listed in Table 7. We must emphasize that the values of D are not dependent on the absolute vibrational numbering. Subsequently, the accuracy to which the ground state binding energy is known is a function of the LeRoy-Bernstein extrapolation and the correct assignment of the separated atomic limits. The accuracy of the excited state vibrational frequency and binding energy will depend on the correct vibrational assignment.

The dissociation energies, D , listed in Table 7 correspond to the difference in energy between the zero point level of the molecule and a particular excited state of the $\text{Co}^+ + \text{Ar}(\text{Kr})$ separated atoms. It is not possible for these

Table 7. Experimental Molecular Constants for $^{59}\text{Co}^{40}\text{Ar}^+$ and $^{59}\text{Co}^{84}\text{Kr}^+$ in cm^{-1} .

	CoAr^+			CoKr^+		
State	A	B	C	A	B	C
T_{∞}	13081	13380	14458	13336	13874	14674
ω_e'	165.4	120.9	175.8	148	117.8	159.0
$\omega_e x_e'$	3.20	2.21	3.28	1.47	1.36	1.76
$\omega_e y_e'$	0.017	0.011	0.016	-0.002	0.003	0.003
k_e (N/m)	38.5	20.6	40.1	44.8	28.4	51.7
ν_D^a		55.3	55.6		88.9	93.5
D^b	15758	15433	17370	17395	16840	18911
$D_o'{}^{(c)}$	2595	1993	2825	3985	2886	4158
$D_e'{}^{(d)}$	2677	2053	2912	4059	2945	4237

^aNumber of bound vibrational levels.

^bDiabatic threshold.

^cExcited state binding energy; $D_o' = D_e' - 1/2\omega_e' + 1/4\omega_e x_e' - 1/8\omega_e y_e'$.

^dExcited state equilibrium dissociation energy; $D_e' = D - T_{\infty}$.

dissociation limits to correspond to excited argon(krypton) atoms. Comparison of the observed D values in CoAr^+ and CoKr^+ with the Co^+ atomic energy levels³⁷ suggests the assignment of the C state dissociation limit as $3d^8\ ^3P_2\ \text{Co}^+ + ^1S\ \text{Ar(Kr)}$ and the B state limit as $3d^74s\ ^3F_2\ \text{Co}^+ + ^1S\ \text{Ar(Kr)}$ at $13\ 261.1\ \text{cm}^{-1}$ and $11\ 321.5\ \text{cm}^{-1}$ above separated $3d^8\ ^3F_4\ \text{Co}^+ + ^1S\ \text{Ar(Kr)}$ (ground state) atoms, respectively. This places the A state dissociation at $11\ 645\ \text{cm}^{-1}$ above ground state atoms where no Co^+ electronic states presently are assigned. This observation does not, at present, invalidate the assignment of the C and B state limits because a number of predicted Co^+ atomic terms are still undetected in this energy region.

The adiabatic dissociation energy of the ground state of CoAr^+ or CoKr^+ is simply the difference between any experimentally determined excited state dissociation limit, D, and the isolated Co^+ promotion energy to the state corresponding to that limit. From Table 7 and the above assignment of the B and C state limits, the adiabatic dissociation energies of the X states of CoAr^+ and CoKr^+ are found to be $4110\ \text{cm}^{-1}$ and $5585\ \text{cm}^{-1}$, respectively.

Once D has been determined for a particular excited electronic state, the vibrational binding energy, $(D - E(v))$, is used to derive the number of bound vibrational levels in the potential via the application of Eq.(3) to yield v_D . The number of bound levels in each potential is the largest integer less than v_D . These values are listed in Table 7.

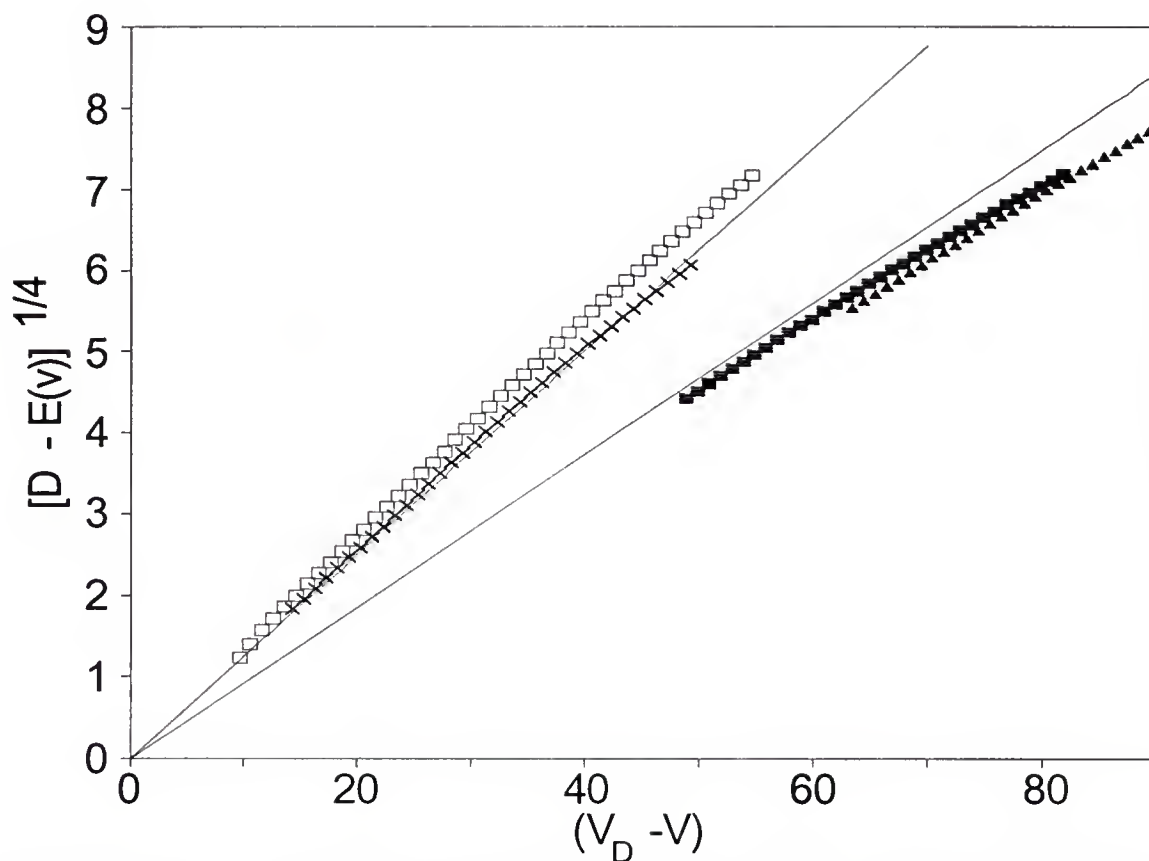


Figure 24. Vibrational Binding Energy for CoAr⁺ and CoKr⁺ States.

The Figure displays a plot of the vibrational binding energy to the 1/4 power versus the vibrational index, $(v_D - v)$, for the C (open squares) and B (crosses) states of CoAr⁺ and the C (triangles) and B (solid squares) state of CoKr⁺. The quantity v_D is the hypothetical vibrational index of the dissociation limit of the potential, i.e., $E(v_D) = D$. The solid lines are the predicted vibrational binding energy from Eq. (19) using the literature values for the polarizability of argon or krypton.

The number of bound levels for the A state of either CoAr^+ or CoKr^+ have not been determined due to the perturbations and limited number of observed vibronic levels. However a significant number of the total vibrational levels are observed for many of the other states; over 80% for C state of CoAr^+ .

Figure 24 shows a plot of the vibrational binding energies to the $1/4$ power versus vibrational quantum number for the B and C states of CoKr^+ and CoAr^+ . Also shown in the figure is the predicted dependence (lines) of vibrational binding energy for CoAr^+ and CoKr^+ using Eq. (19) and literature values for the rare-gas polarizabilities ($1.66 \times 10^{-24} \text{ cm}^3$ for Ar and $2.52 \times 10^{-24} \text{ cm}^3$ for Kr). Again, as was the case for $\text{VAr}^+(\text{Kr})$ systems, the agreement between this simple model for the vibrational structure of these systems is extremely good.

Resonant Photodissociation of ZrAr^+

The following discussion will look at the results for a second row transition metal cation, Zr^+ , with a physisorbed rare-gas atom, Ar. The photodissociation spectrum for this system also displays several vibronic progressions. Unfortunately, the spectroscopic information does not lend itself to the rigorous analysis found in the cobalt and vanadium systems discussed previously. We will see that only

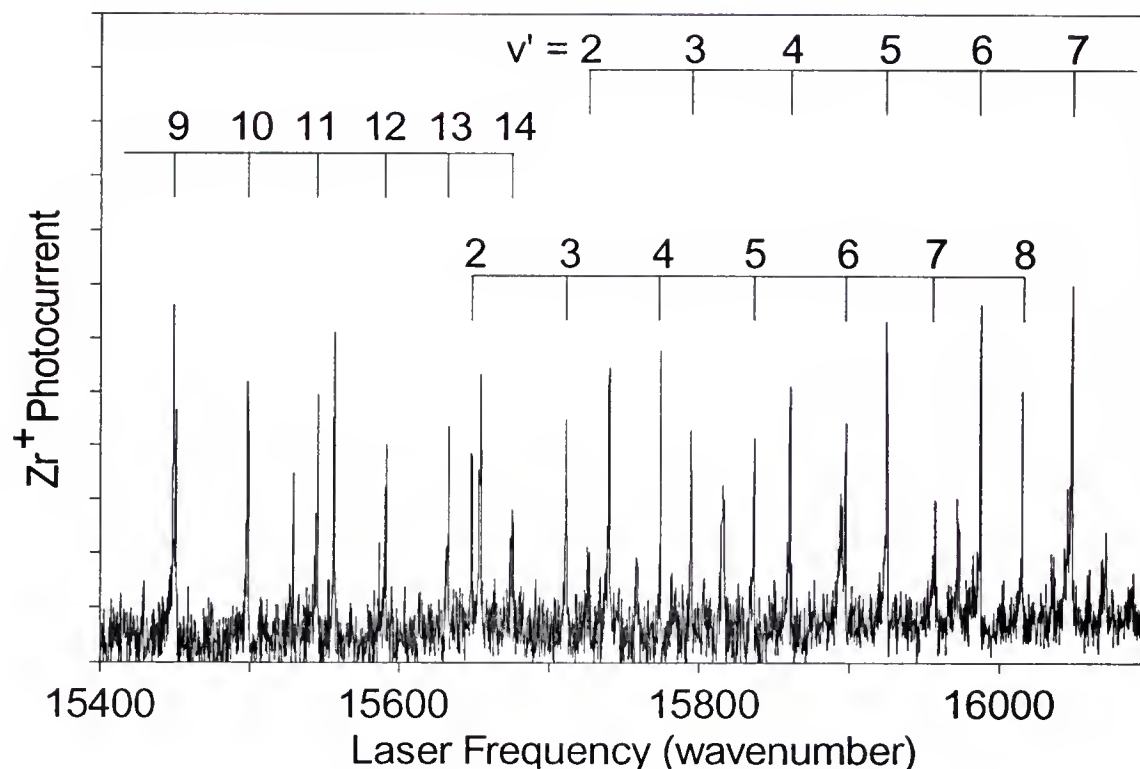


Figure 25. Resonant Photodissociation of ZrAr^+ .

The figure displays the resonant photodissociation spectrum for the process of $\text{ZrAr}^+ \rightarrow \text{Zr}^+ + \text{Ar}$ in the visible region of 15400 to 16500 cm^{-1} . Three prominent vibronic progressions are annotated with the vibrational index determined from isotopic analysis. All observed transitions are red degraded.

ca. 30% of the vibrational levels for a given electronic state are observed compared to 80% of CoAr⁺ A and B states.

A portion of the photoexcitation spectrum for the one-photon dissociation process of $^{90}\text{Zr}^{40}\text{Ar}^+ \rightarrow ^{90}\text{Zr}^+ + \text{Ar}$ over the visible region of 15 400 to 16 100 cm⁻¹ is displayed in Figure 25. A vibrational index marks the band positions for each of three prominent vibronic progressions. Under current laser linewidth (ca. 0.1 cm⁻¹) the bands are only partially rotationally resolved. Thus, insufficient for complete rotational analysis but nonetheless revealing a distinctive red degraded peak shape for all observed bands. For convenience the states giving rise to these three progressions have been labelled A, B, and C in accordance with increasing energy of the electronic term. Lower lying states will undoubtedly be discovered in the future and will necessitate the revisal of this labelling.

Line positions, corrected to vacuum, for the three progressions are listed in Table 8. Several other bands belonging to fragmented progressions are also observed in the same region. These bands, grouped by progression, are listed in Table 9 for completeness but are currently unassigned with regard to vibrational index (see following text).

The vibrational frequencies (ω_e') and anharmonicities ($\omega_e x_e'$) of each of the progressions are found by fitting the observed transition to $(v' + 1/2)$ and $(v' + 1/2)^2$ in the following well known equation, resubmitted here;

Table 8. Line Positions for assigned vibronic transitions of $^{90}\text{Zr}^{40}\text{Ar}^+$ in wavenumbers.

A-X			B-X			C-X		
v'	observed	o-c ^a	v'	observed	o-c ^a	v'	observed	o-c ^a
1	14987.72	0.18	2	15646.20	0.67	2	15723.83	0.17
2	15051.75	0.36	3	15709.54	-0.42	3	15793.61	0.95
3	15113.10	-0.30	4	15772.30	-0.75	4	15858.46	-0.68
4	15173.31	-0.25	5	15834.46	-0.36	5	15922.72	-0.37
5	15231.66	-0.22	6	15895.63	0.40	6	15984.83	0.30
6	15288.09	-0.26	7	15955.04	0.75	7	16045.83	2.38
7	15343.07	0.09	8	16012.36	0.34	8	16097.28	-2.56
8	15395.31	-0.47	9	16067.78	-0.63	9	16152.19	-1.52
9	15447.05	0.32				10	16203.50	-1.57
10	15496.80	0.97				11	16253.69	-0.21
11	15543.25	0.15				12	16300.33	0.12
12	15588.89	0.38				13	16345.79	1.78
13	15630.70	-1.39				14	16387.59	2.31
14	15674.26	0.43				15	16425.70	1.68
						16	16460.05	-0.21
						17	16491.40	-2.57

(a) Observed minus calculated from vibrational fit.

Table 9. Unassigned line positions (cm⁻¹) for $^{90}\text{Zr}^{40}\text{Ar}^+$ grouped by progression.

Progression 1	Progression 2*	Progression 3
15662.04	16169.95	15527.0
15738.23	16220.07	15554.6
15813.84	16266.17	16110.0
15893.41	16310.52	
15969.59	*	
	*	
	16431.57	
	16469.89	

(*) Absent transition in progression.

$$E(v) = T_{eo} + \omega'_e(v' + 1/2) + \omega_e x'_e(v' + 1/2)^2. \quad (20)$$

Due to the cooling nature of the adiabatic expansion, hot bands are absent from the photodissociation spectra and all assigned peaks correspond to transitions originating in the ground state vibrationless level. The zero of energy for this fit, and all following discussion, is then conveniently taken as the zero-point level of the ground electronic state. The quantity T_{eo} , which is directly determined from a fit of the observed bound-bound transitions, is therefore, $1/2\omega_e$ smaller than the electronic term commonly denoted^{45, 89} as T_e' . An accurate determination of the vibrational frequency, however, depends on the correct assignment of the upper state vibrational index, v' .

Simultaneous photodissociation of zirconium isotopic variants in the diatomic ($^{90}\text{Zr}^{40}\text{Ar}^+$, $^{92}\text{Zr}^{40}\text{Ar}^+$, and $^{94}\text{Zr}^{40}\text{Ar}^+$ in 51.4, 17.1 and 17.5% natural abundance respectively)³³ provide isotopic shifts necessary to assign the vibrational index for these excited states. For vibronic bands, the isotopic shift is a function of the spectroscopic parameters and vibrational index of both the ground and excited states. One may eliminate terms involving second and higher anharmonic terms for regions of low v' in the standard expression:^{45, 89}

$$\Delta v_{isotopic} = (1-\rho) [\omega_e'(v'+1/2) - \omega_e''(v''+1/2)] - (1-\rho^2) [\omega_e \chi_e'(v'+1/2)^2 - \omega_e \chi_e''(v''+1/2)^2] + \dots \quad (21)$$

Here ρ is a constant equal to the square root of the ratio of reduced masses of the two isotopes. In practice, the determination of the vibrational numbering begins with a guess. The spectroscopic parameters of the upper state are then established from Eq. (20). The ground state ω_e'' is then adjusted in Eq. (21) to minimize the root-mean-square (rms) deviation of the isotope shifts while approximating $\omega_e \chi_e' = \omega_e \chi_e''$. Since Eq. (21) is quantized in v' , only a few possible numbering schemes provide a reasonable ground state vibrational frequency.

The A state isotopic shifts, $\Delta\nu$, for $^{90}\text{Zr}^{40}\text{Ar}^+$ minus $^{94}\text{Zr}^{40}\text{Ar}$ (squares) and $^{90}\text{Zr}^{40}\text{Ar}^+$ minus $^{92}\text{Zr}^{40}\text{Ar}$ (triangles) as a function of upper state vibrational index are displayed in Figure 26. The solid lines represent the calculated isotopic shift with the vibrational numbering scheme listed in Table 8. The dotted curves are calculated by shifting the vibrational assignment plus and minus one quanta. Similar isotopic analysis was performed for the B and C state. The vibrational index determined by this method accompanies the bands listed in Table 8. Equation (20) accurately describes the observed vibrational levels with less than 1.5 cm^{-1} residual error for all transitions listed in the A and B state. The C state is

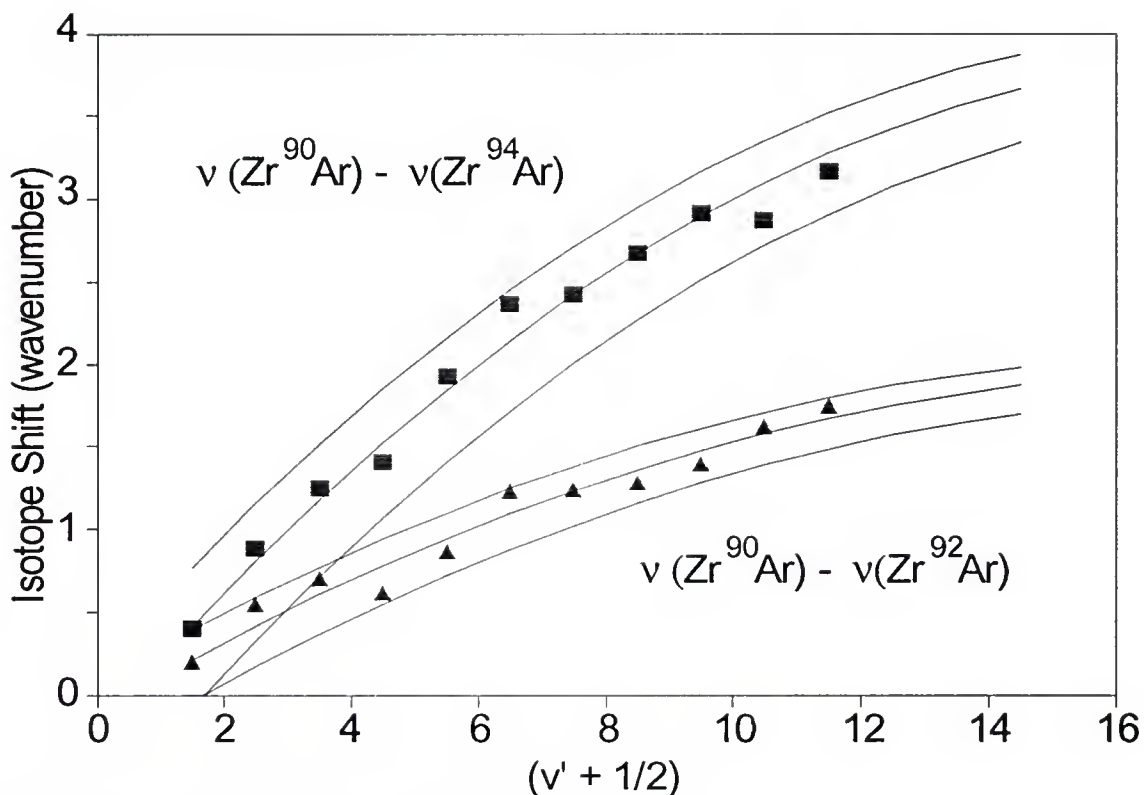


Figure 26. Isotopic Shifts for ZrAr^+ .

The figure displays the isotopic shifts for $^{90}\text{Zr}^{40}\text{Ar}^+$ minus $^{94}\text{Zr}^{40}\text{Ar}^+$ (squares) and $^{90}\text{Zr}^{40}\text{Ar}^+$ minus $^{92}\text{Zr}^{40}\text{Ar}^+$ (triangles) versus the vibrational index $(v' + 1/2)$ for $A \leftarrow X$. Centrally located solid lines for both sets of isotopic data represents the best fit of ω_e'' for vibrational data with the vibrational index given in Table 8. Curves above and below the central curve are calculated by shifting the vibrational assignment by plus and minus one quanta, respectively.

Table 10. Spectroscopic Parameters of Excited State in ZrAr^+ .

State	T_{∞} (cm^{-1})	ω_e' (cm^{-1})	$\omega_e\chi_e'$ (cm^{-1})	Δ Bound Levels ^a (cm^{-1})
A-X	14 888.3	67.5	0.92	686.6
B-X	15 478.6	68.5	0.67	421.6
C-X	15 540.1	76.6	1.26	767.6

^aThe difference of the bluest and reddest assigned vibronic bands.

slightly perturbed and does not fit as well with some residual errors being ca. 2.5 cm^{-1} . Nonetheless, the vibrational fits for all states are quite good for overall experimental accuracy of 1.5 cm^{-1} . The residual (observed minus calculated) values are also listed in Table 8. Figure 27 displays the vibrational fit of the three vibrational progressions. Symbols mark the experimental values and the solid lines represent the calculated values. The curves for each of states are roughly parallel over the observed region with a separation of ca. 85 and 750 cm^{-1} between B and C, and between A and C respectively. The vibrational frequencies and anharmonicities for each of these state are listed in Table 10.

Dissociation Limits

Since the Franck-Condon factors reveal only the vibrational levels near the bottom of the excited state

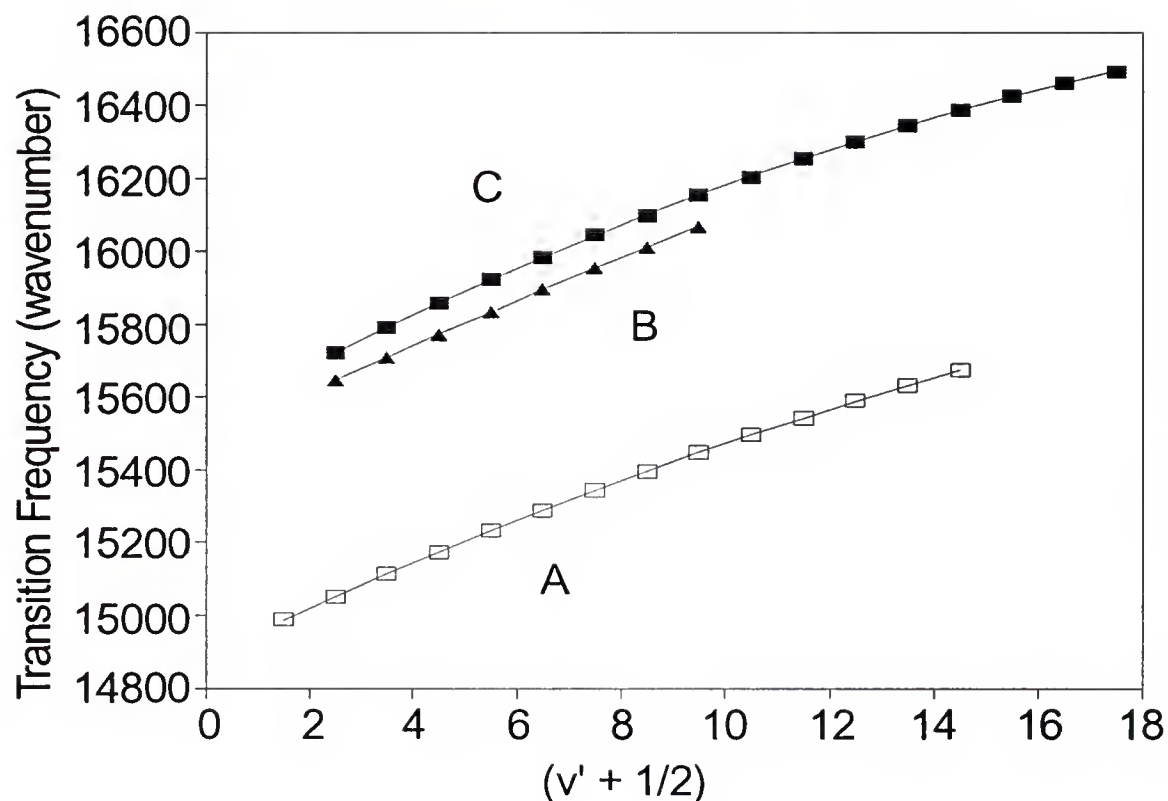


Figure 27. Vibrational Fit of ZrAr^+ .

The figure displays the vibrational fit for the three vibronic progressions of ZrAr^+ annotated in Figure 25. Observed transitions for each state are plotted versus vibrational index with symbols (A = pluses, B = triangles, and C = squares). The solid line represents the fit to a second order polynomial in $(v' + 1/2)$. The curves for all three states are roughly parallel. A lower limit to the upper state binding energies of ca. 686, 829 and 768 cm^{-1} for the A, B, and C state, respectively, is determined by the range of bound-bound transitions.

potential energy surface, determination of an upper state dissociation limit is a moderate extrapolation. In the C state, and to a lesser degree the A state, vibrational levels are sufficiently close to the dissociation limit to attempt the procedure pioneered by LeRoy and Bernstein. The vibrational information of the B state is insufficient and may be estimated with the less rigorous Birge-Sponer extrapolation. An experimental lower limit for each of the excited states however, may be set by the range of observed bound-bound transitions. These are 686, 422, and 767 cm⁻¹ for states A, B, and C respectively. Applying, the Birge-Sponer extrapolation, $D_e = \omega_e/4\omega_e\chi_e$, the dissociation energies for A, B, and C state are 1238, 1750, 1164 cm⁻¹, respectively. Calculations of this type typically underestimate the dissociation energy because of failure to account for long-range forces. In first-row transition-metal rare-gas (Ar, Kr) diatomic systems, they are known to be 10 to 20% too low. The Birge-Sponer extrapolation for the B state is suspiciously high and may be inaccurate due to a vibrational fit on a limited number of vibronic levels ($v' = 2 \rightarrow 9$).

The LeRoy and Bernstein method provides a more accurate method for determining the dissociation energy by accounting for long-range attractive forces. The application of this procedure has been discussed previously.

Figure 28 displays a plot of $\Delta G^{4/3}$ as a function of incident laser-frequency for the C state. The solid squares

correspond to experimental points. The solid line represents the calculated slope from a least-squares fit of the lower four data points, while the dotted line is the theoretical slope, determined from Eq. (15), intersecting the last available data point. The intercept of the abscissa corresponds to the diabatic dissociation limit of the excited state. The dissociation limit of the excited state is simply the difference of the diabatic limit and the electronic term $D_e - T_{co}$.

Since vibrational data is sufficiently far away from the diabatic limit (only ca. 30% of vibrational levels are observed in the C state) it must be treated with caution. The inclusion of one more data point in the fit would bring the slope in line with the predicted value. The perturbations of the C state are reflected in the undulating $\Delta G^{4/3}$ values with transition frequency. It is for these reasons that no significance is attached to the small but apparent deviation (ca. 13% relative deviation) of the calculated and predicted slope. Nonetheless, the intercepts of the two lines are

Table 11. Dissociation Energy for $ZrAr^+$ Excited States.

State	Birdge-Sponer (cm^{-1})	LJ[8,4] (cm^{-1})	Born-Meyer [exp,4] $D_e:\omega_e$ (cm^{-1})	LeRoy-Berstein (cm^{-1})
A-X	1238	871	1333:67.6	1286±150
B-X	1750	888	-	-
C-X	1164	1031	1306:76.8	1185±25

believed to roughly bracket D_e' at $1185 \pm 25 \text{ cm}^{-1}$. A similar treatment was used to determine the dissociation energy of the A state as $1286 \pm 150 \text{ cm}^{-1}$. Unfortunately, the limited vibrational information of the B state is not sufficient to warrant a similar procedure. However, the initial premise, that the attractive force of the system is governed by charge-induced dipole forces, is apparently valid.

Adiabatic Energy

In order to determine the adiabatic binding energy one must know the separated atomic limits. Unfortunately, the dissociated atomic configurations, in addition to the molecular term symbols, that correspond to the observed progressions are not known unequivocally. An energy range, however, may be intelligently set to suggest likely candidates for the atomic configurations of the dissociation limits. Photodissociation into an ionic or excited state of Ar is energetically impossible since the first metastable state and ionization potential for Ar is 13.5 and 27.6 eV respectively. This is well above the first ionization potential of zirconium at 6.74 eV.

Fortunately, the atomic energy levels are relatively sparse as well as complete in the visible region for zirconium cation. Since the ground state binding energy is larger than any excited state, $T_{co} > \Delta E_{atomic}$ (separated atomic limit). The

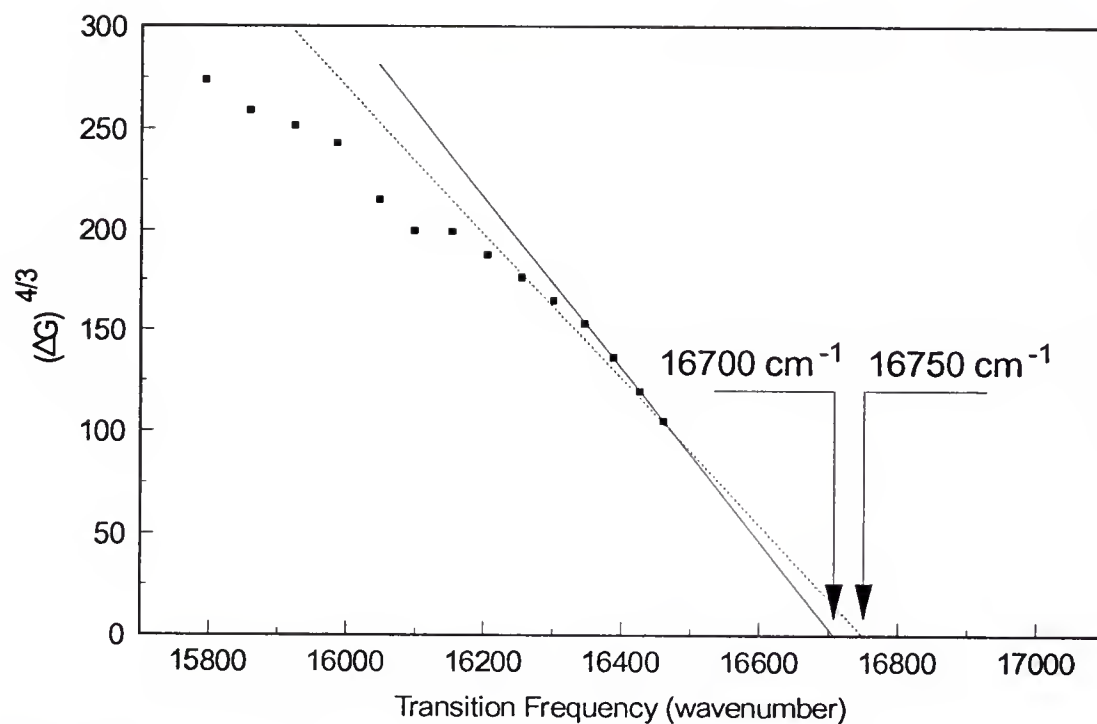


Figure 28. ZrAr^+ C State Dissociation Limit.

The figure displays the LeRoy-Bernstein plot of the derivative of the vibrational energy to the $4/3$ power versus the transition frequency. The solid line is determined from a least squares fit of the last four experimental points (squares). The dotted line, which intersects the last available data point, has a theoretical slope predicted from Eq. (15) using the polarizability of the rare gas atom and an $-C/r^4$ attractive potential. The linear extrapolation of these lines is believed to bracket the diabatic threshold of the C state.

upper limit is therefore determined by the largest electronic term, $T_{\infty} = 15542 \text{ cm}^{-1}$ (C state). For the lower limit to our energy window, recall

$$D_0'' - D_c' = T_{\infty} - \Delta E_{\text{atomic}}.$$

As the lower limit to the energy window drops the difference between the binding energy of the upper and lower states increases. For an energy difference as high as 0.55eV, $E_{\text{atomic}} > \text{ca. } 10000 \text{ cm}^{-1}$, using this time the smallest T_{∞} of the three progressions for the calculation. An energy difference of 0.55eV corresponds the adiabatic dissociation energy of NiAr^+ , a first row transition metal cation.

Within this energy window of 10,000 to 15542 cm^{-1} one finds eight energy levels corresponding to four terms symbols for Zr^+ . These are, in increasing energy: $^2\text{H} (4d^3)$, $^2\text{D} (4d^3)$, $^2\text{G} (4d^25s)$, and $^2\text{D} (4d 5s^2)$. The separated atomic limits for the ground state diatomic correspond to the respective atomic ground states, $^4\text{F}_{3/2} (4d^25s) \text{ Zr}^+$ and $^1\text{S Ar}$. The difference in vibronic transitions for a given v' between the A and C state is $752 \pm 7 \text{ cm}^{-1}$ (over the range $v' = 2 - 14$) and is suggestive of the j spacing interval in the $^2\text{D}_j = 734.4 \text{ cm}^{-1}$ ($^2\text{D}_{3/2} = 13\,428.50$, $^2\text{D}_{5/2} = 14162.90$). This would appropriately assign the B state to $^2\text{G}_{7/2} = 14059.76 \text{ cm}^{-1}$. These assignments are tentative at best and should be considered with caution. The corresponding molecular term symbols constructed from the above atomic terms suggest the observed bound-bound transition in photoexcitation spectra of ZrAr^+ involve a change in spin

state, $^2\Lambda \leftarrow ^4\Lambda$. This would be considered strictly forbidden if both ground and excited state were either Hund's coupling case A or Hund's coupling case B.

Using the tentative assignment of the separated atomic limits and the dissociation limit of the C state derived from the LeRoy-Bernstein method the ground state dissociation energy would be ca. 0.3 eV. One may determine a lower limit to the adiabatic binding energy by subtracting the largest possible separated atomic limit for Zr^+ from the sum of the energy range of bound-bound states and the electronic term; $D_e' > \Delta\text{Bound} + T_{\text{co}} - \Delta E_{\text{atomic}}$. This yields a lower limit to the adiabatic binding energy of ca. 0.2eV. The adiabatic binding energy of first-row transition metal argon diatomics has been shown to be ca. 0.3 to 0.55 eV.

Photodissociation of CaKr^+

This final section of metal-cation rare-gas systems will discuss some preliminary data for the photodissociation of CaKr^+ .

In light of the reactive nature of pure calcium special care must be taken to minimize ambient air contact. Calcium will quickly oxidize in moist air to form CaO with the liberation of hydrogen gas. Additionally, the vaporization laser power typically used for refractory transition metals will virtually cut the sample rod in half. The heat of

sublimation is approximately half that of cobalt.⁵¹ Nonetheless, atomic cations are easily made after some surface cleaning with the vaporization laser.

Figure 29 shows the photofragmentation process for $\text{CaKr}^+ \rightarrow \text{Ca}^+ + \text{Kr}$. Three prominent bands along with a small but perceptible fourth band are observed in this region corresponding to an excited state of CaKr^+ . Isotopic analysis of the krypton substituted system reveals that the reddest transition at ca 14 216 cm^{-1} corresponds to the origin band. Vibrational analysis determines the vibrational frequency at 52 cm^{-1} with an electronic origin of 14 192 cm^{-1} . The bands are distinctly red degraded and imply a ground state of smaller internuclear distance.

Even though this data is meager compared with the vibrational information of previously discussed systems it is still revealing. Due to the simple electronic nature of the calcium cation the separated atomic limits are known without dispute. Excitation or charge transfer to the rare-gas atom is impossible at the photointerrogation wavelength. Consultation of atomic energy levels tables reveal that only one separated atomic scheme is possible, $\text{CaKr}^+ \rightarrow {}^2\text{D Ca}^+ + {}^1\text{S Kr}$ which correspond to an s to d transition in the calcium cation. Two j components exist for the calcium cation at ${}^2\text{D}_{3/2}$ (13 650 cm^{-1}) and ${}^2\text{D}_{5/2}$ (13 710 cm^{-1}).³⁷ These separated atomic limits for the cation of calcium are the only ones available within 4 eV of the ground state.

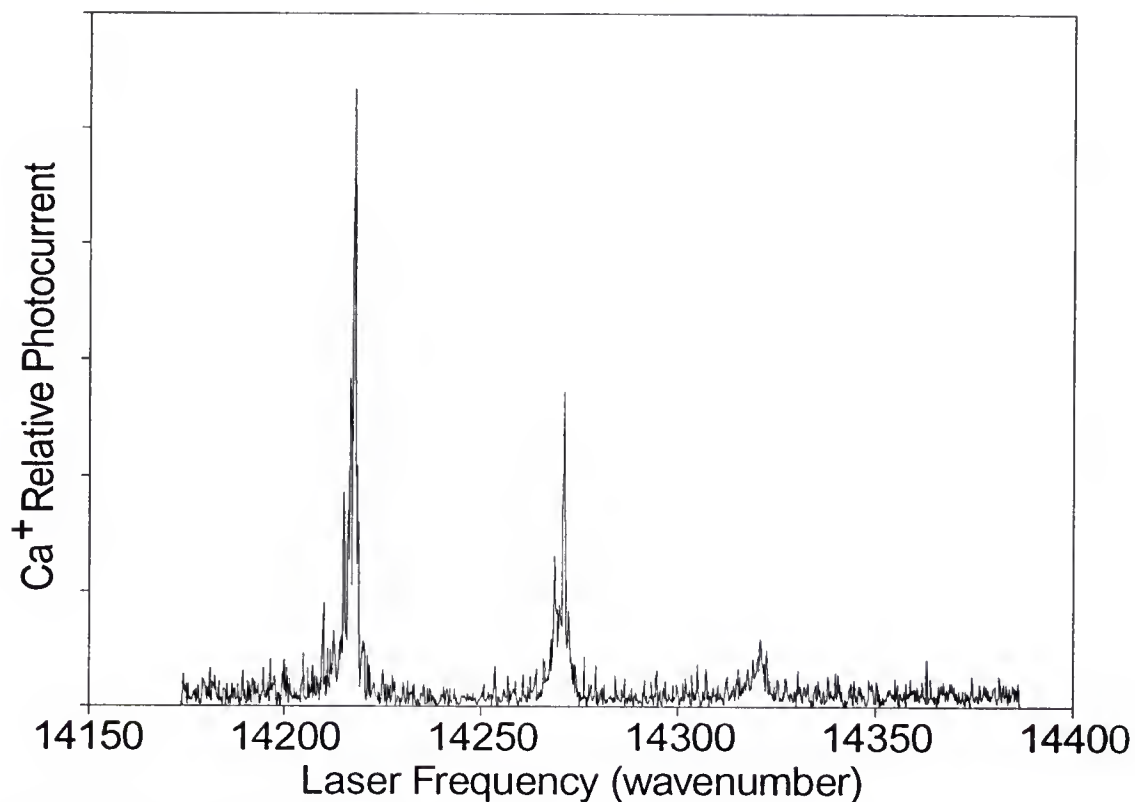


Figure 29. Photodissociation of CaKr^+ .

The figure displays the photodissociation spectrum for the process $\text{CaKr}^+ \rightarrow \text{Ca}^+ + \text{Kr}$ in the visible region of 14 150 to 14 400 cm^{-1} . Three red degraded bands of an excited state progression are observed in this region. Isotopic analysis confirms the transition at ca. 14 220 cm^{-1} corresponds to the origin band.

Unfortunately, the vibrational information is not sufficient to estimate the dissociation energy of the excited state. However, one may speculate on the term symbol corresponding to the observed excited state. The angular momentum coupling of a 2D with a 1S will result in $^2\Sigma$, $^2\Pi$, and $^2\Delta$ molecular term symbols. Considering the nature of inductive forces, the binding energy will increase with smaller internuclear separation. Since the ground state valence electron configuration of the cation corresponds to a diffuse 4s orbital, it should be bound less than a cation containing a 3d electron. This is opposite to what the presence of red-degraded bands suggest. The sigma molecular state may however limit the approach of the rare-gas atom since the valence electron of the cation lies along the internuclear axis.

Discussion

The spectroscopic parameters for the excited and ground states of the metal rare-gas diatomic systems (MRg^+) studied in this chapter are collected in Table 12 and Table 13, respectively. Several observations are worth mentioning concerning this data.

Table 12. Spectroscopic Parameters for Excited States.

Ion	config. ^a	D ₀ [cm ⁻¹]	T _{eo} [cm ⁻¹]	ω _e ' [cm ⁻¹]	ω _e x _e ' [cm ⁻¹]
VAr ⁺	3d ³ 4s	1368	15166	94	1.95
CoAr ⁺ (A)		2594	13081	165	3.20
CoAr ⁺ (B)	3d ⁷ 4s	1993	13380	121	2.21
CoAr ⁺ (C)	3d ⁸	2824	14458	176	3.28
ZrAr ⁺ (A)			14888	68	0.92
ZrAr ⁺ (B)			15479	69	0.67
ZrAr ⁺ (C)			15540	77	1.26
CaKr ⁺	3d		14192	52	0.08
VKr ⁺	3d ³ 4s	2047	15310	99	1.40
CoKr ⁺ (A)		3985	13336	148	1.47
CoKr ⁺ (B)	3d ⁷ 4s	2907	13874	118	1.36
CoKr ⁺ (C)	3d ⁸	4158	14674	159	1.76

^aMetal ion atomic configuration in separated atom limit.

Table 13. Ground State Adiabatic Bond Strength.

Ion	config. ^a	D ₀ Expt. [eV]	D ₀ Theory [eV]	obs-cal [eV]	%err.
VAr ⁺	3d ⁴	0.370	0.291 ^b	0.079	-21%
CrAr ⁺	3d ⁵	0.29	0.246 ^c	0.04	-15%
CoAr ⁺	3d ⁸	0.510	0.392 ^b	0.118	-23%
NiAr ⁺	3d ⁹	0.55	0.450 ^d	0.10	-18%
VKr ⁺	3d ⁴	0.473			
CoKr ⁺	3d ⁸	0.69			

^aMetal ion atomic configuration in separated atom limit.^bRef [62], ^cRef [63], ^dRef[61]

Application of the LeRoy-Bernstein procedure to the vibronic data of this Chapter has determined that the attractive force is governed by charge induced-dipole forces. Recall from the introductory Chapter that attractive chemical forces may be described as consisting of four types of interaction: covalent, electrostatic, inductive, and dispersive. In order to provide some perspective, it is helpful to compare the binding energy of systems that exhibit other types of bonding. We have shown that metal cations will be bound to a rare-gas atom by ca. 0.3 to 0.5 eV. As expected, a MRg^+ diatomic is bound considerably less than a covalent diatomic such as H_2 at 4.7 eV⁽¹⁾ or N_2 at 9.9 eV.⁽¹⁾

However the binding energy of a MRg^+ is considerably larger than a van der Waals (dispersive interaction) bound dimer, such as Ar_2 (0.0105 eV)¹, NaAr (0.004 eV)⁵² or AlAr (0.02 eV)⁵³ for example. The neutral diatomic system, CdAr , which is perhaps more relevant to transition-metal containing MRg^+ systems, is also expected to be bound by van der waals forces and has a bond energy of ca. 0.012 eV.⁵⁴

The binding energy of the ground states for the systems of CoAr^+ , VAr^+ , CrAr^+ , and NiAr^+ determined in this study may be compared to enthalpies of other MRg^+ diatomics. The enthalpies for several alkali metal rare-gas diatomics have been determined by ion mobility studies: LiAr^+ (0.276 eV⁽⁵⁵⁾, 0.550 eV⁽⁵⁶⁾), NaAr^+ (0.211 eV)⁵⁶, KAr^+ (0.119 eV)⁵⁶, LiKr^+

(0.710 eV)⁵⁶, NaKr⁺ (0.285 eV)⁵⁶, and KKr⁺ (0.161 eV)⁵⁶. These alkali containing diatomic systems are generally less bound than the transition-metal containing diatomic systems. This may be explained by the larger orbital radius predicted for the alkali metal cations over a transition-metal cation in a given row of the periodic table.

One may also compare our finding directly to the mobility studies of CrAr⁺ which predicts the dissociation energy as 0.284 ± 0.018 eV⁽⁵⁷⁾, and the collision-induced-dissociation data⁵⁸ of VRg⁺; Rg = Ar (0.2 ± 0.2 eV), and Kr (0.4 ± 0.2 eV). These determinations are in excellent agreement with our findings. The binding energy of HgAr⁺ has been determined spectroscopically to 0.23 eV with a ground state vibrational frequency of 99 cm⁻¹.⁽⁵⁹⁾ This also compares favorably with the data presented here.

A number of ab initio calculations have been carried out on the systems described in this paper^{60,61,62} and are listed in the table of ground state adiabatic binding energies for comparison. Although the calculations predict, qualitatively, the trend experimentally observed for the binding energies they are typically low by ca. 20%.

One may understand the contribution of inductive forces in the bond energy of an electrostatically bound metal cation and a water molecule. The enthalpies of the following systems have been determined from high pressure mass spectrometer technique: Li(H₂O)⁺ (1.47 eV)⁶³, Na(H₂O)⁺ (1.04 eV)⁶³, K(H₂O)⁺

(0.78 eV)⁶³, and $\text{Ag}(\text{H}_2\text{O})^+$ (1.43 eV)⁶⁴. Additionally, we may compare directly to the following data:⁶⁵ $\text{Ca}(\text{H}_2\text{O})^+$ (1.26 eV), $\text{V}(\text{H}_2\text{O})^+$ (1.57 eV), $\text{Cr}(\text{H}_2\text{O})^+$ (1.26 eV) $\text{Co}(\text{H}_2\text{O})^+$ (1.61 eV) and $\text{Ni}(\text{H}_2\text{O})^+$ (1.52 eV). Here one observes a significant increase in bond dissociation energy, ca. a factor of 3-4, from the metal cation argon systems to the metal cation water systems by the presence of a permanent dipole. One may speculate that inductive forces play a significant role in the total enthalpy of solvation for cations in aqueous solution, as much as 25%.

As a first approximation, these systems may be thought of as simple inductively bound complexes. All attractive forces are electrostatic and depend only on the overall charge and the polarizability of the neutral partner. Under such an assumption the ion and neutral are taken as covalently inert and behave as closed shell atoms. In this sense the only difference in behavior, for systems containing the same rare atom, depends on the state of the charged atom and the repulsive interaction it has with the neutral partner.

One may consider a simple analytic potential surface (in which the attractive part of the potential is governed by inductive forces) at this point to help understand the differences in binding energy of the various systems. A more detailed description of analytic potentials and their parameterization will be given in the next chapter. Presently, for the Lennard-Jones type potential the equilibrium dissociation energy (D_e) is proportional to α/r^4

where α is the polarizability of the rare-gas atom and r is the internuclear distance. For VAr^+ versus VKr^+ or $CoAr^+$ versus $CoKr^+$ (ground states), considering the change in polarizabilities, krypton-containing molecules should be bound ca. 52% more than the argon-containing molecules. A 30% increase is observed experimentally. This discrepancy may be accounted for by the smaller atomic radii⁶⁶ of Ar (0.659×10^{-8} cm) in comparison to that of Kr (0.795×10^{-8} cm). A smaller radii will be favorable for a larger binding energy. Nonetheless, it is apparent that an increase in the polarizability of the neutral partner will typically increase the binding energy of a cation rare-gas system.

It is interesting to note, that both theoretical⁶⁷ and experimental⁶⁸ findings suggest that many transition-metal helides (helium) are bound more strongly than their neides (neon) counterparts even though the polarizability of the latter is greater. Thus, from a simplistic notion, the shorter internuclear distance of the helide will win out over the larger polarizability of the neide in determining the final dissociation energy.

In comparing systems that contain the same rare-gas atom one would expect the binding energy to be governed solely by the internuclear distance. In consulting the table of ground state adiabatic bond strengths one notices that an increase in bond strength occurs due to the radial contraction of the 3d orbital for the diatomics $CrAr^+$, $CoAr^+$, and $NiAr^+$. The only

anomalous behavior is observed for VAr^+ . This system has a larger binding energy than $CrAr^+$ but a smaller metal cation atomic number.

One may account for this discrepancy by considering the bonding nature of the 3d orbitals in V^+ . For transition metals that have less than a half-filled 3d subshell, vacant molecular orbitals along the metal rare-gas internuclear axis are possible, i.e., there is zero valence electron density on the axis. Of course, core electron density derived from the cation is still present. The unspherical nature of the d valence configuration allows a closer approach of the rare-gas atom to the cation than systems containing a half-filled 3d subshell. Thus, VAr^+ ($3d^4$) is bound by more than $CrAr^+$ ($3d^5$). However, it is apparent that the 3d orbital contraction will at some point across the transition-metal row in the periodic table provide a metal cation of smaller radii than the effective radii derived from a vacant 3d orbital. An ab initio calculation provides support for our interpretation of the bonding found in VAr^+ .⁶⁹

In all spectra generated in this chapter the vibronic bands were decidedly red-degraded (implying a shorter ground state internuclear distance). This is consistent with our assignment of the separated atomic limits. Upon promotion of the electron from a 3d to a 4s, one would expect the binding energy to decrease due the larger radial extent of the 4s electron. This is observed between the VAr^+ ($3d^4$) ground

state and $\text{VAr}^+ (3d^3 4s)$ excited binding energy of 0.37 to 0.17 eV, and in $\text{CoAr}^+ (3d^8)$ ground and $\text{CoAr}^+ (3d^7 4s)$ excited state of 0.51 to 0.25 eV. Basically, the binding energy is halved for a 4s containing atom. For hydrogenlike orbitals the radial extent of a 4s orbital is ca. 3 times larger than the radial extent of a 3d orbital.⁷⁰

DIATOMIC POTENTIAL ENERGY SURFACES

Analytic Potentials

One of the most important and powerful concepts in chemistry is that of a potential energy surface (PES). For a diatomic system under the Born-Oppenheimer approximation, a potential surface will completely describe the force of interaction between the atom pair. Recall, the interatomic force is derived from the gradient, with respect to internuclear distance, of the potential energy function. In this chapter we will look at the ability of several simple analytic potential energy surfaces (PES) to describe the spectroscopic information determined from metal rare-gas diatomics of the previous chapter.

The extensive vibrational information of many of the metal rare-gas diatomic systems discussed in the preceding chapter provides a unique opportunity for the construction of an accurate analytic potential energy surface. We have already seen that the attractive part of the potential for inductively bound systems is proportional to $1/r^4$. With the experimental knowledge of either the vibrational frequency or

dissociation energy one may easily parameterize a Lennard-Jones type potential. This potential has the form

$$U(r) = \frac{\beta}{r^n} - \frac{C}{r^m} \quad (22)$$

where n and m determine the internuclear dependence on the repulsive and attractive wall respectively. One may use a shorthand notation in which a Lennard-Jones potential is symbolized by $[n,m]$. The constant C may be determined from the polarizability of the neutral partner and is equal to $(\alpha e^2)/2$. The Lennard-Jones potential then becomes a one-adjustable function in β . This parameter may be determined from either the dissociation energy or the vibration frequency. Once β is known, the three most important characteristics of a diatomic systems are determined, i.e., the vibration frequency, the dissociation energy, and the internuclear distance.

Equations relating β to the vibrational frequency and the dissociation energy have been derived for three Lennard-Jones potentials: $[6,4]$, $[8,4]$ and $[12,4]$ and are listed Appendix C. In cases where the experimental information is limited to either a knowledge of the vibrational frequency or the dissociation energy, but not both, one may estimate the internuclear distance and the unknown parameter. This analysis has been performed before on $VAr^+/VKr^{+(43)}$, $CoAr^+/CoKr^{+(38)}$, and $NiAr^{+(71)}$.

For the systems of CoAr/Kr⁺ and VAr/Kr⁺ both the dissociation energy and the vibrational frequency have been determined by other means (see Chapter on inductively-bound diatomics). The Lennard-Jones potential is then overdetermined and we may compare the dissociation energy derived from the LeRoy-Bernstein method with the dissociation energy derived from adjusting β to the vibrational frequency. It must be noted that fitting β to the dissociation energy results in an overestimation of vibrational frequency with respect to fitting the vibrational levels to Eq. (6). The parameterization of a PES with a Lennard-Jones potential apparently provides only a moderately accurate estimate of the behavior of an inductively-bound system.

In cases where both the vibrational frequency and dissociation energy are known, a two adjustable potential may be parameterized. The Born-Meyer potential is of the form

$$U(r) = be^{-r/\rho} - C/r^4 \quad (23)$$

where b and ρ are determined from the experimentally determined vibrational frequency and dissociation energy. Consequently, one may relate the internuclear distance to the vibrational frequency and the dissociation energy (see Appendix C). Again, the constant C may be determined from the polarizability of the rare-gas atom. But how may we test the accuracy of the Born-Meyer PES? A rigorous inversion of vibrational data to a potential surface is possible through

the Rydberg, Klein, and Rees (RKR) procedure⁷² but only if at least partial rotational information is available. Unfortunately, rotational analysis has been limited and is therefore insufficient for a RKR analysis.

Vibrational Eigenvalues from the WKB Approximation

The utility of some of these analytical potentials may be rigorously tested by applying a numerical procedure for the determination of the vibrational eigenvalues. The numerical calculation that shows particular promise for such a task is the Wentzel, Kramers and Brillouin (WKB)⁷³ approximation. This method is a semiclassical quantization of the molecular vibration.

Under the Born-Oppenheimer approximation the motion of the nuclei in a diatomic system is governed by a potential $U(r)$. Presently, we will ignore the rotation of the system. We may now describe the vibrational bound states, $E(v)$, of a given potential with a one-dimensional Schroedinger equation.

$$\left[-\frac{h^2}{8\pi^2\mu} \frac{d^2}{dr^2} + U(r) \right] \psi_v = E_v \psi_v. \quad (24)$$

Following a classical formalism, as the nuclei oscillate periodically between the turning points r_{in} and r_{out} , kinetic and potential energy are exchanged with the total energy remaining a constant. This oscillation may be thought of a

trajectory in phase space. Since the total energy is given by the following equation,

$$E = \frac{p^2}{2\mu} + U(r), \quad (25)$$

the momentum trajectory as a function of internuclear distance will be given by

$$p(r) = \pm [2\mu (E - U(r))]^{1/2}. \quad (26)$$

Invoking the quantization rules postulated by Bohr and Sommerfeld⁷⁴ ('old' quantum theory) one may quantize the action over one complete period as a half integer multiple of h ;

$$\oint p(r) dr = (n + 1/2)h. \quad (27)$$

Substitution of Eq. (26) into Eq. (27) results in an expression relating the potential surface, $U(r)$, of a diatomic system to a vibrational index, v ;

$$(2\mu)^{1/2} \oint [E(v) - U(r)]^{1/2} dr = h(v + 1/2). \quad (28)$$

These results can also be obtained by considering a classical approximation to the wave function.^{75,76}

To lend some credence to the effectiveness of the WKB approximation, one may show that the vibrational eigenvalues for a harmonic potential are described exactly. The harmonic potential is given by, $U(r) = 1/2kr^2$, where k is the force constant for a diatomic system. The action integral may be

described conveniently by noting that harmonic potential is a symmetric function with zero potential energy at $r = 0$. The boundary conditions of the closed loop integral of Eq. (27) may then be then expressed as,

$$4(2\mu)^{1/2} \int_0^r [E(v) - U(r)]^{1/2} dr = h(v + 1/2). \quad (8)$$

Substitution of the harmonic oscillator eigenvalues for $E(v)$ and consultation of integration relations³³ results in an expression for the integrand of the above equation,

$$\frac{1}{2} \int_0^r r \left[2(v+1/2) \frac{h\omega}{k} - r^2 \right]^{1/2} + \frac{2r(v+1/2) h\omega \sin^{-1}}{k \left[2(v+1/2) \frac{h\omega}{k} \right]^{1/2}}. \quad (9)$$

The boundary r for a harmonic oscillator may be expressed as a function of the vibrational index. Since,

$$U(r) = \frac{1}{2}kr^2 = (v + 1/2)h\omega \quad (10)$$

the variable r is easily expressed as,

$$r = [2(v + 1/2)h\omega]^{1/2}.$$

Applying the bounds to the integrand of Eq. (30) and combining with the prefactor of the righthand side of Eq. (27) results in the relation

$$\frac{2\pi\omega\mu^{1/2}h}{k^{1/2}} (v + 1/2).$$

Recall that the force constant k is defined as $(2\pi\omega)^2\mu$, thus lefthand side of Eq. (27) is $h(v + 1/2)$ and the WKB approximation is exact for a harmonic oscillator.

Unfortunately, real diatomic systems are not accurately described by a harmonic potential surface. However the WKB approximation will allow one to predict the vibrational bound levels of more realistic potential surfaces numerically. For a given potential energy surface, $U(r)$, one may determine the vibrational energy levels, $E(v)$, that quantize the action integral with vibrational index, v . These numerically derived vibrational eigenvalues may be compared to the observed vibrational levels. Indeed, one may parameterize an analytic potential function by minimizing the root-mean-square (rms) deviation of observed and calculated vibrational levels. Clearly, this is easily accomplished with the one-adjustable Lennard-Jones potential mentioned early in this Chapter.

One may extend this procedure to a two-adjustable potential. Consider the Born-Meyer potential, Eq. (23). The parameter b and ρ will be uniquely determined from a given ω_e , D_e pair. It is possible to independently vary ω_e and D_e over a range and note the rms value.

An rms contour plot for the CoKr^+ C state versus the ω_e , D_e grid is shown in Figure 30. A minimum for the fit is observed within a small range near a vibrational frequency of

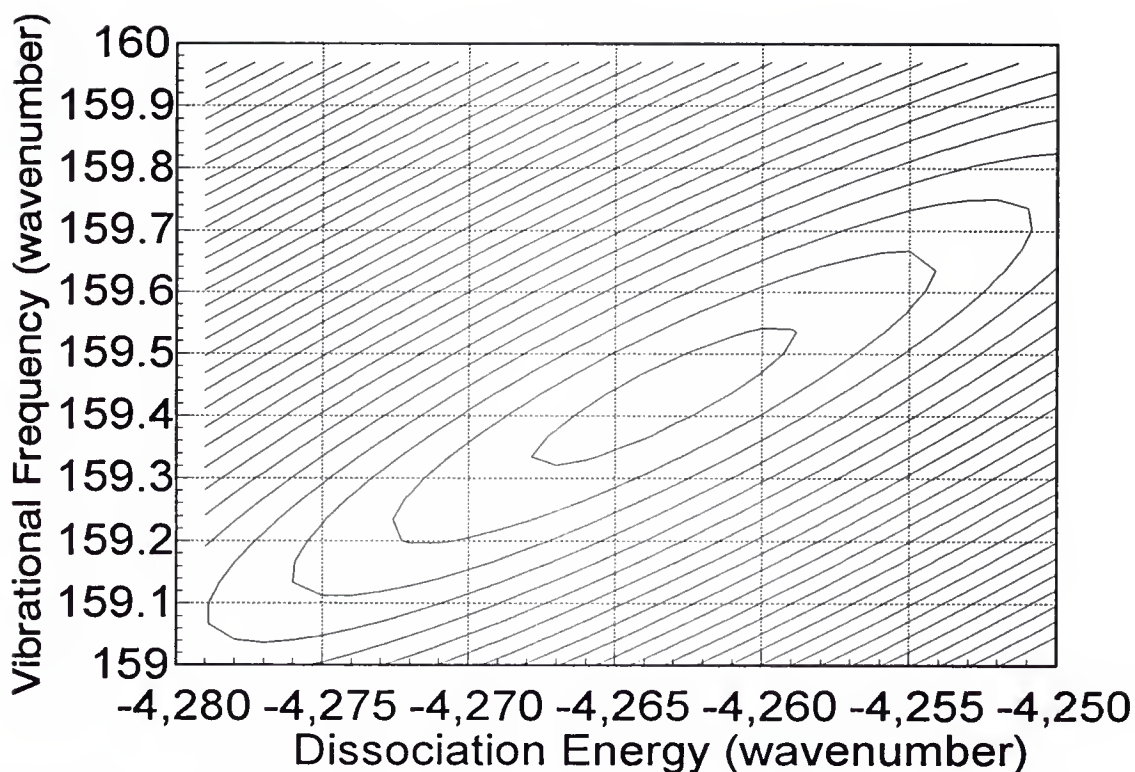


Figure 30. RMS Contour Plot of CoKr^+ C state.

The figure displays the root-mean-square (rms) contour for the observed vibrational levels versus the WKB predicted values for the C state of CoKr^+ . The two adjustable parameters for a Born-Meyer potential are uniquely determined by the dissociation energy and the vibrational frequency. The central contour corresponds to an rms of 1.6 cm^{-1} with each successively larger ring increasing by 0.2 cm^{-1} . The minimum rms suggests that the dissociation energy is 4263 cm^{-1} with vibrational frequency of 159.4 cm^{-1} . This is in good agreement with the experimentally determined value of 4158 cm^{-1} and 159 cm^{-1} for the dissociation energy and vibrational frequency respectively.

159 cm^{-1} and a dissociation energy of 4263 cm^{-1} . The central contour is the minimum rms contour and corresponds to 1.6 cm^{-1} within each adjacent contour increasing by 0.2 cm^{-1} . Over the 27 observed vibrational levels that encompass an energy range of 2600 cm^{-1} the fit is quite good. The vibrational frequency determined from Eq. (6) of 159 cm^{-1} and the dissociation energy of 4237 cm^{-1} are in superb agreement.

The vibrational levels for many of the systems discussed in the previous chapter have been used to parameterize the Born-Meyer potential using the WKB approximation. The adjustable parameters corresponding to a minimum in the root-mean-square deviation are listed in Table 14 along with corresponding diatomic characteristics, r_e , ω_e , and D_e . The WKB parameterization of the Born-Meyer potential results in a potential energy surface that describes the observed vibrational levels for most systems with small rms deviation. The largest deviation occurs for the C state of CoAr^+ . In this system, all but 9 bound vibrational levels encompassing 99% of the binding energy are observed experimentally. Further refinement of the analytic potential may be necessary to reduce the rms.

Notice that the vibrational frequency and dissociation energy agrees extremely well with previously determined values listed in Table 12 of excited state parameters. In most cases the vibrational frequency, within a wavenumber, is exactly matched. For those molecules in which the dissociation energy

Table 14. WKB Parameterization of Born-Meyer Potential with Experimental Eigenvalues.

MRg ⁺	v/v _D ^a	%E ^b	ρ Å	β cm ⁻¹ /10 ⁶	RMS ^c cm ⁻¹	r _e Å	D _e cm ⁻¹	ω_e cm ⁻¹
VAr ⁺	37/49	43	0.302	4.26	0.2	2.4	1420	94
VKr ⁺	41/69	48	0.291	8.65	2.7	2.4	2130	99
CoAr ⁺ A	19/		0.216	37.43	6.9	2.1	2720	166
CoAr ⁺ B	36/55	65	0.276	6.03	3.1	2.2	2065	120
CoAr ⁺ C	47/56	99	0.205	58.48	10.9	2.1	2930	179
CoKr ⁺ A	19/		0.259	11.38	7.4	2.5	4080	149
CoKr ⁺ B	34/89	80	0.281	8.15	3.3	2.2	3000	118
CoKr ⁺ C	27/94	63	0.245	17.35	1.5	2.1	4263	159
ZrAr ⁺ A	14/		0.359	1.29	0.6	2.3	1333	68
ZrAr ⁺ C	16/		0.318	3.09	1.8	2.4	1297	77

^aRatio of observed to predicted bound vibrational levels.^bPercentage of potential well depth observed over vibrational bound states.^cRoot-mean-square deviation of WKB calculated versus experimental vibrational eigenvalues.

have been determined via the LeRoy-Bernstein method, the comparison to WKB determined dissociation energy is also quite good, the relative error is less than 2% in each case. In the worst case, the WKB procedure overestimated the experimental value by a mere 1.87%.

Figure 31 displays the rms-minimized potential surface and vibrational eigenvalues determined from the WKB approximation and the Born-Meyer PES for the three observed excited states of CoKr^+ . In the figure, it is easy to see where perturbations of vibrational levels may occur. Also notice that since the A state has a larger binding energy than that of the B state and happens to corresponds to a larger promotion energy in the cobalt cation. The Born-Meyer potential surface suggests a internuclear distance of ca. 2.1 Å.

With the WKB technique it is possible to parameterize the one-adjustable Lennard-Jones type potentials. This becomes important when the experimental information is limited. Here we may compare the ability of a Lennard-Jones [6,4] and [8,4] with that of the Born-Meyer to describe the spectroscopic parameters. Figure 33 displays the residual error for vibrational eigenvalues of VKr^+ determined by the WKB approximation for several analytic potential functions. In each case the adjustable parameter(s) was optimized by minimizing the rms value. From the figure it is apparent that only the Born-Meyer ([exp,4]) potential adequately describes

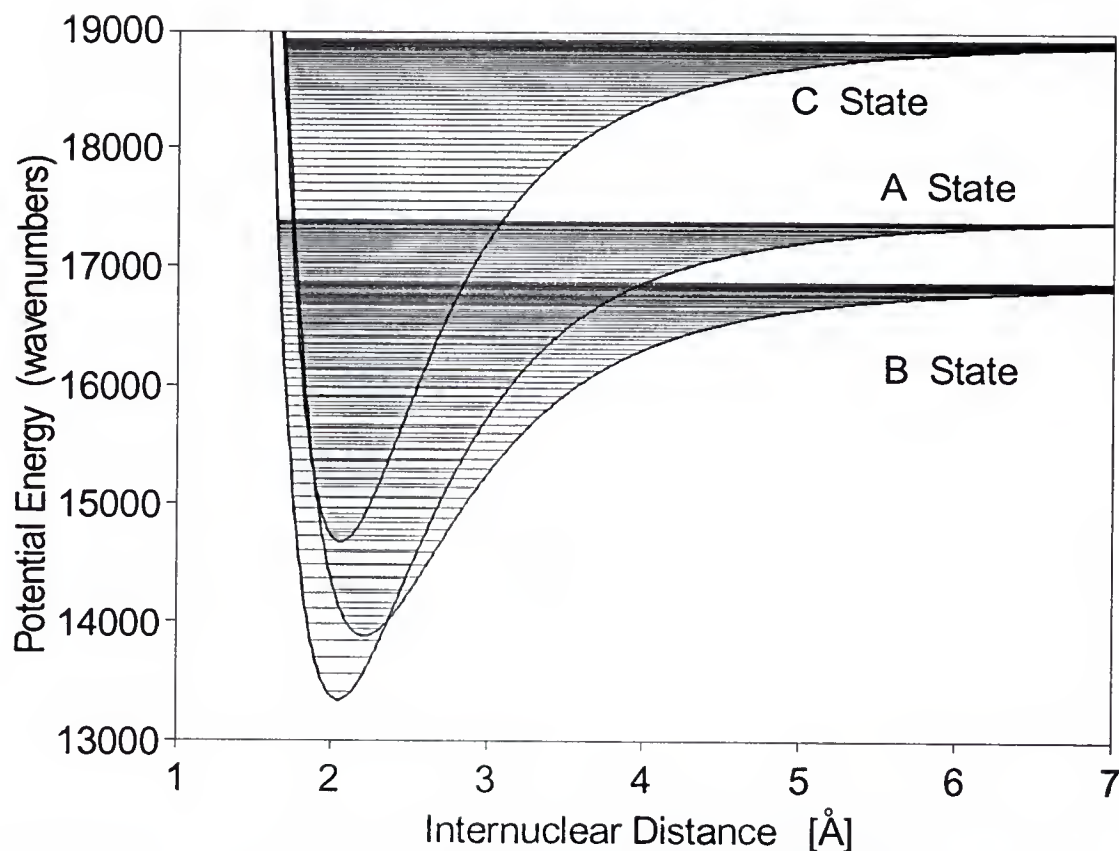


Figure 31. Potential Energy Curves of CoKr⁺ Excited States.

The figure displays the potential energy curves of the excited states, A, B, and C using the best fit parameters via the WKB approximation. The A state curve crosses the B state such that the A state has a higher dissociation energy and a lower potential minimum. Note the extremely short predicted equilibrium separation of ca. 2 Å.

the observed vibrational levels. For the system VKr⁺, the Lennard-Jones [6,4] potential provides a better fit than the [8,4] potential. However, assuming that the Born-Meyer potential accurately predicts the internuclear bond distance, the [8,4] provides a closer match (see Figure 34).

One immediate question that arises for this procedure is how accurate is the approximation, and how accurate is the computer code. The code is included in the Appendix B. Two iterative procedures along with an integration will introduce some inaccuracy in the determination of the vibrational eigenvalues. One may test the accuracy of the program against the known eigenvalue of the harmonic oscillator. A variety criteria for the root finder procedure and minimizing routine, along with varying the step size of the integrator have been tried. A set of conditions that have been found in which the computer calculated eigenvalues are within a 0.2 cm⁻¹ of the known harmonic eigenvalues over a range of 4000 cm⁻¹.

As has been shown previously in this Chapter, the WKB approximation applied to a harmonic potential is exact. Comparison of WKB generated vibrational eigenvalues using the harmonic PES will provide a good test of the computer code. For such a calculation the rms was found to ca. 0.05 cm⁻¹ for 40 vibrational levels spanning a well depth of ca 4000 cm⁻¹.

One may further test the source code on non-harmonic potential surfaces. A small change in potential energy near

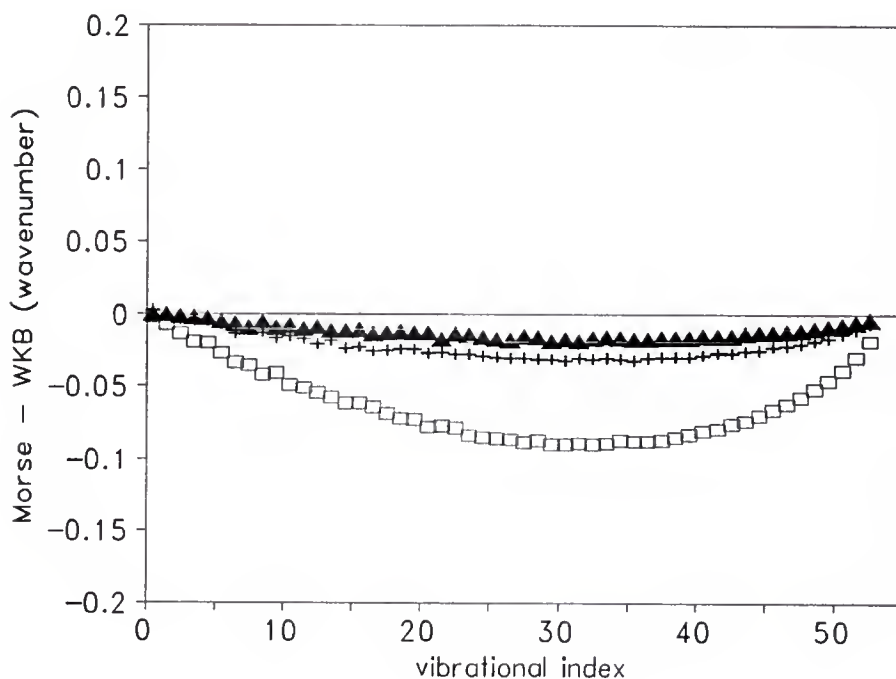


Figure 32. WKB Error for Morse Potential.

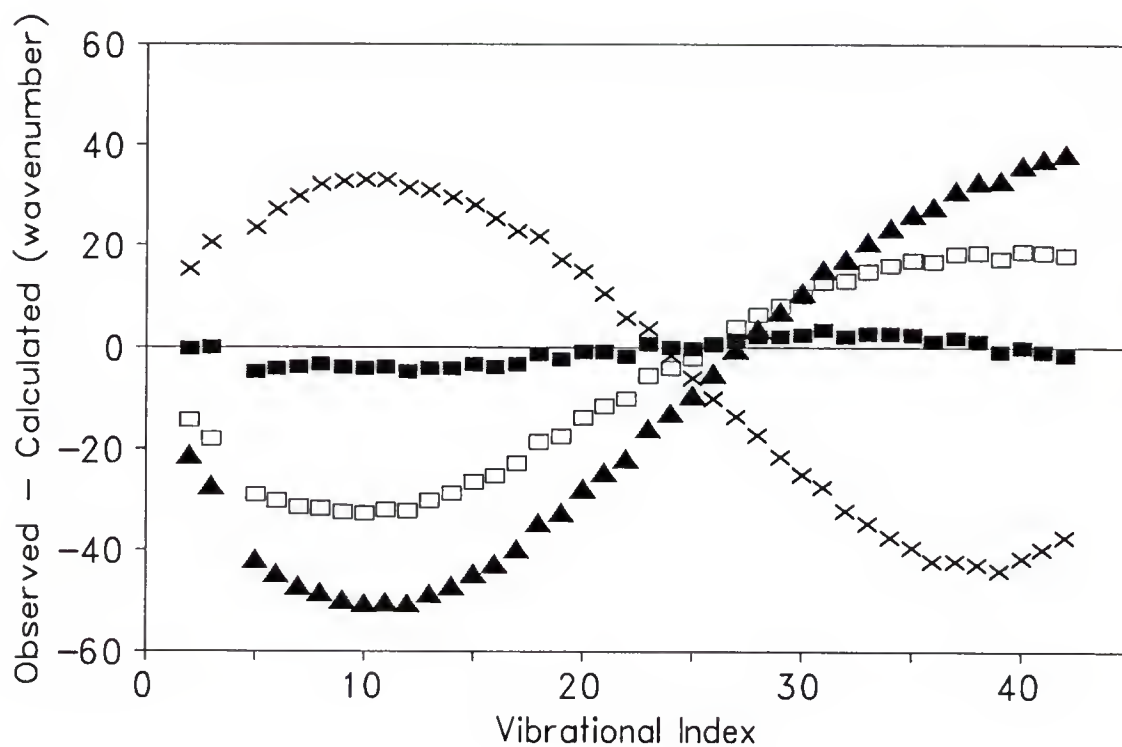
The figure displays the error for the WKB-generated vibrational eigenvalues for the Morse potential. The Morse potential was parameterized by using the vibrational frequency and dissociation energy of CoKr^+ B state. The rigorously determined vibrational eigenvalues using Eq. (34) are compared to the semi-classical WKB method. Over the range of bound levels $0 \rightarrow 52$, an rms value of 0.068 cm^{-1} is observed with a 1000 step integration (squares). Increasing the number of integration steps to 2000 (crosses) or 3000 (triangles) results in an rms value of 0.024 cm^{-1} and 0.013 cm^{-1} , respectively.

the attractive portion of the surface will result in a large change in internuclear distance. A convenient non-harmonic PES one may easily test with the WKB approximation is a Morse potential. For a Morse potential the vibrational eigenvalues may be determined rigorously.⁷⁷

$$E(v) = \beta \left(\frac{D_e h}{2\pi^2 c \mu} \right)^{1/2} (v + 1/2) - \frac{h\beta^2}{8\pi^2 c \mu} (v + 1/2)^2 \quad (34)$$

Here β and D_e are in cm^{-1} , μ is the reduced mass in grams and h and c are the usual in cgs units.

Figure 32 displays the relative error of the Morse vibration eigenvalue minus the WKB determined eigenvalue. The dissociation energy of the potential was adjusted to correspond to the rms minimized CoKr^+ C state data. The number of integration steps were increased from 1000, to 2000, and finally 3000. Obviously, as the number of integration steps increase the accuracy improves. However calculation time is directly proportional to the number of integration steps. We see that the results for a 1000 step integrator are still significantly less than one wavenumber and therefore more than adequate in modelling vibrational eigenvalues determined in our experiment. The generation of an rms contour plot requires ca. 9 hrs. of 486 33 Mhz computer processor time.



■ [exp, 4] ▲ [8, 4] □ [6, 4] × [Morse]

Figure 33. Residuals to WKB.

The figure displays the residual error (observed minus calculated) for several analytic potentials parameterized via the WKB approximation. The best fit of the vibrational levels is achieved for the Born-Meyer potential, annotated in the graph legend as [exp,4] which corresponds to Eq. 118. The Lennard-Jones potentials, [8,4] and [6,4] along with the Morse potential, poorly describe the experimental vibrational levels.

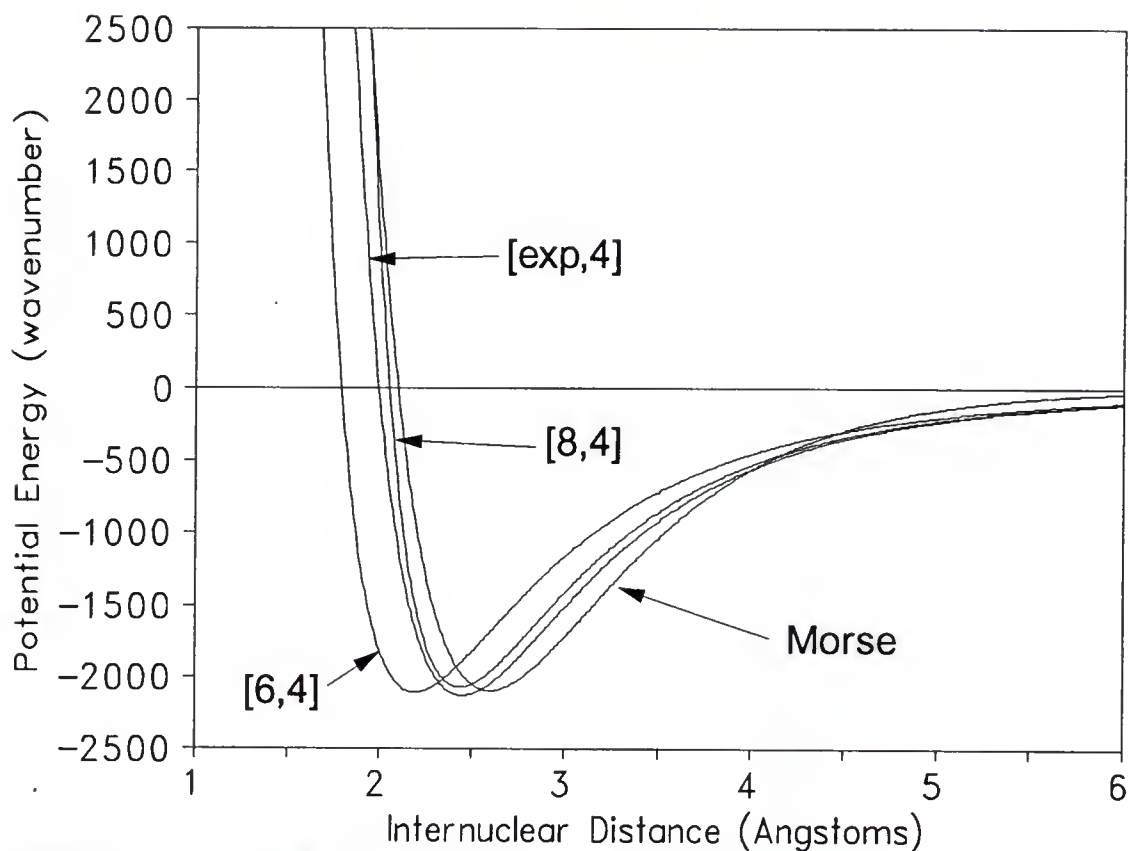


Figure 34. Potential Energy Surfaces for VKr⁺.

The figure displays the potential energy surfaces used in modelling the vibrational levels via the WKB approximation. The internuclear distance of the Morse potential has been arbitrarily adjusted to approximately agree with the other potentials. Notice that the internuclear distance is ca. 2.4 Å for both the [exp,4] and [8,4] potentials

METAL RARE-GAS CLUSTERS

One normally thinks of a dissolved ion as strongly associated with a small number of polarized solvent molecules. The solvent molecules very close to or 'touching' the ion, which comprise the primary solvation sphere, will significantly affect the solute ions' diffusivity and chemical reactivity. Solvent molecules further away than this first 'shell' are much more loosely associated with ion position and have a subsequently smaller effect on the ion's solvated properties. Simple electronically closed shell ions, for instance alkali ions, will attract the solvent almost exclusively with charge dipole or charge induced-dipole electrostatic forces. The number of molecules in the first solvation shell will largely depend on the ability of the solvent to pack around the ion. Open shell ions (in particular transition metals) would be expected to have interactions above and beyond the simple electrostatic, ranging from mild preference for a particular coordination number to covalent interactions so strong that the ion-plus-solvation shell is best thought of as a single molecule (coordination complex).

The experimental apparatus has been demonstrated to be capable of generating a variety of transition-metal rare-gas diatomics. The cluster properties of the expansion may additionally 'solvate' a ionic species with several rare-gas atoms. Here, we will define solvation to include all types of ligands, and not just water molecules. Aqueously solvated ions represent only one special case of complex. As will soon be apparent, a unique stability is often associated with a specific number of rare-gas atoms.

Figure 35 shows a TOFMS of cobalt argon clusters obtained under three different ion source expansion conditions. The top trace in Figure 35 shows the observed positive ion mass spectrum with p_0d (the product of stagnation pressure in Torr and the nozzle diameter in cm) of about 1 Torr-cm. The pressure of the Co^+ -containing plasma upstream of the expansion orifice is only a few Torr under these conditions and is insufficient to promote homogeneous cobalt clustering beyond the dimer or trimer. With the same laser fluence and five times the stagnation pressure, Co_n^+ ($2 < n < 10$) clusters are observed in quantity. The top panel of Figure 35 shows that Co^+ clustering with the Ar in the carrier gas to form CoAr_n^+ is a dominant process under these conditions. The middle panel and bottom panels of Figure 35 show the TOFMS resulting from still lower stagnation pressure ($p_0d = 0.7$ Torr-cm and 0.3 Torr-cm, respectively). The vertical scale in this figure has been reduced by a factor of

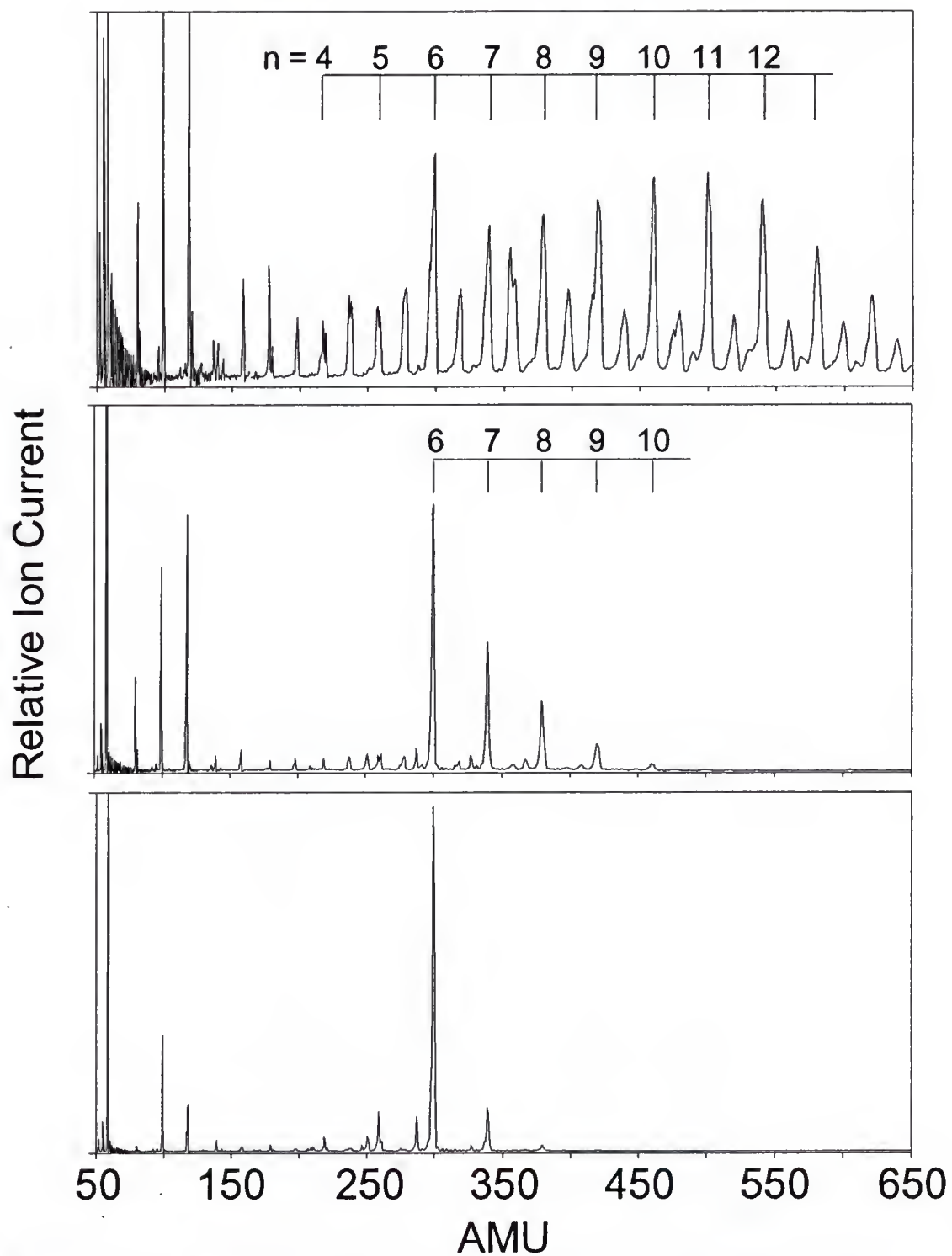


Figure 35. Mass Spectra for the Uniquely Stable CoAr_6^+ .

three from the top to the middle (= bottom) panels. The absolute as well as the relative abundance of CoAr_6^+ ions detected increases with decreasing stagnation pressure over this pressure interval. We interpret this as an indication of a kinetic or thermodynamic significance to the CoAr_6^+ molecule.

Kinetics and energetics play complicated roles in determining the observed ion abundance in this experiment. The average size of the cobalt argon clusters may be reduced by a reduction in backing pressure for two reasons: 1) the average number of $\text{Co}^+ - \text{Ar}$ collisions has been reduced (nucleation is restricted) or 2) the final temperature of the ion ensemble is higher (unimolecular dissociation is enhanced). Effect 1) can be demonstrated by operating at very low Ar concentrations but moderate total stagnation pressure, at which point the only cobalt argon cluster represented in the mass spectrometer is the CoAr^+ ion because the probability of a CoAr^+ encountering and capturing another Ar atom is too small. In this case the cobalt argon cluster abundance is simply and completely nucleation rate limited. At higher Ar concentrations at the same total pressure, multiple Ar encounters will be the rule rather than the exception and nucleation rates for any particular cluster will depend on the lifetime of the ion-argon encounter complex and the rate of collisional energy removal from the ion. The survival of any ion thus formed will further depend on its unimolecular decomposition rate at the final temperature of the molecular

beam for the duration of the 1 ms transit to the mass spectrometer. At present, we cannot uniquely separate the individual influence of these distinct processes. Conditions of high Ar concentrations but low total pressure as in Figure 35 would first promote nucleation to large sized clusters followed by attrition by unimolecular dissociation due to unquenched internal energy. Thus, small CoAr_n^+ clusters with fast nucleation rates would be small in number and large clusters with small per atom binding energies would 'thermally' dissociate. One might expect rather rapid nucleation of the unshielded central ion until the first 'solvation' shell is complete and closed.

Figure 36 shows the relative abundance for transition metal-argon complex ions as a function of the number of rare-gas atoms in the molecule for two different metals, V^+ and Co^+ . The relative abundance is derived for source conditions similar to that giving rise to the bottom panel of figure Figure 35. The total pressure is insufficient to effectively cool their total binding energy. Thus, metastable decay mediates the size of the complexes detected in the mass spectrometer. Presumably, larger clusters have undergone unimolecular decomposition in the ca. 1 ms between ion formation and mass analysis leaving by attrition only the most kinetically and/or energetically stable species, i.e. VAr_4^+ and CoAr_6^+ .

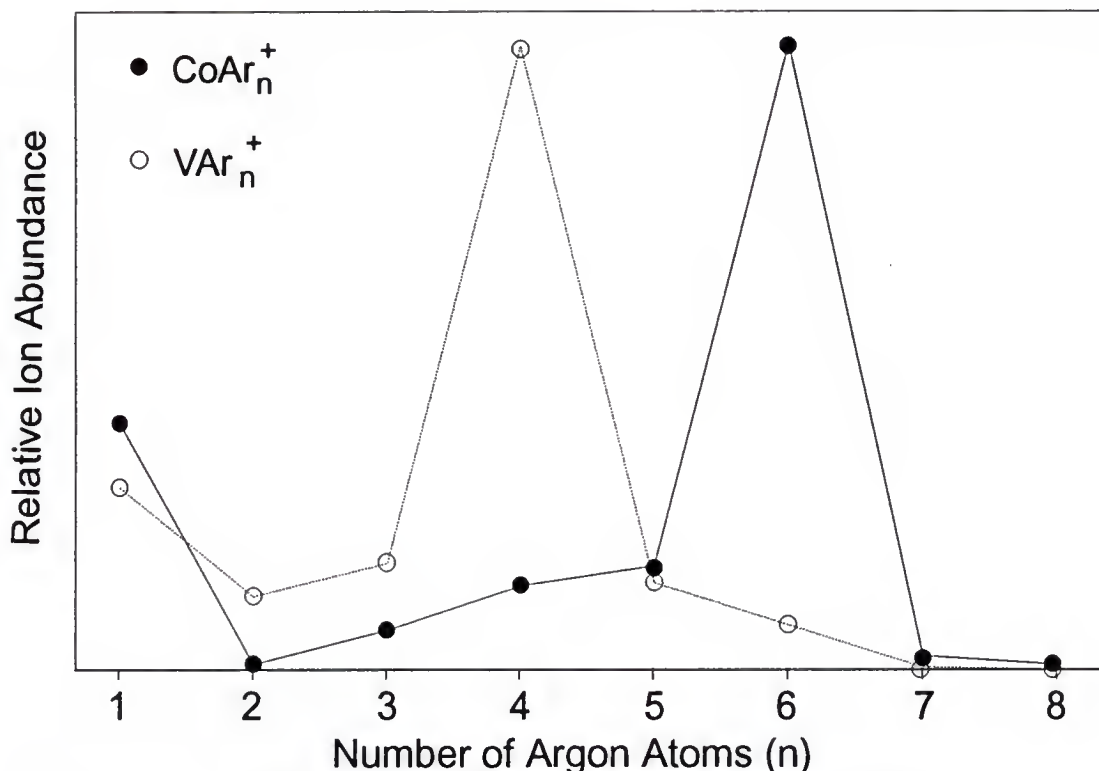


Figure 36. Relative Abundance of VAr_n^+ and $CoAr_n^+$.

The figure displays the relative abundance of transition-metal-argon complex ions as a function of the number of argon atoms in the molecule. The horizontal axis (bottom of the figure) indicates zero relative abundance. These data are derived from mass spectra obtained under ion source conditions such that extensive metastable decay due to the excess internal energy of the ions occurs in the ca. 1 ms between in creation and mass analysis. The anomalous abundance of VAr_4^+ and $CoAr_6^+$ indicates an unusual kinetic and or thermodynamic stability of these species. This behavior is taken to imply a preferred coordination of V^+ and Co^+ with argon of 4 and 6, respectively.

As further proof of the unique stability of a given metal rare-gas system, one may observe the collision-induced dissociation (CID) of larger MRg_n^+ systems. Figure 37 shows the fragment ion distribution following CID of $CoAr_{11}^+$. The loss of a single Ar atom for the cluster is a large channel but cannot be quantified with the present apparatus. Otherwise the major fragment is always the formation of $CoAr_6^+$.

Similar experimental manipulations have been applied to other transition-metal containing systems. Below is a complete list of transition-metal rare-gas magic clusters observed: $TiAr_6^+$, VAr_4^+ , $NbAr_4^+$, $CoAr_6^+$, $NiAr_{4,6,8}^+$, $CuAr_6^+$, $AgAr_{10}^+$ and $FeAr_6^+$.

An additional factor contributing to the enhanced stability of the $CoAr_6^+$ molecule is the ligand field stabilization of transition metal ions in the coordination complex. However, the 'ligands' surrounding the central atom are not point charges or dipoles in this case but point induced dipoles, leading to a much weaker ligand (crystal) field splitting than is normally observed in strongly bound covalent or ionic d-orbital complexes. Nonetheless, cobalt argon complexes, with their central d^8 $Co(I)$, would be expected to favor the octahedral symmetry in $CoAr_6^+$ as the isoelectronic species $Ni(II)F_6^{-4}$, $Ni(II)(H_2O)_6^{+2}$, and $Cu(III)(H_2O)_6^{+3}$ do. The energy realized by the ligand field

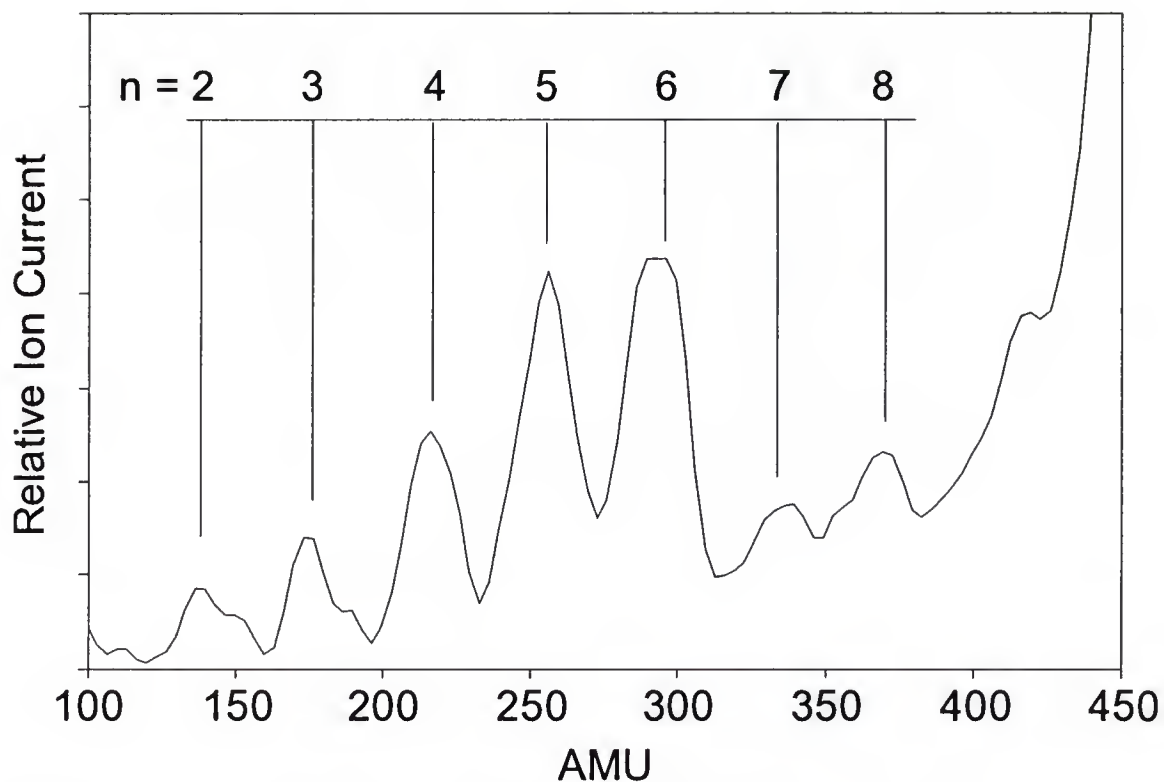


Figure 37. Collision Induced Dissociation of CoAr_{11}^+ .

The figure displays the collision-induced dissociation of mass-selected CoAr_{11}^+ . Aside for the $\text{CoAr}_n^+ \rightarrow \text{CoAr}_{n-1}^+ + \text{Ar}$ channel, the production of CoAr_6^+ is always observed to be a dominant channel for parent ions with $n \geq 8$. This behavior indicates a greater relative stability for the CoAr_6^+ ion.

breaking of the degeneracy of the d-orbitals on the Co^+ and thus lowering its energy is in addition to the net charge-induced dipole binding energy of bringing up the Ar atoms to the ion. However, the per atom binding energy based on simple electrostatic forces does not seem to be a very sharp function of Ar atom count unlike the very structure dependent ligand field stabilization. Thus, the ligand field stabilization of octahedral CoAr_6^+ might play a key role in making CoAr_6^+ uniquely stable.

Using the vibrational structure of metal rare-gas diatomic systems, we have seen that it is possible to parameterize simple analytic potentials. Because the nature of the binding between the metal ion and the rare-gas ligand is simply inductive in nature, one would expect the forces in systems containing multiple rare-gas atoms to be pairwise additive as a first level of approximation. Molecular dynamics calculations that incorporate a Lennard-Jones [8,4] potential for the metal cation rare-gas pair and a Lennard-Jones [12,6] potential for the rare-gas interactions have been carried out on VAr_n^+ complexes.⁷⁸ The lowest energy geometries for VAr_n^+ were found to be as follows: $n = 2$, bent with bond angle 147° ; $n = 3$, planar equilateral triangle; $n = 4$, tetrahedral; $n = 5$, face-capped tetrahedral; $n = 6$, octahedral; $n = 7-8$, face-capped tetrahedral; $n = 9-14$, edge- and face-capped tetrahedral.

The molecular dynamic calculations also support the unique stability of VAr_4^+ observed experimentally. The calculations reveal a significant drop in per atom binding energy after the fourth physisorbed argon atom. Additionally, the heat of solvation of a V^+ in liquid Ar was determined as ca. 28.5 kcal/mol. This suggests, in comparison to the aqueous solvation energy for Rb^+ of 81.5 kcal/mol, that inductive forces make a significant contribution to the total binding energy of an ion in an aqueous media.

Monte Carlo calculation have also been carried out on several metal-cation rare-gas containing systems via a simulated annealing procedure.⁷⁹ Some of these calculations considered three body terms arising from the interaction of the charge-induced dipoles in neighboring argon atoms. The inclusion of the three body term was found to lower the total binding energy and lower the symmetry of a given cluster.

METAL CATIONS WITH PHYSORBED POLYATOMICS

Predissociation of $V(OCO)^+$

Transition metal-containing molecules and surfaces are known to be important in the catalysis of many types of chemical reactions both at interfaces⁸⁰ and in solution⁸¹. Therefore, the role of partially filled d orbitals in the lowering of activation barriers for bond cleavage, for example, is of fundamental importance in organic and inorganic chemistry. The structure and dynamics of simple gas-phase transition-metal-containing species may be useful in modelling such processes if sufficient detail may be deduced.

Most catalytic reactions proceed through a weakly bound or 'physisorbed' state of the reactants complexed by non-covalent forces. This precursor state is a stable but weakly bound species which is a local minimum in the reaction coordinate. If these complexes can be formed and isolated, the reaction between two species may be photochemically studied as a unimolecular process and thus without the intrinsic averaging over impact parameters and collision energies as in a scattering experiment. In principle, spectroscopic methods could reveal the shape of the potential

energy surface for the reaction, and, in particular, elucidate the nature of the reaction barrier.

If a chemical transformation can be studied from an isolated, weakly-bound reactant 'cluster', great control is possible in the choice of the initial conditions of the reaction. In particular, specific vibrational motions in the cluster can be photoexcited and any chemistry dependent on this motion revealed. Such non-statistical behavior monitored on a molecular level will allow the refinement of absolute reaction rate theories and have consequence in the understanding of extended systems. This section reports the results of the photodissociation of $V(OCO)^+$ which demonstrates partial vibrational mode-specificity.

When a laser-induced plasma of solid vanadium is expanded supersonically in a carrier gas of He and 0.2 % CO_2 , a variety of $V_x^+(CO_2)$ cluster ions are formed, but, under typical experimental conditions, no VC^+ or VCO^+ ions are detected. The ion VO^+ is present but in the same amount regardless of whether a He/ CO_2 mixture or pure He is used in the ion source. This implies that the ensemble of ions spectroscopically probed in this work is comprised of electrostatic complexes and not high-temperature ion-molecule reaction products. Additional evidence for an electrostatically bound $V(OCO)^+$ may be derived from collision induced dissociation; only V^+ is detected as a CID fragment of $V(OCO)^+$.

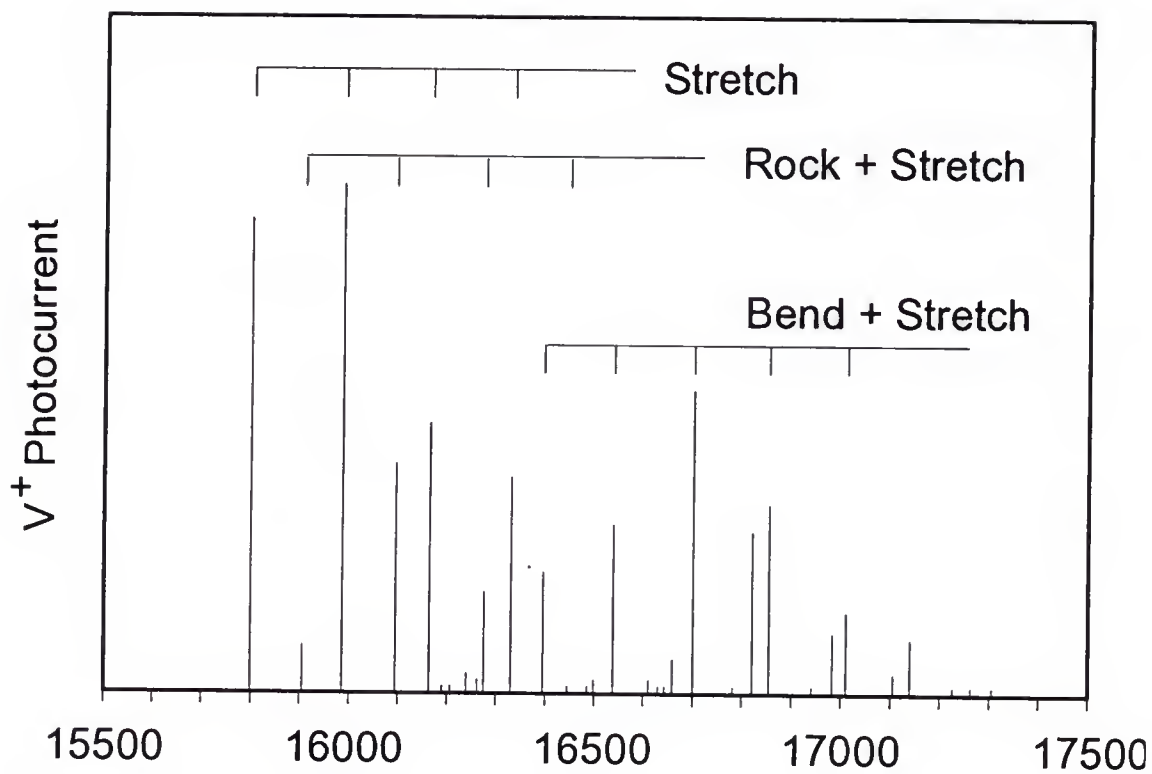


Figure 38. Stick Plot of $V(OCO)^+$ Photodissociation.

Stick plot of the photodissociation of $V(OCO)^+$ fragmenting into V^+ and OCO as a function of laser frequency. The relative intensities depicted are normalized to laser power and parent ion current to about 20%. The three prominent vibrational progressions annotated in the spectrum correspond to a pure stretching motion (marked stretch), a stretching progression in combination with a rocking of the CO_2 relative to the V^+ atom (marked rock+stretch), and a stretching progression in combination with a CO_2 bend (marked bend-stretch).

Photofragmentation of the $V(OCO)^+$ molecular ion in the visible shows sharp resonant absorption features and two distinct dissociation pathways: $V(OCO)^+ \rightarrow V^+ + CO_2$ and $V(OCO)^+ \rightarrow VO^+ + CO$. The excitation spectrum of this molecule appears quite similar to that of the electrostatically bound VAr^+ , VKr^+ and $V(H_2O)^+$ molecules which result from predissociation of a long-lived excited electronic state. The spectral breadth of the transitions observed in $V(OCO)^+$ places a lower limit to the lifetime of the photoexcited level at about 1 ps.

Figure 38 shows a stick plot representing the positions and intensities of the peaks in the photodissociation excitation spectrum of $V^+(OCO) \rightarrow V^+ + OCO$ in the range of 15 500 to 17 500 cm^{-1} . The relative peak intensities have been normalized to incident laser power and parent ion intensity and should be representative of the actual photodissociation cross section to about 20%. A progression in an excited state vibration is evident indicating a frequency of 196 cm^{-1} and an anharmonicity of 4.7 cm^{-1} . In addition, vibrational progressions of this mode in combination with two other modes (frequencies of 105 and 600 cm^{-1}) are seen.

The intensity distribution in the spectrum indicates only a moderate change in geometry of the molecule upon excitation, and, in comparison to the previously studied systems (VAr^+ , VKr^+ and $V(H_2O)^+$) both upper and lower states of $V(OCO)^+$ are

electrostatically bound. If this is the case, the vibrational modes of the CO_2 moiety might be considered separable from (two) modes arising entirely from the new electrostatic 'bond'. In accord with this idea, preliminary assignment of this spectrum places the origin at the reddest peak ($15\,800\text{ cm}^{-1}$), the $\text{V}^+-\text{(OCO)}$ stretching mode at 196 cm^{-1} and the $\text{V}^+-\text{(OCO)}$ 'rocking' motion at 105 cm^{-1} . The bending motion of the OCO moiety is observed then at 600 cm^{-1} which is reduced by 66 cm^{-1} from the gas phase value⁸². Estimation of the geometry of the system from classical electrostatics suggests that a distorted T-shape (C_s not C_{2v}) is the global minimum structure.

Unfortunately, spectral information is insufficient for rigorous determination of the geometry. The vibrational assignment of the V(OCO)^+ spectrum is also tentative and will be checked by spectroscopic shifts induced by isotopic substitution of the CO_2 and subsequent normal mode analysis.

Figure 39 shows that the photofragmentation excitation spectra of V(OCO)^+ to produce VO^+ or V^+ are identical in structure (to within our signal to noise). Thus, the V^+ and VO^+ photofragments not only arise from the same isomeric form of V(OCO)^+ but are the result of the unimolecular decomposition of the same excited electronic state. Moreover, the branching ratio for VO^+/V^+ production is dependent on the

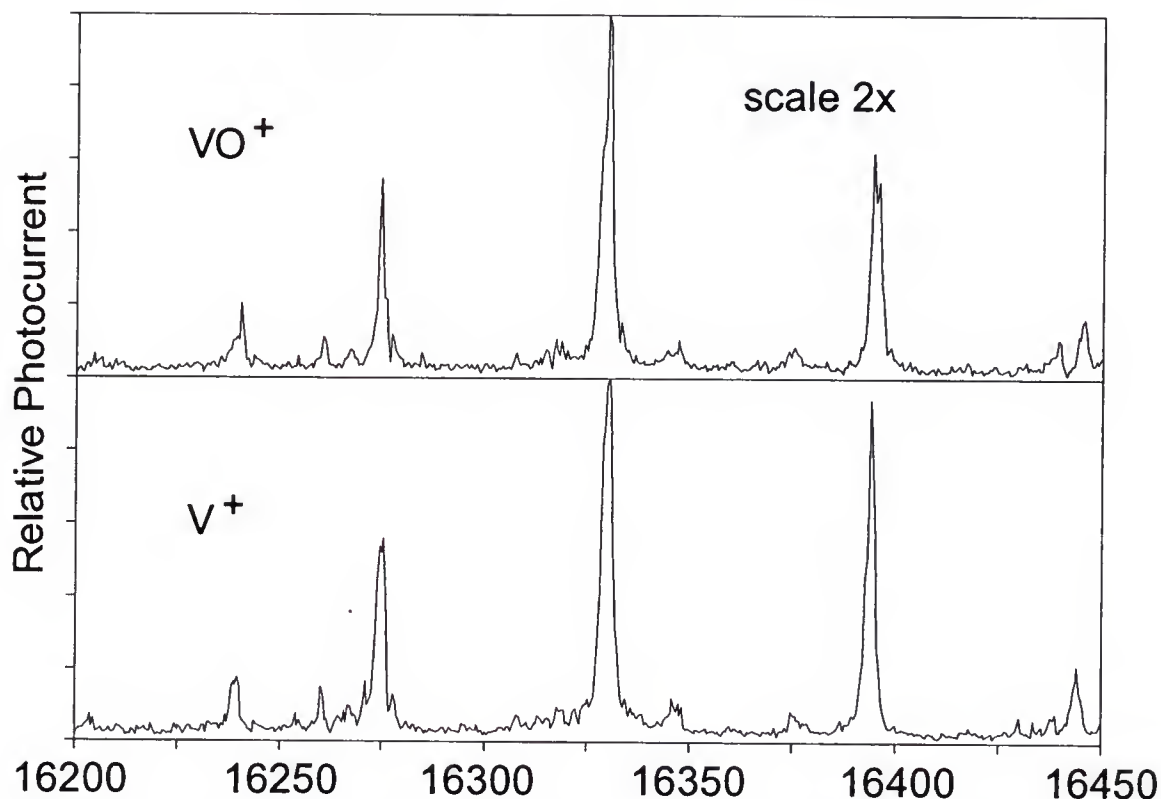


Figure 39. Photoexcitation Spectrum of $V(OCO)^+$.

The figure displays the photodissociation excitation spectrum of $V(OCO)^+$ in the visible region. The relative photofragment current (vertical axis) is plotted versus the incident photon frequency (horizontal axis) for the $V(OCO)^+ \rightarrow V^+ + CO_2$ (bottom curve) and $V(OCO)^+ \rightarrow VO^+ + CO$ (top curve) photofragmentation processes. The VO^+ product ion intensity has been multiplied by a factor of two to elucidate comparison of the spectra. Power dependence of these signals show that both fragmentation events follow a one-photon absorption by $V(OCO)^+$ and thus the two fragmentation processes proceed via the same photoexcited intermediate.

photoexcitation transition (note the bands at 16330 cm^{-1} and 16390 cm^{-1}).

Figure 40 shows this VO^+/V^+ branching ratio at fixed laser frequencies which correspond to strong transitions in the spectrum. The experimental data are shown as symbols with vertical error bars corresponding to two standard deviations of the mean. Each data point corresponds to 25 separate experimental trials.

The dissociation limit of $\text{V}(\text{OCO})^+ \rightarrow \text{VO}^+ + \text{CO}$ may be shown thermochemically to be 0.45 eV lower than that of $\text{V}(\text{OCO})^+ \rightarrow \text{V}^+ + \text{OCO}$ through the accurately known $\text{V}-\text{O}^+$ and $\text{O}-\text{CO}$ bond energies.^{83,1} The upward trend in the VO^+ production as a function of the internal energy of the parent molecule (Figure 40) indicates an energetic barrier for the production of VO^+ over that of V^+ . This barrier is not unexpected considering that strong covalent bonds must be made and broken to form the products. In analogy⁸⁴ with N_2O , the adiabatic dissociation of CO_2 to form ground state fragments is spin forbidden (the spin allowed dissociation is 2 eV higher than the adiabatic limit) which also may contribute to the existence of this barrier.

The non-monotonic increase of VO^+ production with energy indicates mode specificity in the fragmentation of $\text{V}(\text{OCO})^+$. Using the tentative vibrational assignment of the photodissociation spectrum above, it is suggestive to compare the branching ratio for VO^+/V^+ production for the origin band

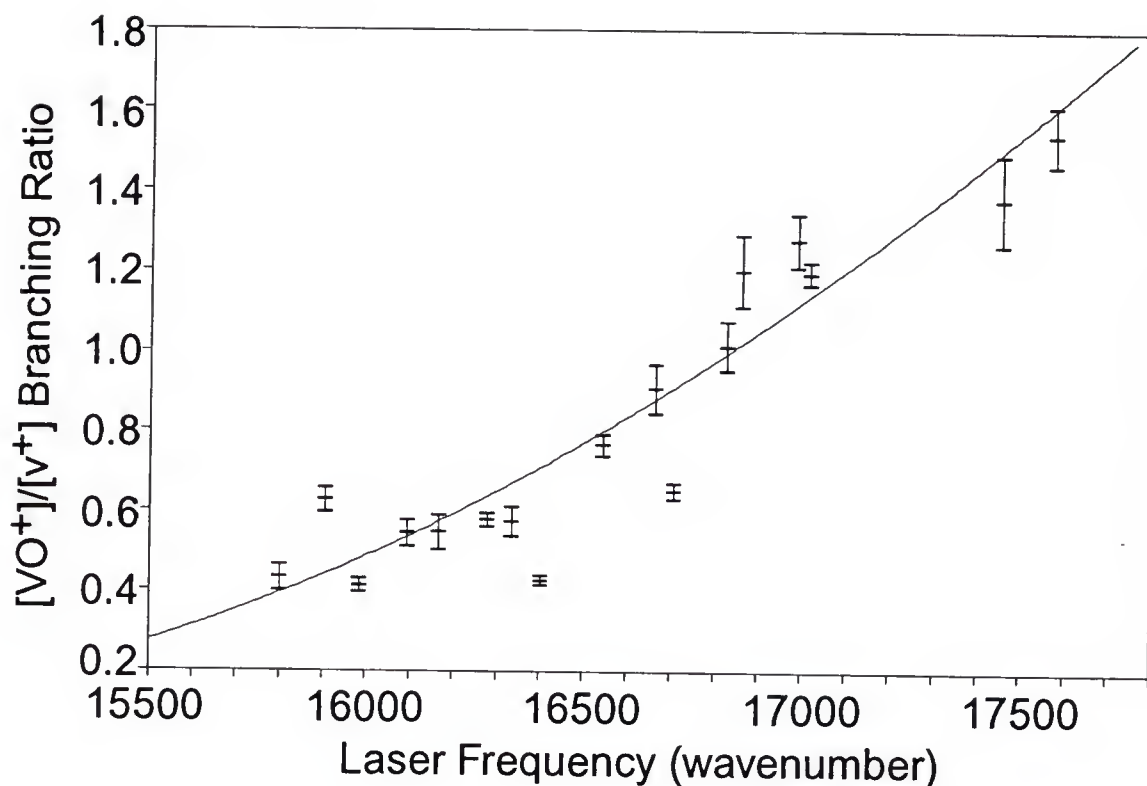
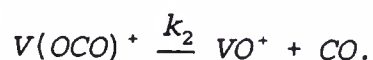
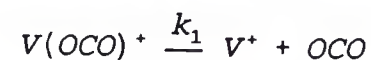


Figure 40. $[VO^+]/[V^+]$ Branching Ratio.

The figure displays the $[VO^+]/[V^+]$ branching ratio for absorption transitions of $V(OCO)^+$ as a function of excitation frequency. The branching ratio is measured by fixing the excitation source to the desired transitions and alternately determining V^+ and VO^+ product ion intensities. The symbols in the figure represent the experimental data with vertical error bars representing two standard deviations of the mean. The solid line is a RRK model of the data yielding an activation energy for the formation of VO^+ of 1.6 eV.

and the bands corresponding to one quanta of stretch, rock, and CO₂ bend. To within experimental error, the branching ratios corresponding to no vibrational excitation in the initially excited V(OCO)⁺ and excitation of one quanta of stretch or CO₂ bend are identical. However, excitation of one quanta of the rocking motion increases the relative VO⁺ production by 50% as might be expected because this motion would force the V⁺ and O atoms closer together. Excitation of more vibrational quanta in the initial state leads to a greater relative VO⁺ yield but with less obvious mode-specificity.

Nonetheless, the overall trend in the branching ratios seems to be describable by simple RRK^{85,86} theory (the solid curve in Figure 40). The chemical equation for the two photodissociation pathways are described as follows:



For two parallel and competing reactions one may equate the ratio of the rate constants to the ratio of cationic products,

$$\frac{k_1}{k_2} = \frac{[VO^+]}{[V^+]}$$

The ratio of products is easily measured from the fragmentation spectra of the parent ion. RRK theory states that for a systems of classical oscillators, *s*, the rate

constant is related the relative percentage of a system's total energy, E above some critical energy, E_0 :

$$k = A \left(\frac{E - E_0}{E} \right)^{s-1}.$$

For our treatment s is determined by the vibrational degrees of freedom. One may easily show that the branching ratio $[VO^+]/[V^+]$ is related to critical energy of each dissociation pathway,

$$\ln \frac{[VO^+]}{[V^+]} = \ln \frac{A_1}{A_2} + (s-1) \ln \left(\frac{E-E_1}{E-E_2} \right). \quad (38)$$

The variables E_1 and E_2 refer to the critical energy barrier for the two dissociation pathways. The total system energy is given by the transition frequency.

Under the assumption that the system $V(OCO)^+$ is electrostatically bound, there should be no reaction barrier to form the products of V^+ and CO_2 . The barrier is at the adiabatic dissociation limit which is estimated to be about 1 eV. One may adjust E_1 to minimize the error of the branching ratio. The calculated curve in Figure 40 places an estimate for the barrier in the process $V(OCO)^+ \rightarrow VO^+ + CO$ at 1.6 eV (37 kcal/mol). This determination is insensitive to the dissociation energy estimate of the electrostatically bound complex; a binding energy change of 25% corresponds to less than 5% change in derived activation energy.

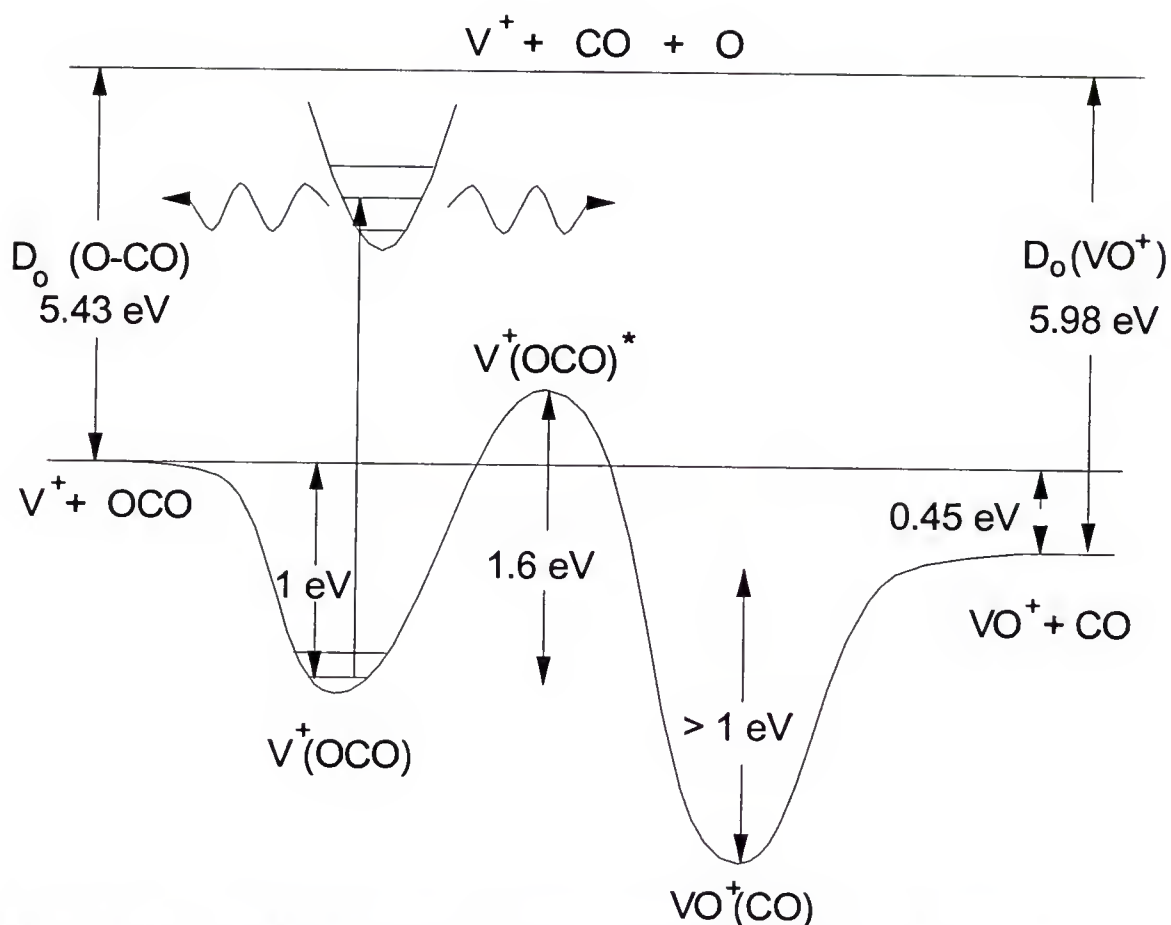


Figure 41. Energetics for Photodissociation of VCO_2^+ .

The figure displays the relative energy for isomers involved in the photodissociation of VCO_2^+ . The figure does not represent a reaction coordinate. Photoexcitation to quasi-bound vibrational levels of an excited state will subsequently dissociate along two distinct pathways; $VCO_2^+ \rightarrow V^+ + CO_2$ and $VCO_2^+ \rightarrow VO^+ + CO$.

Figure 41 displays the energetics in the photodissociation of VCO_2^+ . The initial state of species is not the global minimum. Presumably the $\text{VO}^+\text{-CO}$ species is energetically more stable than $\text{V}^+\text{-OCO}$, since the binding forces in the former system include permanent dipole interactions. Photoexcitation the $\text{V}^+\text{-OCO}$ isomeric form leads to a metastable electronic state which dissociates by two pathways.

The relative fragmentation rates of two dissociation pathways in the predissociation of electrostatically bound V(OCO)^+ have been measured as a function of vibronic state. The overall trend in this branching ratio places an estimate on the barrier to CO_2 bond activation in the presence of a transition metal but the predissociation does not appear to be entirely statistical.

Vibration Structure of Electrostatically Bound $\text{V}^+\text{-(H}_2\text{O)}$

A natural progression from metal-cation rare-gas diatomics is the study of metal cations with polyatomic ligands. The gas-phase analysis of molecular clusters provides a unique and powerful way to study the intermolecular interactions commonly found in condensed phases. Moreover, such model systems may be chosen judiciously to be of chemical interest and yet simple enough to be tractable, both in theory

and experiment. Recent research has successfully characterized inductive binding in the absence of covalent interactions in transition-metal rare-gas complexes. The analysis of these prototypical systems has motivated the study of more complex species exemplifying polyatomic intermolecular forces. In this section, we begin an analysis of the potential surface of a vanadium ion electrostatically bound to a H_2O molecule.

Vanadium atomic and cluster ions are generated by laser vaporization of the target metal under a high pressure (ca. 1 atm) of helium carrier gas. This flow is then supersonically and adiabatically expanded in a vacuum. When the carrier gas is spiked with ca. 0.3 mole percent water, aggregates of $\text{V}_x(\text{H}_2\text{O})_y$ form in the supersonic expansion. Source conditions determine the range of x and y and are optimized for the ion of interest, namely the ion-water pair.

Resonant one-photon dissociation of VH_2O^+ and its isotopic variants is observed to occur over the range of 15 200 to 18 500 cm^{-1} . Figure 42a shows a portion of the spectrum of VH_2O^+ . A series of nine prominent features with an interval of ca. 340 cm^{-1} , immediately suggests a single upper state vibrational progression with approximately this vibrational frequency. This progression begins with the reddest and most intense feature at 15 880 cm^{-1} and shows a monotonically decreasing intensity with increasing photon energy. The abrupt onset of the progression is indicative of

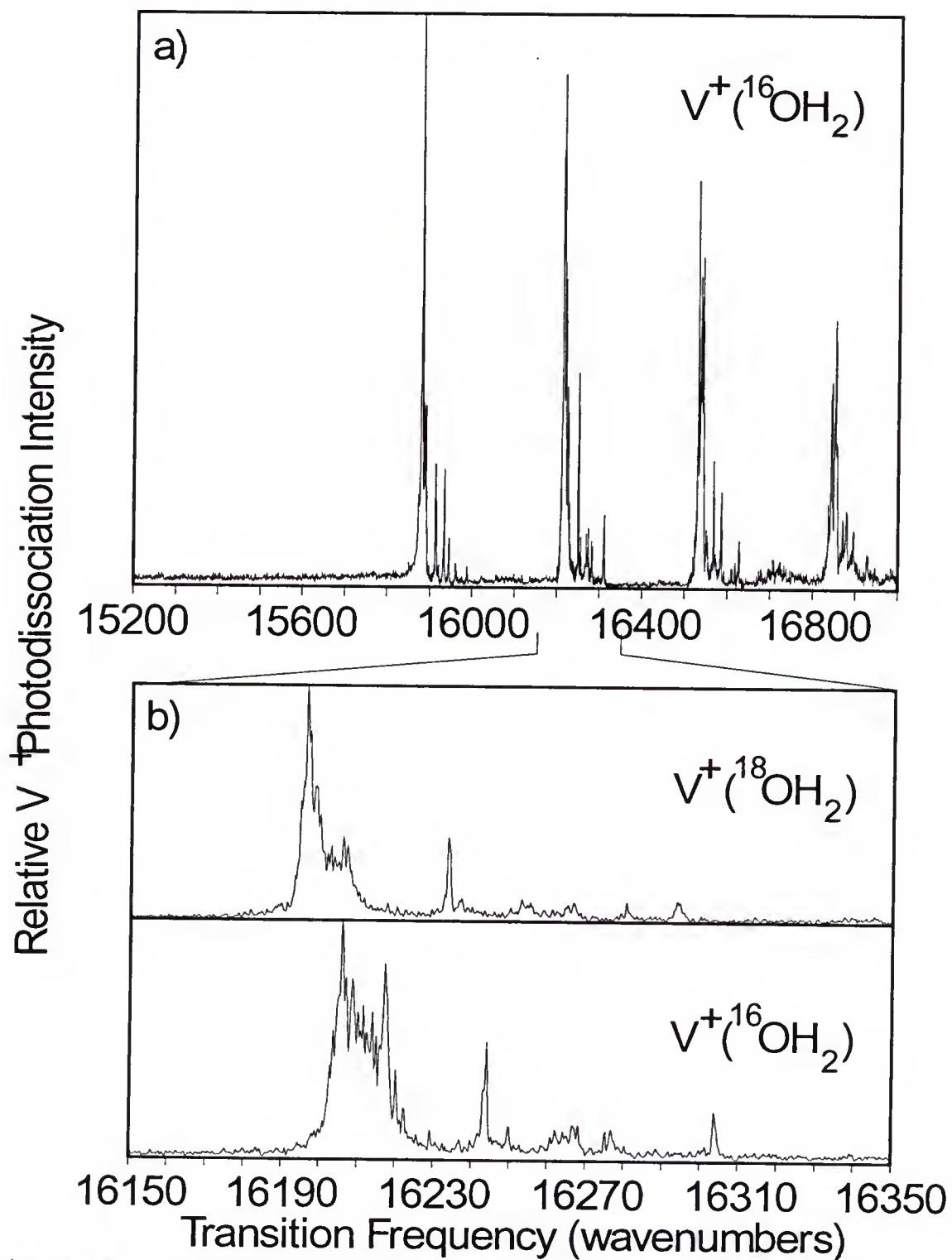


Figure 42. Resonant Photofragmentation Spectrum of $V(H_2O)^+$.

the origin of the electronic transition at this energy (isotopic analysis has confirmed this). No hot band transitions have been observed due to the extensive vibrational (and rotational) cooling the parent molecules suffer in the supersonic expansion. Furthermore, no high frequency vibrational intervals indicative of V-H stretching or H₂O normal modes are evident in this spectrum.

The spectrum of V(H₂O)⁺ may be casually compared to the resonant photodissociation spectra of VAr⁺ and VKr⁺, which also occur in a similar spectral region. These diatomics show a single predominant electronic transition in the visible which arises from a parity forbidden (⁵P [3d³4s] ← ⁵D [3d⁴]) transition in isolated V⁺. Due to the significant change in ionic radius of the V⁺ 3d³4s excited state relative to the 3d⁴ ground state, a long upper state vibrational progression is observed in the VAr⁺ and VKr⁺ spectrum. Both theoretical⁸⁷ and experimental evidence indicate little covalent nature in the binding of these ions.

Analysis of the V(H₂¹⁶O)⁺, V(D₂¹⁶O)⁺, V(HD¹⁶O)⁺, and V(H₂¹⁸O)⁺ isotopic species is used to determine the identity of the upper state vibrational progression and confirm the nature and structure of the carrier of the spectrum in Figure 42. Two plausible structures of the V(H₂O)⁺ ion exist: the electrostatically bound V⁺(OH₂) and the chemically bound inserted H-V-OH⁺ structure. The existence of the inserted structure has been suggested from analysis of guided ion beam

data.^{88,89} The insertion process has been asserted to have a small or zero activation barrier.

Several observations make it impossible for the H-V-OH^+ molecule to be the carrier of the spectrum reported here. First, the VHDO^+ spectrum should contain contributions from two distinct isomers, H-V-OD^+ and D-V-OH^+ . Only a single progression is observed in the VHDO^+ spectrum. Moreover, if the upper state progression is in fact a symmetric stretch or bending mode (the H-V-OH^+ is treated as a quasitriatomic here, i.e. the OH a quasiatom) a large isotope shift (ca. 25% of the fundamental) should be observed between the H-V-OH^+ , H-V-OD^+ , and $\text{H-V-}^{18}\text{OH}^+$ species; and between the D-V-OH^+ and D-V-OD^+ species. This is not observed. The only mode of the inserted structure which could exhibit a small enough isotope shift upon deuterium substitution of the lone proton to be consistent with experimental observation is the asymmetric stretch. A very small V-O stretching force constant (ca. 15% of a typical single bond) would have to be assumed to be consistent with a 340 cm^{-1} vibrational frequency for this mode which is inconsistent with the existence of a true covalent interaction. Thus, the H-V-OH^+ inserted structure is ruled out.

If the $\text{V(H}_2\text{O)}^+$ ion spectrum in fact arises from the electrostatically bound structure, then the upper state vibrational progression should represent the $\text{V}^+(\text{OH}_2)$ stretch, in analogy with the VAr^+ and VKr^+ spectra. $\text{V}^+(\text{OH}_2)$ is treated

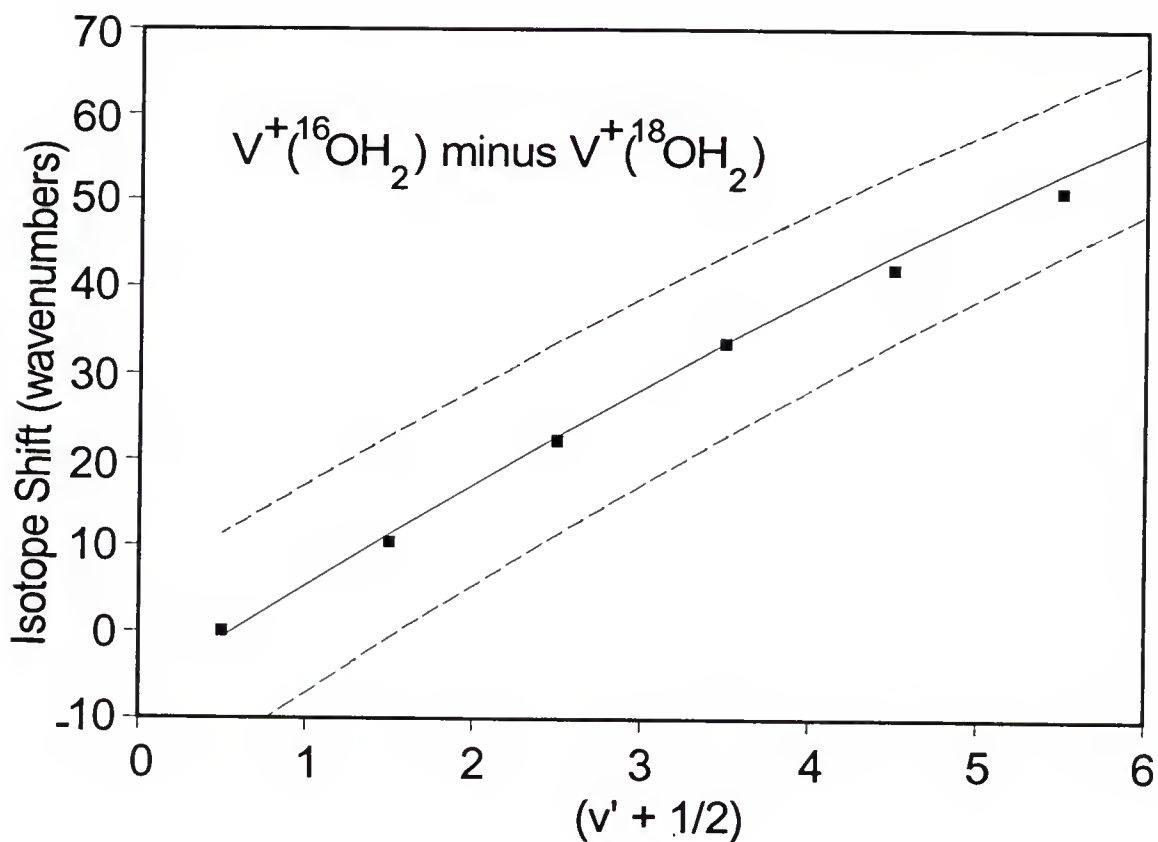


Figure 43. Isotope Shifts of $V^+(^{18}\text{OH}_2)$ minus $V^+(^{16}\text{OH}_2)$.

Isotope Shift of $V^+(^{18}\text{OH}_2)$ minus $V^+(^{16}\text{OH}_2)$. The observed (symbols) and calculated (curves) isotopic shifts versus upper state stretching quantum number for the first six bands of the spectrum in the previous figure. The solid curve is derived from the fit vibrational constants ($\omega_e' = 339 \text{ cm}^{-1}$, $\omega_e'' = 420 \text{ cm}^{-1}$, $\omega_e\chi_e' = \omega_e\chi_e'' = 4.5 \text{ cm}^{-1}$) assuming the electronic origin at $15\,880 \text{ cm}^{-1}$. Dotted curves are calculated by shifting the vibrational assignment by plus and minus one quanta.

as a quasi-diatomic and the masses of the V^+ and H_2O moieties are used to calculate^{45, 89} the $V^+(^{18}OH_2) - V^+(^{16}OH_2)$ isotope shift. These two species have the most similar band contours (see Figure 42b) and provide the most accurate isotope shift data.

Figure 43 shows the observed (symbols) and calculated (curves) isotope shift: $\nu[V^+(^{16}OH_2)] - \nu[V^+(^{18}OH_2)]$ versus excited state vibrational quantum number. The solid curve assumes a vibrational numbering which assigns the reddest observed band as the electronic origin and the dotted curves change this vibrational assignment by plus or minus one quanta. The upper state constants were derived from a fit to the standard form^{45, 89} of the $V^+(OH_2)$ band positions and yields $w_e' = 339 \pm 5$ and $w_e x_e' = 4.5 \pm 2 \text{ cm}^{-1}$, respectively with a root mean square deviation of 0.6 cm^{-1} . The ground state w_e'' was adjusted to fit the isotope shift data fixing $w_e x_e'' = w_e x_e'$ to yield $w_e'' = 420 \pm 75 \text{ cm}^{-1}$. The excellent agreement between observed and calculated shifts confirm the identity of the vibrational progression as the $V^+-(OH_2)$ stretching motion and the assignment of the origin band at $15\,880 \text{ cm}^{-1}$.

Figure 44 displays the photodissociation spectra for the $v' = 0$, and $v' = 1$ stretching bands of deuterated $V^+(\text{water})$ systems. The bands have been normalized to the largest feature in each case. The band substructure is apparently more sensitive to deuterium substitution than the isotopic substitution of oxygen (see Figure 42b). However, the photodissociation

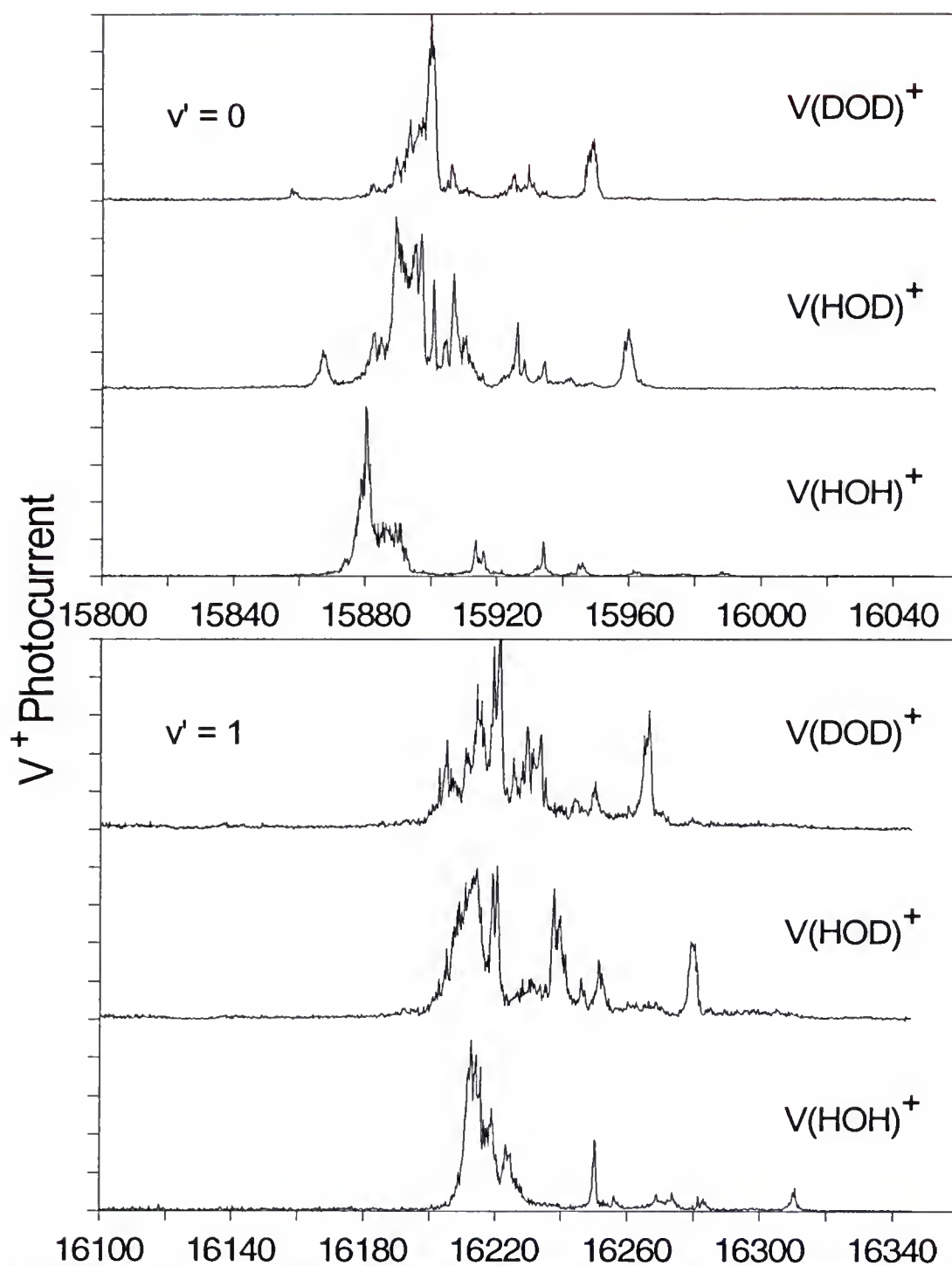


Figure 44. Photodissociation Spectra of Deuterated Isotopes of $V(\text{Water})^+$

spectrum for $V^+(HOD) \rightarrow V^+ + HOD$ indicates only one structure is present in the beam.

The electronic origin of the one-photon dissociation transition places an upper limit to the ground state adiabatic dissociation energy of 1.97 eV. This is consistent with theoretical⁹⁰ and experimental estimates of this dissociation limit of ca. 1.5 eV.

The spectroscopic characterization of an electrostatically bound ion-water complex has been demonstrated. The V^+-OH_2 stretching frequency has been determined in two different electronic configurations of the ion. These results represents a significant step toward the elucidation of electrostatic charge-solvent potential energy surfaces necessary to model condensed phase chemical reactions.

Resonant Photodissociation of $V(NH_3)^+$

The study of physisorbed molecules on a vanadium cation nucleation center have been very congenial with regard to photodissociation spectra. The separated atomic limit for the vanadium cation are believed to be same as in the rare-gas and previous polyatomic ligand cases. Figure 45 displays the photodissociation spectrum of $V(NH_3)^+$ dissociating to a cation with mass of approximately V^+ . However, the secondary mass resolution is not sufficient enough to distinguish between a

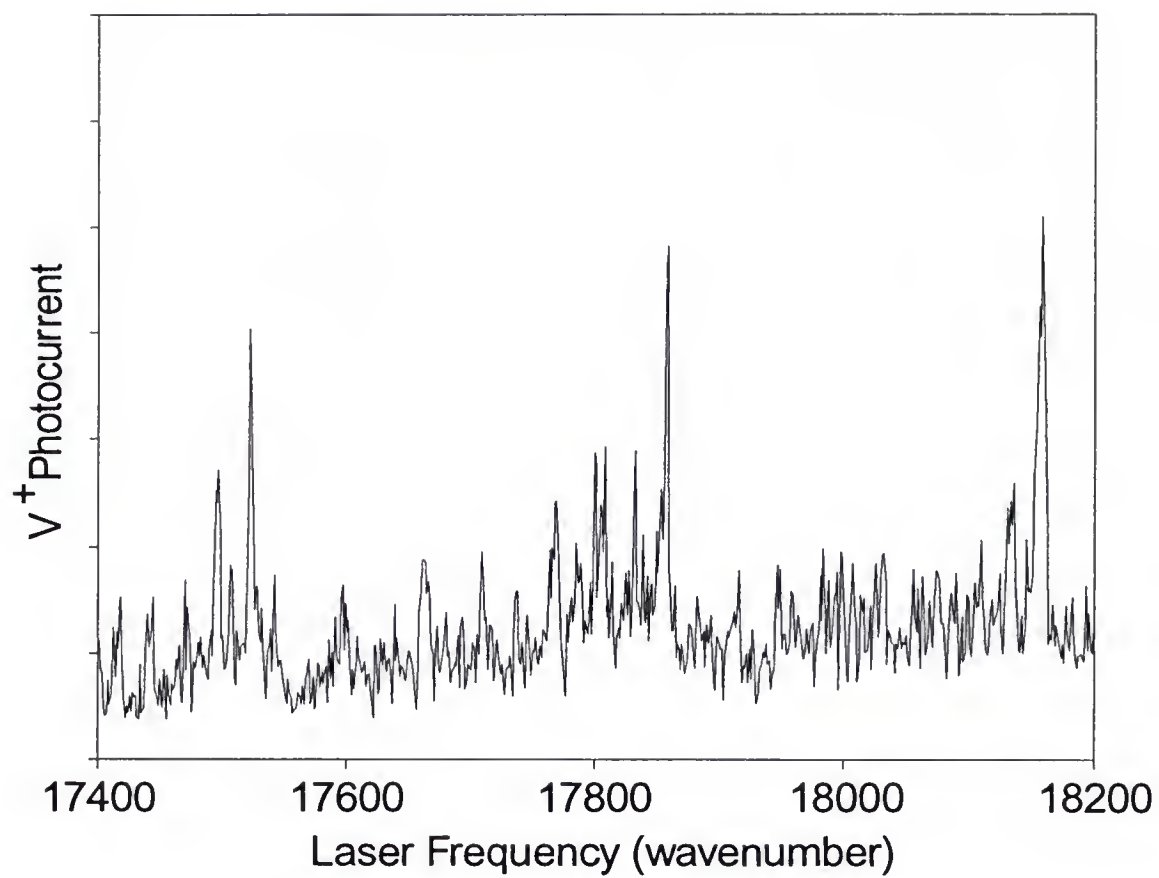


Figure 45. Resonant Photodissociation of $V(NH_3)^+$.

hydrated and bare cation. Nonetheless, a sector scan of the photofragments reveals an isolated peak center on 51 amu corresponding to the naked V^+ cation.

The spectrum consists of three bands of a progression which provide a vibrational frequency of ca. 318 cm^{-1} . The structure is not known unequivocally but is believed to be determined by the orientation of the permanent dipole in the ligand with the charge on the vanadium cation. This electrostatic reasoning would therefore place the nitrogen nearest the cation. Several smaller bands are seen to the red of the major progression and have a spacing of about 30 cm^{-1} . In an electrostatically bound system one would expect the vibrational modes of the uncomplexed ammonium ligand to not be significantly shifted. The vibrational frequency of the normal modes found in ammonia have been determined previously. The two symmetric modes are ca. 3300 cm^{-1} and ca. 930 cm^{-1} . The other modes are ca. 1600 cm^{-1} and ca. 3000 cm^{-1} .

This system has the smallest difference in ionization potential between the transition metal and the ligands of all the systems studied thus far and therefore significant covalent character may be found in the bonding forces. Currently, we have not looked for charge transfer.

Resonant Photodissociation of $\text{Cr}(\text{N}_2)^+$

The photodissociation spectrum of $\text{Cr}(\text{N}_2)^+$ displays a threshold to a diabatic threshold. This spectrum is similar in appearance to the threshold spectra of $\text{NiAr}^+ \rightarrow \text{Ni}^+ + \text{Ar}$ and $\text{CrAr}^+ \rightarrow \text{Cr}^+ + \text{Ar}$ discussed in the chapter on inductively bound diatomics.

Figure 46 displays the photodissociation spectrum for $\text{Cr}(\text{N}_2)^+ \rightarrow \text{Cr}^+ + \text{N}_2$ in the region of 16 900 to 17 300 cm^{-1} . This particular spectrum has a signal-to-noise level of ca. 2 to 1 due to the poor stability of the parent system. However a large and dramatic change is observed by the significant increase in Cr^+ photocurrent near 17 100 cm^{-1} .

As in the case of metal rare-gas diatomic molecules, one would not expect photodissociation into charged nitrogen molecules. The difference in IP is $\text{Cr}[6.763]^{37} - \text{N}_2[15.581]^1 = 8.818 \text{ eV}$. We confirmed this experimentally by looking for photodissociation into charged N_2^+ ; there was no production.

The onset to photodissociation presumably corresponds to some promotion of Cr^+ plus the adiabatic binding energy. We find that the only spin allowed transition in the cation within 5.8 eV of the ground state is ^6D at 12 148.0 cm^{-1} . Thus, the adiabatic dissociation energy is given by the difference of diabatic threshold and the separated atomic limit as $0.61 \pm 0.4 \text{ eV}$. The uncertainty in the adiabatic dissociation limit

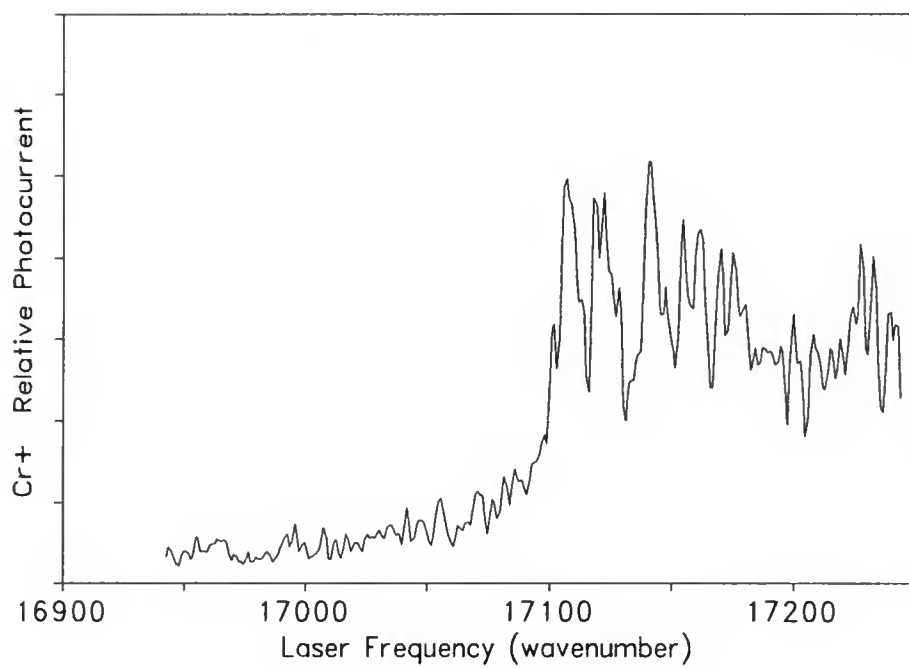


Figure 46. Photodissociation Threshold for $\text{Cr}(\text{N}_2)^+ \rightarrow \text{Cr}^+ + \text{N}_2$.

is a consequence not knowing the exact J state of the Cr^+ ion in promotion.

Dissociation into a vibrationally excited state of N_2 is a possibility. The molecular vibrational frequency is 2359 cm^{-1} or 0.292 eV .⁽¹⁾ Excitation of one quanta of the nitrogen stretch would lower the predicted dissociation energy to ca. 0.318 eV . These values may be compared to the theoretically determined equilibrium dissociation energy of 0.53 eV . The theoretical number agrees well with the experimental binding energy of 0.61 eV . Recall that the ab initio calculations of binding energies for metal rare-gas diatomics are consistently 20% lower than experimental.

Unfortunately, the experimental information is not sufficient to determine the electrostatic vibrational frequencies or the configuration of the electrostatically bound system. However, the results of ab initio calculations predict that the predominant interaction is charge-induced quadrupole; CrN_2^+ is expected to be linear due to the negative quadrupole moment.

Resonant Photodissociation of $\text{Ca}(\text{N}_2)^+$

Another nitrogen containing system that we have studied is $\text{Ca}(\text{N}_2)^+$. The photodissociation spectrum for this molecule is displayed in Figure 47. The production of Ca^+ is monitored as a function of incident laser frequency. A very

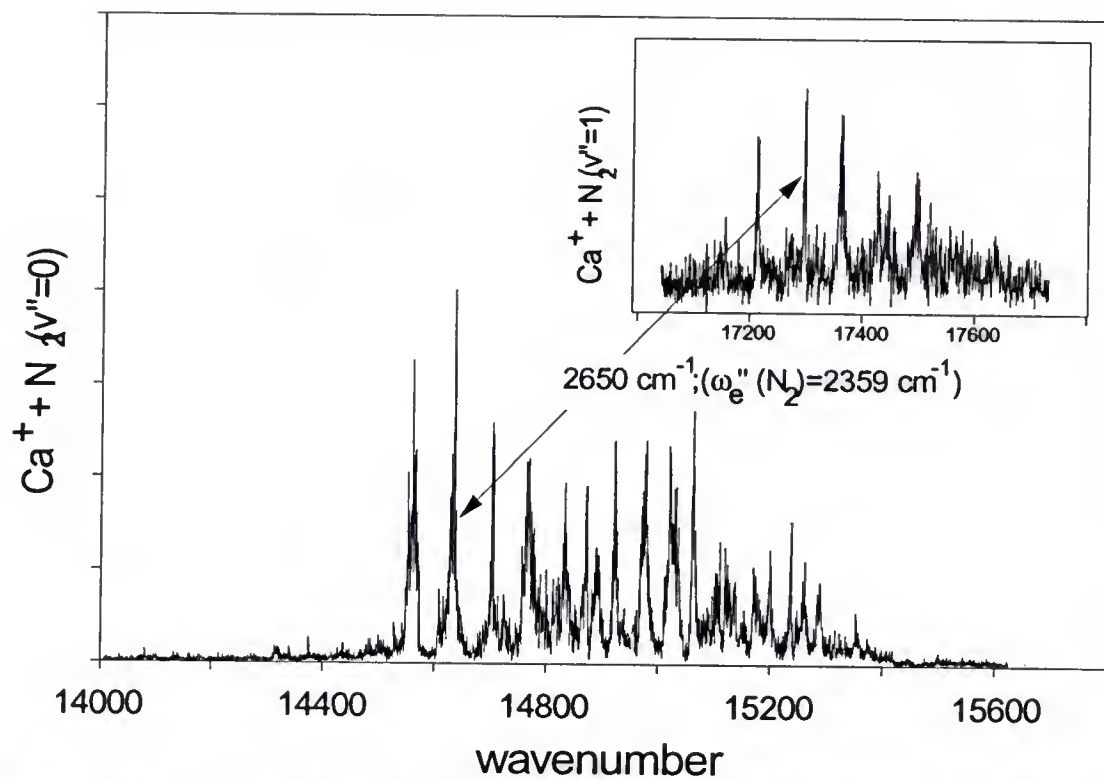


Figure 47. Vibrationally Excited Photofragments of Ca(N₂)⁺.

complicated photoexcitation spectrum is observed in the region of 14 400 to 15 400 cm^{-1} . A vibrational progression ends abruptly going toward the red at ca. 14 570 cm^{-1} . This has been assigned to the origin band.

For the cation of calcium there is only one possible atomic state in the vicinity of the spectroscopic region; 2D which has two J components corresponding to 13 650 and 13 710 cm^{-1} . The 60 cm^{-1} spin orbit splitting is similar to the vibrational spacing dominant in the progression. The complicated nature of the spectrum may be due to this spin-orbit component. Also, the molecule will have more than one low frequency vibrational mode which may be seen as a separate vibrational progression or a series of combination bands.

This particular molecule displays a progression built upon an excited state of the nitrogen molecule in the wavelength region of 17 100 to 17 700 cm^{-1} (see inset of the figure). The nitrogen excited progression is shifted from the primary progression by 2650 cm^{-1} which may be compared to the molecular nitrogen stretch of 2359 cm^{-1} . In both regions of the spectrum only Ca^+ is observed as a photodissociation product.

We may speculate as to the configuration of system. The author believes the system is linear. A T-shaped system would probably not account for the increase in vibrational frequency. If anything, the vibrational frequency should go down due to the electron withdrawal along the nitrogen bond

axis. A linear configuration would however account for the increase in frequency. Here, the observed vibrational frequency would correspond to an approximate symmetric mode localized in the nitrogen stretch. The added electrostatic bond would require additional energy to excite the approximate nitrogen mode.

The electronic origin is to the blue of the separate atom limit and implies that the ground state is bound by more than the excited state. One may set as a lower limit the dissociation energy of the ground state by the range of observed vibrational transitions of 0.1 eV. This will set a lower limit to the adiabatic binding energy of 0.217 eV.

METAL-METAL SYSTEMS



Transition metal clusters have drawn the interest of many theorists and experimentalists because of the central role these species play in the expansion of predictive chemistry beyond the main group elements. Transition metal-containing systems are also of significant importance as catalysts. At present, however, the nature of metal-metal bonding is poorly understood. Experiment has provided insufficient conclusive detail about the nature of transition metal clusters (or their ions) to significantly affect theory, and ab initio theory seems to be taxed to its limits in the description of even the simplest transition metal dimers.

Perhaps the single most important characteristic of a diatomic system is its bond energy. High temperature equilibrium studies have provided thermodynamically derived metal-metal bonds strength in several transition-metal systems.^{91,92} For a recent review of neutral transition metal diatomics, see Morse.⁽²⁾ Unfortunately, no such extensive literature exists for transition-metal diatomics in non-zero

charge states. The bonding in charged species is at least as interesting as the neutrals and comparison of the nature of different charge states should provide insight into orbital contraction and its effect upon s-d hybridization. In this Chapter will present the spectroscopic data for three cationic metal dimers, Ni_2^+ , Cr_2^+ , and Ca_2^+ .

Recent results from collision-induced dissociation of Ni_2^+ have determined the bond dissociation energy at 2.08 ± 0.07 eV.⁹³ The neutral diatomic binding energy has been spectroscopically established at 2.07 ± 0.01 eV.⁹⁴ Coupling this information with the appearance potential of Ni_2^+ in a mass spectrometer predicts the binding energy as 3.3 ± 0.2 eV,⁹⁵ a > 1 eV difference in these two experiments. Theoretical determinations are no less incongruous. The theoretical calculation of Upton and Goddard⁹⁶ predict a bond dissociation energy of 4 eV. While Bauschlicher et al⁹⁷ predict a dissociation energy, D_0 of 1.82 eV. In this section we will look at photodissociation spectra of Ni_2^+ and also introduce a novel technique for determining the bond dissociation energy of Ni_2^+ through the photodissociation of its van der Waals adduct.

Figure 48 shows the low mass portion of the TOF mass spectrum obtained with the energy analyzer set to transmit 1.45 keV (single positive charge) ions. This figure represents the stable (lifetime > 1 ms) positive ion distribution emanating from the source operating with 'pure'

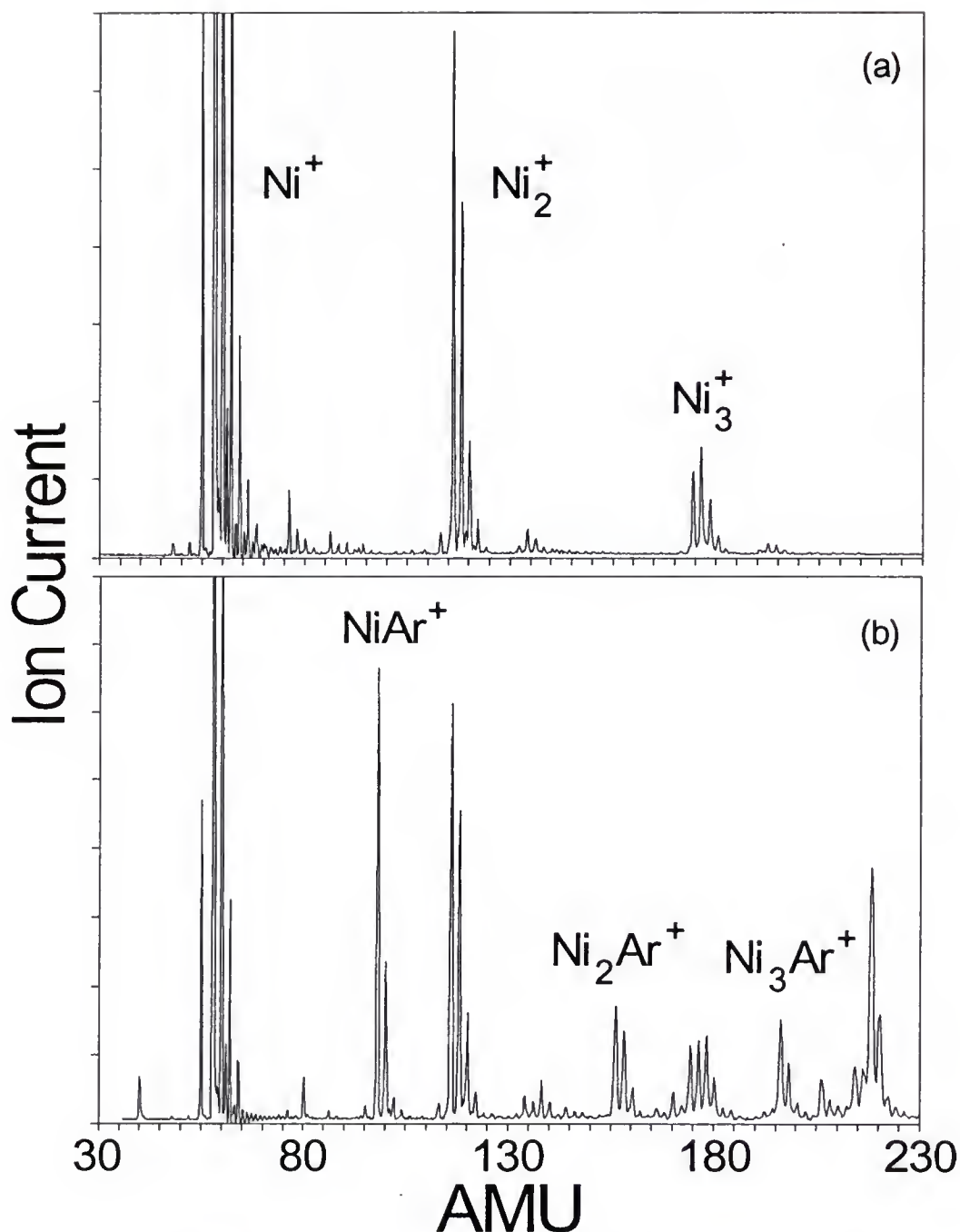


Figure 48. Mass Spectrum of Argon Seeded Nickel Beam. The figure displays time-of-flight mass spectrum of the positive ion distribution generated in a laser-driven nickel plasma seeded in a supersonic expansion. The top panel corresponds to an expansion in a pure He carrier gas. The bottom panel corresponds to an expansion in ca. 2% Ar/He gas mixture. Note the appearance of Ni_xAr_y^+ with this carrier gas.

He as a carrier gas (Figure 48a) and ca. 2% Ar/He (Figure 48b). Negatively charged ions are observed under the same source conditions, but at no time has any evidence for stable multiply charged species been discerned. Due to the chemical reactivity of small transition metal clusters and their positive ions, unavoidable contamination of the ion source with H_2O , CO_2 , hydrocarbons, etc. leads to the production of partially ligated metal cluster ions such as M_xO^+ which are clearly evident in the mass spectra in Figure 48a. Figure 48b reveals that presence of argon in the source produces Ar^+ and Ar_2^+ as well as species of the series M_xAr^+ and M_xAr_2^+ .

The M_xAr_y^+ ions are particularly interesting because they provide a spectroscopically important analog to the bare M_x^+ cluster itself. Since the ionization potential of Ar (15.755 eV) is much higher than that of the nickel atom (7.633 eV) which in turn is higher than that of the nickel clusters (<7 eV), we expect the nature of M_xAr_y^+ to be that of $\text{M}_x^+(\text{Ar})_y$, i.e., polarized rare-gas atoms loosely bound to the electric field of the relatively unperturbed charged metal cluster. An estimation of the binding energy of the Ar atom to the metal ion might be made by comparison with the binding energy of another charge induced-dipole bound complex, $\text{H}_3^+.\text{Ar}$, which has recently been characterized,⁹⁸ and its binding energy has been estimated to be approximately 0.29 eV. We would therefore expect the binding of Ar to Ni_2^+ , for instance, to

be of this order. The binding energy of Ar to larger metal cluster ions would be expected to be a decreasing function of cluster size because the electric field at the 'surface' of a larger cluster is weaker than that of a smaller one. For a roughly spherical cluster, one would expect the binding energy to be proportional to $x^{-4/3}$ (where x is the metal atom count). The binding energy of additional argon atoms to a fixed size metal cluster would be expected to decrease only slightly until the Ar atoms 'cover' the metal ion and thus complete the first 'solvation shell' at which point the binding energy should drop drastically. The concept of a solvation shell for these gas-phase ions has been supported by the observation of the anomalously large abundance of particular sized clusters (for example NiAr_4^+ as can be seen in the figure in the ion beam under somewhat different source conditions, implying a special kinetic or energetic stability of these molecules.

Our picture of the nature of the M_xAr_y^+ molecule has another important consequence: The UV-Visible electronic absorption spectrum of the M_xAr_y^+ ion should be almost the same as the bare M_x^+ ion itself. However, all the M_xAr_y^+ levels accessed by visible and UV photoabsorption are above the dissociation threshold to $\text{M}_x^+ + \text{Ar}$. This means that the spectrum of the M_xAr_y^+ ion will be lifetime broadened with respect to the M_x^+ ion, but the former's one-photon absorption may be detected with near unit efficiency in a tandem mass spectrometer.

How the $M_xAr_y^+$ ion photofragments will depend on exactly what photon energy is absorbed. Consider the photodissociation of Ni_2Ar^+ , for example. If the photoexcited Ni_2Ar^+ has internal energy above its lowest dissociation threshold, that into Ni_2^+ and Ar, and below all other dissociation limits, then all the Ni_2Ar^+ will fragment into $Ni_2^+ + Ar$, and no other products will be observed. The rate at which the unimolecular decomposition occurs may depend strongly upon the detailed nature of the photoexcited state but would be expected to be somewhat shorter than the timescale for secondary mass analysis in this experiment (10^{-5} s). However, if the internal energy of the Ni_2Ar^+ is somewhat larger than the energy required to break the Ni-Ni bond, then one would expect facile photodissociation of Ni_2Ar^+ into $Ni^+ + Ni + Ar$. Therefore, the observation of the products formed from the photodissociation of Ni_2Ar^+ as a function of photon energy allows the Ni_2^+ bond dissociation energy to be estimated.

Figure 49 shows the laboratory kinetic energy spectrum of Ni_2Ar^+ which has been photoexcited after initial TOF mass selection but before entering the energy analyzer. The entrance and exit apertures of this analyzer have been opened sufficiently to give maximum detection efficiency for parent (Ni_2Ar^+) and daughter (photofragment) ions and maintain an energy resolution of approximately 8 (mean energy/energy FWHM). Since the greatest possible center of mass kinetic

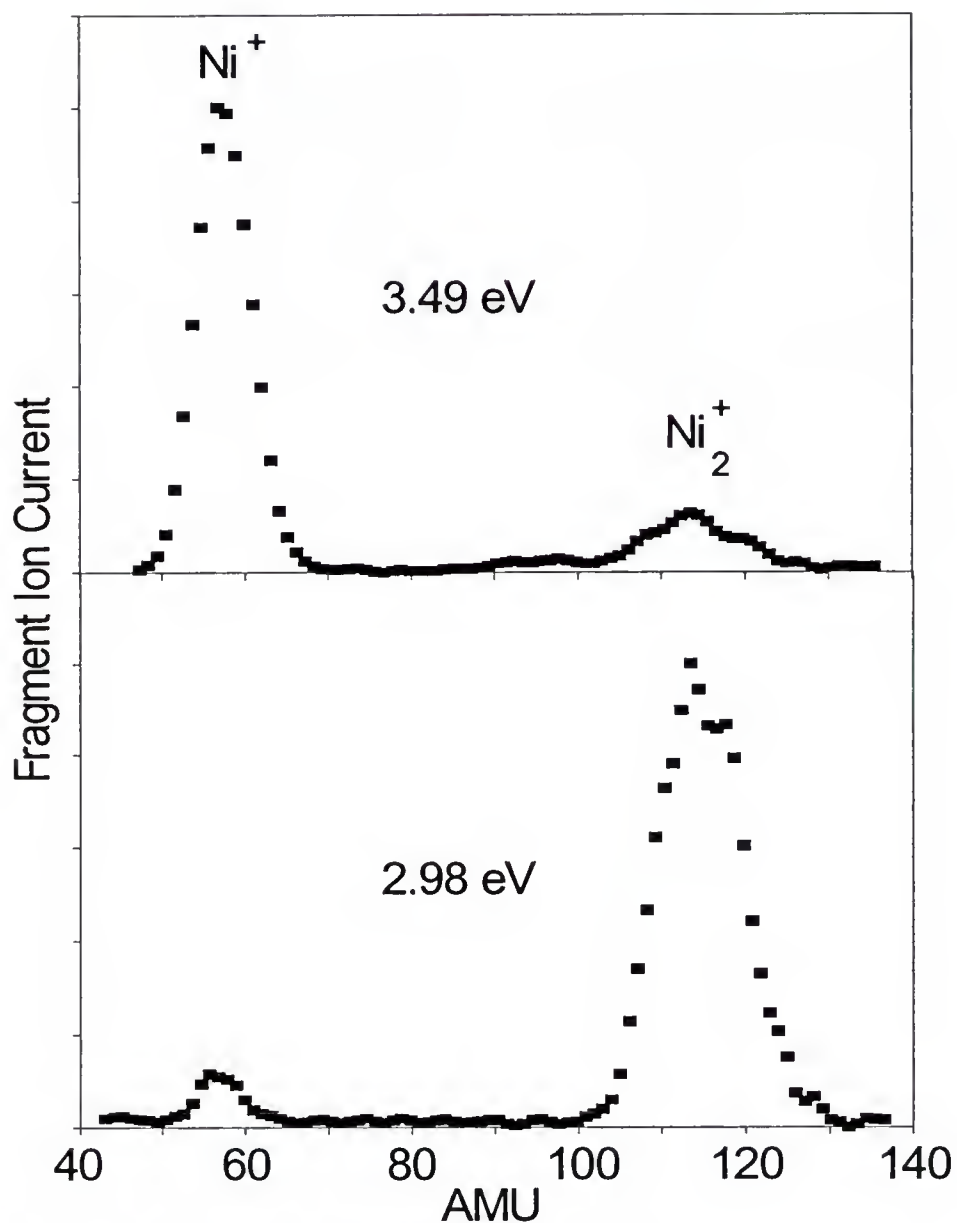


Figure 49. Photofragmentation of Ni_2Ar^+ .

The figure displays the kinetic energy analysis of photoexcited Ni_2Ar^+ . For a photoexcitation energy of 3.49 eV, Ni^+ is the dominant fragment. At 2.98 eV, Ni_2^+ is the dominant fragment. The reversal of the major photofragment channel indicates that the bond energy of Ni_2^+ is between 2.98 and 3.49 eV.

energy release in the photofragmentation of our parent ion would be entirely veiled by the energy analyzer resolution, the lab kinetic energy spectrum may be considered a secondary mass spectrum where the ratio of parent to daughter kinetic energies is equal to the ratio of parent to daughter masses. Taking these considerations and the parent ion beam energy of 1.45 keV into account, the ordinate axis has been converted from lab energy into a mass axis. The feature in Figure 49 have been labeled as to their identities as Ni^+ and Ni_2^+ 58 amu and 116 amu, respectively.

The relative abundance of the photoproduct channels shown in the figure may be interpreted as follows: At 3.0 eV photon energy (416 nm generated by Stokes shifting the Nd:YAG third harmonic in H_2 ; 5 mJ/cm²; bottom panel of Figure 49), one-photon excitation of the parent Ni_2Ar^+ molecule does not provide sufficient internal energy to break the Ni-Ni bond. However, a small but almost unavoidable fraction of the parent ensemble absorbs two or more laser photons (>6.0 eV) and photofragments into $\text{Ni}^+ + \text{Ni} + \text{Ar}$. At 3.5 eV (355 nm Nd:YAG third harmonic, 5mJ/cm²; top panel in Figure 49), most of the Ni_2Ar^+ photofragments into $\text{Ni}^+ + \text{Ni} + \text{Ar}$, indicating one laser photon is sufficient to cleave the metal ion itself. However, a small fraction of the Ni_2Ar^+ ensemble fragments into $\text{Ni}_2^+ + \text{Ar}$ at this photon energy. The dissociation limit of Ni_2^+ might lie slightly above 3.5 eV, but most of the molecules in the ensemble have enough thermal excitation to

photodissociate anyway. Or, the optically excited $(\text{Ni}_2^+)^*\text{Ar}$ is 'caged' by collision of an outgoing Ni or Ni^+ colliding with the Ar atom, resulting in a translationally hot Ar atom and a bound Ni_2^+ ion. The latter caging effect is presently being investigated in our laboratory by the use of increased kinetic energy resolution in the photofragmentation detection. Either explanation, however, would indicate 3.5 eV to be rather close to the dissociation threshold of Ni_2^+ .

Measurement of the Ni_2^+ bond dissociation threshold by this method yields a reasonable result, $3.0 < D_0(\text{Ni}_2^+) < 3.5$ eV. As discussed in the beginning of this section, our determination is in agreement with the previous estimates of Kant of $D_0(\text{Ni}_2^+) = 3.3 \pm 0.2$ eV. However, it is at odds with that determined by Armentrout et al of 2.08 ± 0.07 eV.

Further insight into the nature of the bonding interaction of Ni_2^+ may be found by direct spectroscopic probing of the uncomplexed ion. Figure 50 shows the Ni^+ ion current arising from the laser photodissociation of $\text{Ni}_2^+ \rightarrow \text{Ni}^+ + \text{Ni}$ as a function of frequency on the interval from 16 940 to 16 980 cm^{-1} . The top trace of this figure is the spectrum arising from $^{58}\text{Ni}_2^+$ and the bottom trace is the simultaneously acquired $^{60}\text{Ni}^{58}\text{Ni}^+$ spectrum. These data were recorded in a single sweep of 0.08 cm^{-1}/s at a laser fluence of ca. 3 mJ/cm^2 . A small continuous photodissociation is evident between the sharp features which is attributable to non

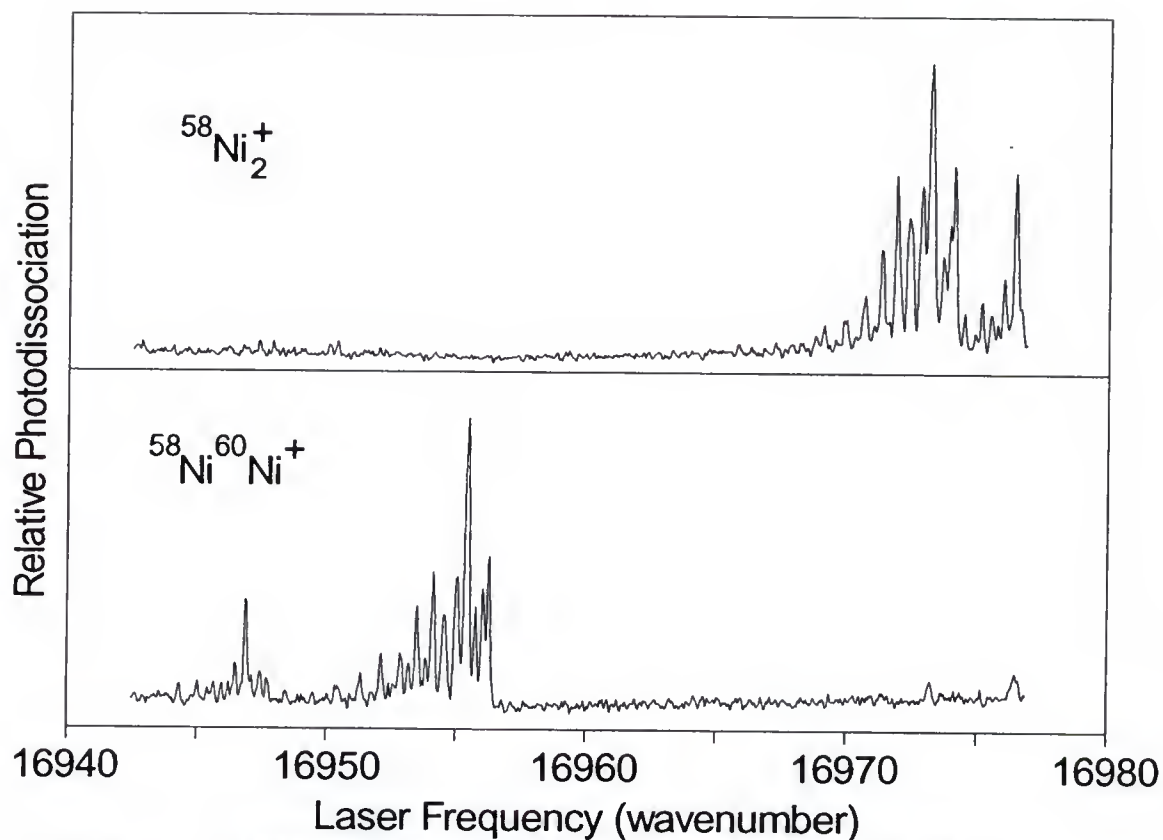


Figure 50. Resonant Two-Photon Dissociation of Ni_2^+ .

The figure displays the resonant 2-photon dissociation spectrum of Ni_2^+ over the region 16 940 to 16 980 cm^{-1} . The upper panel of this figure is the spectrum arising from the $^{58}\text{Ni}_2^+$ isotope and the bottom panel is the simultaneous acquired $^{58}\text{Ni}^{60}\text{Ni}^+$ spectrum. The vertical scale in the lower spectrum has been multiplied by 2.6 to account for the naturally less abundant $^{58}\text{Ni}^{60}\text{Ni}^+$ isotope. The spectrum displays a partially rotationally resolved band for the $B \leftarrow X$ state.

Table 15. Line Positions for R2PD of Ni_2^+ (cm^{-1}).

A-X	$^{58}\text{Ni}_2^+$		$^{58}\text{Ni}^{60}\text{Ni}^+$	
	freq.	o-c	freq.	o-c
18	16346	-0.4	16321	-0.4
19	16506	0.5	16479	-0.3
20	16664	0.1	16637	0.3
21	16821	0.3	16793	0.0
22	16976	-0.7	16947	-0.5
23			17101	0.0
24	17285	0.2	17253	0.0

B-X	$^{58}\text{Ni}_2^+$		$^{58}\text{Ni}^{60}\text{Ni}^+$	
	freq.	o-c	freq.	o-c
8	16317	-0.2		
9	16484	-0.2	16469	-2.0
10	16649	0.4	16633	-1.0
11	16812	0.6	16796	-0.5
12	16973	-0.2	16955	-1.0
13	17132	0.0	17114	-0.6
14	17289	-0.4	17270	-0.2
15	17444	-0.5	17425	0.4
16	17599	0.6	17581	3.8

C-X	$^{58}\text{Ni}_2^+$		$^{58}\text{Ni}^{60}\text{Ni}^+$	
	freq.	o-c	freq.	o-c
8	16424	0.4		
9	16581	-0.7	16568	
10	16740	0.4	16726	

-resonant multiphoton absorption. The peak of the resonant features correspond to less than 1% depletion of the parent ensemble at this laser fluence. The vertical scale in the panel has been multiplied by 2.6 to allow comparison of the spectrum of the naturally less abundant $^{60}\text{Ni}^{58}\text{Ni}^+$ to that of $^{58}\text{Ni}_2^+$.

The sharp photodissociation features in Figure 50 exhibit a non-linear laser fluence dependence indicating that a two-photon absorption leads to the production of Ni^+ from Ni_2^+ . This is consistent with the recent determination of the binding energy of Ni_2^+ from the photodissociation of Ni_2Ar^+ of $3.0 < D_0(\text{Ni}_2^+) < 3.5$ eV, i.e. the absorption of two photons at this frequency deposits 4.21 eV of energy into the molecule which is sufficient to dissociate the Ni-Ni⁺ bond. Sharp R2PD features have been observed in this study up to photon energies of 2.95 eV confirming the lower limit to the dissociation of Ni_2^+ at ca. 3.0 eV.

Figure 50 represents only a small portion of the frequency range that resonant dissociation occurs in the Ni_2^+ ion, but this plot is representative of the nature of the data recorded. Vibrational progressions in several (at least six) different electronic transitions have been observed in the visible region of which vibronic bands from two such transitions are displayed in the figure. Below 17 450 cm^{-1} (2.16 eV), the Ni_2^+ spectrum is relatively simple and unperturbed in appearance. However, the R2PD spectrum becomes

more congested and less amenable to analysis above this energy. The change in the nature of the spectrum is not accompanied by a change in absorption cross section nor a discernable change in the linewidth of the spectral features.

This figure displays two vibronic bands (with partially resolved rotational structure) belonging to two different electronic transitions in the Ni_2^+ ion. Note that the $^{60}\text{Ni}^{58}\text{Ni}^+$ spectral features are shifted to lower energy with respect to the corresponding features in $^{58}\text{Ni}_2^+$ indicating a large upper state vibrational quantum number. These isotope shifts are used to assign an absolute vibrational numbering to the vibronic bands in Ni_2^+ . The two prominent bands in Figure 50 have been assigned by this method to the (18,0) band of the A-X transition and the (8,0) band transition of the B-X transition. Positions of other bands belonging to these electronic transitions and one other (the C-X system) are listed in the table. The nomenclature for the three assigned excited states in this study as the A, B, and C states reflects only the order of their electronic origins and is not meant to imply that the so called A state is the lowest lying excited state nor that no undetected states lie between the origins of the assigned states. For the table, the frequency of the most intense feature in the vibronic band is taken as the vibronic band origin.

All the bands observed in this study are red degraded indicating a longer equilibrium internuclear distance in the

excited states than the ground state. The rotational structure of these bands is only partially resolved at the current resolution and firm assignment of the ground and excited state electronic symmetries has not yet been made. No vibrational or electronic hot band spectra have yet been obtained due to the low internal excitation of the parent Ni_2^+ ion prior to photoabsorption.

The table also lists the residuals to the least squares fit of the vibronic bands to the standard formula

$$E(v) = T_{\infty} + w_e(v+1/2) - w_e x_e(v+1/2)^2$$

from which the constants T_{∞} , w_e , $w_e x_e$, $w_e y_e$ are derived. The zero of energy for this fit and all the following discussion is taken as the zero-point level of the ground electronic state of the molecule.

The table lists the molecular constants of $^{58}\text{Ni}_2^+$ derived from the fit of the data in the table to the above equation. No ground state molecular constants have yet been obtained due to the absence of any apparent hot bands.

The discussion of the bonding character of Ni_2^+ focuses on the comparison to its neutral variant, Ni_2 . The interaction of two ground state $3d^8 4s^2$ Ni atoms is not expected to form a chemical bound Ni_2 as the radial extent of the 3d orbitals is significantly smaller than that of the 4s and the overlap of the $4s^2$ closed subshells will be repulsive. However, promotion of both Ni atoms to a $3d^9 4s$ configuration (promotion energy 0.03 eV) will lead to a favorable overlap of

the half filled 4s shells leading to a single 4s sigma bond similar to that of in the alkali metals or H_2 . The weakly interacting 3d holes will lead to a manifold of 100 electronic states, all essentially of the same bonding character and nearly isoenergetic. This picture of exclusively s-s bonding in the low-lying states of Ni_2 is supported by ab initio calculation⁹⁹ and experimental data^{100,101}. Resonant two-photon ionization spectroscopy has placed the ground state dissociation energy of Ni_2 at 2.07 eV and the equilibrium bond length at 2.20 Angstroms.

In contrast, the R2PD spectrum of Ni_2^+ shows that this species has a much more sparse electronic state density than Ni_2 at similar excitation energies. Moreover, the ground state of Ni_2^+ seems to have a uniquely short internuclear separation relative to the excited states accessed by optical probes. These excited electronic states exhibit a much smaller vibrational frequency (see the table) than the low lying excited states¹⁰² of Ni_2 (ca. 180 cm^{-1} for Ni_2^+ relative to ca. 330 cm^{-1} for Ni_2). A large increase in bond length and a reduction in vibrational frequency upon excitation might be explained by the description of the ground state as arising from $3d^9 4s Ni + 3d^8 4s Ni^+$ atomic configurations with a full 4s sigma bond and the excited states arising from $3d^9 4s Ni + 3d^9 Ni^+$ separated atoms with only a 1/2 order sigma bond. This explanation does not seem consistent with the sparse electronic state density of Ni_2^+ or the large (over 1 eV)

difference in ground state bond energy of Ni_2^+ over Ni_2 . Ab initio calculations do suggest however a shortening of the bond length and an increase in bond energy of Ni_2^+ as compared to Ni_2 .

Resonant two-photon dissociation (R2PD) has been demonstrated as a method for the spectroscopic interrogation of small transition metal molecular ions cations. Only by virtue of the reduced internal temperature of the ion target is the complex nature of the spectrum simplified enough for interpretation. Preliminary analysis of the Ni_2^+ electronic spectrum has revealed significant differences in the bonding of Ni_2^+ in comparison with Ni_2 .

The accuracy of the appearance potential is somewhat surprising since we now know through rotational analysis of the Ni_2^+ R2PD spectrum that the ionization of Ni_2 is not vertical but involves a significant bond length change.

Threshold Photodissociation of Cr_2^+

Chromium dimer represents a particularly interesting chemical bond. The ground electronic state chromium dimer is $^1\Sigma$ whereas the ground state of the Cr atom is 7S . This represents a change from the lowest to the highest spin state of the valence electrons upon dissociation of the system into separated atoms. Indeed, a sextuplet bond is suggested to be

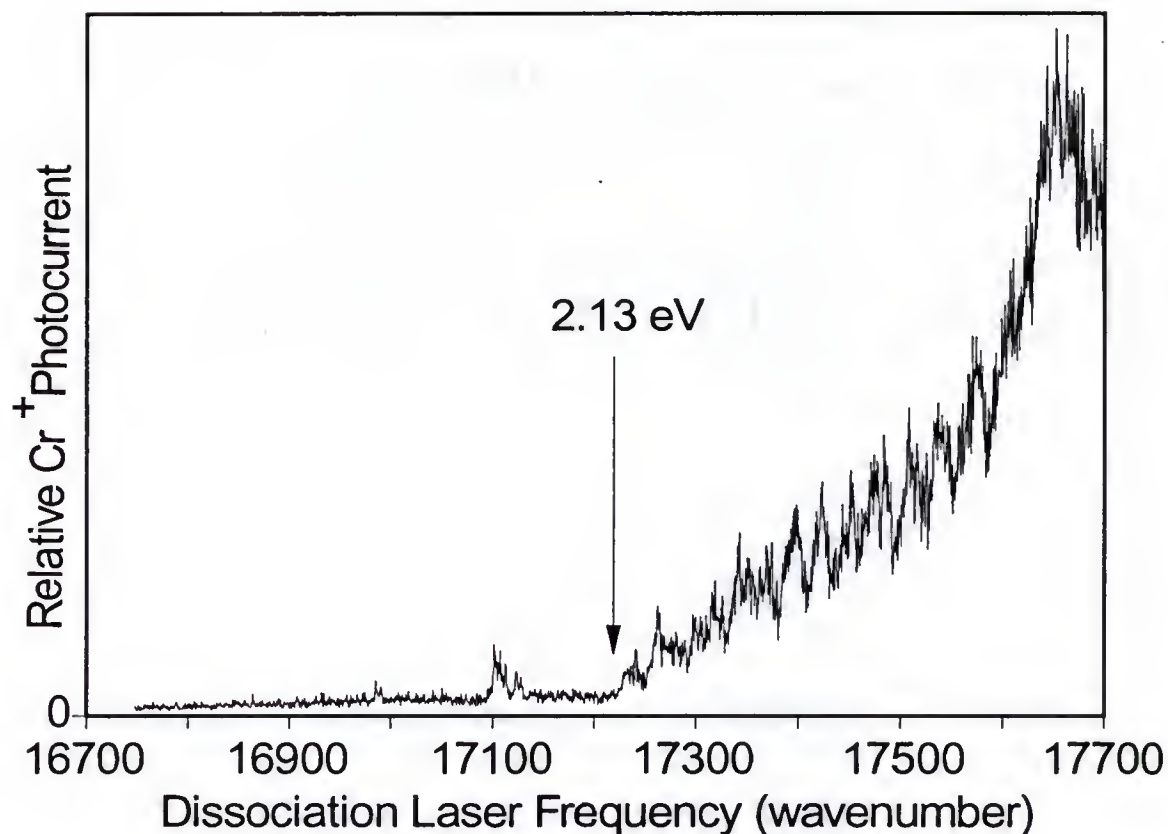


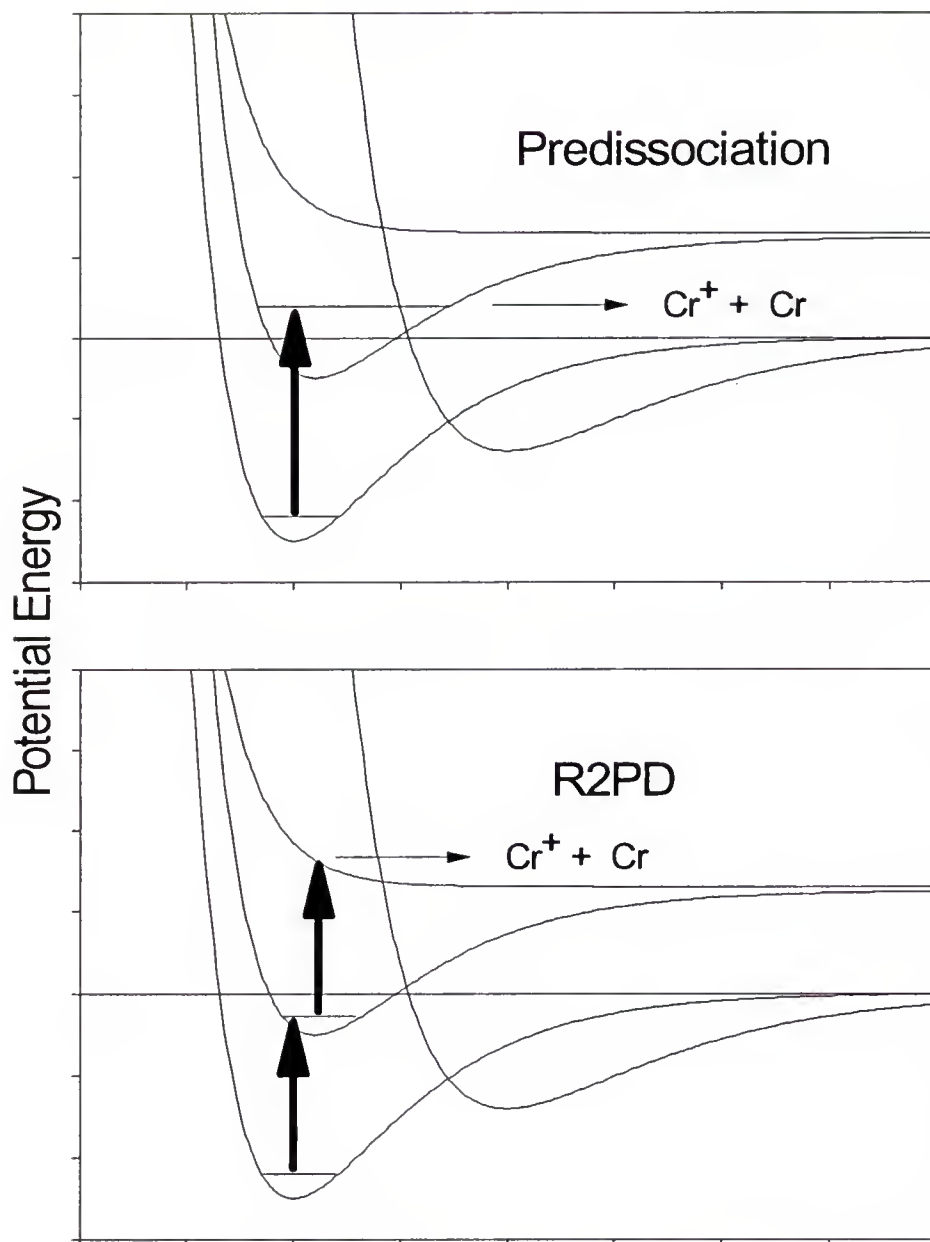
Figure 51. Photodissociation Threshold of $\text{Cr}_2^+ \rightarrow \text{Cr}^+ + \text{Cr}$.

The figure displays a portion of photodissociation spectrum for the process $\text{Cr}_2^+ \rightarrow \text{Cr}^+ + \text{Cr}$. Relative photocurrent for production of Cr^+ is monitored as a function of dissociation laser frequency. The onset of one-photon predissociation is indicated by an arrow at 2.13 eV.

formed in Cr_2 originating from all the $4s3d^5$ valence atomic orbitals on each nuclei.^{103,104,105} The high bond order is in accord with the experimental determination of the equilibrium internuclear distance of ca. 1.7 \AA ^(106,107,108) and the vibrational frequency of ca. 450 cm^{-1} ^(109,110) in the ground state of Cr_2 . The dissociation energy of this sextuple bond has been determined by high-pressure mass spectrometry to be a surprisingly low $1.47 \pm 0.05 \text{ eV}$ ⁽¹¹¹⁾. This section outlines the investigation of the dissociation energy of Cr_2^+ through a non-equilibrium method (photodissociation) which will place an upper limit to the binding energy of neutral chromium dimer at 1.77 eV .

Figure 51 shows the relative photodissociation cross-section for the process $\text{Cr}_2^+ \rightarrow \text{Cr} + \text{Cr}^+$ as a function of dissociation laser frequency. For laser energies of greater than 2.13 eV , the spectrum appears as a lumpy but apparently continuous one-photon dissociation. At energies lower than 2.13 eV , relatively sharp and sparse vibrational progressions become discernable at high laser fluence ($>5 \text{ mJ/cm}^2$). These features appear to the red of 14300 cm^{-1} (1.77 eV).

The figure shows hypothetical potential energy curves as a function of internuclear separation for the Cr_2^+ ion and a cartoon of the processes that give rise to the spectrum in Figure 51. For photon energies above 2.13 eV , one-photon absorption populates states of similar internuclear separation to that of the ground state but above the adiabatic dissociation limit (shown with the dashed line) of the



Internuclear Separation

Figure 52. Cr_2^+ Photodissociation Mechanisms. The figure displays hypothetical potential energy curves which explain the photodissociation features in the spectrum of Cr_2^+ . The upper diagram displays the phenomenon of predissociation leading to the vibrationally modulated slope observed in Figure 51 for energies above 2.13 eV. The lower diagram represents the mechanism of R2PD. Two photons are required to dissociate Cr_2^+ and will result in sharp vibronic features seen below 2.13 eV.

molecule. Small isotope shifts of the 'lumps' on the dissociation spectrum indicate only moderate vibrational excitation in the initially prepared upper level. This level is non-radiatively coupled to levels that are truly unbound at this energy and may rapidly predissociate. The photodissociation action spectrum obtained from this process contains only 'smeared out' remnants of vibrational structure of the state initially populated by photoabsorption. The top panel of the figure indicates this predissociation mechanism.

Below 2.13 eV the photoabsorption event populates a truly bound vibronic state and no dissociation can occur unless a second photon populates an unbound or quasi-bound level at higher energy. This incoherent Resonant 2-Photon Dissociation (R2PD) is diagrammed in the bottom panel of the figure. The R2PD signal is modulated by the bound-bound transition probability and gives a sharp spectrum. Predissociation may only occur above the adiabatic dissociation energy (bond strength) of the target molecule whereas R2PD may occur to as far red as half this energy.

Chromium dimer specifically, and transition metal clusters in general, present some experimental difficulty because of the facile competition between one-photon predissociation and R2PD. The large transition probabilities and high density of electronic states in transition metal complexes make multi-photon processes competitive or even overwhelming under moderate conditions of dissociation laser

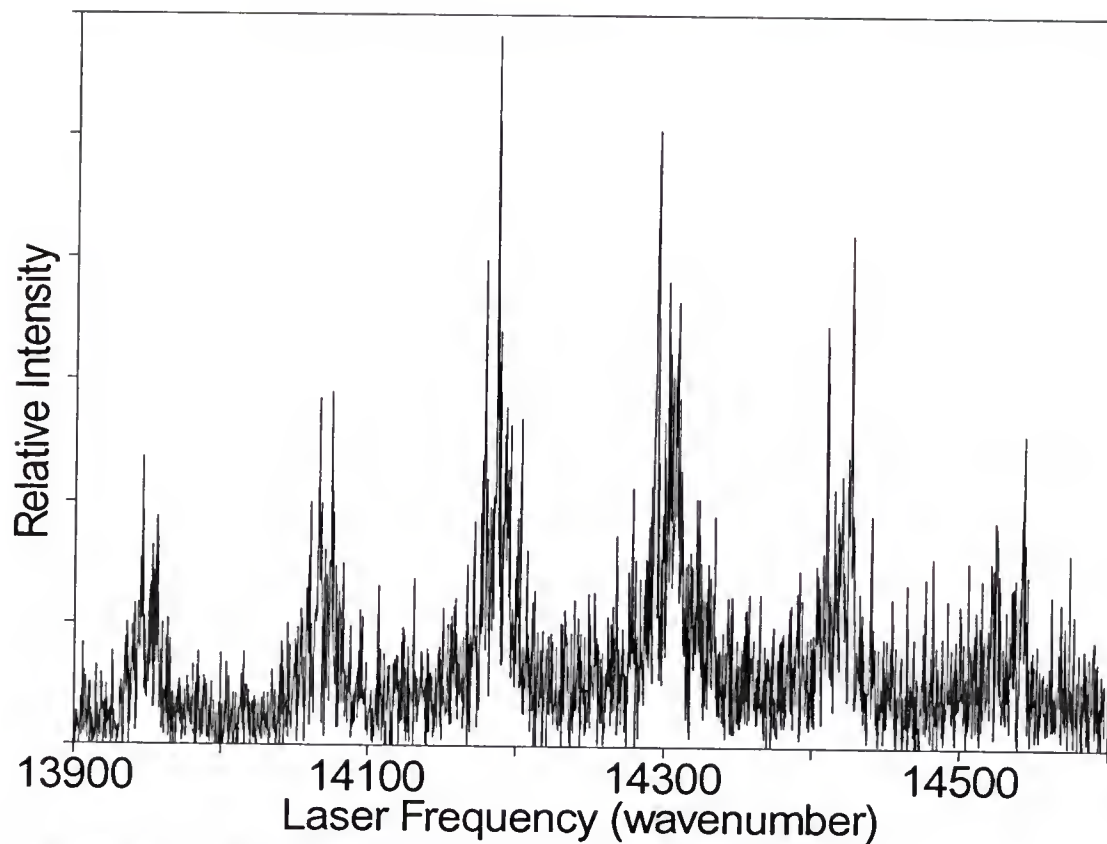


Figure 53. R2PD of Cr_2^+ .

The figure displays a portion of the resonant 2-photon dissociation spectrum of $\text{Cr}_2^+ \rightarrow \text{Cr}^+ + \text{Cr}$ over the region of 13 900 to 14 600 cm^{-1} . Six vibronic bands of a common excited state are separated by ca. 120 cm^{-1} . The identity of the state is currently unknown.

fluence. Suppose Cr_2^+ has a small one-photon absorption cross section at energies near 2 eV, but also, a very large probability of absorbing a second photon from the initially photoexcited level. R2PD might mask the one-photon predissociation threshold in this case. With this under consideration, an upper limit to the bond strength of Cr_2^+ may be assigned at 2.13 eV, the apparent one-photon fragmentation threshold in Figure 51.

It is unlikely that the observed threshold corresponds to the production of any excited fragment. The smallest possible promotion energy in either Cr^+ (11962 cm^{-1}) or Cr (7593 cm^{-1}) would make the derived bond strength of Cr_2^+ improbably small.

The application of the literature values for the ionization potential of Cr_2 (6.4 ± 0.2 eV) and Cr (6.763 eV)³⁷ places an upper limit to the bond strength of Cr_2 neutral as 1.77 eV. This is in accord with experimental determinations of the dissociation limit by Kant and Strauss¹¹² of 1.78 ± 0.35 eV and a more recent measurement by Hilpert and Ruthardt of 1.47 ± 0.05 eV.

The bond energy of the neutral dimer, at < 1.77 eV, seems weak for a sextuple bond of a 1.7 Å bond length and 450 cm^{-1} vibrational frequency. The resemblance of theory to experiment has been discussed before.¹¹³ Good agreement with experiment is shown by the *ab initio* calculation of Goodgame and Goddard.¹¹⁴ This calculation indicates the ground state potential energy surface has a double minimum. A global

minimum has a well depth of 1.86 eV at 1.61 Å and is dominated by the interaction of the valence d orbitals. At larger internuclear separation, a second but smaller minimum exists due to the interaction of s orbitals alone. There is experimental evidence for this double minimum ground state.¹¹⁵

A strict upper limit to dissociation for Cr_2^+ has been determined spectroscopically for the first time as 2.13 eV. From this, the neutral dimer adiabatic dissociation limit is determined to be < 1.77eV confirming the surprisingly weak binding energy of this molecule.

189 shows possible mechanisms leading to photodissociation of Cr_2^+ with reference to hypothetical potential surfaces. The upper diagram displays predissociation giving rise to the vibrational progression displayed in Figure 51. Excitation to a level in the excited state which lies above the dissociation limit of the ground state (dashed line) results in coupled predissociation. The lower diagram displays Resonant 2-Photon Dissociation (R2PD). Here the transition of the first photon lies below, in energy, of the adiabatic dissociation energy. A second photon is required to photodissociate Cr_2^+ , resulting in sharp vibronic features in the photodissociation spectrum.

Photodissociation of Ca_2^+

The photodissociation spectrum of Ca_2^+ is displayed in the Figure 54. Several blue degraded bands are observed through resonant photodissociation. The progression is seen to end abruptly with the reddest transition at $19\,021\text{ cm}^{-1}$. This transition is believed to correspond to the electronic origin band. Currently, this assignment has not been confirmed with isotopic analysis. A vibrational fit to Eq. (6) with the reddest transition assigned to $v' = 0$ determines a vibrational frequency of 67 cm^{-1} .

This is the first blue degraded spectrum that has been observed in this laboratory and implies a shortening of the internuclear distance upon excitation. For the neutral diatomic, the ground state has been spectroscopically determined as a $^1\Sigma_g^+$ characterized by a $\sigma_g^2\sigma_u^2$ valence electron configuration.¹¹⁶ Thus, molecular orbital theory would predict a zero bond order. Nonetheless the ground state has binding energy of $1075 \pm 150\text{ cm}^{-1}$ with a vibrational frequency of 64.93 cm^{-1} . The bond energy is surprising large considering the dominant interactions are presumed to be van der Waals.

One would speculate that the cation analogue of the neutral calcium dimer would be bound more strongly. Under the convention of molecular orbital theory the bond order would increase from zero to $1/2$. In addition, simple classical electrostatics would suggest that the presence of a charge may

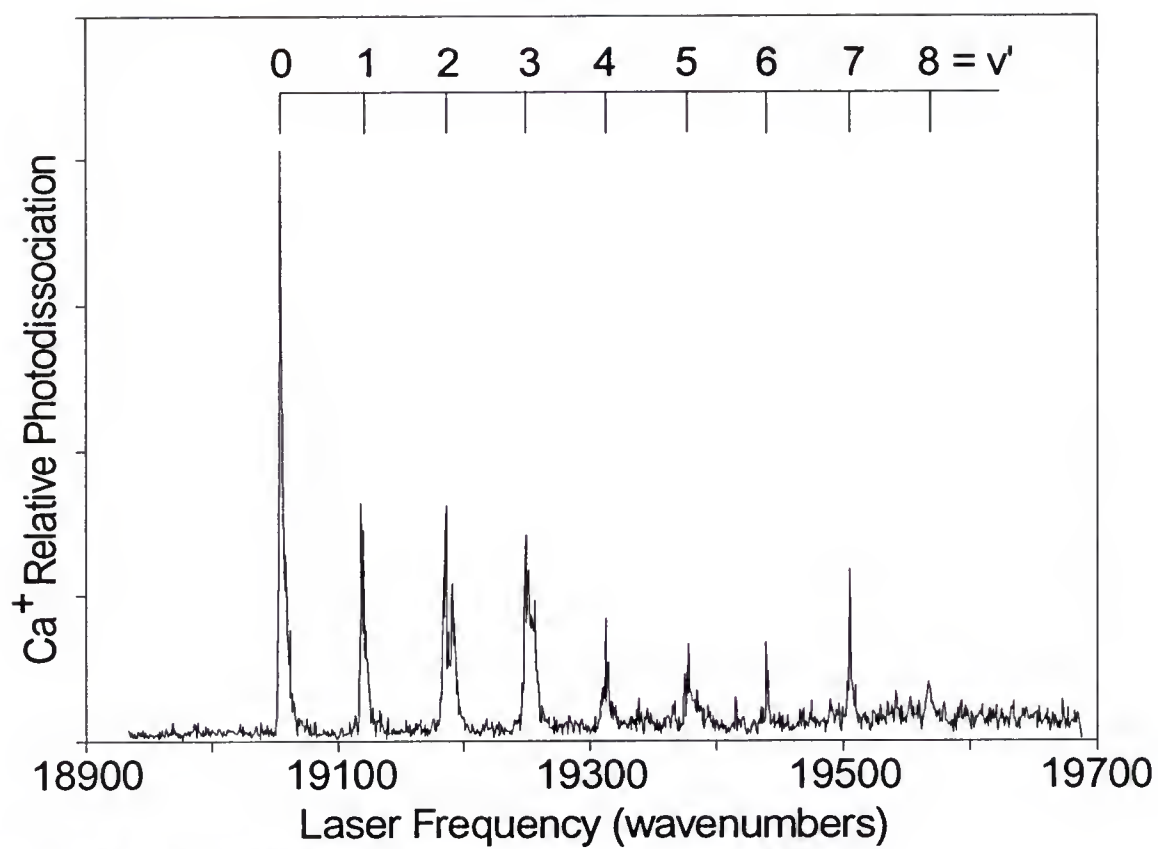


Figure 54. Resonant Photodissociation of Ca₂⁺.

increase the bonding energy via the addition of inductive forces. This implies the ionization potential of the neutral dimer is smaller than that of the atom which is often the case for transition metals, see for example, the systems of Ni_2^+ and Cr_2^+ discussed previously in this Chapter.

With this in mind, one would also assume that the binding energy of the cation would be bound by more than the neutral dimer. Intuitively, the vibrational frequency should increase in the following sequence: $\omega_e'' (\text{Ca}_2) < \omega_e'' (\text{Ca}_2^+) < \omega_e' (\text{Ca}_2^+)$. The vibrational analysis of the excited state of Ca_2^+ determines ω_e' as 67 cm^{-1} while the ω_e'' of Ca_2 is ca. 65 cm^{-1} . Thus, the possibility exists that the cation dimer is bound by less than the neutral dimer in spite of the prediction of molecular orbital theory and classical electrostatics.

CONCLUSIONS

A variety of small clusters systems have been spectroscopically probed in the visible region by photodissociation of mass-selected ions. The spectra allow the accurate determination of ground and excited state dissociation limits of many of these ions, as well as their vibrational structure. The ground and excited state parameters for the inductive and electrostatically bound metal-ligand species presented in this work are included in Table 16 and Table 17, respectively.

For an inductively bound system the only influence the identity or state of the charged atom has upon the binding energy is through the repulsive interaction it has with the neutral partner. Due to the disparity of the ionization potential between the metal atom and the rare-gas atom, both the ion and neutral partner are considered covalently inert. Thus, the binding energy of a metal-cation rare-gas diatomic will be determined by the polarizability of the rare-gas atom and its limiting approach to the cation. An increase in polarizability is always accompanied by an increase in binding energy. Naturally, the internuclear distance is governed by the radial extent of the interacting atoms. This is displayed

Table 16. Excited State Parameters for Metal-Ligands.

Ion	config ^a	D ₀ [cm ⁻¹]	T _∞ [cm ⁻¹]	ω _e ' [cm ⁻¹]	ω _e x _e ' [cm ⁻¹]
VAr ⁺	3d ³ 4s	1368	15166	94	1.95
CoAr ⁺ (A)		2594	13081	165	3.20
CoAr ⁺ (B)	3d ⁷ 4s	1993	13380	121	2.21
CoAr ⁺ (C)	3d ⁸	2824	14458	176	3.28
ZrAr ⁺ (A)			14888	68	0.92
ZrAr ⁺ (B)			15479	69	0.67
ZrAr ⁺ (C)			15540	77	1.26
CaKr ⁺	3d		14192	52	
VKr ⁺	3d ³ 4s	2047	15310	99	1.40
CoKr ⁺ (A)		3985	13336	148	1.47
CoKr ⁺ (B)	3d ⁷ 4s	2907	13874	118	1.36
CoKr ⁺ (C)	3d ⁸	4158	14674	159	1.76
V(H ¹⁶ OH) ⁺	3d ³ 4s	6200	15712	339	4.5
V(H ¹⁸ OH) ⁺	3d ³ 4s	6300	15719	326	4.1
V(OCO) ⁺	3d ³ 4s		15703	196	4.7
				105	
				600	
V(NH ₃) ⁺			17342	370	17.5

^a Metal ion atomic configuration in separated atom limit.

Table 17. Ground State Adiabatic Bond Strength.

System	config ^a	ω_e cm ⁻¹	D ₀ Expt. [eV]	D ₀ Theory [eV]	obs-cal	%err.
VAr ⁺	3d ⁴		0.370	0.291 ^b	0.079	-21%
CrAr ⁺	3d ⁵		0.29	0.246 ^c	0.04	-15%
CoAr ⁺	3d ⁸		0.510	0.392 ^b	0.118	-23%
NiAr ⁺	3d ⁹	235	0.55	0.450 ^d	0.10	-18%
VKr ⁺	3d ⁴		0.473			
CoKr ⁺	3d ⁸		0.69			
V(HOH) ⁺	3d ⁴	420				
Cr(N ₂) ⁺	3d ⁵		0.61			

^aMetal ion atomic configuration in separated atom limit.

^bRef [61], ^cRef [62], ^dRef[60]

in the progression across the transition-metal row with the an increase in binding energy due to the d orbital contraction for the following systems; CrAr⁺, CoAr⁺, NiAr⁺. However, the radial extent of the metal cation may not always be spherically symmetric. In the case of V⁺(3d⁴) ground state the neutral rare-gas atom will minimize the internuclear distance by forming an molecular orbital along an empty metal d orbital. This explains the anomalously larger binding energy of VAr⁺ compared to CrAr⁺.

The comparison of binding energy of VAr⁺(Kr) with V(H₂O)⁺ suggest that inductive forces will contribute significantly to the enthalpy of solvation for a given monovalent cation. The photodissociation of electrostatically bound V(HOH)⁺ provides, for the first time, details for a cation-water pair potential.

The spectroscopic data has demonstrated that the system of $V(OH_2)^+$ is electrostatically bound. Although an inserted isomer may also exist for this system, there is certainly a barrier to isomerization.

Metal-cation ligated clusters may be thought of as molecular 'models' ideal for the study of the non-covalently bound systems. Insight into the nature of this type of bonding has been revealed through the vibrational structure of many inductively and electrostatically bound systems. Optical interrogation has been shown to provide the ultimate technique for direct measurement of the quantal details in these systems. In some cases, the vibrational information for a metal rare-gas diatomic is so extensive that an accurate potential surfaces may be parameterized using the WKB approximation.

APPENDIX A
ELECTRICAL CIRCUITS

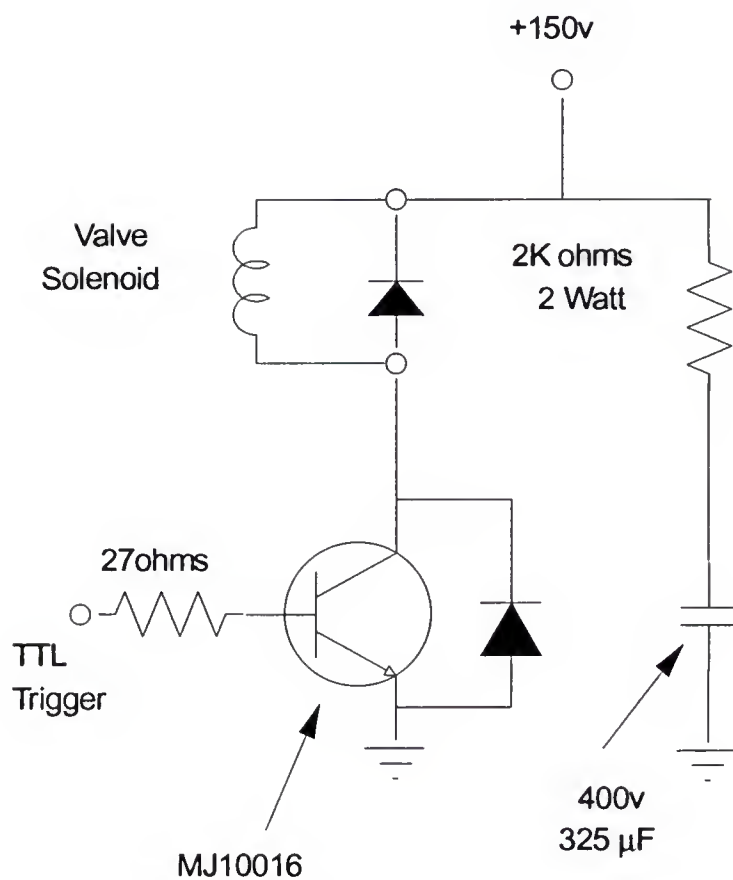


Figure 55. Valve Driver Circuit.

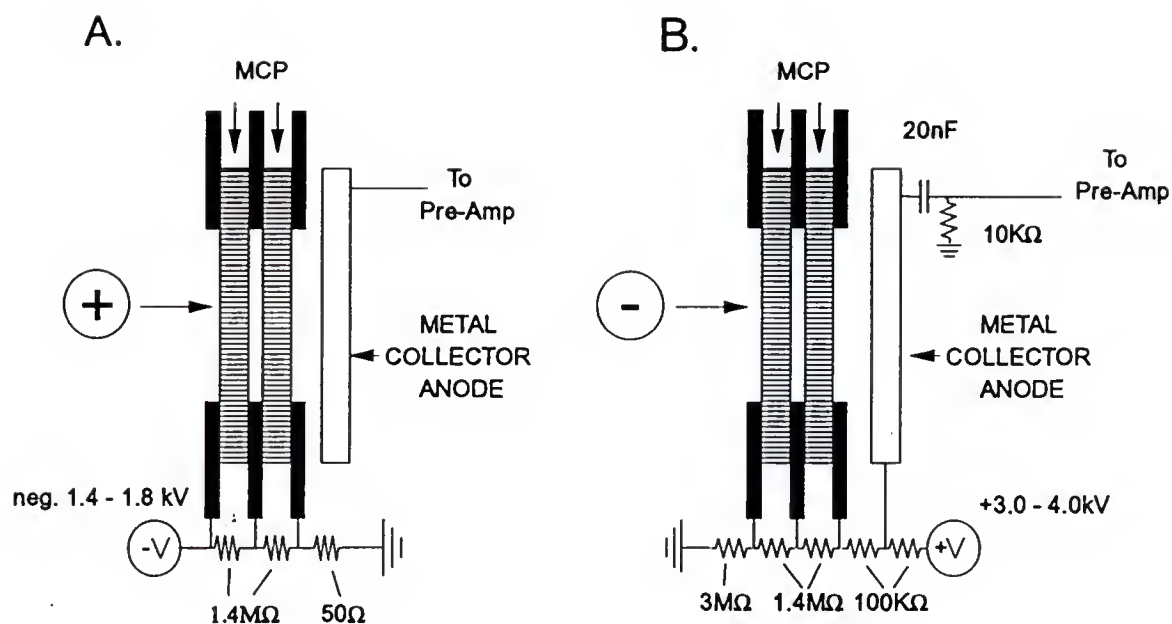


Figure 56. Bias Conditions for Microchannel Plate Detector.

The figure displays the electrical connections for detecting cations (part A) and anions (part B). In each case, the interaction of the charged species with the first MCP results in the emission of secondary electrons which in turn strike a second MCP. This electron cascade is accelerated with the appropriate field to the anode.

APPENDIX B
COMPUTER CODE

WKB Grid Program

```
#include <conio.h>
#include <iostream.h>
#include <stdio.h>
#include <stdlib.h>
#include <math.h>
#include <fstream.h>

#define BANNER "<wkb> GRID Version DANO 1.1 7/21/92\n"
#define HCONST 12.899226 /* for u(r) in cm^-1 <not used> */

/***** FUNDAMENTAL CONSTANTS *****/
#define PI 3.14159265359 /* dimensionless */
#define CSPEED 2.997925e10 /* cm/sec */
#define NAVAGADRO 6.02217e23 /* dimensionless */
#define ECHARGE 4.80298e-10 /* esu */
#define HPLANCK 6.6256e-27 /* erg.sec */
#define GRID_STEP 20

/***** GLOBAL VARIABLES *****/

FILE *dfile;

char fnam[80];
int v, z=0, v_index[50], num_pts, isteps=1000;
float trans[50];
double (*u)(double);
double rms,
       e,
       rmin,
       rin,
       rout,
       rinstart, routstart,
       rstep = 1e-3,
       recrit = 1e-6,
```



```

    estart,
    estep = 10.0,
    ecrit = 1e-4,
    emincrit = 1e-15,
    emin,
    hcon,

    /*mu=31.7333333, re=2.1, De=-2047.0, we=99.0,
      VKr excited state*/
    mu =23.83838383, re=2.0, De=-2594.0, we=165.0,
      /* CoAr+ A state */
    k,
    alpha=1.66,
    acon,
    bcon=3e5,
    ccon,
    dcon,
    rho;

/*****
double igrator(double (*funcnam)(double), double a, double
b, int steps)          /* integrator */
{
    double aa, bb, inc, sum=0.0, x, val;
    int i;
    if (a==b) return(0.0);
    aa=(b>a)?a:b;
    bb=(b>a)?b:a;
    inc=(bb-aa)/(double) steps;
    for(x=aa+inc; x<bb; x+=inc)
        sum += (*funcnam)(x);
    sum += ((*funcnam)(bb)+(*funcnam)(aa))/2.0;
    sum *= inc;
    return(sum);
}

/*****Root Finder*****/
double rootfinder(double (*funcnam)(double), double
start, double inc, double crit)
{
    double guess=start, oldvalue, value, abs crit;
    int oposflag, posflag;
    abs crit=fabs(crit);
    oldvalue = (*funcnam)(guess);
    oposflag = (oldvalue>0.0)?1:0;
    do
    {
        guess += inc;
        value = (*funcnam)(guess);
        posflag = (value>0.0)?1:0;
        if(posflag!=oposflag) /* value has changed sign */
            {

```

```

        if (fabs(value)<abscrit) return(guess);
        /* good enough? */
        inc /= -2.001; /* step slower and change
direction */
    }
    else /* value has same sign */
    {
        if (fabs(value) > fabs(oldvalue))
            /* change direction? */
        {
            inc = -inc;
            guess += inc; /* restore guess */
            value = oldvalue;
            posflag = oposflag; /* restore results
*/
        }
    }
    oldvalue = value;
    oposflag = posflag;
} while (value != 0.0);
return(guess); /* got lucky */
}
/*****/
double minimizer(double (*funcnam)(double),double
start,double step,double crit)
{
    double guess,oldvalue,value,abscrit,test;
    guess=start;
    abscrit = fabs(crit);
    oldvalue = (*funcnam)(guess);
    do
    {
        guess += step;
        value = (*funcnam)(guess);
        if (value > oldvalue)
            step /= -2.001;
        test = value-oldvalue;
        test = fabs(test/step);
        if (test < abscrit) return(guess);
        oldvalue=value;
    } while (1);
}

/*****/

/* BORN MAYER POTENTIAL */
double uBM(double r)
{
    double ret,r4;
    r4 = r*r;

```

```

    r4 *= r4;
    ret = -r/rho;
    ret = exp(ret);
    ret *= bcon;
    ret -= (ccon/r4);
    return(ret);
}

/*****/
double BM_pot(double r)
{
    double ret,dum;
    ret=bcon*exp(-r/rho);
    dum=r*r*r*r;
    ret-=ccon/dum;
    return(ret);
}

double tp(double r)
{
    double ret;
    ret = e - u(r);
    return(ret);
}

double momentum(double r)
{
    double ret;
    ret = e - u(r);
    if (ret<=0.0) return(0.0);
    ret = sqrt(ret);
    return(ret);
}

double doit(double energy)
{
    double ret;
    e=energy;
    ret= -rstep;
    rin=rootfinder(tp,rinstart,ret,recrit);
    rout=rootfinder(tp,routstart,rstep,recrit);
    rinstart=rin;
    routstart=rout;
    ret = 2.0*igrator(momentum,rin,rout,isteps);
    ret -= hcon*((double)v + 0.5);

    /*printf("%18.11lf\b\b\b\b\b\b\b\b\b\b\b\b\b\b\b\b\b",e);*
    /
    return(ret);
}

/*****/

```

```

double rho1(double r)
{
    double ret;
    ret = r*r*r*r*r;
    ret *= De/ccon;
    ret += r;
    ret /= 4.0;
    return(ret);
}

double rho2(double r)
{
    double ret,dum;
    dum = r*r*r*r*r;
    dum *= k;
    dum += (20.0*ccon/r);
    ret = 4.0*ccon/dum;
    return(ret);
}

double bBM(double r)
{
    double ret;
    ret = exp(r/rho);
    ret *= 4.0*rho*ccon;
    ret /= (r*r*r*r*r);
    return(ret);
}

double rrootBM(double r)
{
    double ret;
    ret = rho1(r)-rho2(r);
    return(ret);
}

/*****/

void BM_menu()
{
    int i;
    double temp,rcalc,dum_rms,energy,dum_k;
    emin=De;
    rms=0.0;
    rmin = rootfinder(rrootBM,re,0.001,1e-10);
    re=rmin;
    rho=rho1(rmin);
    bcon=bBM(rmin);
    routstart = rinstart = rmin;
    printf("\nDe = %5.4lfcm-1\twe = %3.2lfcm-1\tre = %2.6lf[A]",emin,we,rmin);
    estart = emin + (v_index[0]+0.5)*we;
}

```

```

u=uBM;
estart = (estart>0.0)?(-2.0*estep):estart;
printf("\nrho = %lf[A]\tbcon = %lfcml",rho,bcon);
printf("\n\nCalculating Vibrational Levels,
working...\n\n");
printf("\nIndex\tObserved\tCalculated\tDev.\n");
    for(i=0;i<num_pts;i++)
    {
        v=v_index[i];
        while ((estart+estep)>0.0) estep /= 2.0001;
        energy=rootfinder(doit,estart,estep,ecrit);
        estart = energy;
        dum_rms=trans[i]-(energy-emin);
        rms+=(dum_rms*dum_rms);
        cprintf("%3d    %12.4lf    %12.4lf    %12.4lf
%10.4lf\r\n",
                v,trans[i],energy,(energy-emin),dum_rms);
    }
    rms/=num_pts;
    rms=sqrt(rms);
    z+=1;
}

/*****/

void input()
{
    char  fnam[20],dum[80];
    int i,j;

    dfile=fopen(fnam,"r");
    printf("\n File to Fit ? ");
    gets(fnam);

    if((dfile = fopen(fnam,"r")) == NULL)
    {
        printf("<%s> NOT FOUND\n",fnam);
        exit(0);
    }

    fscanf(dfile,"%d \n",&num_pts);

    for(i=0;i<num_pts;i++)
    {
        fscanf(dfile,"%d",(v_index+i));fscanf(dfile,"%f
\n",(trans+i));
    }

    fclose(dfile);
    printf("\n The number of points is %d",num_pts);
    for(i=0;i<num_pts;i++)

```

```

        printf("\n v = %d  Transition = %f",v_index[i],
trans[i]);
        getch();
    }

void root_finder_parms()
{
    printf("\nUse default accuracy criteria (* /n)? : ");
    if('n'==getche())
    {
        printf("\ninput recrit (%20.2le): ",recrit);
        cin >> recrit;
        printf("\ninput  ecrit (%20.2le): ",ecrit);
        cin >> ecrit;
        printf("\ninput isteps (%d): ",isteps);
        cin >> isteps;
    }
}

/*****
void main()
{
    char c;
    int i=0,j,n;
    double x,w;
    double      we_beg=118.0,
                we_end=122.0,
                De_beg=-2050.0,
                De_end=-2200.0,
                we_step,
                De_step;
    textcolor(YELLOW);
    we_step=(we_end-we_beg)/GRID_STEP;
    De_step=(De_end-De_beg)/GRID_STEP;
    clrscr();
    printf("\n");
    printf(BANNER);

    printf("filename for output: ");
    gets(fnam);
    printf("\nGrid program for Born Mayer with 1/r4
attraction");
    printf("\nReduced Mass is %lf",mu);
    printf("\nPolarizability of neutral atom = %lf",alpha);

    hcon=(HPLANCK*NAVAGADRO)/(2.0*CSPEED);
    hcon=1e8*sqrt(hcon/mu);
    ccon =alpha*5.0e7*ECHARGE*ECHARGE/(HPLANCK*CSPEED);

    input();
    dfile=fopen(fnam,"a");
    fprintf(dfile,BANNER);

```



```

fprintf(dfile, "\n\n");
fprintf(dfile, "rho\t\tbcon\t\ttrms\t\ttDe\t\ttwe\t\ttre\n");
fflush(dfile);
fclose(dfile);

    for(j=0;j<GRID_STEP;++j)
    {
        for(n=0;n<GRID_STEP;++n)
        {
            we=we_beg+(double)j*we_step;
            k=(2.0*PI*we*CSPEED);
            k *= k;
            k *= mu/(NAVAGADRO); /* Force constant in Dynes/cm
*/
            k /= HPLANCK*CSPEED*1.0E16; /*Force constant in
cm-1/A^2*/
            De=De_beg+(double)n*De_step;
            clrscr();
            cprintf("\nOutput Data in file  %s",fnam);
            printf("\nCalculating Grid point %d of
%d", (i+1), (GRID_STEP*GRID_STEP));
            printf("\nPrevious rms value = %lf",rms);
            BM_menu();
            dfile=fopen(fnam,"a");

fprintf(dfile,"%2.7lf\t%10.4lf\t%12.4lf\t%6.2lf\t%4.2lf\t%2.
5lf\n",
            rho,bcon,rms,De,we,rmin);
            fflush(dfile);
            fclose(dfile);
            i+=1;
        }
    }
}

```

CAMAC Low Level Routines

FILENAME CAMAC.C

```

#define LINT_ARGS
#include <camac.h>                                /* for crate setup */

#define IBMC 0x24F /* CAMAC crate control register */
#define WH 0x240 /* CAMAC high write port */
#define WM 0x241 /* CAMAC middle write port */
#define WL 0x242 /* CAMAC low write port */
#define AC 0x243 /* CAMAC subaddress register */
#define FC 0x244 /* CAMAC function code register */
#define NC 0x245 /* CAMAC station # register */
#define ZC 0x246 /* CAMAC Z,C,I register */
#define CC 0x247 /* CAMAC start cycle register */
#define LL 0x248 /* CAMAC LAM,X,Q register */
#define RH 0x249 /* CAMAC high byte read register */
#define RM 0x24A /* CAMAC middle byte read register */
#define RL 0x24B /* CAMAC low byte read register */
#define DMA_EN 0x0A /* DMA controller enable register */
#define DMA_MODE 0x0B /* DMA controller mode register */
#define DMA_CLR 0x0C /* DMA controller clear register */
#define DMA_RD 0x45 /* DMA mode for read */
#define DMA_WRT 0x49 /* DMA mode setting for write */
#define DMA_ADX 2 /* DMA address register */
#define DMA_CNT 3 /* DMA count register */
#define DMA_PAGE 0x83 /* DMA page register (top 4 bits of
address) */

/*****
camac_z() /* clears all modules in the camac crate */
{
    outp(ZC,1);
    outp(WL,0);
    outp(WM,0);
    outp(WH,0);
    outp(IBMC,0);
    outp(CC,0); /* sends Z and initiates CAMAC cycle */
    outp(ZC,2);
    outp(CC,0); /* send a C as well (why not) */
}

/*****
camac_c() /* initializes all modules in the camac crate */

```

```

{
    outp(ZC,2); outp(CC,0); /*sends C and initiates CAMAC
cycle */
}

/*****/
unsigned camac_in(n,f,a)
/* inputs 16 bit word data from camac crate */
unsigned n,f,a;
{
    unsigned lowbyte,highbyte;
    outp(NC,n); outp(FC,f); outp(AC,a); outp(CC,0);
    lowbyte = inp(RL); highbyte = inp(RM);
    return (lowbyte + (highbyte << 8));
}

/*****/
unsigned long camac_lin(n,f,a)
/* inputs 24 bit word from crate */
unsigned n,f,a;
{
    unsigned lowbyte,highbyte,midbyte;
    unsigned long ret=0;
    outp(NC,n); outp(FC,f); outp(AC,a); outp(CC,0);
    lowbyte = inp(RL); midbyte = inp(RM); highbyte=inp(RH);
    ret = ((unsigned long)lowbyte +
        ((unsigned long)midbyte << 8)
        + ((unsigned long)highbyte << 16));
    return(ret);
}

/*****/
camac_out(n,f,a,d)
/* outputs 16 bit word to crate (high 8 bits zeroed) */
unsigned n,f,a,d;
{
    outp(NC,n); outp(FC,f); outp(AC,a);
    outp(WL,(d & 0xFF)); outp(WM,(d >> 8)); outp(WH,0);
    outp(CC,0);
}

/*****/
camac_lout(n,f,a,d)
/* outputs 24 bit word to crate */
unsigned n,f,a;
unsigned long d;
{
    unsigned d1,d2;
    outp(NC,n); outp(FC,f); outp(AC,a);
    d1 = d & 0xFFFF; d2 = d>>16;
    outp(WL,(d1 & 0xFF)); outp(WM,(d1 >> 8)); outp(WH,d2);
    outp(CC,0);
}

```

```

    }

/*****
unsigned camac_q()
/* returns 1 if q is set (does NOT cycle crate) */
{
    return (0x01 & inp(LL));
    /* returns 1 if q is set, 0 otherwise */
}

/*****
unsigned camac_lam()
/* returns station of highest LAM set (0 if none) */
{
    /* does NOT cycle the crate */
    unsigned dummy;
    dummy = inp(LL);
    dummy >>= 2;
    dummy &= 31;
    return(dummy);
}

/*****
dma_inlq(station,length,page,offset)
/* for retrieving TR8837F data (8 bit) */
unsigned station,length,page,offset;
/* DMA q-stop transfer */
{
    int q,i=0x500;
    outp(ZC,0x28); /* clear acl and keep camac buss */
    outp(NC,station);
    outp(FC,2);
    outp(AC,0); /* send F(2)A(0) to station */
    outp(CC,0); /* cycle crate */
    outp(DMA_PAGE,page); /* set DMA page for channel 1 */
    outp(DMA_CLR,0x46); /* set first/last flip/flop */
    outp(DMA_ADX,(offset & 0xFF));
    outp(DMA_ADX,(offset >> 8));/*Set Address Register */
    outp(DMA_CLR,0x46); /* set first/last flip/flop */
    outp(DMA_CNT,(length & 0xFF));
    outp(DMA_CNT,(length >> 8));/*set maximum cycle count */
    outp(DMA_MODE,DMA_RD); /* set dma mode to read */
    outp(DMA_EN,1); /* enable DMA channel 1 */
    outp(IBMC,0x44);/*DMA to read 1 byte in q-stop mode */
    do {
        i--;
        q = camac_q();
    } while (q && i);
    /* wait for q=0 */
    outp(IBMC,0);
    /* clear IBMC */

```

```

    outp(DMA_EN,5);
/* disable DMA */
    outp(ZC,0x10);/*free camac buss for other controllers */
}

/*****
dma_in3q(station,length,page,offset)
/* for retrieving SA4100 data (24 bit) */
unsigned station,length,page,offset;
/* DMA q-stop transfer */
{
    int q,i=0x2000;
    outp(ZC,0x28);/* clear acl and keep camac buss */
    outp(NC,station);
    outp(FC,2);
    outp(AC,0); /* send F(2)A(0) to station */
    outp(CC,0); /* cycle crate */
    outp(DMA_PAGE,page); /* set DMA page for channel 1 */
    outp(DMA_CLR,0x46); /* set first/last flip/flop */
    outp(DMA_ADX,(offset & 0xFF));
    outp(DMA_ADX,(offset >> 8));/*Set Address Register */
    outp(DMA_CLR,0x46); /* set first/last flip/flop */
    outp(DMA_CNT,(length & 0xFF));
    outp(DMA_CNT,(length >> 8));/*set maximum cycle count*/
    outp(DMA_MODE,DMA_RD);/*set dma mode to read */
    outp(DMA_EN,1);/* enable DMA channel 1 */
    outp(IBM_C,0x46);/* DMA to read 3 bytes in q-stop mode */
    do {
        i--;
        q = camac_q();
    } while (q && i);
/* wait for q=0 */
    outp(IBM_C,0);
/* clear IBM_C */
    outp(DMA_EN,5);
/* disable DMA */
    outp(ZC,0x10);/* free camac buss for other controllers
*/
}

/*****
setup_sa(nshots,reclen,pretrig,period)
/* Setup SA4100 & TR2100S Combo */
signed nshots,reclen,pretrig,period;
{
    unsigned long outword,dum;
    outword = (pretrig%8);
    switch (period)
    {
        case 10: dum = 0; break; /* period in nanoseconds */
        case 20: dum = 1; break;
        case 50: dum = 2; break;
    }
}

```



```

        case 100: dum = 3; break;
        case 200: dum = 4; break;
        case 500: dum = 5; break;
        case 1000: dum = 6; break;
        case 0: dum = 7; break; /* external */
        default: dum = 0;
    }
    outword += (dum << 6);
    switch (reclen)
    {
        case 32768: dum = 6; break;
        case 16384: dum = 7; break;
        case 8192: dum = 0; break;
        case 4096: dum = 1; break;
        case 2048: dum = 2; break;
        case 1024: dum = 3; break;
        case 512: dum = 4; break;
        case 256: dum = 5; break;
        default: dum = 0; break;
    }
    outword += (dum << 3);

    /* Load TR2001S */
    camac_out(TR2001S,9,0,0);
    /* Clear TR */
    camac_lout(TR2001S,16,0,outword);
    /* set rec len, pretrig, period */
    camac_out(TR2001S,26,0,0);
    /* enable LAM */
    /* Load SA4100 */
    if (dum < 6) outword = (dum << 6);
    else outword = 0;
    /*maximum array length in SA4100 is 8k */
    camac_out(SA4100,24,1,0); /* disable averaging */
    camac_out(SA4100,26,0,0); /* enable LAM */
    camac_lout(SA4100,16,0,outword);
    /* Set rec len in SA4100 */
    camac_out(SA4100,17,0,(unsigned)(0x10000L - nshots));
    /* set shot counter */
    camac_out(SA4100,9,0,0); /* clear and enable */
}

/*****
setup_td(reclen,pretrig,period)
unsigned reclen,pretrig,period;
{
    unsigned long outword,dum;
    outword = (pretrig%8);
    switch (period)
    {
        case 32: dum = 0; break; /* period in nanoseconds */
        case 64: dum = 1; break;

```



```

        case 125: dum = 2; break;
        case 250: dum = 3; break;
        case 500: dum = 4; break;
        case 1000: dum = 5; break;
        case 2000: dum = 6; break;
/* case 0: dum = 7; break; */ /* external */
        default: dum = 0;
    }
    outword += (dum << 4);
    switch (reclen)
    {
        case 8192: dum = 7; break;
        case 7168: dum = 6; break;
        case 6144: dum = 5; break;
        case 5120: dum = 4; break;
        case 4096: dum = 3; break;
        case 3072: dum = 2; break;
        case 2048: dum = 1; break;
        case 1024: dum = 0; break;
        default: dum = 3; break;
    }
    outword += (dum << 8);

    camac_out(TR8837F,17,0,0);
/* set CAMAC read Mode */
    camac_lout(TR8837F,16,0,outword);
/* set rec_len, pretrig, period */
    camac_out(TR8837F,24,0,0);
/* disable LAM */
    camac_out(TR8837F,9,0,0); /* Clear TR */
}

/*****
setup_P3655(station,delay,recycle)
unsigned station,*delay,recycle;
{
    unsigned i,outword=0;
    if (recycle) outword = 64; /* Set recycle bit */
    outword += 62;
/* set clock to 1 MHz and enable all pulses */
    camac_out(station,17,0,outword);
    camac_out(station,24,9,0);
/* Disable inhibit assert */
    camac_out(station,17,13,0); /* Clear LAM mask */

    for(i=0;i<8;i++)
        camac_out(station,16,i,delay[i]);
}

*****/
setup_P4222(station,delay)
unsigned station;

```

```

unsigned long *delays;
{
    unsigned i;
    camac_out(station,24,0,0); /* enable access to P4222 */
    for(i=0;i<4;i++)
        camac_lout(station,16,i,delays[i]);
        /* load delays */
    camac_out(station,26,0,0);
        /* disable access & go! */
}

/*****/
read_qadc(values)
unsigned *values;
{
    values[0] = (0x07FF & camac_in(QADC2249W,2,0));
        /* Get DATA */
    camac_out(QADC2249W,9,0,0);
        /* Clear ADC */
}

/*****/
read_adc(values)
unsigned *values;
{
    unsigned i;
    for(i=0;i<5;i++)
        values[i] = (0x0FFF & camac_in(ADC1612,0,i));
}

/*****/
load_dac(values)
unsigned *values;
{
    unsigned i;
    for(i=0;i<6;i++)
        camac_out(DAC3016,16,i,values[i]);
}

```

CAMAC Header File

FILENAME: CAMAC.H

```
#define TR2001S      4
#define SA4100       8
#define P3655A      20
#define P3655B      19
#define P4222       18
#define ADC1612     23
#define DAC3016     21
#define QADC2249W   13
#define TR8837F     10
#define TR2262      12
```

Control Program

This program is compiled with Microsoft C, version 5.1 software. The compiler line options are as follows:

```
cl=/FPI87 /G2/ Ot/ LINK/ ST:0X4000 pjb
```

FILENAME: DRGATO3A.EXE

```
#include <pjb.h>
#include <camac.h>
```

```
#define HEADLN      "<drgato3>      Version 3      4/9/91
/pjb/rla/del\n"
#define ARRLEN      2048
#define SCANLEN     4096
#define XRES        512
#define SCANLENGTH  128
#define TDARRLEN    1024
#define TDFREQ       32
#define TDPERIOD     31.25
#define GRID        1
```

```
/***** HV Supply Parameter *****/
```

```
#define VMUL0       7.53815
#define VOFF0       (0x8000-12)
#define VMUL1       -7.57578
#define VOFF1       (0x8000-15)
#define VMUL2       3.2768
#define VOFF2       0x8000
#define VMUL_DET    -7.46714456
#define VOFF_DET    (0x8000-13)
```

```
/***** MEMORY ALLOCATION *****/
```

```
#define PLOTBUF     0x4E00
```

```

#defineTMPSCRN      0x5700
#define AXSC        0x5300
#define SABUF       0x5000
#define DMAPAGE     5
#define DMAOFF      0x2000
#define TDBUF       0x5200
#define SCANBUF     0x5B00
#define STSCPG      0x6B00
#define SCRNUM      13
/***** MACRO'S *****/
#define set_sa()
setup_sa(iparm.n,iparm.arrlen,iparm.pretrig,iparm.period)
#define initiate() camac_out(P3655A,25,0,0)
/***** FLAGS AND COUNTERS *****/
unsigned
    AVGNUM=16,
    AVGNUMD,
    toc=0,
    scanner=0,
    action=16,
    tddone=0,
    alte = 0,
    len = ARRLEN,
    bin = 0,
    didon = 0,
    nsave,
    did1,did2,iscanid=0,
    sachan[3][4],
    iscanlen,scannumber=0;

long
    bininc=1L, start=0L, send=300L,
    vchargelamp=30000L,
/*    dchargelamp=48000L, now iparm.scan[9] */
    doff1,doff2;

char avgnumid[30] ="Number of shots to average",
    avgnumidd[30];

char    signal_name[6][40]={"SA Signal One","SA Signal
Two","SA Signal Three",
    "TD Signal","Etalon","Diss Power"};

char lab_date_string[10];

/***** FLAG MASKS *****/
/*    for <action> */
#define SAPLOT      0
#define CRATEOK     1
#define READSA      2
#define READADC     4

```

```

#define CLEARSA      8
#define RECYCLE      16
#define INHIBDMA     32
#define NEWI         64
#define INVALID      128
#define DIDDLE       256
#define ISCAN        512
#define ESCAN        1024
#define ASCAN        2048
#define TDPLOT       4096
#define SCANPLOT     8192
#define TICTOC       16384

```

```

/***** PLOTTING *****/
unsigned

```

```

    new_axis,
    new_pvec,
    s_o=1,
    lock_zero=0,
    time_axis=0,
    scalemod=32,
    opage=0,
    page=6;

```

```

#define SA      (6)
#define TD      (7)

```

```

double
    yi[8]      = { 0, 0, 0, -200, -2000, -10, 256, 256 },
    ys[8]      = { 128, 128, 128, 1024, 2048, 1024, -255, -255 };
/*      = { SA1, SA2, SA3, OPTO, ETAL, POW, SA, TD } */
int
    xi[8]      = { 0, 0, 0, 0, 0, 0, 0, 0 },
    xs[8]      = { 128, 128, 128, 128, 128, 128, ARRLLEN,
128 };

```

```

struct    pvec          vec[XRES];

```

```

/***** DATA STRUCTURES *****/

```

```

struct iparms {
    char    scanid[12][30],
           pulseid[20][10];
    unsigned n,
           arrlen,
           pretrig,
           period,
           p3655a[8],
           p3655b[8],
           dac3016[16];
    long    scan[12];
    unsigned long p4222[4];

```

```

};

struct eparms {
    unsigned sweep,
              adc[16];
};

struct sdata {
    long      sa[6];
};

/***** FILE CONTROL *****/
char filnam[80],fnam[80];
FILE *dfile;

struct file_counting_control {
    int  a, f, i, t, v;
}      file_count= {0,0,0,0,0};

/***** INITIALIZE *****/
struct sdata sdat = {0L,0L,0L,0L,0L,0L}, zero =
{0L,0L,0L,0L,0L,0L},vdat;

struct iparms temppar,iparm={
    "(00) Nozzle -> Vfire  [us]",
    "(01) VFire  -> Accel  [us]",
    "(02) Accel  -> SAsstop [ns]",
    "(03) SAsstop -> Dfire  [ns]",
    "(04) SAsstop -> TDstop [ns]",
    "(05) Dfire  -> Marker [ns]",
    "(06) VLamp  -> VFire  [us]",
    "(07) DLamp  -> DFire  [us]",
    "(08) Detector (-)  [Volts]",
    "(09) Dcharge -> Lamp  [us]",
    "(10) Sector (+)   [Volts]",
    "(11) Alternate Dfire (03) ",

    "B Trig      ",
    "Nozzle      ",
    "Vfire       ",
    "Accel       ",
    "<unused>    ",
    "<unused>    ",
    "<unused>    ",
    "<unused>    ",
    "Vlamp       ",
    "Dlamp       ",
    "<unused>    ",
    "Dcharge     ",
    "Vcharge     ",
    "<unused>    ",
    "<unused>    ",

```



```

        "<unused> ",
        "Dfire      ",
        "SAstop      ",
        "TDstop      ",
        "Marker      ",

        0,ARRLEN,0,20,

        60000,60001,60002,60003,60004,60005,60006,60007,

        60000,60001,60002,60003,60004,60005,60006,60007,

        0x8000,0x8000,0x8000,0x8000,0x8000,0x8000,0x8000,0x8000,

        0x8000,0x8000,0x8000,0x8000,0x8000,0x8000,0x8000,0x8000,

        /*"(00) Nozzle -> Vfire  [us]"*/          600L,
        /*"(01) VFire  -> Accel  [us]"*/          620L,
        /*"(02) Accel  -> SAstop [ns]"*/          35000L,
        /*"(03) SAstop -> Dfire  [ns]"*/          19900L,
        /*"(04) SAstop -> TDstop [ns]"*/          0L,
        /*"(05) Dfire  -> Marker [ns]"*/          5500L,
        /*"(06) VLamp  -> VFire  [us]"*/          390L,
        /*"(07) DLamp  -> DFire  [us]"*/          340L,
        /*"(08) Detector (-) [Volts]"*/          0L,
        /*"(09) Dcharge -> lamp  [us]"*/          44000L,
        /*"(10) Sector (+)   [Volts]"*/          310L,
        /*"(11) Alternate Dfire (03)"*/          25000L,

        0L,0L,0L,0L

};

struct eparms      eparm;

/***** Help Strings *****/
char
hmenu[40][80]={
    "F1 - internal parameter menu",
    "F2 - average shots",
    "F3 - diddle internal parameters",
    "F4 - diddler off",
    "F5 - setup scan parameters",
    "F6 - scan off",
    "F7 & 8 - this menu",
    "F9 - toggle to current scan page",
    "F10 - toggle to single shot TD",
    "rt arrow - expand-compress-offset",
    "lt arrow - horizontally",
    "up arrow - expand-compress-offset",

```

```

"dn arrow - vertically",
"Ins - toggle Scaling or Origin",
"1 - SA signal 1 screen (F9)",
"2 - SA signal 2 screen (F9)",
"3 - SA signal 3 screen (F9)",
"4 - Opto signal screen (F9)",
"5 - Etalon signal screen (F9)",
"6 - Power signal screen (F9)",
"Esc - quit",
"b - give the big picture",
"c - toggle time and bin number",
"d - dump screen page",
"g - display screen page",
"h - tddone",
"i - input a file",
"k - clear averaging (F2)",
"l - lock zero",
"n - shots to average (F2)",
"o - output a file 'automatic'",
"O - output a file 'manual'",
"p - new pvec",
"q - quit",
"r - refresh screen",
"s - save screen page",
"t - set SA channel period",
"x - set x axis scale",
"y - set y axis scale",
"z - set LAB date"

```

```
};
```

```
char
```

```

h_choice[40] = {
    59,
    60,
    61,
    62,
    63,
    64,
    66,
    67,
    68,
    77,
    75,
    72,
    80,
    82,
    '1',
    '2',
    '3',
    '4',
    '5',
    '6',

```

```

        27,
        'b',
        'c',
        'd',
        'g',
        'h',
        'i',
        'k',
        'l',
        'n',
        'o',
        'O',
        'p',
        'q',
        'r',
        's',
        't',
        'x',
        'y',
        'z'
};

/*****
caldelay() {
    iparm.p3655a[0] = 1;
    iparm.p3655a[1] = iparm.scan[6] + 1;
    iparm.p3655b[0] = iparm.scan[0];
    iparm.p3655a[2] = iparm.p3655a[1] + iparm.p3655b[0];
    iparm.p3655a[3] = iparm.p3655a[2] + iparm.scan[1];
    iparm.p4222[1] = iparm.scan[2];
    iparm.p4222[0] = iparm.scan[3] + iparm.p4222[1];
    iparm.p4222[2] = iparm.scan[4] + iparm.p4222[1];
    iparm.p4222[3] = iparm.scan[5] + iparm.p4222[0];
    iparm.p3655b[1] = (iparm.p4222[0]/1000L) +
iparm.p3655a[3] - iparm.scan[7];
    iparm.p3655b[2] = 1;          /* recycle past 64 ms */
    iparm.p3655b[4] = 44574 + iparm.p3655b[0]-vchargelamp;
    iparm.p3655b[3] = 44574 + iparm.p3655b[1]-
        iparm.scan[9];
}

/*****
clear_sa() {
    int timeout=0x1000;
    camac_out(SA4100,9,0,0);
    do {
        timeout--;
    } while ((!camac_q()) && timeout);
    if (timeout) tddone = 0;
}

*****/

```

```

unsigned read_sa() {
    /* readout SA4100 to DMAPAGE */
    unsigned ret=10;
    camac_out(SA4100,24,1,0);
    /* disable averaging and set LAM */
    do {ret--;if(!ret) return(0);} while (camac_lam() !=
SA4100);
    tddone = (0x400 & camac_in(SA4100,0,0)); /* test
for LAM type */
    camac_out(SA4100,16,1,0);
    camac_out(SA4100,16,1,0);
    /*Set readout and first channel to 0 */
    ret = camac_in(SA4100,1,0);
    /* read shot counter register */
    dma_in3q(SA4100,0x2000,DMAPAGE,0);
    /* perform array transfer to buffer */
    camac_out(SA4100,16,1,0);/* reset to channel 0 */
    camac_out(SA4100,10,0,0);/* clear LAM set by f24a1*/
    if (!tddone)
        camac_out(SA4100,26,1,0);
    /*enable if nhots incomplete */
    return(ret);
}

/*****/
read_td() { /* readout TR8837F to DMAPAGE+DMAOFF */
    int timeout=10;
    camac_out(TR8837F,17,0,0); /* Set readout */
    camac_out(TR8837F,27,0,0);
    do {timeout--; if(!timeout) return;}
        while (!camac_q());
    if (action & CRATEOK)
        dma_in1q(TR8837F,0x500,DMAPAGE,DMAOFF);
    camac_out(TR8837F,9,0,0);
}

/*****/
load_i() {
    unsigned i;

    iparm.dac3016[0] = VMUL0 * iparm.scan[10] + VOFF0;
    iparm.dac3016[1] = VMUL1 * iparm.scan[10] + VOFF1;
    iparm.dac3016[10]= VMUL_DET * iparm.scan[8] + VOFF_DET;
    for (i=0;i<10;i++)
        camac_out(DAC3016,16,i,iparm.dac3016[i]);
    setup_P3655(P3655A,iparm.p3655a,0);
    setup_P3655(P3655B,iparm.p3655b,0);
    setup_P4222(P4222,iparm.p4222);
}

/*****/
lab_date_set() {

```

```

struct          dosdate t lab_date;
unsigned labmonth, labday, labyear;
unsigned char  c;
char          s1[80], s2[80], s3[80];

_dos_getdate(&lab_date);
do {
printf("\nCurrent date:
%d/%d/%d is this correct (y/*)?",
lab_date.month, lab_date.day, lab_date.year - 1900);
c=getch();
if(c=='y') break;
do {
printf("\n\nEnter date in form MM/DD/YY: ");
scanf("%d/%d/%d",
&labmonth, &labday,&labyear);
lab_date.month = labmonth;
lab_date.day = labday;
lab_date.year = labyear + 1900;
} while (_dos_setdate(&lab_date) != 0);
printf("\n%d/%d/%d is this correct (*/*)? ",
lab_date.month, lab_date.day, lab_date.year - 1900);
c=getch();
} while(c=='n');
printf("\n");
if (lab_date.month < 10)
sprintf(s1,"0%d\0",lab_date.month);
else sprintf(s1,"%d\0",lab_date.month);
if (lab_date.day < 10)
sprintf(s2,"0%d\0",lab_date.day);
else sprintf(s2,"%d\0",lab_date.day);
sprintf(s3,"%d", lab_date.year -1900);
sprintf(lab_date_string, "%s%s%s\0", s1, s2, s3);
}

init() {
int i;
set_mode(6);
camac_z();
for (i=0;i<0x1000;i++)
wmove(0,(unsigned)&zero,SCANBUF,i*24,12,0);
if ((camac_in(ADC1612,6,0)) == 1612)action |= CRATEOK;
setup_td(TDARLEN,0,TDFREQ);
caldelay();
set_sa();
action |= TICTOC;
ticon();
/* and away we go !! */
}

/*****
leave() {
ticoff();

```



```

    set_mode(3);
    fcloseall();
    camac_z();
}

/*****/
diddle() {
    int reset=0;
    if (eparm.adc[0] > 3000) reset = 1;
    else didon = 0;
    if (didon) {
        reset = 0;
        iparm.scan[did1] = doff1 + (eparm.adc[1] >> 2);
        iparm.scan[did2] = doff2 + (eparm.adc[2] >> 2);
        caldelay();
    }
    if (reset) {
        doff1 = iparm.scan[did1] - (eparm.adc[1] >> 2);
        doff2 = iparm.scan[did2] - (eparm.adc[2] >> 2);
        didon = 1; reset = 0;
    }
}

/*****/
escanner() {
    unsigned i,signal;
    long buf=0;
    if (scanner == (AVGNUM-1)) action != READSA;
    sdat.sa[4] += (long)eparm.adc[4]-0x800L;
    /* etalon markers */
    sdat.sa[5] += (long)eparm.adc[3]-0x800L;
    /* diss laser pwr */
    for (i=0;i<sachan[2][3];i++) {
        move(TDBUF,(sachan[0][3]+i),0,(unsigned)&buf,1,0);
        sdat.sa[3] -= (long)buf;
        move(TDBUF,(sachan[1][3]+i),0,(unsigned)&buf,1,0);
        sdat.sa[3] += (long)buf;
    }
    if (!scanner) {
        for (signal=0;signal<3;signal++)
            for (i=0;i<sachan[2][signal];i+=3)
                bmove(SABUF,(sachan[0][signal]+i),0,(unsigned)&buf,3,0);
                sdat.sa[signal] -= (long)buf;
                bmove(SABUF,(sachan[1][signal]+i),0,(unsigned)&buf,3,0);
                sdat.sa[signal] += (long)buf;
    }
    for (signal=0;signal<6;signal++)
        iparm.dac3016[2+signal] =
(unsigned)(sdat.sa[signal]) + 0x8000;
    wmove(0,(unsigned)&sdat,SCANBUF,(bin*24),12,0);
}

```



```

        sdat = zero;
        bin++;
    }
    scanner++; scanner %= AVGNUM;
}

/*****
iscanner() {
    unsigned i, signal;
    long      buf = 0;

    if (scanner == (AVGNUM-1)) action != READSA;

    sdat.sa[5] += (long)eparm.adc[3]-0x800L;
    /* diss laser pwr */
    for (i=0;i<sachan[2][3];i++)
    {
        bmove(TDBUF, (sachan[0][3]+i), 0, (unsigned)&buf, 1, 0);
        sdat.sa[3] -= (long)buf;
        bmove(TDBUF, (sachan[1][3]+i), 0, (unsigned)&buf, 1, 0);
        sdat.sa[3] += (long)buf;
    }

    if (!scanner) {
        wmove(SCANBUF, (bin*24), 0, (unsigned)&vdat, 12, 0);
        for (signal=0;signal<3;signal++)
            for (i=0;i<sachan[2][signal];i+=3) {
                bmove(SABUF, (sachan[0][signal]+i), 0, (unsigned)&buf, 3, 0);
                vdat.sa[signal] -= (long)buf;

                bmove(SABUF, (sachan[1][signal]+i), 0, (unsigned)&buf, 3, 0);
                vdat.sa[signal] += (long)buf;
            }
        vdat.sa[3]+=sdat.sa[3];
        vdat.sa[4]++; /* the number of passes per bin */
        vdat.sa[5]+=sdat.sa[5];
        for (signal=0;signal<6;signal++)
            iparm.dac3016[2+signal] =
(unsigned)(sdat.sa[signal]) + 0x8000;
        wmove(0, (unsigned)&vdat, SCANBUF, (bin*24), 12, 0);
        sdat = zero;
        bin++;
        iparm.scan[iscanid] = start + (bininc * bin);
        caldelay();
    }
    scanner++;
    scanner %= AVGNUM;
    bin %= iscanlen;
}

*****/

```

```

aescanner() {
    unsigned i,signal;
    long buf=0;

    sdat.sa[4] += (long)eparm.adc[4]-0x800L;
    /* etalon markers */
    sdat.sa[5] += (long)eparm.adc[3]-0x800L;
    /* power */
    if (scanner == (AVGNUM-1)) {
        action != READSA;
        if (alte) iparm.p4222[0] = iparm.scan[3] +
            iparm.p4222[1];
        else iparm.p4222[0] = iparm.scan[11] +
            iparm.p4222[1];
    }

    for (i=0;i<sachan[2][3];i++) {
        bmove(TDBUF, (sachan[0][3]+i), 0, (unsigned)&buf, 1, 0);
        sdat.sa[3] -= (long)buf;

        bmove(TDBUF, (sachan[1][3]+i), 0, (unsigned)&buf, 1, 0);
        sdat.sa[3] += (long)buf;
    }
    if (!scanner) {
        for (signal=0;signal<3;signal++)
            for (i=0;i<sachan[2][signal];i+=3) {
                bmove(SABUF, (sachan[0][signal]+i), 0, (unsigned)&buf, 3, 0);
                sdat.sa[signal] -= (long)buf;

                bmove(SABUF, (sachan[1][signal]+i), 0, (unsigned)&buf, 3, 0);
                sdat.sa[signal] += (long)buf;
            }
        for (signal=0;signal<6;signal++)
            if (!alte) {
                vdat.sa[signal] += sdat.sa[signal];
            }
        wmove(0, (unsigned)&vdat, SCANBUF, (bin*24), 12, 0);
        sdat=zero;
    } else {
        vdat.sa[signal] -= sdat.sa[signal];
        iparm.dac3016[2+signal] =
            (unsigned)(sdat.sa[signal]) + 0x8000;
        vdat.sa[5] = iparm.scan[iscanid];
    }
    wmove(0, (unsigned)&vdat, SCANBUF, (bin*24), 12, 0);
    sdat = zero;
    bin++;
    caldelay();
}
alte ^= 1;

```

```

    }
    scanner++;
    scanner %= AVGNUM;
    bin %= iscanlen;
}

/*****
tic() {
    if (action & TICTOC) {
        if (toc) { /* this is a toc */
            read_td();
            if (!(action & INHIBDMA))
                if (((action & READSA) || (camac_lam()==SA4100))
&& !tddone) {
                    eparm.sweep = read_sa();
                    if (tddone) eparm.sweep = iparm.n;
                    else eparm.sweep -= (unsigned)(0x10000L -
iparm.n);

                    if (!(action & CRATEOK)) eparm.sweep=1;
                    action &= ~READSA;
                    if (action & RECYCLE) action |= CLEARSA;
                }
                if (action & (READADC | DIDDLE | ESCAN))
read_adc(eparm.adc);
                if (action & CLEARSA) {
                    clear_sa();
                    action &= ~CLEARSA;
                }
            } else { /* this is a tic */
                load_i();
                initiate();
                if ((action & NEWI) && !(action & INVALID)) {
                    caldelay();
                    set_sa();
                    action &= ~NEWI;
                }
                if (action & ESCAN)          escanner();
                if (action & ISCAN)          iscanner();
                if (action & ASCAN)          aescanner();
                if (action & DIDDLE)         diddle();
            }
            toc ^= 1;
        } else { /* dummy tictoc */
            if (!toc) { initiate(); }
            toc ^= 1;
        }
    }
}

/*****
plot() {
    static int      flag;          /* if(flag) then pvec
valid! */

```

```

    if (action & TDPLOT) {
        wmove(TDBUF,0,PLOTBUF,0,0x200,0);

    if(gen(PLOTBUF,(unsigned)(xi[page]),xs[page],1,vec)) {
        axis(TDPLOT);
        pltvec(vec,yi[page],ys[page]);
    } else {
        axis(TDPLOT);
        pplot(1,1);
    }
} else {
    if (action & SCANPLOT) {
        axis(SCANPLOT);
        scanplot();
    } else {
        if ((new_pvec) && (eparm.sweep)) {
            action |= INHIBDMA;
            wmove(SABUF,0,PLOTBUF,0,0x1000,0);
            nsave = eparm.sweep;
            action &= ~INHIBDMA;

            if(gen(PLOTBUF,(unsigned)(xi[page]*3),xs[page],3,vec)) {
                flag = 1;
                axis(SAPLOT);
                if (nsave)

pltvec(vec,yi[page]*nsave,ys[page]*nsave);
            } else {
                flag = 0;
                if (nsave) {
                    axis(SAPLOT);
                    pplot(3,nsave);
                }
            }
            new_pvec=0;
        } else if(nsave) {
            if(flag) {
                axis(SAPLOT);

pltvec(vec,yi[page]*nsave,ys[page]*nsave);
            } else {
                axis(SAPLOT);
                pplot(3,nsave);
            }
        }
    }
}

/*****/
axis(axistype)

```

```

    unsigned   axistype;
{
    double      ix,fx;

    if (new_axis) {
        cls();
        switch(axistype) {
            case TDPLOT:
                if(time_axis) {
                    ix= ((double)iparm.scan[2] +
(double)iparm.scan[4] +
                    (double)xi[page]*TDPERIOD)/1000;
                    fx= ix + (double)xs[page]*TDPERIOD/1000;
                    locate(23,0);printf("time[us]->");
                } else {
                    ix = (double)(xi[page]);
                    fx = (double)(xi[page]+xs[page]);
                    locate(23,0);printf("31.3ns/chan");
                }
                locate(1,35);printf("SINGLE SHOT TR8837F");
                break;
            case SCANPLOT:
                ix = (double)(xi[page]*bininc+start);
                fx = (double)((xi[page]+xs[page])*bininc +
start);

                locate(1,38);
                printf("%s",signal_name[page]);
                if (action & (ISCAN | ASCAN)) {

locate(24,30);printf("%s",iparm.scanid[iscanid]);
                }
                break;
            case SAPLOT:
                if(time_axis) {
                    ix= ((double)iparm.scan[2] +
(double)xi[page]*iparm.period)/1000;
                    fx= ix +
(double)xs[page]*iparm.period/1000;
                    locate(23,0);printf("time[us]->");
                } else {
                    ix = (double)(xi[page]);
                    fx = (double)(xi[page]+xs[page]);

locate(23,0);printf("%3uns/chan", iparm.period);
                }
                break;
        }
        axes(ix,fx,yi[page],yi[page]+ys[page],GRID);
        if (action & DIDDLE) {
            locate(3,39); printf("%26s
=", iparm.scanid[did1]);

```



```

        locate(4,39); printf("%26s
=",iparm.scanid[did2]);
    }
    if (!(action & CRATEOK)) {
        locate(2,39);printf("\nCRATE FAILURE");
    }
    wmove(0xB800,0,AXSC,0,0x2000,0);
    if(axistype != SCANPLOT)new_axis = 0;
} else wmove(AXSC,0,0xB800,0,0x2000,0);
locate(0,0);
printf((s_o)?"<SC> ":"<OR> ");
printf((lock_zero)?"<LZ>":"< >");
locate(1,70); printf("%5u",nsave);
if (action & DIDDLE) {
    locate(3,67);
printf("%6ld",iparm.scan[did1]);
    locate(4,67);
printf("%6ld",iparm.scan[did2]);
}
if (action & (ESCAN | ISCAN | ASCAN)) {
    locate(1,15);      printf("%5u",bin);
}
if (action & (ISCAN | ASCAN)) {
    if(bin==0) scannumber++;
    locate(1,25);      printf("%3u",scannumber);
}
locate(1,0);  printf("%-12s",filnam);
}

/*****
unsigned gen(arrseg,arroff,len,bytes,vec)
    unsigned    arrseg,arroff,bytes;
    int         len;
    struct pvec    *vec;
{
    unsigned    n=0,i=0,k=0,mergenum;
    long        ldum=0;
    float       fdum=0;

    if (len <= XRES) return(0);
    if ((len % XRES) != 0) return(0);
    else {
        mergenum = (unsigned)(len/XRES);
        for (k=0;k<XRES;k++) {

bmove(arrseg,arroff+n,0,(unsigned)&ldum,bytes,0);
            fdum = (float)ldum;
            n += bytes;
            vec[k].h = vec[k].l = fdum;
            for (i=1;i<mergenum;i++) {

bmove(arrseg,arroff+n,0,(unsigned)&ldum,bytes,0);

```



```

        fdum = (float)ldum;
        n += bytes;
        vec[k].h = (fdum >
vec[k].h)?fdum:vec[k].h;
        vec[k].l = (fdum <
vec[k].l)?fdum:vec[k].l;
    }
    if (k) {
        if(vec[k].h < vec[k-1].l) vec[k].h=
vec[k-1].l;
        if(vec[k].l > vec[k-1].h) vec[k].l=
vec[k-1].h;
    }
}
return (1);
}

#define TOP 1.0
#define BOT 180.0
#define LEFT 110
#define RIGHT 622
#define TOPBOT -179.0 /* TOP minus BOT */

/*****
void pltvec(vec,yorig,yscale)
    struct pvec *vec;
    double yorig,yscale;
{
    unsigned x, y1, y2, chan;
    double dum;

    for (chan=0;chan<XRES;chan++) {
        x = chan + LEFT;
        dum= BOT + ((TOPBOT) * (vec[chan].h -
yorig))/yscale;
        if (dum < TOP) dum = TOP;
        if (dum > BOT) dum = BOT;
        y1 = dum;
        if (y1 < TOP) y1 = TOP;
        if (y1 > BOT) y1 = BOT;
        dum = BOT + ((TOPBOT) * (vec[chan].l -
yorig))/yscale;
        if (dum < TOP) dum = TOP;
        if (dum > BOT) dum = BOT;
        y2 = dum;
        if (y2 < TOP) y2 = TOP;
        if (y2 > BOT) y2 = BOT;
        stl6(x,y1,x,y2);
    }
}

```

```

/*****/
symbol(x,y)
    unsigned    x, y;
{
    unsigned    yy;

    for (yy=y-1;yy<=y+1;yy++)    stl6(x-2,yy,x+2,yy);
}

topsymbol(x)
    unsigned    x;
{
    unsigned    yy;

    for (yy=TOP;yy<=TOP+3;yy++)
stl6(yy-TOP+x,yy,TOP-yy+x,yy);
}

botsymbol(x)
    unsigned    x;
{
    unsigned    yy;

    for (yy=BOT;yy>=BOT-3;yy--)
stl6(yy-BOT+x,yy,BOT-yy+x,yy);
}

scanplot() {
    int          i, x, y1, y2;
    double        mul;
    struct sdata  one;

    mul= (XRES/(double)xs[page]);
    if(bin) {
        for (i=(new_axis)?0:(bin-1);i<bin;i++) {
            wmove(SCANBUF,i*24,0,(unsigned)&one,12,0);
            x = LEFT + (i-xi[page])*mul;
            if ((x>=LEFT) && (x<=RIGHT)) {
                y1=BOT +
TOPBOT*((one.sa[page]-yi[page])/ys[page]);
                if (y1<TOP) topsymbol(x);
                else if (y1>BOT) botsymbol(x);
                else symbol(x,y1);
            }
        }
        wmove(0xB800,0,AXSC,0,0x2000,0);
        new_axis=0;
    }
}

/*****/
pplot(bytes,scale)

```

```

    unsigned bytes, scale;
{
    unsigned mul, i, x1, y1, x2, y2,
        origoff, shiftlimit;
    double dum;
    unsigned long one=0L;

    mul= (XRES/xs[page]);
    origoff = bytes*xi[page];
    shiftlimit = (bytes*xs[page])+origoff;
    bmove(PLOTBUF,origoff,0,(unsigned)&one,bytes,0);
    x1 = LEFT;
    dum = BOT +
TOPBOT*(((double)one/scale)-yi[page])/ys[page]);
    if (dum<TOP) dum=TOP;
    if (dum>BOT) dum=BOT;
    y1 = dum;
    if (y1<TOP) y1=TOP;
    if (y1>BOT) y1=BOT;
    for (i=origoff;i<shiftlimit;i+=bytes) {
        bmove(PLOTBUF,i,0,(unsigned)&one,bytes,0);
        x2 = LEFT + ((i-origoff)/bytes)*mul;
        if (x2<LEFT) x2=LEFT;
        if (x2>RIGHT) x2=RIGHT;
        dum = BOT +
TOPBOT*(((double)one/scale)-yi[page])/ys[page]);
        if (dum<TOP) dum=TOP;
        if (dum>BOT) dum=BOT;
        y2 = dum;
        if (y2<TOP) y2=TOP;
        if (y2>BOT) y2=BOT;
        stl6(x1,y1,x2,y2);
        y1=y2;x1=x2;
    }
}

#undef TOP
#undef BOT
#undef TOPBOT
#undef LEFT
#undef RIGHT

/*****/

filo(fnam, c)
    char c, *fnam;
{
    unsigned temp, seg, off;
    int i, signal;
    char video[0x400];
    unsigned long buf = 0L;

```

```

temp = action;
action = 0;
fpreset();
if((dfile = fopen(fnam, (c=='v')?"ab":"a")) == NULL) {
    printf("UNABLE TO CREATE FILE <%s>",fnam);
    getch();action = temp;return;
}
if (c!='v') {
    fprintf(dfile,"%12s\n",fnam);
    fprintf(dfile,HEADLN);
    fprintf(dfile,"sweeps= %5u\nperiod=
%5u\npretrig=%5u\n",
        eparm.sweep,iparm.period,iparm.pretrig);
    for (i=0;i<12;i++)
        fprintf(dfile,"%30s %10ld\n",
            iparm.scanid[i],iparm.scan[i]);
}
locate(17,15);

switch(c) {
case 'e':
    printf("outputting FREQUENCY SCAN data to diskfile
<%s>",fnam);
    for (signal=0;signal<4;signal++)
        fprintf(dfile,"signal%2d data=%5d base=%5d
number=%5d\n",

signal,sachan[0][signal],sachan[1][signal],sachan[2][signal]
);
        fprintf(dfile,"bin=%4u\n",bin);
        fprintf(dfile,"%30s %10u\n",avgnumid,AVGNUM);
        fprintf(dfile,"\nEXTERNAL SCAN data
follows:\n\n\n");
        for (i=0;i<bin;i++) {

wmove(SCANBUF, (unsigned) (i*24), 0, (unsigned)&sdat, 12, 0);
            for (signal=0;signal<6;signal++)
                fprintf(dfile,"%ld ",sdat.sa[signal]);
            fprintf(dfile,"\n");
        }
        break;
case 'i':
    printf("outputting INTERNAL SCAN data to diskfile
<%s>",fnam);
    for (signal=0;signal<4;signal++)
        fprintf(dfile,"signal%2d data=%5d base=%5d
number=%5d\n",

signal,sachan[0][signal],sachan[1][signal],sachan[2][signal]
);

```

```

        fprintf(dfile, "\nstart= %10ld\nbininc=
%10ld\niscanlen= %4u\n\n", start, bininc, iscanlen);
        fprintf(dfile, "%30s %10u\n", avgnumid, AVGNUM);
        fprintf(dfile, "\nINTERNAL SCAN data
follows:\n\n\n");
        for (i=0; i<iscanlen; i++) {
wmove(SCANBUF, (unsigned) (i*24), 0, (unsigned) &sdat, 12, 0);
            for (signal=0; signal<6; signal++)
                fprintf(dfile, "%ld ", sdat.sa[signal]);
            for (signal=0; signal<3; signal++)
                fprintf(dfile, "%12.8lf ",
((double) sdat.sa[signal]/sdat.sa[4]));
            fprintf(dfile, "\n");
        }
        break;
    case 'v':
        printf("outputting SCREEN PAGE data to diskfile
<%s>", fnam);
        for (i=0; i<(SCRNUM<<4); i++) {
wmove((STSCPG+(i*0x40)), 0, 0, (unsigned) video, 0x200, 0);
            fwrite(video, 1, 0x400, dfile);
        }
        break;
    default:
        printf("outputting TOFMS data to diskfile
<%s>", fnam);
        fprintf(dfile, "\nTOF data follows:\n");
        seg = SABUF;
        for (i=0; i<ARRLEN; i++) {
            off = i*3;
            bmove(seg, off, 0, (unsigned) &buf, 3, 0);
            fprintf(dfile, "%10lu\n", buf);
        }
    }
    fclose(dfile);
    strcpy(filnam, fnam);
    action = temp;
}

filp(testp)
    int      testp;
{
    char      aa, bb, c, dummy, filename[80];

    locate(5, 30); printf("'e' = External scan");
    locate(6, 30); printf("'i' = Internal scan");
    locate(7, 30); printf("'v' = Video dump");
    locate(8, 30); printf("'*' = TOFMS");

```



```

locate(9,30);printf("Enter file type? ");
c = getche();

if (testp) {
    locate(12,15);printf("filename please: ");
    if (skeyin(filename) == 0) return;
    filo(filename,c);
} else {
    switch(c) {
        case 'e': aa = file_count.f / 26 + c;
                  bb = file_count.f % 26 + 'a';
                  file_count.f ++;
                  break;
        case 'i': aa = file_count.i / 26 + c;
                  bb = file_count.i % 26 + 'a';
                  file_count.i ++;
                  break;
        case 'v': aa = file_count.v / 26 + c;
                  bb = file_count.v % 26 + 'a';
                  file_count.v ++;
                  break;
        default : c = 't';
                  aa = file_count.t / 26 + c;
                  bb = file_count.t % 26 + 'a';
                  file_count.t ++;
    }
    printf(filename,"%s%c%c.prn\0", lab_date_string,
aa, bb);
    filo(filename,c);
    locate(13,15);printf("If you want to save this to
A: or B: drive");
    locate(14,15);printf("Enter 'a' or 'b': ");
    dummy = getche();
    if ((dummy=='a')||(dummy=='b')) {
        sprintf(filename,"%c:\\%s%c%c.prn\0",
            dummy, lab_date_string, aa, bb);
        filo(filename,c);
    }
}

fili()
{}
/* {
    unsigned temp,seg,off;
    int i;
    char c,video[0x400],dum[120];
    unsigned long buf = 0L;
    locate(10,25);printf("filename please: ");
    if (skeyin(fnam) == 0) return;
    locate(11,30);printf("file type:");
    locate(11,42);printf("'e' = External scan");

```



```

locate(12,42);printf("'i' = Internal scan");
locate(13,42);printf("'v' = Video dump");
locate(14,42);printf("'*' = TOFMS)? : ");
c = getche();
temp = action;
action = 0;
fpreset();
locate(17,30);
if((dfile = fopen(fnam,(c=='v')?"rb":"r")) == NULL)
{
    printf("<%s> NOT FOUND",fnam);
    getch();action = temp;return;
}
if (c!='v')
{
    fscanf(dfile,"%12s\n",fnam);
    fscanf(dfile,"%[^\\n]\\n",dum);
    fscanf(dfile,"sweeps= %5u\\nperiod=
%5u\\npretrig=%5u\\n\\n",

&eparm.sweep,&iparm.period,&iparm.pretrig);
    for (i=0;i<12;i++)
        fscanf(dfile,"%29c
%10ld\\n", (iparm.scanid+i), (iparm.scan+i));
    }
    locate(16,15);
    switch(c)
    {
    case 'e':
        {
            printf("inputting EXTERNAL SCAN data from diskfile
<%s>",fnam);
            fscanf(dfile,"\\nsasig= %5u\\nsabas=
%5u\\nsachan= %5u\\nsa2sig= %5u\\nsa2bas= %5u\\nsa2chan=
%5u\\n",
                &sasig,&sabas,&sachan,&sa2sig,&sa2bas,&sa2chan);

            fscanf(dfile,"bin=%4u\\ntdsig= %5u\\ntdbas=
%5u\\ntdchan= %5u\\n",&bin,&tdsig,&tdbas,&tdchan);

            fscanf(dfile,"\\n%29c %5u\\n",avgnumidd,AVGNUMD);
            if (AVGNUMD!=0) AVGNUM=AVGNUMD;
            fscanf(dfile,"\\nEXTERNAL SCAN data
follows:\\n\\n\\n");
            fscanf(dfile,"%[^\\n]\\n",dum);
            for (i=0;i<bin;i++)
            {
                fscanf(dfile,"%10ld%10ld%10ld%10ld\\n",

&sdat.sa1,&sdat.sa2,&sdat.td,&sdat.etalon);

wmove(0,(unsigned)&sdat,SCANBUF,(unsigned)(i<<4),8,0);

```

```

    }
    } break;
case 'i':
{
    printf("inputting INTERNAL SCAN data from diskfile
<%s>",fnam);
    fscanf(dfile,"\nsasig= %5u\nsabas=
%5u\nsachan= %5u\nsa2sig= %5u\nsa2bas= %5u\nsa2chan=
%5u\n",
        &sasig,&sabas,&sachan,&sa2sig,&sa2bas,&sa2chan);

    fscanf(dfile,"\nstart= %10ld\nbininc=
%10ld\niscanlen= %4u\n\n",&start,&bininc,&iscanlen);
    fscanf(dfile,"\ntdsig= %5u\ntdbas=
%5u\ntdchan= %5u\n",
        &tdsig,&tdbas,&tdchan);
    fscanf(dfile,"\n%29c %5u\n",avgnumidd,AVGNUMD);
    if (AVGNUMD!=0) AVGNUM=AVGNUMD;
    fscanf(dfile,"\nINTERNAL SCAN data
follows:\n\n\n");
    fscanf(dfile,"%[^\\n]\\n",dum);
    for (i=0;i<iscanlen;i++)
    {
        fscanf(dfile,"%10ld%10ld%10ld%10ld\n",
&sdatt.sa1,&sdatt.sa2,&sdatt.td,&sdatt.etalon);
wmove(0,(unsigned)&sdatt,SCANBUF,(unsigned)(i<<4),8,0);
    }
    bin = iscanlen;
    } break;
case 'v':
{
    printf("inputting SCREEN PAGE data from diskfile
<%s>",fnam);
    for (i=0;i<(SCRNUM<<4);i++)
    {
        fread(video,1,0x400,dfile);

wmove(0,(unsigned)video,(STSCPG+(i*0x40)),0,0x200,0);
    }
    } break;
default:
{
    printf("inputting TOFMS data from diskfile
<%s>",fnam);
    fscanf(dfile,"\nTOF data follows:\n");
    seg = SABUF;
    for (i=0;i<ARRLEN;i++)
    {
        off = i*3;
        fscanf(dfile,"%10lu\n",&buf);
    }
}
}
}

```

```

        bmove(0, (unsigned) &buf, seg, off, 3, 0);
    }
}
fclose(dfile);
strcpy(filnam, fnam);
action = temp;
}
*/
/*****
svscrn() {
    int      num, add;
    char      c, scrnnam[40];

    locate(0,0);  printf("-> ");
    locate(0,2);
    num = (int)inf();
    locate(2,37); printf("-> ");
    skeyin(scrnnam);

    if((num < SCRNUM) && (num>=0))    {
        add = STSCPG+num*(0x400);
        wmove(0xB800,0, (unsigned)add, 0, 0x2000, 0);
    } else    {
        locate(0,2);
        printf("INVALID #");
        getch();
    }
}

/*****
dump() {
    unsigned  a[SCRNUM], i, row=5, col;

    cls();
    for (i=0; i<SCRNUM; i++) a[i]=0;
    set_mode(3);
    locate(20,0);
    printf("\tto select screens to be printed, move cursor
to screen number\n");
    printf("\t\t<spacebar> toggles select\n");
    printf("\t\t->this line starts print\n");
    printf("\t\t->this line aborts");
    do {
        for (i=5; i<SCRNUM+5; i++) {
            locate(i,10);
            printf("[%2d]", i-5); printf((a[i-5])?"
<PRINT>":"");
        }
        locate(row,20);
        use_curs(&row, &col, ' ');
        if((row<SCRNUM+5) && (row>=5))    a[row-5] ^= 1;

```

```

        if(row == 22) {
            set_mode(6);
            for(i=0;i<SCRNUM;i++)
                if(a[i]) {

wmove((STSCPG+i*0x400),0,0xB800,0,0x2000,0);
                locate(0,0);    printf("->%2d",i);
                prscrn();
                bdos(5,12,0);

                }
            return;
        }
    } while (row < 23);
    set_mode(6);
}

/*****
gtscrn() {
    int          num=0, add;
    double        inf();
    char          c, d=0;

    wmove(0xB800,0,TMPSCRN,0,0x2000,0);
    do {
        add = STSCPG+num*(0x400);
        wmove(add,0,0xB800,0,0x2000,0);    /* retrieve
saved screen */
        locate(0,0);    printf("->%2d    ",num);
        c = getch();
        if ( c==0 ) d=getch();
        else {
            d=0;
            if (c=='b') wmove(add,0,AXSC,0,0x2000,0);
        }
        if(d == 77) num = (num>=(SCRNUM-1)) ? 0:(num+1);
        if(d == 75) num = (num<=0) ? (SCRNUM-1):(num-1);
    } while ((c != 27) && (d != 117));
    wmove(TMPSCRN,0,0xB800,0,0x2000,0);
}

/*****
dum_data() {
    int          i, d1=245, d2=210;
    long         ld1=250, ld2=200;

    for (i=0;i<TDARRLEN;i++)
bmove(0,(unsigned)&d1,TDBUF,i,1,0);
        for (i=0;i<TDARRLEN;i+=4)
bmove(0,(unsigned)&d2,TDBUF,i,1,0);
        for (i=0;i<ARRLEN*3;i+=3)
bmove(0,(unsigned)&ld1,SABUF,i,3,0);

```

```

        for (i=0;i<ARRLEN*3;i+=30)
bmove(0,(unsigned)&ld2,SABUF,i,3,0);
        tddone = 1;
        eparm.sweep = 1;
    }

/***** MENU'S *****/
help_menu() {
    unsigned        i, j, row=1, col=40, choice;

    set_mode(3);
    locate(0,30);
    printf("DRGATO Help Menu");
    for(i=0;i<20;i++) {
        locate(i+2,1); printf("%s",hmenu[i]);
        locate(i+2,41); printf("%s",hmenu[i+20]);
    }
    locate(24,0);
    printf("Use arrow keys to get on command then press
<Enter>");
    do {
        locate(row,col);
        use_curs(&row,&col,13);
    } while (row>21);
    if(row<2) {
        set_mode(6);
        return;
    }
    if(col<40)        choice = row - 2;
    else              choice = row + 18;
    set_mode(6);
    new_axis = new_pvec = 1;
    plot();
    if (choice<14) {
        ungetch((char)h_choice[choice]);
        s_hand(0);
    }
    else s_hand((char)h_choice[choice]);
}

iparm_menu() {
    unsigned        i, j, row=17, col=35;

    set_mode(3);
    locate(4,0); printf("%35s\n",avgnumid);
    locate(5,0); for (i=0;i<12;i++)
        printf("%35s\n",iparm.scanid[i]);
    do {
        locate(4,35); printf("%10u",AVGNUM);
        for (i=0;i<12;i++) {
            locate(5+i,35);
            printf("%10ld",iparm.scan[i]);

```



```

    }
    locate(row,col);
    use_curs(&row,&col,'c');
    if ((row>=4) && (row<17)) {
        j = (row-5);
        locate(row,35);
        printf("->          ");
        locate(row,37);
        action |= INVALID;
        if (row==4) AVGNUM=(long)inf();
        else iparm.scan[j] = (long)inf();
        action &= ~INVALID;
        action |= NEWI;
        temppar=iparm;
    }
} while ((row >= 4) && (row < 17));
display_t();
set_mode(6);
}

/*****
display_t() {
    int i;

    cls();
    locate(2,0); printf("%22s","Lecroy 4222");
    locate(2,30); printf("%22s","Kinetic 3655 'B'");
    locate(2,55); printf("%22s","Kinetic 3655 'A'");
    for (i=0;i<8;i++) {
        locate(4+i,50);
printf("%20s",iparm.pulseid[i]);
        printf("%5u",iparm.p3655a[i]);
        locate(4+i,25);
printf("%20s",iparm.pulseid[i+8]);
        printf("%5u",iparm.p3655b[i]);
    }
    for (i=0;i<4;i++) {
        locate(4+i,0);
printf("%15s",iparm.pulseid[i+16]);
        printf("%10lu",iparm.p4222[i]);
    }
    locate(14,0);
    printf(
"
DAC\n");
    printf(
"      1      2      3      4      5
6      7\n");
    printf(
"      Sect (+)   Sect (-)   SAout   SA2out   TDout
etalonSout   A VTOP\n");
    printf(

```



```

"          8          9          10          11          12
13      14\n");
    printf(
"      A VBOT      A HFAR      A HNEAR      B VTOP      B VBOT      B
HFAR      B HNEAR\n\n");
    printf(
"                                ADC\n");
    printf(
"          0          1          2          3          4
5      6\n");
    printf(
"      DIDDLE0  DIDDLE1  DIDDLE2  Power      etalons
<unused>  <unused>\n");

```

```

    getch();
}

```

```

/*****

```

```

diddle_menu() {
    int i;
    char c;

    cls();
    locate(5,0);
    for (i=0;i<12;i++) printf("%35s\n",iparm.scanid[i]);
    do {
        locate(20,10);
        printf("enter scan number to be associated with
adc channel 1:");
        did1 = (unsigned)inf();
        } while (did1 >= 12);
    do {
        locate(21,10);
        printf("enter scan number to be associated with
adc channel 2:");
        did2 = (unsigned)inf();
        } while (did2 >= 12);
    locate(23,0);
    printf("<DIDDLE> procedure cannot be activated during
time or voltage scan.");
    locate(24,20);    printf("Proceed with <DIDDLE>
(y/*)?:");
    c = getche();
    if ((c=='y') && !(action & ISCAN)) action |= (DIDDLE |
RECYCLE);
    cls();
}

```

```

/*****

```

```

scan_menu() {
    int i, j, signal;
    unsigned temp;

```

```

char c;
cls();
for (signal=0;signal<3;signal++) {
    printf("%s",signal_name[signal]);
    printf("\n\tion channel start <%5u>
:",sachan[0][signal]/3);
    temp=(unsigned)inf();
    if (temp) sachan[0][signal]=temp*3;
    printf("\n\tbaseline channel start <%5u> :",
        sachan[1][signal]/3);
    temp=(unsigned)inf();
    if (temp) sachan[1][signal]=temp*3;
    printf("\n\tchannels to be integrated <%5u> :",
        sachan[2][signal]/3);
    temp=(unsigned)inf();
    if (temp) sachan[2][signal]=temp*3;
    printf("\n");
}
printf("%s",signal_name[3]);
printf("\n\tion channel start <%5u> :",sachan[0][3]);
temp=(unsigned)inf();
if (temp) sachan[0][3]=temp;
printf("\n\tbaseline channel start <%5u>
:",sachan[1][3]);
temp=(unsigned)inf();
if (temp) sachan[1][3]=temp;
printf("\n\tchannels to be integrated <%5u>
:",sachan[2][3]);
temp=(unsigned)inf();
if (temp) sachan[2][3]=temp;
printf("\n");

locate(17,0);
printf("\tScan type:");
printf("\t'e' = (stripchart) external scan\n");
printf("\t\t\t'i' = internal paramenter scan\n");
printf("\t\t\t'a' = alternating Dfire internal
scan\n");
printf("\t\t\t'*' =      none\n\t\t\t?");

c = getche();
if (c=='e') escan_menu();
if (c=='i') {
    cls();
    for (j=0;j<12;j++) {
        locate((1+j),0);
        printf("%35s",iparm.scanid[j]);
        locate((1+j),35);
        printf("%10ld",iparm.scan[j]);
    }
    iscan_menu();
}

```

```

    if (c=='a') {
        cls();
        for (j=0;j<12;j++){
            locate((1+j),0);
            printf("%35s",iparm.scanid[j]);
            locate((1+j),35);
            printf("%10ld",iparm.scan[j]);
        }
        ascan_menu();
    }
    cls();
    sdat = zero;
    scanner = 0;
}

escan_menu()
{
    char c;
    start=0L;
    bininc=1L;
    locate(23,34);printf("<STRIPCHART>:");
    locate(24,28);printf("Clear SCAN buffer (y/*)?:");
    c = getche();
    if (c=='y') {
        bin = 0;
        action |= (ESCAN | RECYCLE | CLEARSA);
    }
}

iscan_menu() {
    long li;
    unsigned i;
    char c;
    do{locate(14,10);printf("Parameter to be scanned
(0->11)?:");i=(int)inf();}
    while ((i<0) && (i>=12));
    iscanid = i;
    locate(14,10);printf("Scanning:
<<%s>>",iparm.scanid[iscanid]);
    locate(15,10);printf("Scan start (%5ld): ",start);
    li = (long)inf();
    if(li) start = li;
    do {
        locate(16,10);printf("Scan end (%5ld): ",send);
        li = (long)inf();
    } while ((li <= start) && (li));
    if (li) send = li;
    locate(17,10);printf("Scan increment per bin (%3ld):
",bininc);
    li = (long)inf();
    if (li) bininc = li;
}

```

```

iscanlen = (send-start)/bininc;
send = iscanlen*bininc + start;
locate(16,10);printf("End of scan is: %5ld
",send);

locate(24,28);printf("Clear SCAN buffer(y/*)?:");
c = getche();
if (c=='y') {
    bin = scannumber = alte =0;
    for (i=0;i<0x1000;i++)
        wmove(0,(unsigned)&zero,SCANBUF,i*24,12,0);
    action |= (ISCAN | RECYCLE | CLEARSA);
}
}

ascan_menu() {
    long          li;
    unsigned      i;
    char          c;
    do {
        locate(14,10);printf("Parameter to be scanned
(0->11)?:");
        i=(int)inf();
    } while ((i<0) && (i>=12));
    iscanid = i;
    locate(14,10); printf("Scanning:
<<%s>>",iparm.scanid[iscanid]);
    locate(15,10); printf("Scan start (%5ld): ",start);
    li = (long)inf();
    if(li) start = li;
    do {
        locate(16,10); printf("Scan end (%5ld): ",send);
        li = (long)inf();
    } while ((li <= start) && (li));
    if (li) send = li;
    locate(17,10); printf("Scan increment per bin (%3ld):
",bininc);
    li = (long)inf();
    if (li) bininc = li;

    iscanlen = (send-start)/bininc;
    send = iscanlen*bininc + start;
    locate(16,10);printf("End of scan is: %5ld
",send);

    locate(24,28);printf("Clear SCAN buffer(y/*)?:");
    c = getche();
    if (c=='y') {
        bin = scannumber = alte =0;
        for (i=0;i<0x1000;i++)
            wmove(0,(unsigned)&zero,SCANBUF,i*24,12,0);
    }
}

```

```

        action |= (ASCAN | RECYCLE | CLEARSA);
    }
}

firstc(d)
    char          d;
{
    double        dum, per;
    int i;

    switch(d) {
    case '1':
    case '2':
    case '3':
    case '4':
    case '5':
    case '6':
        if(action & SCANPLOT) {
            for(i=0;i<6;i++) {
                xi[i]=xi[page];
                xs[i]=xs[page];
            }
            page = d - '1';
            new_pvec = new_axis = 1;
        }
        break;
    case 's': svscrn();                break;
    case 'g': gtscrn();                break;
    case 'd': dump();new_axis=new_pvec=1;        break;
    case 'c': time_axis ^=1; new_axis=1;        break;
    case 'r': new_pvec=new_axis=1;            break;
    case 'l': lock_zero ^=1;                break;
    case 'n': locate(10,20);printf("Input shots to average:
");
                iparm.n = (unsigned)inf();action |= NEWI;
                new_axis=new_pvec=1;                break;
    case 'k': action |= CLEARSA;                break;
    case 'h': tddone = 1;                break;
    case 'p': new_pvec = 1;                break;
    case 'o': filp(0);                break;
    case 'O': filp(1);                break;
    case 'i': fili();new_axis=new_pvec=1;        break;
    case 't': locate(10,20);printf("input SA channel period
(ns):");
                iparm.period = (unsigned)inf(); action |= NEWI;
                new_axis=new_pvec=1;                break;
    case 'y': /* manual y scale factors */
                locate(10,20);printf("Input vertical scale : ");
                ys[page] = inf();
                locate(11,20);printf("Input vertical offset: ");
                yi[page] = inf();
                new_axis = 1;
    }
}

```



```

        break;
    case 'b':
        if(!(action & SCANPLOT)) {
            if(xs[page] != (action &
TDPLOT)?TDARRLEN:ARRLEN) {
                if (action & TDPLOT) {
                    xs[TD] = xs[page];
                    xi[TD] = xi[page];
                    xs[page] = TDARRLEN;
                    xi[page] = 0;
                } else {
                    xs[SA] = xs[page];
                    xi[SA] = xi[page];
                    xs[page] = ARRLEN;
                    xi[page] = 0;
                }
            } else {
                if (action & TDPLOT) {
                    xs[page] = xs[TD];
                    xi[page] = xi[TD];
                } else {
                    xs[page] = xs[SA];
                    xi[page] = xi[SA];
                }
            }
            new_axis = 1;
        }
        break;
    case 'x': /* manual x scale factors */
        locate(10,20); printf("Input horizontal scale
in");
        printf((time_axis)?" us:  ":" chan:  ");
        per = (action & TDPLOT)?TDPERIOD:iparm.period;
        dum = inf();
        if(time_axis && !(action & SCANPLOT))
dum=dum*1000/per;
        dum = (dum>len)?len:dum;
        dum = (dum<32)?32:dum;
        scalemod = (dum>XRES)?XRES:32;
        xs[page] = dum;
        xs[page] -= (xs[page]%scalemod);
        xs[page] = (xs[page]<scalemod)?scalemod:xs[page];
        locate(10,51);
        printf("%8.3lf[us]  (%4d chan)",
            (double)xs[page]*per/1000,xs[page]);
        locate(11,20); printf("Input horizontal offset
in");
        printf((time_axis)?" us:  ":" chan:  ");
        dum = inf();
        if(time_axis && !(action & SCANPLOT)) {
            dum = (dum*1000 - iparm.scan[2])/per;
            if(action & TDPLOT) dum -= iparm.scan[4]/per;

```



```

    }
    dum = ((xs[page]+dum)>len)?(len-xs[page]):dum;
    dum = (dum<0)?0:dum;
    xi[page] = dum;
    locate(11,51);
    dum = (xi[page]*per+iparm.scan[2])/1000;
    if(action & TDPLOT) dum += iparm.scan[4]/1000;
    printf("%8.3lf[us] (%4d chan)",dum,xi[page]);
    new_pvec = new_axis = 1;
    break;
case 'z':
    lab_date_set();
    strcpy(filnam,lab_date_string);
    break;
case 'q':
case 27 :
case 32 :break;
default:
    help_menu();
    new_pvec = new_axis = 1;
    break;
}
}

/*****
s_hand(key)
    char      key;
{
    char      c;

    len = (action & TDPLOT)?TDARRLEN:ARRLEN;
    if (action & SCANPLOT) len = SCANLEN;
    if(key!=0) firstc(key);
    else
        switch(c=getch()) {
            /* c switch */
            case 77:
                if (s_o) {
                    /* change scale */
                    xs[page] /=2;
                    xs[page] = (xs[page]>len)?len:xs[page];
                    scalemod = (xs[page]>XRES)?XRES:32;
                    xs[page] -= (xs[page]%scalemod);
                    xs[page] =
(xs[page]<scalemod)?scalemod:xs[page];
                } else {
                    /* change origin */
                    xi[page] -= xs[page]/2;
                    xi[page] = (xi[page]<0)?0:xi[page];
                }
                new_pvec=new_axis=1;
                break;
            /* right arrow */
            case 75:
                if (s_o) {
                    /* change scale */

```

```

        xs[page] *=2;
        xs[page] = (xs[page]>len)?len:xs[page];
        scalemod = (xs[page]>XRES)?XRES:32;
        xs[page] -= (xs[page]%scalemod);
        xs[page] =
((xs[page]<scalemod)?scalemod:xs[page];
        if ((xs[page]+xi[page])>len)
            xi[page] = (len-xs[page]);
        } else {
            /* change origin */
            xi[page] += xs[page]/2;
            xi[page] =
((xs[page]+xi[page])>len)?(len-xs[page]):xi[page];
        }
        new_pvec=new_axis=1;
        break;
        /* left arrow */
case 72:
    if (s_o) {
        /* change scale */
        ys[page] /= 2;
        if (lock_zero) yi[page]/=2;
    }
    else /* change origin */
        yi[page] -= ys[page]/8;
    new_axis=1;
    break;
        /* up arrow */
case 80:
    if (s_o) {
        /* change scale */
        ys[page] *= 2;
        if (lock_zero) yi[page]*=2;
    }
    else /* change origin */
        yi[page] += ys[page]/8;
    new_axis=1;
    break;
        /* dn arrow */
case 115:
    xi[page] += xs[page]/8;
    xi[page] =
((xs[page]+xi[page])>len)?(len-xs[page]):xi[page];
    new_pvec=new_axis=1;
    break;
        /* control left arrow */
case 116:
    xi[page] -= xs[page]/8;
    xi[page] = (xi[page]<0)?0:xi[page];
    new_pvec=new_axis=1;
    break;
        /* control right arrow
*/
case 73:
    break;
        /* PgUp */
case 81:
    break;
        /* PgDn */
case 82:
    s_o ^= 1;
    locate(0,0);

```

```

        printf((s_o)?"<SC> ":"<OR> ");
        break;
        /* Ins */
case 83:
        break;
        /* Del */
case 59:
        iparm_menu();
        new_axis = 1;
        break;
        /* F1 */
case 60:
        action ^= RECYCLE;
        break;
        /* F2 */
case 61:
        if(!(action & DIDDLE)) {
            diddle_menu();
            new_axis = 1;
        }
        break;
        /* F3 */
case 62:
        if (action & DIDDLE) {
            action &= ~DIDDLE;
            didon = 0;
            new_axis = 1;
            temppar=iparm;
        }
        break;
        /* F4 */
case 63:
        if(!(action & (ESCAN | ISCAN | ASCAN))) {
            temppar=iparm;
            scan_menu();
        }
        break;
        /* F5 */
case 64:
        if (action & (ESCAN | ISCAN | ASCAN)) {
            action &= ~(ESCAN | ISCAN | ASCAN);
            action |= INVALID;
            iparm=temppar;
            action &= ~INVALID;
            action |= NEWI;
            if(action & SCANPLOT) {
                opage=page;
                page=6;
                action &= ~SCANPLOT;
                new_axis=1;
            }
        }
        break;
        /* F6 */
case 67:
        if (!(action & TDPLOT)) {
            action ^= SCANPLOT;
            if (action & SCANPLOT)    page = opage;
            else {
                opage = page;
            }
        }

```

```

        page = 6;
    }
}
new_axis = 1;
break;
/* F9 */
case 68:
    if(!(action & SCANPLOT)) {
        action ^= TDPLLOT;
        if (action & TDPLLOT)    page = 6;
        else {
            page = 7;
        }
    }
    new_axis = 1;
    break;
/* F10 */
case 104: break;
/* Alt F1 */
case 113: break;
/* Alt F10 */
default:
    help_menu();
    new_axis = 1;
    break;
}
if (new_axis || new_pvec) plot();
}

/***** MAIN *****/
main()
{
    char c=0;
    int i;
    cls();
    printf(HEADLN);

    lab_date_set();
    strcpy(filnam, lab_date_string);

    printf("\n\n\t!! Insure the CAMAC crate is on and
connected to the AT !!\n");
    printf("\t!! then hit {enter}    !!");
    getch();

    init();
    if(!(action & CRATEOK)) dum_data();
    do {
        set_mode(6);
        s_hand('r');
        do {
            do{ while (scanner);
                if (action & (ESCAN | ISCAN | ASCAN))
                else action |= READSA;
                if (kbhit()) s_hand(c=getch());
            } while (1);
        } while (1);
    } while (1);
}

```

```

        else s_hand(c='p');
    } while (!tddone && (c!='q') && (c!=27));
    s_hand('p');
    do {
        if (kbhit()) s_hand(c=getch());
    } while (tddone && (c!='q') && (c!=27));
    } while ((c!='q') && (c!=27));
    set_mode(3);
    locate(5,10);
    printf(HEADLN);
    printf("\n\t\tAre You Ready to Exit This Routine
(*/)?)");
    getch();
    printf("\n\t\tAll Experimental Control Will
Cease(*/)?)");
    getch();
    printf("\n\t\t hit <q> to exit (<q>/?):");
    c=getch();
    } while (c!='q');
    leave();
}

```

Supporting Assembly Language Routines

FILENAME: BMOVE.ASM

PAGE 60,132

TITLE BMOVE - BLOCK MOVE FUNCTION (SMALL memory model)

```

;*****
; void
bmove(unsigned,unsigned,unsigned,unsigned,unsigned,unsigned)
;
;
; A simple byte string block move function to be called from
C progs.
;
; use in form
;
bmove(from_seg,from_off,to_seg,to_off,count,direction)
;
;where from_seg = source segment ( 0 uses current DS
from C prog.)
; from_off = source offset
; to_seg = destination segment ( 0 uses current ES
from C prog.)
; to_off = destination offset
; count = number of bytes to move

```

```

;   direction= direction of move ( 0=foreward, else
backward)
;
;
;*****

.286c
_TEXT      SEGMENT BYTE PUBLIC 'CODE'
          ASSUME  CS:_TEXT

PUBLIC  _bmove

_bmove  proc   NEAR

    push bp
    mov  bp,sp
    pusha
    push ds
    push es
    cld
    mov  ax,[bp+14]
    or   ax,ax
    jz   set_regs
    std
set_regs:
    mov  si,[bp+6]
    mov  ax,[bp+8]
    or   ax,ax
register?:
    jz   this_seg
    mov  es,ax
this_seg:
    mov  di,[bp+10]
index:
    mov  cx,[bp+12]
    mov  ax,[bp+4]
    or   ax,ax
DS register?:
    jz   doit
    mov  ds,ax
doit:
    rep  movsb
    cld
(required for C)
    pop es
    pop ds
    popa
    mov  sp,bp
    pop  bp
    ret
_bmove  endp

```



```

_TEXT      ends
end
;*****

```

FILENAME: DOS.ASM

PAGE 60,132

NAME dos

TITLE dos GENERAL int 21h FUNCTION CALL (SMALL memory model)

COMMENT \$

```
void dos(unsigned *,unsigned *,unsigned *,unsigned *);
```

To be called from a C program the in form:

```
dos(&ax,&bx,&cx,&dx);
```

where &ax = pointer to variable (int) which is the ax register

contents at time of the DOS function call.

ah selects the particular DOS function called

al is used for value returns from the DOS function

&bx, &cx, &dx = pointers to 16bit variables for the

bx,cx,and dx registers at time of DOS call.

\$

.286c

```
_TEXT SEGMENT BYTE PUBLIC 'CODE'
```

```
ASSUME CS:_TEXT
```

```
PUBLIC _dos
```

```
_dos PROC NEAR
```

```
push bp
```

```
mov bp,sp
```

```
pusha
```

```
;
```

```
push ds
```

```
;
```

```
push es
```

```
;
```

```
mov si,[bp+4]
```

```
; get pointer to ax value
```

```
mov ax,[si]
```

```
; put in ax register
```

```
mov si,[bp+6]
```

```
; get pointer to bx value
```

```
mov bx,[si]
```

```
mov si,[bp+8]
```

```
; get pointer to cx value
```

```
mov cx,[si]
```

```
mov si,[bp+10]
```

```
; get pointer to dx value
```

```
mov dx,[si]
```

```

        int 21h                ; make the DOS call
        mov si,[bp+10]         ; get pointer to dx storage area
for return
        mov [si],dx
        mov si,[bp+8]          ; now update

```

FILENAME: DOS6.ASM

page 60,132

COMMENT \$

```

;*****
;               dot6.asm               Version 09-10-86
;
;    /pjb
;    Places a dot on the screen in the position (x,y)
(MODE 6 ONLY!)
;
;    use in form      dot6(x,y)      x,y unsigned or int
;
;    in mode 6:              0 <= x < 640    0 <= y <
200
;
;    (0,0) is the upper left hand corner
of the screen
;
;    For the 80286!
;
;    No choice of color or erase provided
;    No range checking on input x,y performed
;    For Microsoft C Version 3 code calls
;*****
$
.286c
TEXT      SEGMENT  BYTE PUBLIC 'CODE'
TEXT      ENDS
CONST     SEGMENT  WORD PUBLIC 'CONST'
CONST     ENDS
BSS SEGMENT  WORD PUBLIC 'BSS'
BSS ENDS
DATA      SEGMENT  WORD PUBLIC 'DATA'
DATA      ENDS
DGROUP    GROUP    CONST,    BSS,    DATA
ASSUME CS: TEXT, DS: DGROUP, SS: DGROUP, ES: DGROUP
TEXT      SEGMENT
public _dot6

_dot6     proc near
;----- Save registers on the stack-----
        push bp
        mov bp,sp
        pusha
        push ds
        push es

```

```

;----- Set Video Segment -----
    mov ax,0B800h
    mov ds,ax
;----- Calculate bit mask and store x for later -----
    mov ax,[bp+4]      ; fetch x
    mov di,ax          ; store x in di
    and ax,00007h      ; mask off first three bits of
x
    mov cx,ax          ; set count register to x%8
    mov ax,00080h      ; load 128 into ax
    shr ax,cl          ; shift ax to the right ax&7
times
    mov cx,ax          ; cx is the pixel mask
;----- Calculate Video address offset -----
    mov ax,[bp+6]      ; fetch y
    mov ah,al          ; move y into al
    and ax,01FEh       ; mask off unwanted parts
    shl ax,3           ; (y/2) *16 + (y%2)*2048
    mov bx,ax          ; into bx
    and bh,7           ; bx = (y/2)*16
    shl ax,2           ; ax = (y/2)*64 + (y%2)*8k
    add bx,ax          ; address = y*80 + adjust for even\odd
    mov ax,di          ; get x-coord
    sar ax,3           ; (x/8)
    add bx,ax          ; this is the video address offset
    or ds:[bx],cl      ; add new pixel
;-----Restore the registers -----
    pop es
    pop ds
    popa
    mov sp,bp
    pop bp
    ret
_dot6    endp
_TEXT    ENDS
        END

```

FILENAME: PIC.ASM

page 60,132

COMMENT \$

TIC FUNCTIONS

Version date = 10/07/86

/pjb

use with Microsoft C version 4.00 (SMALL MEMORY
MODEL)

unsigned ticon(void);

Installs a timer tic interrupt handler at interrupt vector 1C.

present interrupt frequency is 18.2 Hz

Each timer interrupt will invoke a C function named <void tic(void)>

Return Value:

0 if Tic turned on OK

1 if Tic was already on

? offset of int vector 1C if different from expected and

Tic was not on.

void ticoff(void);

Turns off the <tic> function call. MUST BE CALLED BEFORE EXITING

THE MAIN PROGRAM THAT CALLED <ticon()> !!!

unsigned isticon(void);

returns a 1 if tic is being repetatively invoked and 0 if not.

The _CINT_HAND cannot interrupt itself. Therefore a tic routine that takes too long will slow the repetition frequency of interrupts never allow the host program to regain control. Be careful!

----- RESTRICTIONS

The Stack Size of the host C program must not exceed the value of

CSTACK (now 0x2000=8k) minus the stack allocation at the time of the

call to ticon(). The host program must be linked with a stack

segment exceeding this value by the expected size of the interrupt

stack. I suggest a link stack size of 0x4000 giving approximately

8k for the interrupt stacks use.

\$

.286c
.287

EXTRN _tic:NEAR, __fpreset:NEAR

_TEXT SEGMENT BYTE PUBLIC 'CODE'
_TEXT ENDS
_CONST SEGMENT WORD PUBLIC 'CONST'
_CONST ENDS

_BSS SEGMENT WORD PUBLIC 'BSS'
_BSS ENDS

_DATA SEGMENT WORD PUBLIC 'DATA'
_DATA ENDS

DGROUP GROUP _CONST, _BSS, _DATA

_TEXT SEGMENT
PUBLIC _ticon, _ticoff, _isticon ;

INTNUM EQU 01Ch ; Interrupt to be intercepted

VECSEG EQU 0F000h ; Expected Segment of int

1C vec

VECOFF EQU 0FF53h ; Expected offset of int

1C vec

CSTACK EQU 02000h ; Host Stack Size

DOSINT EQU 021h ; DOS function interrupt

GETVEC EQU 035H ; DOS function to get int vec

ES:BX

SETVEC EQU 025h ; DOS function to set int vec

DS:DX

O_VEC dd 0 ; storage for int 1C vector

C_DS dw 0 ; C's data (DGROUP) segment

TIC_SP dw 0 ; sp for tic()

SP_ON_INT dw 0 ; sp upon entry of _CINT_HAND

SS_ON_INT dw 0 ; ss on entry

TIC_ON_FLAG dw 0 ; a flag to see if ticon() is set

RET_VAL dw 0 ; return value for ticon()

DAT dw 100d dup(0) ; Storage for 80287 parameters

STATE dw 100d dup(0) ; Storage for 80287 parameters

ASSUME cs: _TEXT, ds: DGROUP, ss: DGROUP

_ticon PROC NEAR

push bp

mov bp,sp

pusha

push ds

;

;

; push all registers

; save segment regs


```

        push es                ; too!
        cmp [TIC_ON_FLAG],0    ; see if tic is off
        je putiton             ; if not, put it on
        mov [RET_VAL],1        ; otherwise do nothing
but
        jmp return              ; return value 1 (for
tic already on)

        putiton:
        mov [TIC_ON_FLAG],1    ; set flag for additional
calls
        mov [C_DS],ss          ; save DGROUP
        mov ax,sp               ;
        sub ax,CSTACK           ; set interrupt stack CSTACK
below call
        mov [TIC_SP],ax        ; Limits C's stack to
CSTACK !!
        mov al,INTNUM           ; Use DOS int 21 func 35h
        mov ah,GETVEC           ; to get original
        int DOSINT              ; int 1C vector into ES:BX
        mov WORD PTR [O_VEC],bx ; and store in OLD_VEC
        mov WORD PTR [O_VEC+2],es ; ..done
        mov ax, WORD PTR [O_VEC] ;
        cmp ax,VECOFF           ;
        jne bad                 ;
        mov ax, WORD PTR [O_VEC+2] ;
        cmp ax,VECSEG           ;
        jne bad                 ; test for proper initial
vector
        mov [RET_VAL],0        ; set return value 0 for
address ok

        mov dx,OFFSET _CINT_HAND ; set address of _CINT_HAND
        mov ax,_TEXT            ;
        mov ds,ax               ; set code segment as well
        mov al,INTNUM           ; and use DOC func 25h
        mov ah,SETVEC           ; to load it into vector table
        int DOSINT              ; ..done
        jmp return              ;

bad:                                ; if previous interrupt vector
unknown
        mov ax,WORD PTR [O_VEC] ; set return value to
equal
        mov [RET_VAL],ax        ; offset of installed vector
                                ; and return without installation
return:
        pop es                  ;
        pop ds                  ; restore seg regs
        popa                    ; restore all registers
        mov sp,bp              ;
        mov ax,[RET_VAL]       ; send return value in ax

```



```

        pop bp                ; (return is unsigned)
        ret                  ; return to caller
_ticon      ENDP

page
_ticoff     PROC NEAR
        push bp              ;
        mov bp,sp            ;
        pusha                ;

        mov ax,[TIC_ON_FLAG] ; Test flag to see if
<tic> is enabled
        or ax,ax             ;
        jz noton             ;

;must be on
        push ds              ;
        push es              ; save seg regs
        mov [TIC_ON_FLAG],0  ; Clear flag
        mov dx,WORD PTR [O_VEC] ; get vector stored by
_ticon
        mov ds,WORD PTR [O_VEC+2] ;
        mov al,INTNUM         ; and reinstall with DOS
        mov ah,SETVEC         ;
        int DOSINT            ; ..done
        pop es                ;
        pop ds                ; restore seg regs
noton:
        popa                 ; restore all registers
        mov sp,bp            ;
        pop bp               ;
        ret                  ; return to caller
_ticoff     ENDP

_isticon     PROC NEAR ;
        mov ax,[TIC_ON_FLAG] ;
        ret                ;
_isticon     ENDP

page
_CINT_HAND   PROC FAR    ; Far call from ROM BIOS?

        mov [SP_ON_INT],sp ; store whatever was in
sp
        mov [SS_ON_INT],ss ; and ss

        mov sp,[TIC_SP]    ; setup 'interrupt' stack
        mov ss,[C_DS]      ; pointer and segment!

        pusha              ; now push all parameters
        pushf              ;
        push ds            ;

```

```

                push es                ; everything on 286 saved
on stack
wait1:                ; wait until 80287 free
    fnstsw ax
    and ax,08000h
    jnz wait1

    cli
    fsave cs:STATE        ; save 80287 state
    fwait                ; wait til done
    sti

    cld                ; clear direction flag (needed in
C)    mov es,[C_DS]        ; setup other segment
    registers for
        mov ds,[C_DS]        ; 'small' memory model

    call _tic            ; call C tic function (no args)

wait2:                ; wait until 80287 free
    fnstsw ax
    and ax,08000h
    jnz wait2

    cli
    frstor cs:STATE        ; restore 80287 state
    fwait                ; wait til done
    sti

    pop es                ;
    pop ds                ;
    popf                ;
    popa                ; restore 286 registers and flags
    mov sp,[SP_ON_INT]    ; restore old sp
    mov ss,[SS_ON_INT]    ; and ss
    iret                ; return? (we hope!)
_CINT_HAND    ENDP

_TEXT    ENDS
    END
;*****

```

FILENAME: PRSCRN()

PAGE 60,132

COMMENT \$

prscrn() SUBROUTINE:

void prscrn(void);

Calls interrupt 5h to implement screen dump

\$

.286c

```
_TEXT    SEGMENT BYTE PUBLIC 'CODE'
        PUBLIC _prscrn
        ASSUME CS:_TEXT
```

```
_prscrn proc near
```

```
    push bp
    mov bp,sp
    pusha
    push ds
    push es
```

```
    INT    5H                ; call the prscrn interrupt routine
```

```
    pop es
    pop ds
    popa
    mov sp,bp
    pop bp
    ret
```

```
_prscrn ENDP
_TEXT    ENDS
        END
```

FILENAME: PTIC.ASM

page 60,132

COMMENT \$

TIC FUNCTIONS

Version date = 10/07/86

/pjb

use with Microsoft C version 4.00 (SMALL MEMORY

MODEL)

unsigned ticon(void);

Installs a timer tic interrupt handler at interrupt vector 1C.

present interrupt frequency is 18.2 Hz

Each timer interrupt will invoke a C function named

<void tic(void)>

Return Value:

0 if Tic turned on OK

1 if Tic was already on

? offset of int vector 1C if different from
expected and

Tic was not on.

void ticoff(void);

Turns off the <tic> function call. MUST BE CALLED
BEFORE EXITING

THE MAIN PROGRAM THAT CALLED <ticon()> !!!

unsigned isticon(void);

returns a 1 if tic is being repetatively invoked and 0
if not.

The _CINT_HAND cannot interrupt itself. Therefore a
tic routine
that takes too long will slow the repetition frequency
of interrupts
never allow the host program to regain control. Be
careful!

RESTRICTIONS

The Stack Size of the host C program must not exceed
the value of
CSTACK (now 0x2000=8k) minus the stack allocation at
the time of the
call to ticon(). The host program must be linked with
a stack
segment exceeding this value by the expected size of
the interrupt
stack. I suggest a link stack size of 0x4000 giving
approximately
8k for the interrupt stacks use.

```
*****
$
.286c
.287
```

```
EXTRN  __TIC:NEAR, __fpreset:NEAR
```

```
__TEXT  SEGMENT  BYTE PUBLIC 'CODE'
__TEXT  ENDS
```

```

_CONST      SEGMENT  WORD PUBLIC 'CONST'
_CONST      ENDS
_BSS SEGMENT  WORD PUBLIC 'BSS'
_BSS ENDS
_DATA      SEGMENT  WORD PUBLIC 'DATA'
_DATA      ENDS
DGROUP     GROUP      _CONST,  _BSS,  _DATA

TEXT       SEGMENT
PUBLIC     _TICON, _TICOFF, _ISTICON ;

INTNUM      EQU  01Ch      ; Interrupt to be intercepted

VECSEG      EQU  0F000h     ; Expected Segment of int
1C vec
VECOFF      EQU  0FF53h     ; Expected offset of int
1C vec

CSTACK      EQU  02000h     ; Host Stack Size

DOSINT      EQU  021h       ; DOS function interrupt
GETVEC      EQU  035H       ; DOS function to get int vec
ES:BX
SETVEC      EQU  025h       ; DOS function to set int vec
DS:DX

O_VEC       dd  0           ; storage for int 1C vector
C_DS        dw  0           ; C's data (DGROUP) segment
TIC_SP      dw  0           ; sp for tic()
SP_ON_INT   dw  0           ; sp upon entry of _CINT_HAND
SS_ON_INT   dw  0           ; ss on entry
TIC_ON_FLAG dw  0           ; a flag to see if ticon() is
set
RET_VAL     dw  0           ; return value for ticon()
DAT         dw  200d dup(0) ; Storage for 80287 parameters

ASSUME      cs: _TEXT, ds: DGROUP, ss: DGROUP

_TICON      PROC NEAR
    push bp
    mov bp,sp
    pusha
    push ds
    push es
    cmp [TIC_ON_FLAG],0
    je putiton
    mov [RET_VAL],1
but
    jmp return
tic already on)

    putiton:

```



```

        mov [TIC_ON_FLAG],1          ; set flag for additional
calls   mov [C_DS],ss                ; save DGROUP
        mov ax,sp                    ;
        sub ax,CSTACK                ; set interrupt stack CSTACK
below call
        mov [TIC_SP],ax              ; Limits C's stack to
CSTACK !!
        mov al,INTNUM                ; Use DOS int 21 func 35h
        mov ah,GETVEC                ; to get original
        int DOSINT                   ; int 1C vector into ES:BX
        mov WORD PTR [O_VEC],bx      ; and store in OLD_VEC
        mov WORD PTR [O_VEC+2],es    ; ..done
        mov ax, WORD PTR [O_VEC] ;
        cmp ax,VECOFF                ;
        jne bad                      ;
        mov ax, WORD PTR [O_VEC+2] ;
        cmp ax,VECSEG                ;
        jne bad                      ; test for proper initial
vector
        mov [RET_VAL],0              ; set return value 0 for
address ok

        mov dx,OFFSET _CINT_HAND ; set address of _CINT_HAND
;   mov dx, WORD PTR [O_VEC] ; set old vector offset back
(for Debug)
        mov ax,_TEXT                ;
        mov ds,ax                   ; set code segment as well
;   mov ds, WORD PTR [O_VEC+2] ; set old vector segment
backi (for Debug)
        mov al,INTNUM                ; and use DOC func 25h
        mov ah,SETVEC                ; to load it into vector table
        int DOSINT                   ; ..done
        jmp return                   ;

bad:                                     ; if previous interrupt vector
unknown
        mov ax,WORD PTR [O_VEC]      ; set return value to
equal
        mov [RET_VAL],ax             ; offset of installed vector
; and return without installation

return:
        pop es                       ;
        pop ds                       ; restore seg regs
        popa                         ; restore all registers
        mov sp,bp                    ;
        mov ax,[RET_VAL]             ; send return value in ax
        pop bp                      ; (return is unsigned)
        ret                         ; return to caller
_TICON      ENDP

```



```

_TICOFF    PROC NEAR
    push bp
    mov bp,sp
    pusha

    mov ax,[TIC_ON_FLAG]          ; Test flag to see if
<tic> is enabled
    or ax,ax
    jz noton

;must be on
    push ds
    push es
    mov [TIC_ON_FLAG],0          ; save seg regs
    mov dx,WORD PTR [O_VEC]      ; Clear flag
                                ; get vector stored by
_ticon
    mov ds,WORD PTR [O_VEC+2]
    mov al,INTNUM
    mov ah,SETVEC
    int DOSINT
    pop es
    pop ds
                                ; and reinstall with DOS
                                ; ..done
                                ; restore seg regs
noton:
    popa
    mov sp,bp
    pop bp
    ret
                                ; restore all registers
                                ; return to caller
_TICOFF    ENDP

_ISTICON   PROC NEAR
    mov ax,[TIC_ON_FLAG]
    ret
_ISTICON   ENDP

page
_CINT_HAND PROC FAR
    mov [SP_ON_INT],sp
sp
    mov [SS_ON_INT],ss
    mov sp,[TIC_SP]
    mov ss,[C_DS]
    pusha
    pushf
    push ds
    push es
on stack
    mov es,[C_DS]
registers for
    mov ds,[C_DS]

cli

```

```

        fsave _TEXT:DAT                ; save 80287 state in 94
bytes above stack
        fwait                          ; wait til done
        sti
        cld                            ; clear direction flag (needed in
C)

        call _tic                      ; call C tic function (no args)

        cli
        frstor _TEXT:DAT               ; restore 80287 state
        fwait                          ; wait til done
        sti

        pop es                        ;
        pop ds                        ;
        popf                          ;
        popa                          ; restore 286 registers and flags
        mov sp,[SP_ON_INT]            ; restore old sp
        mov ss,[SS_ON_INT]            ; and ss
        iret                          ; return? (we hope!)
_CINT_HAND      ENDP

_TEXT          ENDS
END
;*****

```

FILENAME: SAVE.ASM

```

;*****
;                               SAVE      8-11-85      (SMALL memory
version)
;
; The function to save part of screen.
; Called from C progs in form
;                               save(y1,x1,y2,x2,to_seg)
; where  x1 & y1 = coordinates of upper left corner of the
block to be saved
;         x2 & y2 = coordinates of lower right corner
;         to_seg  = segment address for saving the block
;
;*****
*

```

```

_TEXT      SEGMENT BYTE PUBLIC 'CODE'
          ASSUME  CS:_TEXT

PUBLIC  _save

```

```

x1    dw    ?
y1    dw    ?
x2    dw    ?
y2    dw    ?
count    dw    ?
stop   dw    ?
display1 equ    0B800H
odd     equ    01FFFH

```

```

_save    proc    NEAR

```

```

    push bp
    mov bp,sp
    push ax
    push bx
    push cx
    push dx
    push ds
    push es
    push si
    push di
    mov bx,[bp+6] ; get x1
    mov x1,bx
    mov bx,[bp+4] ; get y1
    mov y1,bx
    mov bx,[bp+10] ; get x2
    mov x2,bx
    mov bx,[bp+8] ; get y2
    mov y2,bx
    mov ax,display1 ; from_seg
    mov ds,ax
    mov bx,[bp+12] ; to_seg
    mov es,bx
    mov ax,y1
    mov dx,320
    mul dx
    add ax,x1
    mov si,ax ; from_off
    mov di,ax ; to_off
    mov ax,x2
    sub ax,x1
    add ax,2
    mov count,ax ; counts
    mov ax,y2
    add ax,1
    mov dx,320
    mul dx
    add ax,x1
    mov stop,ax ; set end
    cmp si,stop
    jg out1
doit:

```

```

    cld
    mov  cx,count
    rep  movsb          ; do the mov [DS:SI] --> [ES:DI]
    add  si,odd         ; do odd row
    add  di,odd
    std
    mov  cx,count
    rep  movsb          ; mov odd row
    sub  si,odd         ; back to even row
    sub  di,odd
    add  si,80
    add  di,80
    cmp  si,stop
    jl   doit
out1:
    cld
    pop  di
    pop  si
    pop  es
    pop  ds
    pop  dx
    pop  cx
    pop  bx
    pop  ax
    mov  sp,bp
    pop  bp
    ret
_save   endp
_TEXT   ends
end

```

FILENAME: STL.ASM

```

;          stl(x1,y1,x2,y2,color)          (SMALL memory
model)
;   version date = 8-11-85
;
; ROUTINE TO DRAW A LINE ON A MEDIUM RESOLUTION SCREEN
; From  "BLUEBOOK OF ASSEMBLY ROUTINES FOR THE IBM PC & XT"
;          By C.L. MORGAN
;   adapted for linking with Microsoft C programs
;          by  pjb
;
_TEXT   SEGMENT  BYTE PUBLIC 'CODE'
        PUBLIC   _stl
        ASSUME   cs:_TEXT
;
;
;
x1      dw      ?

```

```

x2    dw    ?
y1    dw    ?
y2    dw    ?
color      dw    ?
deldx      dw    ?
deldy      dw    ?
delde      dw    ?
delsx      dw    ?
delsy      dw    ?
delse      dw    ?
delp       dw    ?
dels dw    ?
;
;
_stl      proc      NEAR
          push      bp
          mov       bp,sp
          push      bx
          push      cx
          push      dx
          push      si
          push      di
          push      ax
          mov       bx,[bp+4]
          mov       x1,bx
          mov       bx,[bp+6]
          mov       y1,bx
          mov       bx,[bp+8]
          mov       x2,bx
          mov       bx,[bp+10]
          mov       y2,bx
          mov       bx,[bp+12]
          mov       color,bx
          mov       si,1
          mov       di,1
          mov       dx,y2
          sub       dx,y1
          jge       storey
          neg       di
          neg       dx
storey:
          mov       deldy,di
          mov       cx,x2
          sub       cx,x1
          jge       storex
          neg       si
          neg       cx
storex:
          mov       deldx,si
          cmp       cx,dx
          jge       setdiag
          mov       si,0

```

```

                                xchg    cx,dx
                                jmp      storedelsxy
setdiag:
                                mov      di,0
storedelsxy:
                                mov      dels,cx
                                mov      delp,dx
                                mov      delsx,si
                                mov      delsy,di
                                mov      si,x1
                                mov      di,y1
                                mov      ax,delp
                                sal      ax,1
                                mov      delse,ax
                                sub      ax,cx
                                mov      bx,ax
                                sub      ax,cx
                                mov      delde,ax
                                inc      cx
                                mov      dx,color
lineloop:
                                push     ax
                                push     bx
                                push     cx
                                push     dx
                                mov      bh,0          ;    page 0!
                                mov      al,dl
                                mov      cx,si
                                mov      dx,di
                                mov      ah,12          ;    write dot
                                int      10h
                                pop      dx
                                pop      cx
                                pop      bx
                                pop      ax
                                cmp      bx,0
                                jge      diagonal
straight:
                                add      si,delsx
                                add      di,delsy
                                add      bx,delse
                                loop     lineloop
                                jmp      lineexit
diagonal:
                                add      si,deldx
                                add      di,deldy
                                add      bx,delde
                                loop     lineloop
lineexit:
                                cld
                                pop      ax
                                pop      di
                                pop      si

```



```

                pop     dx
                pop     cx
                pop     bx
                mov     sp, bp
                pop     bp
                ret
_stl            endp
_TEXT          ends
end

```

FILENAME: STL6.ASM

page 60,132

COMMENT \$

stl6(x1,y1,x2,y2) x1,x2,y1,y2 unsigned

Version date = 09-03-86

\pjb

ROUTINE TO DRAW A STRAIGHT LINE ON A MODE 6

SCREEN

ADAPTED FROM "BLUEBOOK OF ASSEMBLY ROUTINES FOR THE
IBM PC & XT"

By C.L. MORGAN

for linking with Microsoft C Version 3.0 programs

```

$
.286c
_TEXT      SEGMENT  BYTE PUBLIC 'CODE'
_TEXT      ENDS
_CONST     SEGMENT  WORD PUBLIC 'CONST'
_CONST     ENDS
_BSS       SEGMENT  WORD PUBLIC 'BSS'
_BSS       ENDS
_DATA      SEGMENT  WORD PUBLIC 'DATA'
_DATA      ENDS
DGROUP     GROUP    _CONST, _BSS, _DATA
            ASSUME  CS: _TEXT, DS: DGROUP, SS: DGROUP, ES: DGROUP
_TEXT      SEGMENT

```

```

public _stl6
    x1 dw ?
    x2 dw ?
    y1 dw ?
    y2 dw ?
    deldx dw ?
    deldy dw ?
    delde dw ?

```

```

delsx    dw    ?
delsy    dw    ?
delse    dw    ?
delp     dw    ?
dels dw    ?

```

```

_stl6      PROC      NEAR
            push      bp
            mov       bp,sp
            pusha
            mov       bx,[bp+4]
            mov       x1,bx
            mov       bx,[bp+6]
            mov       y1,bx
            mov       bx,[bp+8]
            mov       x2,bx
            mov       bx,[bp+10]
            mov       y2,bx
            mov       si,1
            mov       di,1
            mov       dx,y2
            sub       dx,y1
            jge       storey
            neg       di
            neg       dx
storey:
            mov       deldy,di
            mov       cx,x2
            sub       cx,x1
            jge       storex
            neg       si
            neg       cx
storex:
            mov       deldx,si
            cmp       cx,dx
            jge       setdiag
            mov       si,0
            xchg      cx,dx
            jmp       storedelsxy
setdiag:
            mov       di,0
storedelsxy:
            mov       dels,cx
            mov       delp,dx
            mov       delsx,si
            mov       delsy,di
            mov       si,x1
            mov       di,y1
            mov       ax,delp
            sal       ax,1
            mov       delse,ax
            sub       ax,cx

```

```

        mov     bx,ax
        sub     ax,cx
        mov     delde,ax
        inc     cx

lineloop:  pusha
          push ds

;   ***       write a dot to x=si y=di       ***

;----- Set video segment -----
        mov ax,0B800h
        mov ds,ax
;----- Calculate Video address offset -----
        mov ax,di                ; fetch y
        mov ah,al                ; move y into al
        and ax,01FEh             ; mask off unwanted parts
        shl ax,3                 ; (y/2) *16 + (y%2)*2048
        mov bx,ax                ; into bx
        and bh,7                 ; bx = (y/2)*16
        shl ax,2                 ; ax = (y/2)*64 + (y%2)*8k
        add bx,ax                ; address = y*80 + adjust for even\odd
        mov ax,si                ; get x-coord
        sar ax,3                 ; (x/8)
        add bx,ax                ; this is the video address offset
;----- Calculate bit mask -----
        mov ax,si                ; fetch x
        and ax,00007h            ; mask off first three bits of
x                                     ;
        mov cx,ax                ; set count register to x%8
        mov ax,00080h            ; load 128 into ax
        shr ax,cl                ; shift ax to the right ax&7
times
        mov cx,ax                ; cx is the pixel mask
        or ds:[bx],cl            ; add new pixel
;----- Restore the registers (done)-----

        pop ds
        popa

        cmp     bx,0
        jge     diagonal

straight:
        add     si,delsx
        add     di,delsy
        add     bx,delse
        loop    lineloop
        jmp     lineexit

diagonal:
        add     si,deldx
        add     di,deldy
        add     bx,delde

```

```

PAGE 60,132
TITLE      _vidio SUBROUTINE          (SMALL  memory version)
;          _VERSION DATE 10-13-86    /pjb
;                                     For use with Microsoft C
version 3.00
;          void _vidio(unsigned *,unsigned *,unsigned
*,unsigned *);
;
;          Call as:                   _vidio(&AX,&BX,&CX,&DX);
;
;          where the arguments are pointers to the C variables AX,
BX, CX, DX.
;
;
.286c
_TEXT      SEGMENT BYTE PUBLIC 'CODE'
PUBLIC _vidio
ASSUME CS:_TEXT
;
;_vidio      proc          NEAR
;          PUSH BP
;          MOV  BP,SP
;          pusha
;          mov si,[BP+4]      ;get pointer to AX
;          mov ax,[si]        ;put AX in ax register
;          mov si,[BP+6]      ;get pointer to BX
;          mov bx,[si]        ;put BX in bx register
;          mov si,[BP+8]      ;get pointer to CX
;          mov cx,[si]        ;put CX in cx register
;          mov si,[BP+10]     ;get pointer to DX
;          mov dx,[si]        ;put DX in dx register
;
;          INT 10H            ; call the _vidio_io interrupt
routine
;
;          mov si,[bp+10]     ;get pointer to DX
;          mov [si],dx        ;update DX value
;          mov si,[bp+8]      ;get pointer to CX
;          mov [si],cx        ;update CX value

```

```

        mov si,[bp+6]          ;get pointer to BX
        mov [si],dx            ;update BX
        mov si,[bp+4]          ;get pointer to AX
        mov [si],ax            ;update AX
        cld                    ; clear direction flag for C return
        popa
        MOV SP,BP
        POP BP
        RET
_vidio   endp
_TEXT   ENDS
        END

```

FILENAME: WMOVE.ASM

PAGE 60,132

TITLE wmove - BLOCK MOVE FUNCTION (SMALL memory model)

```

;*****
; void
wmove(unsigned,unsigned,unsigned,unsigned,unsigned,unsigned)
;
;
; A simple word string block move function to be called from
C progs.
;
; use in form
;
wmove(from_seg,from_off,to_seg,to_off,count,direction)
;
;where from_seg = source segment ( 0 uses current DS
from C prog.)
; from_off = source offset
; to_seg = destination segment ( 0 uses current ES
from C prog.)
; to_off = destination offset
; count = number of bytes to move
; direction= direction of move ( 0=foreward, else
backward)
;
; VERSION DATE = 10-13-1986
/pjb
;*****
*

```

.286c

```

_TEXT   SEGMENT BYTE PUBLIC 'CODE'
        ASSUME CS:_TEXT

```

PUBLIC _wmove

_wmove proc NEAR

```

    push bp
    mov bp,sp
    pusha
    push ds
    push es
    cld
    mov ax,[bp+14]
    or ax,ax
    jz set_regs
    std
set_regs:
    mov si,[bp+6]
    mov ax,[bp+8]
    or ax,ax
register?:
    jz this_seg
    mov es,ax
this_seg:
    mov di,[bp+10]
index:
    mov cx,[bp+12]
    mov ax,[bp+4]
    or ax,ax
DS register?:
    jz doit
    mov ds,ax
doit:
    rep movsw
    cld
(required for C)
    pop es
    pop ds
    popa
    mov sp,bp
    pop bp
    ret
_wmove endp
_TEXT ends
end
;*****
```


APPENDIX C ANALYTIC PAIR POTENTIALS

Lennard-Jones Potentials

One of the goals of this research is to establish a potential energy surface that will accurately describe the interatomic forces of an inductively bound pair. Even with little spectroscopic data, some fundamental analytic potentials may be parameterized. In the case of Lennard-Jones types potentials the determination of single adjustable parameter reveals the vibrational frequency, ν_e , the Dissociation energy, D_e , and the internuclear distance, r_e .

An approximation for the potential energy surface of a transition-metal rare gas diatomic is given in analytic form by Lennard-Jones [8,4]. The attractive part is described by the polarizability over r_e^4 . The repulsive part is proportional to $1/r_e^8$. The form of the potential is then given by the following equation¹⁷

$$U(r) = \frac{\beta}{r^8} - \frac{\alpha e^2}{2r^4} \quad (39)$$

where α is the polarizability for the rare gas species, e is the proton charge, and β is an adjustable parameter fit to

experiment data. For transition-metal rare gas diatomic systems the polarizability may be closely approximated to that of the rare-gas atom. Thus, the analytic equation becomes adjustable with a single parameter, β .

Often experimental data is sufficient enough to determine the equilibrium vibrational frequency, ν_e , or the dissociation energy D_e , and in some instances both. With a single adjustable parameter in the Lennard-Jones expression only one experimentally determined parameter is necessary to determine all the others, i.e., D_e , ν_e , or r_e . This appendix derives expressions relating ν_e or D_e , to β , r_e , and k_e , the force constant, using cgs units.

The first derivative of Eq. (39) is zero at $r = r_e$,

$$\frac{\partial U(r_e)}{\partial r} = -\frac{8\beta}{r_e^9} + \frac{2\alpha e^2}{r_e^5} = 0 \quad (40)$$

The second derivative of Eq. (39) is defined¹¹⁸ as the force constant k_e ,

$$\frac{\partial^2 U(r_e)}{\partial r^2} = \frac{72\beta}{r_e^{10}} - \frac{10\alpha e^2}{r_e^6} = k_e. \quad (41)$$

Solving Eq. (40) for β results in the following expression:

$$\beta = \frac{1}{4}\alpha e^2 r_e^4. \quad (42)$$

Substituting this back into the potential energy Eq. (39), one may express β in terms of the dissociation energy D_e , recall that $U(r_e) = -D_e$,

$$\beta = \frac{\alpha^2 e^4}{16 D_e}. \quad (43)$$

The internuclear distance may be easily expressed in terms of the dissociation energy by combining Eq. (42) and Eq. (43), then solving for r_e ,

$$r_e = \sqrt{\frac{e}{2}} \left(\frac{\alpha}{D_e} \right)^{1/4}. \quad (44)$$

Conversely the dissociation energy may be expressed in terms of r_e :

$$D_e = \frac{\alpha e^2}{4 r_e^4} \quad (45)$$

Substitution of β from Eq. (42) into Eq. (41) results in an expression relating the force constant to internuclear distance as:

$$k_e = \frac{8 \alpha e^2}{r_e^6}, \quad \text{or} \quad r_e = \sqrt{2} e^{1/3} \left(\frac{\alpha}{k_e} \right)^{1/6}. \quad (46)$$

The force constant may be expressed in terms of D_e by substitution of Eq. (44) into Eq. (46), as:

$$k_e = \frac{64 D_e^{3/2}}{e \sqrt{\alpha}}, \quad \text{or} \quad D_e = \frac{(e k_e)^{2/3} \alpha^{1/3}}{16}. \quad (47)$$

For a harmonic oscillator the equilibrium vibrational frequency, ν_e , is a function of the force constant and the reduced mass, μ ,

$$\nu_e = \frac{1}{2\pi} \sqrt{\frac{k_e}{\mu}}. \quad (48)$$

Substitution of k_e from Eq. (47) into Eq. (48) one may relate ν_e and D_e as follows:

$$\nu_e = \frac{4D_e^{3/4}}{\pi\alpha^{1/4}(\mu e)^{1/2}} \quad \text{or} \quad D_e = \left(\frac{\pi\nu_e}{4}\right)^{4/3} \alpha^{1/3} (\mu e)^{2/3}. \quad (49)$$

Another useful equation is the relation of the vibrational frequency to the internuclear distance, which may be determined by the substitution of Eq. (45) into Eq. (49):

$$\nu_e = \sqrt{\frac{2\alpha}{\mu}} \frac{e}{\pi r_e^3} \quad \text{or} \quad r_e = \left(\frac{2\alpha}{\mu}\right)^{1/6} \left(\frac{e}{\pi\nu_e}\right)^{1/3} \quad (50)$$

These manipulations may be done for other Lennard-Jones potential energy expressions. The most relevant of these relations, i.e., with respect to inductively bound systems, the [12,4], [8,4] and [6,4] have been determined, and are displayed in the following tables.

Table 18. Lennard-Jones [8,4] Relations.

	ν_e	D_e
$k_e =$	$\mu (2\pi\nu_e)^2$	$64 \frac{D_e^{3/2}}{\alpha^{1/2}e}$
$\nu_e =$		$\frac{4D_e^{3/4}}{\alpha^{1/4}(\mu e)^{1/2}\pi}$
$D_e =$	$\frac{1}{4^{4/3}} \alpha^{1/3} (\mu e)^{2/3} (\pi\nu_e)^{4/3}$	
$\beta =$	$\frac{1}{2^{4/3}} \left(\frac{\alpha^5 e^{10}}{\mu^2 (\pi\nu_e)^4} \right)^{1/3}$	$\frac{\alpha^2 e^4}{16D_e}$
$r_e =$	$2^{1/6} \left(\frac{\alpha}{\mu} \right)^{1/6} \left(\frac{e}{\pi\nu_e} \right)^{1/3}$	$\frac{1}{\sqrt{2}} e^{1/2} \left(\frac{\alpha}{D_e} \right)^{1/4}$

For CoAr^+ ; $D_e = 2.8688(\nu_e)^{4/3}$ where ν is in cm^{-1} .

For CoKr^+ ; $D_e = 4.2314(\nu_e)^{4/3}$ where ν is in cm^{-1} .

Table 20. Lennard-Jones [6,4] Relations.

	ν_e	D_e
$k_e =$	$\mu (2\pi\nu_e)^2$	$4(6)^{3/2} \frac{D_e^{3/2}}{\alpha^{1/2}e}$
$\nu_e =$		$\frac{6D_e^{3/4}}{\alpha^{1/4}(\mu e)^{1/2}\pi}$
$D_e =$	$(\frac{\alpha}{6})^{1/3} (\mu e)^{2/3} (\nu_e \pi)^{4/3}$	
$\beta =$	$\frac{1}{3} (\frac{\alpha^4 e^8}{\nu_e^2 \pi^2 \mu})^{1/3}$	$\frac{e^3 \alpha^{3/2}}{3\sqrt{6} D_e^{1/2}}$
$r_e =$	$(\frac{\alpha}{\mu})^{1/6} (\frac{e}{\pi \nu_e})^{1/3}$	$\frac{1}{6^{1/4}} e^{1/2} (\frac{\alpha}{D_e})^{1/4}$

Table 22. Lennard-Jones [12,4] Relations.

	ν_e	D_e
$k_e =$	$\mu (2\pi\nu_e)^2$	$16(3)^{3/2} \frac{D_e^{3/2}}{\alpha^{1/2}e}$
$\nu_e =$		$2(3)^{3/4} \frac{D_e^{3/4}}{\alpha^{1/4}(\mu e)^{1/2}\pi}$
$D_e =$	$\frac{1}{3(2)^{4/3}} \alpha^{1/3} (\mu e)^{2/3} (\pi\nu_e)^{4/3}$	
$\beta =$	$\frac{2^{5/3}}{3} \left(\frac{\alpha^7 e^{14}}{\mu^4 \pi^8 \nu_e^8} \right)^{1/3}$	$\frac{\alpha^3 e^6}{54 D_e^2}$
$r_e =$	$2^{1/3} \left(\frac{\alpha}{\mu} \right)^{1/6} \left(\frac{e}{\pi\nu_e} \right)^{1/3}$	$\frac{1}{3^{1/4}} e^{1/2} \left(\frac{\alpha}{D_e} \right)^{1/4}$

Born-Meyer Potential

The second type of analytic potential that has been found to adequately describe the interactions of a transition-metal cation with a rare gas atom is the Born-Meyer potential. The attractive part of this potential is also described with a $1/r^4$ term. The repulsive part of the analytic function involves an exponential term. Again, approximating the polarizability of the interaction with that of the rare-gas atom the Born-Meyer is of the following form:

$$U(r) = be^{-r/\rho} - C/r^4 \quad (51)$$

The two adjustable parameters in the equation, b and ρ may be calculated from the experimentally determined dissociation energy and vibrational frequency. Unlike the Lennard-Jones type potentials, two experimental quantities must be available to uniquely determine the potential surface. For many of the systems previously discussed, both the dissociation energy and the vibrational frequency may be determined, thus leaving only r_e to be predicted by the parameterization of the potential function. In this case a polynomial expression in r_e may be derived as a function of ν_e and D_e .

The first and second derivative of Eq. (51) are listed below. The first derivative is zero at r_e :

$$U'(r_e) = -\frac{b}{\rho} e^{-r_e/\rho} + \frac{4C}{r_e^5} = 0. \quad (52)$$

The second derivative is defined as the force constant, k

$$U''(r_e) = \frac{b}{\rho^2} e^{-r_e/\rho} - \frac{20C}{r_e^6} = k. \quad (53)$$

Equation (51) is equal to the dissociation energy, D_e , at r_e . Solving Eq. (51) for the exponential: (By convention $U(r_e) = -D_e$)

$$e^{-r_e/\rho} = \frac{1}{b} \left(\frac{C}{r_e^4} - D_e \right). \quad (54)$$

Similarly, solving Eq. (52) for the exponential results in

$$e^{-r_e/\rho} = \frac{\rho^4 C}{b r_e^5}. \quad (55)$$

And finally, for Eq. (53) one gets

$$e^{-r_e/\rho} = \frac{\rho^2}{b} \left(k + \frac{20C}{r_e^6} \right). \quad (56)$$

Now we may eliminate both the exponential term and the adjustable parameter b with the combination of Eq. (54) and Eq. (55) and the combination of Eq. (55) and Eq. (56).

Setting Eq. (54) and Eq. (55) equal to other and solving for ρ we get the following equation:

$$\rho = \frac{1}{4C} (Cr_e - D_e r_e^5). \quad (57)$$

Setting Eq. (55) and Eq. (56) equal to each other we get the following equation:

$$\rho \left(k r_e^5 + \frac{20C}{r_e} \right) = 4C. \quad (58)$$

By substituting Eq. (57) into Eq. (58) and rearranging we get a polynomial in r_e ;

$$-\frac{kD_e}{C} r_e^{10} + k r_e^6 - 20D_e r_e^4 + 4C = 0.$$

Recall that the force constant may be expressed in terms of the vibrational frequency and reduced mass as follows:

$$k = 4\pi^2 \omega_e^2 \mu.$$

Substituting this expression into the above equation we get a polynomial in r_e that may be solved numerically given the experimentally determined terms of the vibrational frequency and dissociation energy,

$$(4\pi^2 \omega_e^2 \mu) \left(r_e^6 - \frac{D_e}{C} r_e^{10} \right) - 20D_e r_e^4 + 4C = 0.$$

Once r_e is known one may determine ρ from Eq. (57). The constant C is determined from the polarizability, α , and is

defined as $q^2\alpha/2$, where q is the proton charge. The other adjustable parameter b will follow from Eq.(54).

APPENDIX D

UNASSIGNED PHOTODISSOCIATION SPECTRA

During the course of the research, a number of spectra for various systems have remained unassigned. Many of these spectra are included as figures in this section. Note, none of the spectra have been rigorously calibrated, but they are not inaccurate by more than $\pm 15 \text{ cm}^{-1}$. The relative accuracies of band positions, within a given spectrum, are good to ca. $\pm 2 \text{ cm}^{-1}$.

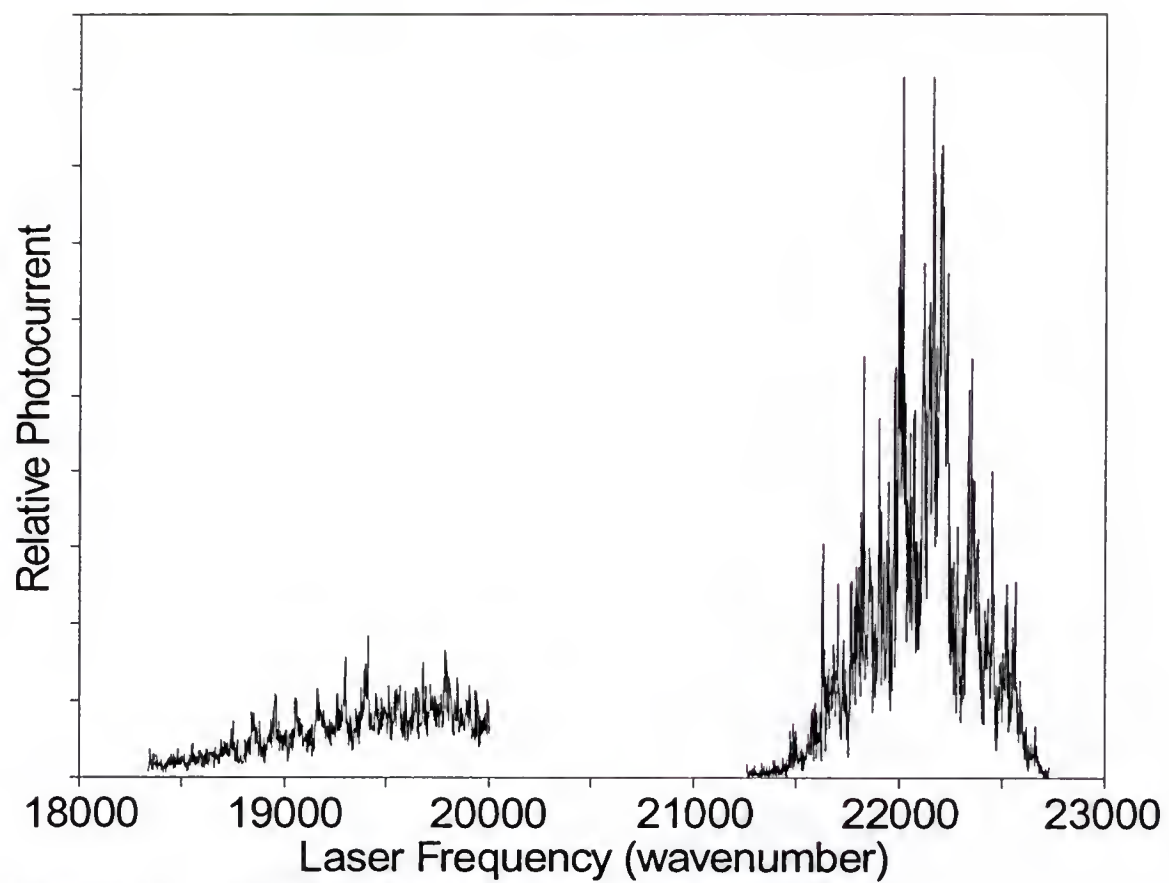


Figure 57. Photodissociation Spectrum of Fe_2^+ .

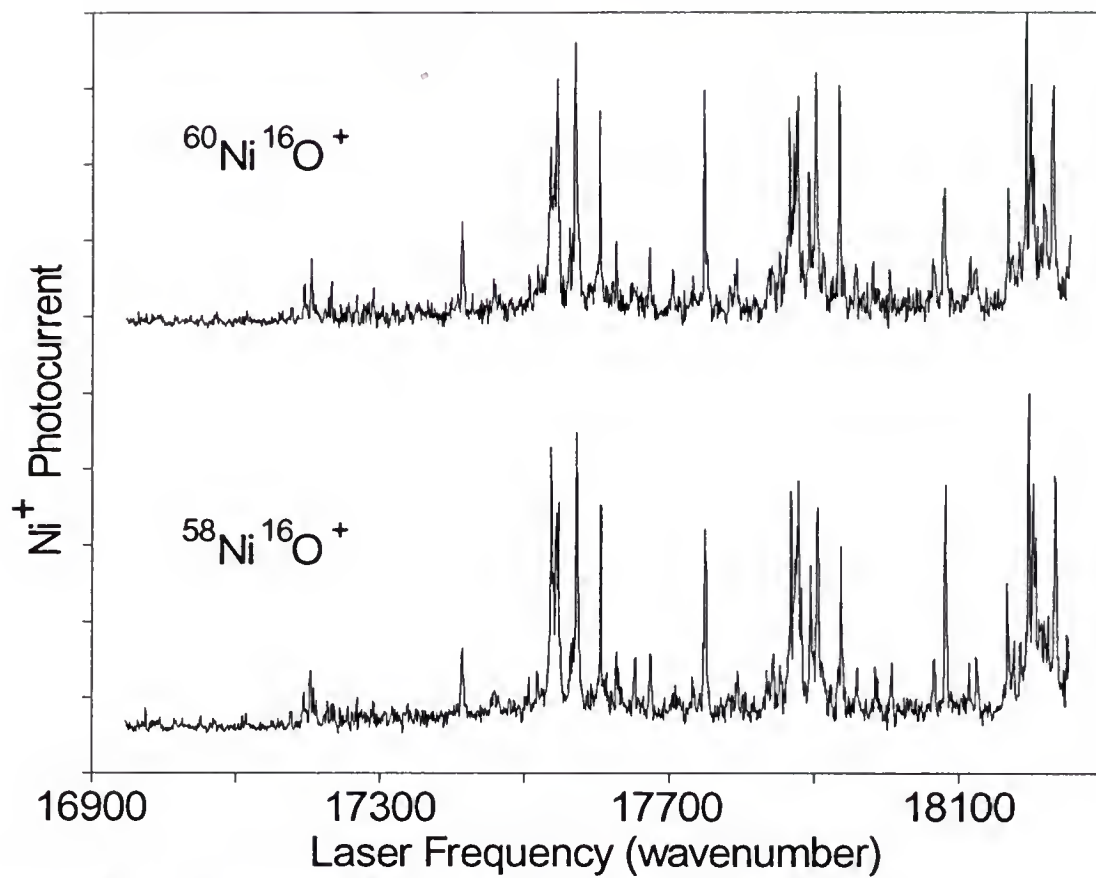


Figure 58. Photodissociation of $\text{NiO}^+ \rightarrow \text{Ni}^+ + \text{O}$.

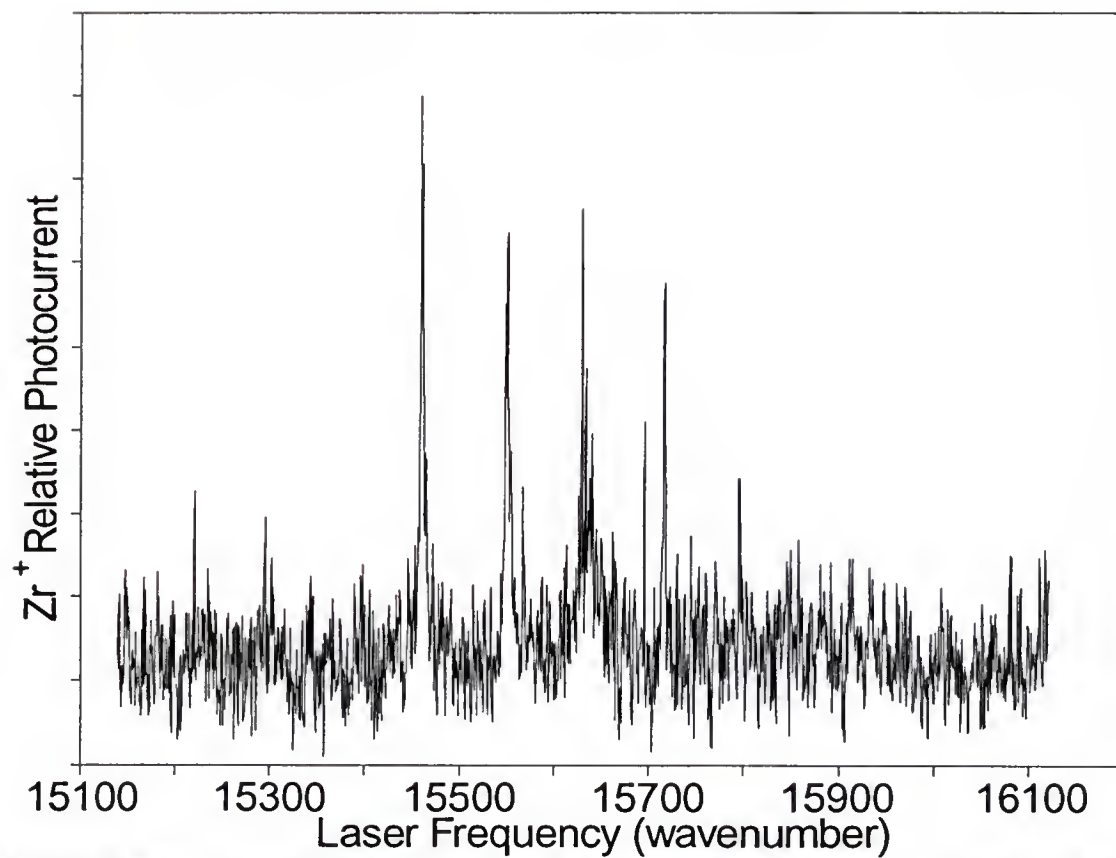


Figure 59. Photodissociation Spectrum of $\text{ZrOAr}^+ \rightarrow \text{ZrO}^+ + \text{Ar}$.

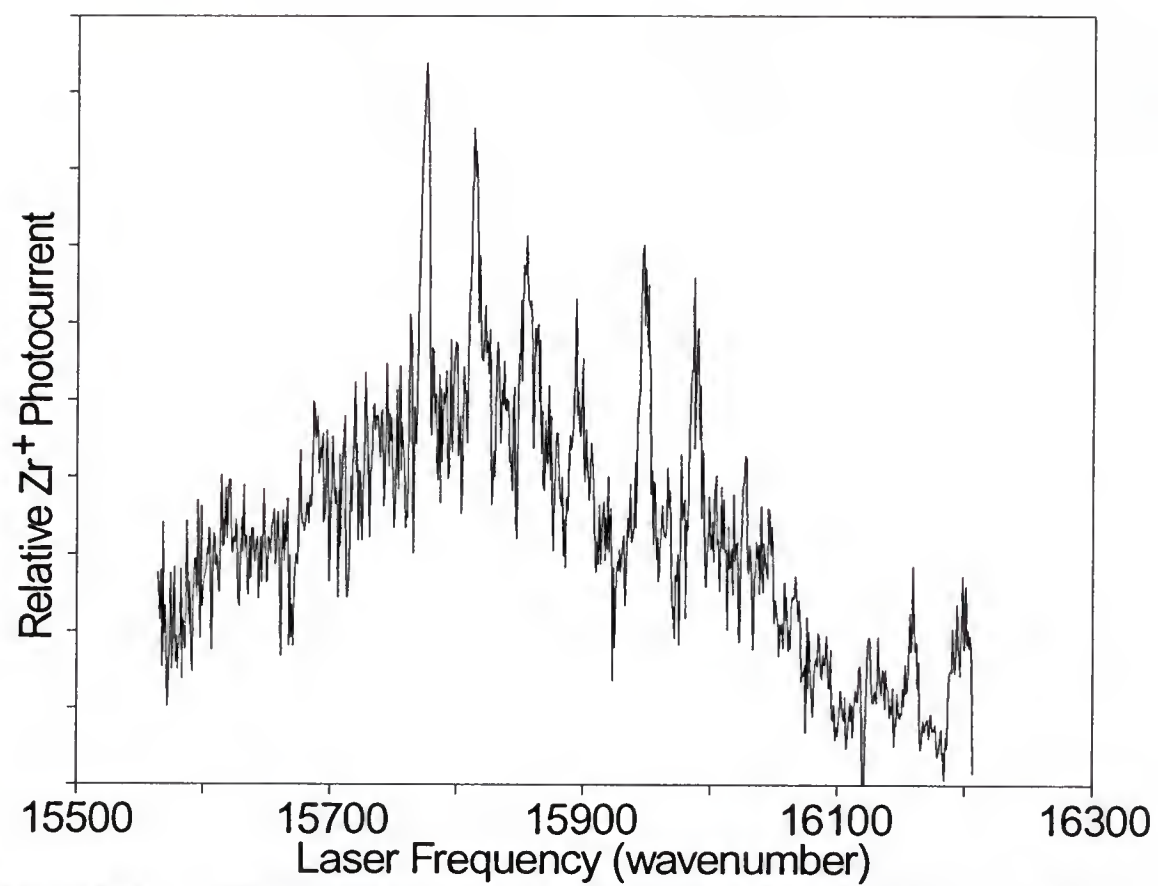


Figure 60. Photodissociation Spectrum for $\text{Zr}(\text{OCO})^+ \rightarrow \text{Zr}^+ + \text{OCO}$.

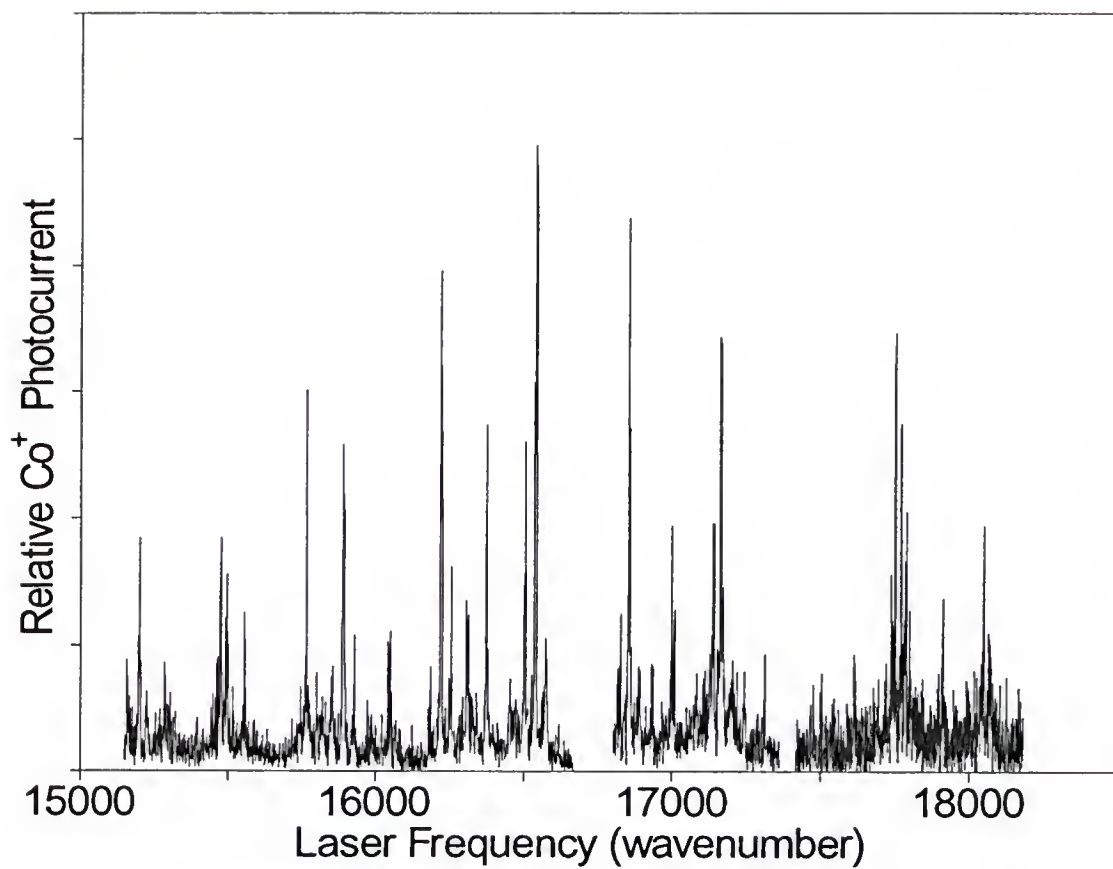


Figure 61. Photodissociation of $\text{Co}(\text{HOH})^+ \rightarrow \text{Co}^+ + \text{H}_2\text{O}$.

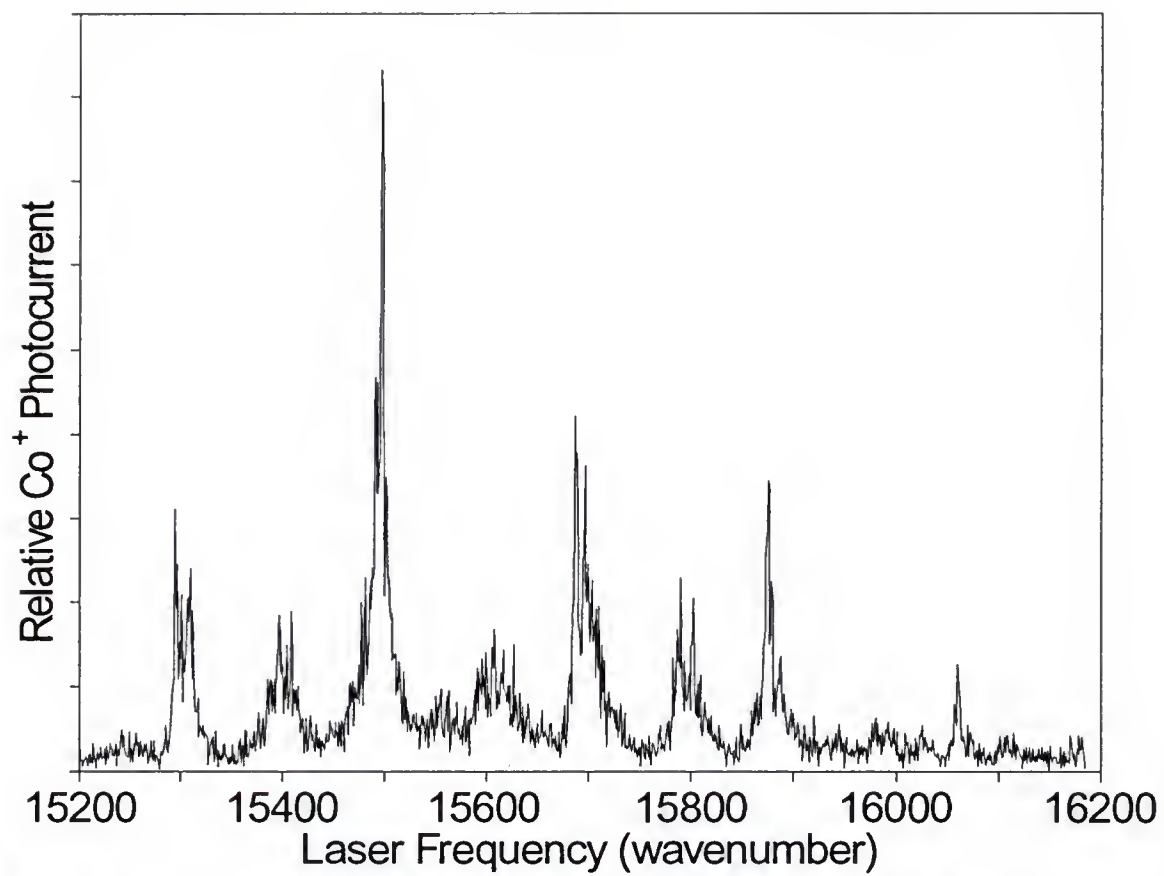


Figure 62. Photodissociation of $\text{Co(OCO)}^+ \rightarrow \text{Co}^+ + \text{CO}_2$.

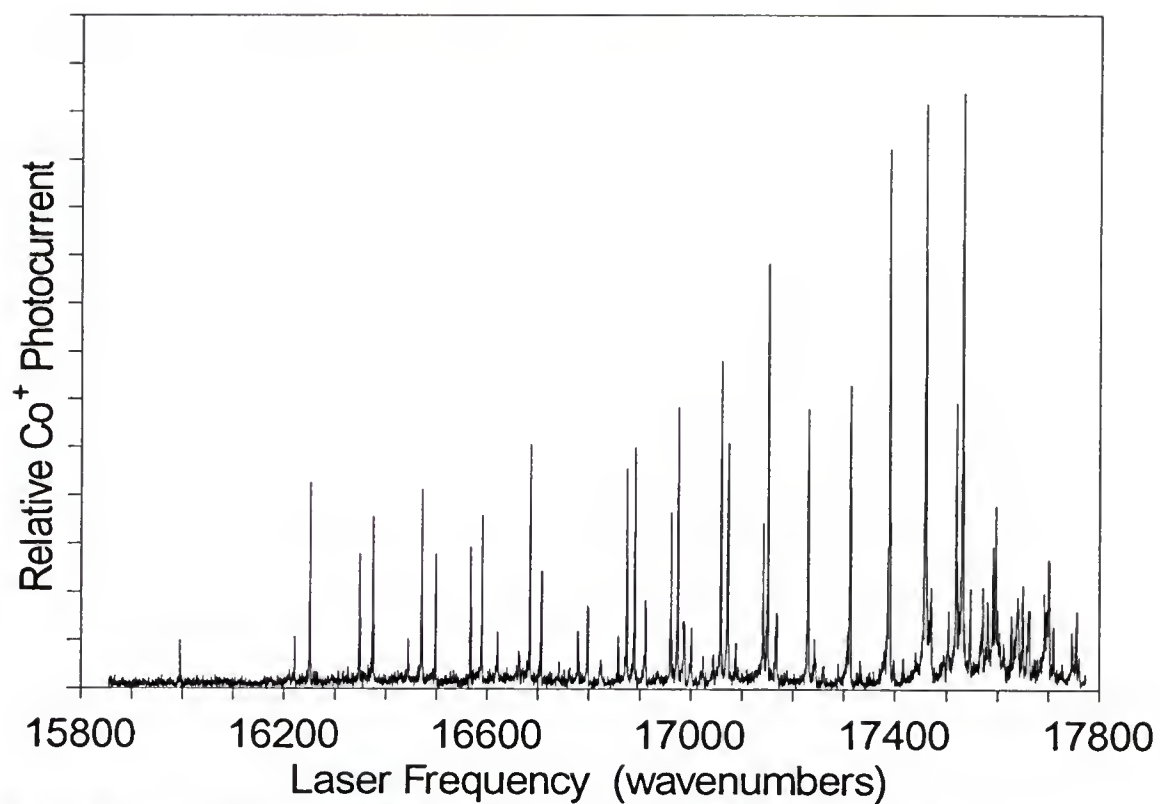


Figure 63. Photodissociation of $\text{Co}(\text{NN})^+ \rightarrow \text{Co}^+ + \text{N}_2$.

REFERENCES

1. K. P. Huber and G. Herzberg, *Constants of Diatomic Molecules* (Van Nostrand, New York, 1979).
2. M. D. Morse, *Chem. Rev.*, 86 (1986) 1049.
3. G. A. Somerjai, *Principle of Surface Chemistry* (Prentice-Hall, Englewood Cliffs, New Jersey, 1972).
4. M. M. Taqui Khan, and A. E. Martell, *Homogeneous Catalysis by Metal Complexes* (Academic, New York, 1974).
5. G. Herzberg, *Spectra of Diatomic Molecules*, (Van Nostrand Reinhold Co., New York, 1950).
6. P. Kebarle, and A. M. Hogg, *J. Chem. Phys.*, 42 (1964) 798.
7. A. W. Castleman Jr. and R. G. Keesee, *Chem. Rev.* 86 (1986) 589.
8. E. E. Ferguson, *Annu. Rev. Phys. Chem.*, 26 (1975) 17.
9. A. W. Castleman, Jr. and D. M. Tilmann, *Gaseous Ion Chemistry and Mass Spectrometry*, edited by J. H. Futrell (John-Wiley, New York, 1986).
10. P. M. Holland and A. W. Castleman, Jr., *J. Chem. Phys.*, 76 (1982) 4195.
11. J. J. Turner, M. B. Simpson, M. Poliakoff, and W. B. Maier, *J. Am. Chem. Soc.*, 105 (1983) 3898.
12. P. M. Hodges, S. A. Jackson, J. Jacke, M. Poliakoff, J. T. Turner, and F. W. Grevels, *J. Am. Chem. Soc.*, 112 (1990) 1234.
13. L. B. Knight, Jr., *Acc. Chem. Res.*, 19 (1986) 313.
14. R. J. Van Zee and W. Weltner, Jr., *J. Chem. Phys.*, 89 (1988).
15. J. P. Maier, *Int. J. Mass Spectrom. Ion Processes*, 104 (1991) 1.

16. J. B. Hopkins, P. R. R. Langridge-Smith, M. D. Morse, and R. E. Smalley, *J. Chem. Phys.*, 78 (1983) 1627
17. L.-S. Zheng, P. J. Brucat, C. L. Pettiette, S. Yang and R. E. Smalley, *J. Chem. Phys.*, 83 (1985) 4274.
18. P. P. Wegener (Editor), *Molecular Beams and Low Density Gasdynamics* (Marcel Dekker, Inc., New York 1974).
19. D. E. Lessen and P. J. Brucat, *Chem. Phys. Lett.*, 149 (1988) 10.
20. R. D. Zucker, *Fundamentals of Gas Dynamics*, (Matrix Publishers, Inc., Champaign, IL, 1977).
21. Klotz and Rosenberg, *Chemical Thermodynamics*, 4th ed., (Benjamin Cummings, Menlo Park, CA, 1986).
22. J. B. Anderson and J. B. Fenn, *Phys. Fluids*, 8 (1964) 780.
23. J. E. A. John, *Gas Dynamics*, (Allyn and Bacon, Boston , 1971).
24. J. P. Toennies and K. Winkelmann, *J. Chem. Phys.*, 66 (1977) 3965.
25. M. Moskovits, *Metal Clusters*, (John Wiley, New York, 1986).
26. W. C. Wiley and I. H. McLaren, *Rev. Sci. Instrum.* 26 1150, (1955).
27. Galileo Detector Assemblies Data Sheet No. 7000, Galileo Corporation, Sturbridge, MA, 1990.
28. A. Ll. Hughes and V. Rojansky, *Phys. Rev.* 34, 284 (1929).
29. A. Ll. Hughes and J. H. McMillen, *Phys. Rev.* 34 (1929) 284.
30. D. L. Andrews, *Laser in Chemistry*, (Springer-Verlag, New York, 1986).
31. K. C. Smyth, P. K. Schenck, *Chem. Phys. Lett.*, 55, 466 (1978).
32. J. K. Nestor, *Applied Optics* 21, 4154 (1982).

33. CRC Handbook of Chemistry and Physics, edited by R. C. Weast (Chemical Rubber, Cleveland, 1984, 65th ed.).
34. W. Demtroder, Laser Spectroscopy, Basic Concepts and Instrumentation, Chemical Physics 5, (Springer-Verlag, 3rd ed., New York, 1988).
35. H. Wollnik, Optics of Charged Particles (Academic Press, Inc. Orlando, FL, 1987).
36. United States Energy Research and Development Administration. National Instrumentation Methods Committee, CAMAC Tutorial Articles, (U.S. Government Print Office, 1976).
37. C. E. Moore, Atomic Energy Levels, NBS Circular No. 467 (Nat'l. Bur. Std., Washington, 1952).
38. D. E. Lessen and P. J. Brucat, J. Chem. Phys., 90 (1989) 6296.
39. D. E. Lessen and P. J. Brucat, Chem. Phys. Lett., 160 (1989) 609.
40. I. N. Levine, Physical Chemistry, 2nd ed., (McGraw Hill, New York, 1983).
41. I. N. Levine, Molecular Spectroscopy, (John Wiley, New York, 1975).
42. J. O. Hirschfelder, C. F. Curtiss and R. B. Bird, Molecular Theory of Gases and Liquids, (John Wiley, New York, 1964).
43. D. E. Lessen and P. J. Brucat, J. Chem. Phys., 91 (1989) 4522.
44. J. D. Graybeal, Molecular Spectroscopy, (McGraw-Hill, New York, 1988).
45. J. I. Steinfeld, Molecules and Radiation, 2nd ed. (MIT Press, Cambridge, MA, 1985).
46. R. J. LeRoy and R. B. Bernstein, J. Chem. Phys., 52 (1970) 3869.
47. R. J. LeRoy and R. B. Bernstein, J. Mol. Spect., 37 (1971) 109.
48. H. J. Fischbeck and K. H. Fischbeck, Formulas Facts and Constants, 2ed., (Springer-Verlag, New York, 1987).

49. J. O. Hirschfelder, C. F. Curtiss and R. B. Bird, *Molecular Theory of Gases and Liquids*, (John Wiley, New York, 1964).
50. C. J. F. Bottcher and P. Bordewijk, *Theory of Electric Polarization*, Vol. II, Elsevier, Amsterdam, 1978.
51. J. A. Dean, Editor, *Lange's Handbook of Chemistry*, 13th ed., (McGraw-Hill, New York, 1985).
52. R. E. Smalley, D. A. Auerbach, P. S. H. Fitch, D. H. Levy and L. Wharton, *J. Chem. Phys.* 66 (1977) 3778.
53. C. L. Callender, S. A. Mitchell, and P. A. Hackett, *J. Chem. Phys.*, 90 (1989) 5252.
54. M. Czajkowski, R. Bobkowski, and L. Krause, *Physical Rev. A*, 41 (1990) 243.
55. I. R. Gatland, *J. Chem. Phys.*, 75 (1981) 4162.
56. M. Takebe, *J. Chem. Phys.*, 78 (1983) 7223.
57. P. R. Kemper, M.-T. Hsu, and M. T. Bowers, *J. Phys. Chem.*, 95 (1991) 10600.
58. N. Aristov and P. B. Armentrout, *J. Phys. Chem.* 90 (1986) 5135.
59. S. H. Linn, J. M. Brom, Jr., W.-B. Tzeng and C. Y. Ng, *J. Chem. Phys.* 82 (1985) 648.
60. C. W. Bauschlicher Jr., S. R. Langhoff, *Chem. Phys. Lett.*, 158 (1989) 409.
61. C. W. Bauschlicher Jr., H. Partridge, S. R. Langhoff, *J. Chem. Phys.*, 91 (1989) 4733.
62. H. Partridge, C. W. Bauschlicher Jr., and S. R. Langhoff, *J. Phys. Chem.*, 96 (1992) 5350.
63. L. Dizic and P. Kebarle, *J. Phys. Chem.* 74 (1970) 1466.
64. P. M. Holland and A. W. Castleman, Jr., *J. Chem. Phys.* 76 (1982) 4195.
65. T. F. Magnera, D. E. David and J. Michl, *J. Am. Chem. Soc.* 111 (1989) 4100.
66. M. Karplus, R. N. Porter, *Atoms & Molecules: An Introduction for Students of Physical Chemistry* (Benjamin/Cummings, New York, 1970).

67. H. Partridge, C. W. Bauschlicher, Jr., and S. R. Langhoff, *J. Phys. Chem.*, 96 (1992) 5350.
68. G. von Helden, P. R. Kemper, M-T Hsu, M. T. Bowers, *J. Chem. Phys.*, 96 (1992) 6591.
69. C. W. Bauschlicher, Jr., H. Partridge, and S. R. Langhoff, *Chem. Phys. Lett.*, 165 (1990) 272.
70. W. W. Porterfield, *Inorganic Chemistry* (Addison-Wesley, Reading, MA, 1984).
71. D. E. Lessen and P. J. Brucat, *Chem. Phys. Lett.*, 25 (1988) 473.
72. R. N. Zare, *J. Chem. Phys.*, 40 (1964) 1934.
73. S. E. Koonin, D. C. Meredith, *Computational Physics* (Addison-Wesley, New York, 1990).
74. A. Messiah, *Quantum Mechanics* (John-Wiley, New York, 1958).
75. L. I. Schiff, *Quantum Mechanics*, (McGraw-Hill, New York, 1955).
76. E. Merzbacher, *Quantum Mechanics*, 2nd. ed. (John Wiley, New York, 1970).
77. P. M. Morse, *Phys. Rev.* 34 (1929) 57.
78. D. Lessen, R. L. Asher and P. J. Brucat, *Int. J. Mass. Spec. Ion. Process.* 102 (1990) 331.
79. R. L. Asher, D. A. Micha, P. J. Brucat, 96 (1992) 7683.
80. G. A. Somerjai, *Principles of Surface Chemistry*, (Prentice-Hall, Inc., Englewood Cliffs, New Jersey, 1972).
81. M. M. Taqui Khan and A. E. Martell, *Homogeneous Catalysis by Metal Complexes*, (Academic Press, New York, 1974).
82. R. M. Silverstein, G. C. Bassler, and T. C. Morrill, *Spectrometric Identification of Organic Compounds*, 4th ed. (Wiley, New York, 1981).
83. N. Aristov and P. B. Armentrout, *J. Phys. Chem.*, 90 (1986) 5135.
84. P. B. Armentrout, L. F. Halle, and J. L. Beauchamp, *J. Chem. Phys.*, 76 (1982) 2449.

85. P. J. Robinson and K. A. Holbrook, *Unimolecular Reactions* (Wiley-Interscience, London, 1972).
86. R. G. Pearson and J. W. Moore, *Kinetics and Mechanisms*, (John Wiley and Sons, New York, 1981).
87. C. W. Bauschlicher, Jr., H. Partridge, and S. W. Langhoff, *J. Chem. Phys.* 91 (1989) 4273.
88. P. J. Marinelli and R. R. Squires, *J. Am. Chem. Soc.*, 111 (1989) 4101.
89. T. F. Magnera, D. E. David and J. Michl, *J. Am. Chem. Soc.*, 111 (1989) 4100.
90. M. Rosi and C. W. Bauschlicher, Jr., *J. Chem. Phys.*, 90 (1989) 7264.
91. K. A. Gingerich, *Faraday Symp. Chem. Soc.*, 14 (1980) 109.
92. J. Drowart and P. Goldfinger, *Angew. Chem. Intern. Ed. Engl.* 6 (1967) 581.
93. L. Lian, C.-X. Su, and P. B. Armentrout, *J. Chem. Phys.*, 96 (1992) 7542.
94. M. D. Morse, G. P. Hansen, P. R. R. Langridge-Smith, L. S. Zheng, M. E. Geusic, D. L. Michalopoulos and R. E. Smalley, *J. Chem. Phys.*, 41 (1984) 5400.
95. A. Kant, *J. Chem. Phys.*, 41 (1964) 1872.
96. T. H. Upton and W. A. Goddard, *J. Am. Chem. Soc.*, 100 (1978) 5659.
97. C. W. Bauschlicher, Jr., H. Partridge, and S. R. Langhoff, 195 (1992) 360.
98. M. Bogey, H. Bolvin, C. Demuynck, J. L. Destombes and B. P. Van Eijck, *J. Chem. Phys.*, 88 (1988) 4120.
99. T. H. Upton and W. A. Goddard III, *J. Am. Chem. Soc.*, 100 (1978) 5659.
100. I. Shim, J. P. Dahl and H. Johansen, *Intern. J. Quantum Chem.*, 15 (1979) 311.
101. J. O. Noell, M. D. Newton, P. J. Hay, R. L. Martin and F. W. Bobrowicz, *J. Chem. Phys.* 73 (1980) 4816.

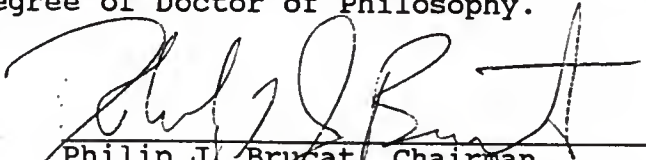
102. M. D. Morse, G. P. Hansen, P. R. R. Langridge-Smith, L.-S. Zheng, M. E. Geusic, D. L. Michealopoulos and R. E. Smalley, *J. Chem. Phys.*, 80 (1984) 5400.
103. A. Wolf and H. H. Schmidtke, *Intern. J. Quantum Chem.* 18 (1980) 1187.
104. B. Delley, A. J. Freeman and D. E. Ellis, *Phys. Rev. Letters* 50 (1983) 448.
105. W. F. Cooper, G. A. Clarke and C. R. Hare, *J. Phys. Chem.* 76 (1972) 2268.
106. D. L. Michalopoulos, M. E. Geusic, S. G. Hansen, D. E. Powers and R. E. Smalley, *J. Phys. Chem.*, 86 (1982) 3914.
107. Y. M. Efremov, A. N. Samoilova, and L. V. Gurvich, *Opt. Spectry.*, 36 (1974) 381.
108. P. A. Montano, H. Purdum, G. K. Shenoy, T. L. Morrison and W. Schulze, *Surface Sci.* 156 (1985) 228.
109. D. P. DiLella, W. Limm, R. H. Lipson, M. Moskovits and K. V. Taylor, *J. Chem. Phys.*, 77 (1982) 5263.
110. V. E. Bondybey and J. H. English, *Chem. Phys. Letters*, 94 (1983) 443.
111. K. Hilpert and K. Ruthardt, *Ber. Bundsenges. Physik. Chem.*, 91 (1987) 724.
112. A. Kant and B. Strauss, *J. Chem. Phys.*, 36 (1966) 3161.
113. M. D. Morse, *Chem. Rev.*, 86 (1986) 1049.
114. M. M. Goodgame and W. A. Goddard III, *Phys. Rev. Letters* 54 (1985) 661.
115. M. Moskovits and W. Limm, *J. Chem. Phys.*, 82 (1985) 4875.
116. W. J. Balfour, and R. F. Whitlock, *Can. J. Phys.*, 53 (1975) 474.
117. G. C. Maitland, M. Rigby, E. B. Smith, and W. A. Wakeham, *Intermolecular Forces* (Oxford, Oxford Press, 1987).
118. I. N. Levine, *Molecular Spectroscopy* (John-Wiley and Sons, New York, 1975).

BIOGRAPHICAL SKETCH

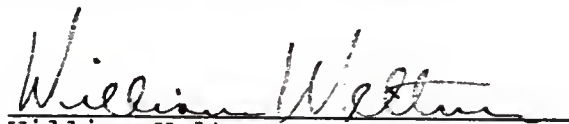
The author was born September 27, 1962, to Donald W. Lessen and Gayle A. Lessen in Lincoln, Illinois. He graduated from Lincoln High School in 1980, enrolled the following fall at Southern Illinois University, and received an Associates degree in electronic technology in the spring of 1982. After one summer of work in this field he returned to SIU in the fall of 1982. Four years later he graduated with a Bachelor of Science degree majoring in chemistry. From the fall of 1986 to the present the author has studied physical chemistry as a graduate student at the University of Florida.

On September 21, 1991, he was married to Christine Erickson.


I certify that I have read this study and that in my opinion it conforms to acceptable standards of scholarly presentation and is fully adequate, in scope and quality, as a dissertation for the degree of Doctor of Philosophy.


Philip J. Brucat, Chairman
Associate Professor of Chemistry


I certify that I have read this study and that in my opinion it conforms to acceptable standards of scholarly presentation and is fully adequate, in scope and quality, as a dissertation for the degree of Doctor of Philosophy.


William Weltner
Professor of Chemistry

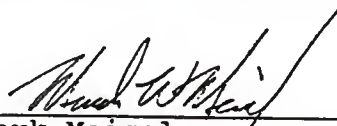
I certify that I have read this study and that in my opinion it conforms to acceptable standards of scholarly presentation and is fully adequate, in scope and quality, as a dissertation for the degree of Doctor of Philosophy.


Martin Vala
Professor of Chemistry

I certify that I have read this study and that in my opinion it conforms to acceptable standards of scholarly presentation and is fully adequate, in scope and quality, as a dissertation for the degree of Doctor of Philosophy.


John Eyler
Professor of Chemistry

I certify that I have read this study and that in my opinion it conforms to acceptable standards of scholarly presentation and is fully adequate, in scope and quality, as a dissertation for the degree of Doctor of Philosophy.



Mark Meisel
Assistant Professor of Physics

This dissertation was submitted to the Graduate Faculty of the Department of Chemistry in the College of Liberal Arts and Sciences and to the Graduate School and was accepted as partial fulfillment of the requirements for the degree of Doctor of Philosophy.

December 1992



Madelyn Lockhart
Dean, Graduate School

UNIVERSITY OF FLORIDA



3 1262 08557 0009